TECHNICAL REPORT DOCUMENTATION PAGE

DRISI-2011 (REV 10/1998)

Lock Data on Form

1. REPORT NUMBER	2. GOVERNMENT ASSOCIATION NUMBER	3. RECIPIENT'S CATALOG NUMBER
CA 23-3679		

4. TITLE AND SUBTITLE Fault Displacement Hazard	5. REPORT DATE Februay 28, 2023
	6. PERFORMING ORGANIZATION CODE
7. AUTHOR Fault displaecemnet hazard group chaired by Prof. Yousef Bozorgnia	8. PERFORMING ORGANIZATION REPORT NO. Report GIRS-2021-08
9. PERFORMING ORGANIZATION NAME AND ADDRESS University of California, Los Angeles (UCLA)	10. WORK UNIT NUMBER
	11. CONTRACT OR GRANT NUMBER 65A0789
12. SPONSORING AGENCY AND ADDRESS Mailbox: 140648, 10889 Wilshire Blvd, Suite 700, Los Angeles, CA 90095-1406	13. TYPE OF REPORT AND PERIOD COVERED Final
	14. SPONSORING AGENCY CODE

15. SUPPLEMENTARY NOTES

16. ABSTRACT

As part of the Fault Displacement Hazard Initiative, a comprehensive database of fault displacement and model to estimate fault displacement were developed. The model includes both median prediction as well as variability of fault displacement estimates. The database and model are publicly available through UCLA Natural Hazards Risk and Resiliency Research Center (NHR3) web site and can be used by Caltrans engineers to estimate the amount of fault displacement in CA. Multiple sub-tasks reports have been drafted and posted at UCLA NHR3 web site at: https://www.risksciences.ucla.edu/nhr3/fdhi/home

17. KEYWORDS	18. DISTRIBUTION STATEMENT	
Fault displacement, earthquake hazard		
19. SECURITY CLASSIFICATION (*of this report*) Public	20. NUMBER OF PAGES 300 pages	21. COST OF REPORT CHARGED

DISCLAIMER STATEMENT

NATURAL HAZARDS RISKS AND RESILIENCY RESEARCH CENTER (NHR3)

UCLA

Fault Displacement Hazard Project

Final Report on the UCLA-Caltrans Research Project

Principal Investigator: Dr. Yousef Bozorgnia

Natural Hazards Risk and Resiliency Research Center (NHR3)

And

Department of Civil and Environmental Engineering

University of California, Los Angeles (UCLA)

February 28, 2023

Introduction

The research project is on *Fault Displacement Hazard*. This project is part of a larger initiative: Fault Displacement Hazard Initiative (FDHI). The contract between Caltrans and UCLA was signed on May 12, 2020. The project has been completed successfully. Bellow is the list of tasks. Each task has its own report, as attached here.

List of Tasks of the Project

According to the Caltrans contract, the research project has six tasks. The list of the tasks, their due dates and status are shown in Table 1.

Deliverable	Description	Due Date	Status
Task 1: Database of international fault rupture	Extract and organize data from the international database "SURE"	12/31/2020	Completed
Task 2: Ridgecrest Fault Data Report	Extract and organize data for the 2019 Ridgecrest earthquake sequence	12/31/2020	Completed
Task 3: Implementation Report	Develop a database and flatfile of the fault displacement	03/31/2021	Completed
Task 4: Post all data at UCLA web site	Organize and post all fault displacement data at UCLA web site	5/31/2021	Complete
Task 5: Fault displacement model	Develop a fault displacement model using empirical data	12/31/2021	Complete
Task 6: Final report	Draft final report for Caltrans	3/31/2022	This Report

Table 1: Tasks, Due Dates, and Status

Tasks 1, 2 and 3

The final report containing the outcomes of Task 1, 2, and 3 (all related to the database development) is attached to this report. It should be noted that the draft report includes the outcomes of the specified Tasks in the Caltrans contract (Tasks 1, 2, and 3) plus additional tasks supported by other agencies. In summary, each funding agency receives the outcomes of its own specific tasks, plus more related to the entire Initiative.

Task 4

The fault displacement database has been posted at UCLA web site at:

https://drive.google.com/file/d/1lrnEQsNsPXG0jRHuFSBuOnkSJbyDYhjZ/view

The database can also be accessed as Appendices of the final report for Task 1, 2, and 3 (as indicated above).

Task 5

A comprehensive model for fault displacement has been developed and it has been documented in a report that is attached to this Final Report.

NATURAL HAZARDS RISKS AND RESILIENCY RESEARCH CENTER (NHR3)

UCLA

Final Report on Tasks 1, 2, and 3: Fault Displacement Database

Cal Poly

Caltech

SCEC
AN NSF+USGS CENTER

UC Irvine

UCLA

UC Santa Barbara

USC

Fault Displacement Hazard Initiative Database

Alexandra Sarmiento, P.E., C.E.G.
Danielle Madugo
Yousef Bozorgnia, Ph.D, P.E.
Andi Shen
Silvia Mazzoni, Ph.D.
University of California, Los Angeles

Grigorios Lavrentiadis, Ph.D.
University of California, Berkeley and Los Angeles

Timothy Dawson, C.E.G.
California Geological Survey Los Angeles

Christopher Madugo, Ph.D.
Albert Kottke, Ph.D., P.E.
Pacific Gas & Electric Company

Stephen Thompson, Ph.D., C.E.G.
Lettis Consultants International

Stéphane Baize, Ph.D.
Institut de Radioprotection et de S? reté Nucléaire

Christopher Milliner, Ph.D.
California Institute of Technology

Fiia Nurminen
Paolo Boncio, Ph.D.
Universit? G. d'Annunzio di Chieti-Pescara

Francesco Visini, Ph.D.
Istituto Nazionale di Geofisica e Vulcanologia

A report on research supported by Pacific Gas & Electric Company, High-Speed Rail Authority, California Department of Transportation, Southern California Gas Company, Los Angeles Department of Water and Power, and California Energy Commission.

Report Report GIRS-2021-08
DOI: 10.34948/N36P48

University of California, Los Angeles (headquarters)

Natural Hazards Risk & Resiliency Research Center

B. John Garrick Institute for the Risk Sciences

Fault Displacement Hazard Initiative Database

Alexandra Sarmiento, P.E., C.E.G.
Danielle Madugo
Yousef Bozorgnia, Ph.D, P.E.
Andi Shen
Silvia Mazzoni, Ph.D
University of California, Los Angeles

Grigorios Lavrentiadis, Ph.D.
University of California, Berkeley and Los Angeles

Timothy Dawson, C.E.G.
California Geological Survey

Christopher Madugo, Ph.D.
Albert Kottke, Ph.D., P.E.
Pacific Gas & Electric Company

Stephen Thompson, Ph.D., C.E.G.
Lettis Consultants International

Stéphane Baize, Ph.D.
Institut de Radioprotection et de S?reté Nucléaire (IRSN)

Christopher Milliner, Ph.D.
California Institute of Technology

Fiia Nurminen
Paolo Boncio, Ph.D.
Universit? G. d'Annunzio di Chieti-Pescara

Francesco Visini, Ph.D.
Istituto Nazionale di Geofisica e Vulcanologia

A report on research conducted with support from Pacific Gas & Electric Company, California High-Speed Rail Authority, California Department of Transportation, Southern California Gas Company, Los Angeles Department of Water and Power, and California Energy Commission.

Report GIRS-2021-08

Natural Hazards Risk and Resiliency Research Center
B. John Garrick Institute for the Risk Sciences
University of California, Los Angeles (Headquarters)

July 19, 2022
Revision 3

ABSTRACT

This report presents the development and results of a new surface rupture mapping and fault displacement database. The new database provides an updated and standardized collection of fault displacement measurements and surface rupture maps. The work was completed as part of the Fault Displacement Hazard Initiative (FDHI) Project, which is a multi-year and community-based research project coordinated by the University of California. Next-generation fault displacement models are being developed through the FDHI Project, and the new models will improve estimates of the probability, amplitude, and spatial distribution of principal and distributed displacements in surface-rupturing earthquakes. The FDHI Database provides a common set of inputs that can be used by model development teams, allowing a more systematic comparison of model performance. Our new database contains metadata and geospatially-controlled surface rupture and fault displacement data from 75 global historical earthquakes of **M** 4.9 to 8.0 and all styles of faulting. The data were collected collaboratively through a literature review and have been assessed in detail for completeness, accuracy, and consistency. Analysis and geologic interpretation of the raw data were performed to meet model development needs, including the development of an event-specific coordinate system for each earthquake, classifying ruptures and measurements as principal or distributed, and developing recommended net slip amplitudes from reported slip components. All information is contained in a structured relational database, and the contents have been aggregated into flatfiles for formal documentation and end-user convenience. The FDHI Database is anticipated to be used by multiple model development teams in the FDHI Project and will also support related research across the geoscience community. The database and its documentation are available through the Natural Hazards Risk and Resiliency Research Center (NHR3) web site (https://www.risksciences.ucla.edu/nhr3).

ACKNOWLEDGMENTS

Support for this project was provided by the Pacific Gas & Electric Company, California High-Speed Rail Authority, California Department of Transportation, Southern California Gas Company, Los Angeles Department of Water and Power, and California Energy Commission. The California Geological Survey, United States Geological Survey, Southern California Earthquake Center, California Institute of Technology, and Lettis Consultants International were partners in this project.

The support of these organizations is gratefully appreciated. The opinions, findings, conclusions, or recommendations expressed in this publication are those of the authors and do not necessarily reflect the views of the study sponsors, the Natural Hazards Risk and Resiliency Research Center (NHR3), or the Regents of the University of California.

In reviewing and compiling datasets for this project, we reached out to many researchers with data requests and queries, and we greatly appreciate the timely and thorough responses we received. The authors also wish to thank Dr. Paolo Zimmaro for early discussions and advice on the relational database schema and for recommending the SchemaSpy software to document the schema in HTML format.

The FDHI database was developed through constructive interactions and teamwork with the FDHI Project team members. The authors are grateful to the model developers for their guidance, feedback, and technical review of the database contents.

ADDENDUM

The initial version of this report was publicly released as Revision 2, dated August 3, 2021. The authors subsequently compiled nine additional historical surface-rupturing earthquake datasets and expanded the dataset for one earthquake. For convenience, the text and appendices of this report has been updated to reflect these additions, including the contents of the digital files in Appendix A. A summary of the changes is provided below. The updated version of this report is Revision 3, dated July 19, 2022.

The following earthquakes were added to the database in Revision 3:

- 2001 **M** 7.8 Kunlun (Kokoxili), Northern Tibet, EQ_ID = 67
- 2019 **M** 4.9 Le Teil, France, EQ_ID = 68
- 2016 **M** 6.2 Norcia (#1), Italy, EQ_ID = 69
- 1979 M_L 5.2 Homestead Valley, California, EQ_ID = 70
- 2018 **M** 7.5 Palu, Indonesia, EQ_ID = 71
- 2009 **M** 6.3 L'Aquila, Italy, EQ_ID = 72
- 1988 **M** 6.77 Spitak, Armenia, EQ_ID = 73
- 1993 **M** 6.2 Killari, India, EQ_ID = 74
- 1953 **M** 7.3 Yenice-Gonen, Turkey, EQ_ID = 75

The dataset for the San Fernando earthquake (EQ_ID = 25) was updated in Revision 3 as follows:

- A new composite rupture map was created from two datasets: CGS (which was previously the rupture map basis in Revision 2), and USGS. The additional USGS linework is generally in the Sylmar area, north of I-210. The geographic coordinates and rank classification were updated for several measurement sites to be consistent with the new linework.

CONTENTS

LIST OF FIGURES

LIST OF TABLES

1 Database Project Overview

The Fault Displacement Hazard Initiative (FDHI) Project is a multi-year and community-based research project coordinated by the University of California. The objective of the project is to develop a next-generation fault displacement database and models to estimate the amplitude and spatial distribution of principal and distributed displacements in surface-rupturing earthquakes. The new models will provide improved estimates of probabilistic and deterministic fault displacement hazard. To support the FDHI Project objective, we have developed a modern database of fault displacement measurements and surface rupture maps, incorporating earthquakes as recent as November 2019.

The FDHI Database was developed in collaboration with model developers, engineering community end-users, and project sponsors. The collaboration included monthly FDHI Project meetings beginning in June 2018, frequent Database Team meetings (nominally bi-weekly), and several topical working group meetings relating to model development. We also convened a one-day workshop in October 2019 to identify end-user needs and interface issues related to the new fault displacement models (Sarmiento et al., 2019a). The workshop was attended by over 40 professionals from industry, government, and academia specializing in seismic field geology, geodesy, model development, and simulations. Interim progress on the FDHI database and models was presented at the 2019 and 2021 Seismological Society of America Annual Meetings (Sarmiento et al., 2019b, 2021; Bozorgnia et al., 2021).

This Chapter presents an overview of the FDHI Database Project, including the motivation, goals, and intended use of the database and related products. We also provide a list of the key contributions of this database to the geoscience community, a summary of the database contents, and describe the report organization.

1.1 MOTIVATION AND GOALS

Surface-rupturing earthquakes produce permanent ground displacements along fault zones that can damage infrastructure (e.g., Proctor et al., 1972; Lee and Loh, 1999; Brandenberg et al., 2019). Surface rupture is generally defined as the instantaneous breaking of the ground surface along a fault in an earthquake. Not all earthquakes break the ground surface, but those that do are differentiated as "surface-rupturing earthquakes." The process and manifestation of surface rupture are distinct from other earthquake-related phenomena (such as liquefaction, lateral spreading, and landsliding), in that surface rupture is the result of a focused earthquake energy release along a fault plane at depth, whereas liquefaction, lateral spreading, and landsliding are deformations triggered by ground shaking (California Geological Survey, 2018). Displacements across a surface rupture can be significant (e.g., 12 m on the Kekerengu Fault in the 2016 **M** 7.8 Kaikoura earthquake; Kearse et al., 2018) and can adversely impact infrastructure. However, site-specific engineering solutions can be developed to allow structures to accommodate fault displacements (e.g., the Trans-Alaska Pipeline; Cluff et al., 2003).

The FDHI Project was initiated to develop a new fault displacement database and models in response to an increasing need to improve fault rupture and displacement hazard estimates for a variety of engineered structures and systems (Baize and Scotti, 2017). Several fault displacement models are currently used in standard practice (e.g., Youngs et al., 2003; Petersen et al., 2011; Moss and Ross, 2011; Wesnousky, 2008; Wells and Coppersmith, 1994); however, these models have significant differences in their input datasets, estimated displacement metrics, modeling techniques, and treatment of uncertainty. The next-generation fault displacement models developed through the FDHI Project will help mitigate these issues by using a common database and producing multiple displacement models in a coordinated research program.

Our new database (the FDHI Database) provides a common set of inputs that have been assessed for data quality and relevant metrics and metadata for use in the development of the new fault displacement models. Similar community-based and coordinated model development projects for ground motions have demonstrated the benefits of using a common database in model development (Chiou et al., 2008; Ancheta et al., 2014; Bozorgnia et al., 2014; Goulet et al., 2014; Bozorgnia and Stewart, 2020; Bozorgnia et al., in press). While the key benefit is that model performance can be more systematically evaluated and compared, the development of a common database is also more efficient for the scientific community and can support other research projects.

The fundamental goal of the FDHI Database Project was to support the development of new fault displacement models by systematically collecting, reviewing, and organizing relevant data in a database. The minimum required content included geospatial control for fault displacement measurements and mapped ruptures, inclusion of measurements on distributed faults, and first-order analysis and interpretation of raw data for global earthquakes of all magnitudes and styles of faulting. The database development was content- and quality-driven, with an emphasis on longevity, and the process involved extensive collaboration with the model developers to ensure the content addressed model development needs.

We performed repeated quality assurance (QA) and quality control (QC) checks on the database, with the support of participatory review from the model developers, to produce a more reliable and stable product. For this project, our data quality evaluations of completeness, accuracy, and consistency were considered to address QA. Data content requests and reviews by the model development teams ensured the final product addressed model development needs, addressing QC.

To further support longevity, the database was constructed as a structured relational database[1] A relational database is readily expandable to new data and new types of data, and it inherently contributes to QA/QC by minimizing errors due to repetition, enforcing data entry constraints, and maintaining references between individual data entries.

1.2 INTENDED USE AND COMMUNITY PRODUCTS

The FDHI Database was developed primarily for model developers to use in developing models that estimate the probability of principal and distributed surface rupture occurrence, as well as the amplitude of principal and distributed net displacement. While the database contents, QA/QC efforts, and analysis and geologic interpretation of the raw data were geared toward model developer needs, other researchers and industry professionals may find this collection of datasets useful. We encourage users of the database and its products to review Chapter 2 of this report, which discusses surface rupture manifestation and data collection and documentation methods, to understand the strengths and limitations of the original datasets used in this database. As discussed in Chapter 3, this database includes only global historical surface-rupturing earthquakes with sufficient data to meet the project event and dataset criteria.

All data, metadata[2], and interpretations are contained across 37 tables and 365 columns in one relational database file. The database contents have been aggregated into flatfiles[3], in *.csv format, for convenience and user-friendly documentation (Appendix A). We recommend most users of the FDHI Database (including model developers, geoscience researchers, and industry professionals) use the flatfiles to access the contents of the database. We used our knowledge of the database schema to produce the flatfiles and check for errors and inconsistencies; therefore, the flatfiles are the formal documentation of the database contents.

As described in Chapter 6 and Appendix A, three flatfiles are required to represent the three distinct information types contained in the database:

1. Measurements flatfile
2. Ruptures flatfile
3. Event-specific coordinate system (ECS) flatfile

For further convenience, these flatfiles are also provided as ESRI shapefiles for use in various Geographic Information System (GIS) software. We also created individual Google Earth

[1] A relational database uses a defined schema to store different data types in individual tables, relate the data between tables using key fields, and hold the information and schema in a single file. See Chapter 5 and Appendix B of this report for discussion.
[2] The term "metadata" is used herein to refer to information supporting data. For example, a displacement measurement is considered data, and information on the measurement technique (e.g., tape measure, optical image correlation) is considered metadata.
[3] A flatfile is a table created from a relational database.

*.kmz files for each earthquake in the FDHI Database. These Electronic Supplements are included in Appendix A.

1.3 PROJECT HIGHLIGHTS

The data quality review, analysis, and geologic interpretation efforts completed in this project are a unique feature of the FDHI Database and have resulted in a reliable and stable product that can be used by model development teams and the broader geoscience community. Significant advancements in this database, relative to other similar compilations, are summarized below.

- Our custom relational database was designed to systematically manage the project data and metadata while establishing a lasting framework that is expandable and extensible as additional earthquake data are available, new measurement techniques develop, and user needs evolve.
- The data were collected through an extensive literature review and were systematically assessed for completeness, accuracy, and consistency.
- Multiple data sources are included for the same event, where available, providing more complete spatial coverage of measurements and surface ruptures and allowing database users to make comparisons of alternative datasets.
- Terrain metrics are included for every measurement site, and geologic information is included for most sites (where available).
- A new event-specific coordinate system algorithm is developed to supplement geographic coordinates with strike-parallel and strike-normal ordinates for all measurement sites and surface rupture linework.
- All surface ruptures in the database are classified as principal or distributed rank based on detailed geologic evaluations.
- We introduce two new fault displacement measurement rank classifications (cumulative and total) to better distinguish measurements associated with multiple ruptures or wide measurement apertures. All fault displacement measurements in the database are classified as total, cumulative, principal, or distributed. Hanging wall and footwall flags are included for distributed measurements in reverse, normal, and oblique style earthquakes.
- Recommended net slip values (preferred and bounding maximum/minimum) are calculated from the reported slip components for each measurement. The basis for the calculations of each value is documented, and we assign a quality code with recommended usage in model development to each value.

1.4 DATABASE CONTENTS SUMMARY

We have assembled a geospatially-controlled relational database of surface rupture maps, measurements, and associated metadata for 75 global historical earthquakes of **M** 4.9 to 8.0 occurring between 1872 and 2019. Figure 1.1 shows the spatial distribution of the epicenters for 71 events in the database for which this information is available, and Figure 1.2 shows the same information for events in the conterminous United States and Mexico. The relative regional distribution of the 75 events is illustrated in the pie chart in Figure 1.3. Approximately 40% of the earthquakes in the database are from Western North America, which includes California, Nevada, Idaho, Montana, Alaska, and Mexico. One quarter of the events are from Japan, China, or Southeast Asia. There are also several events from Australia, which is a stable continental region.

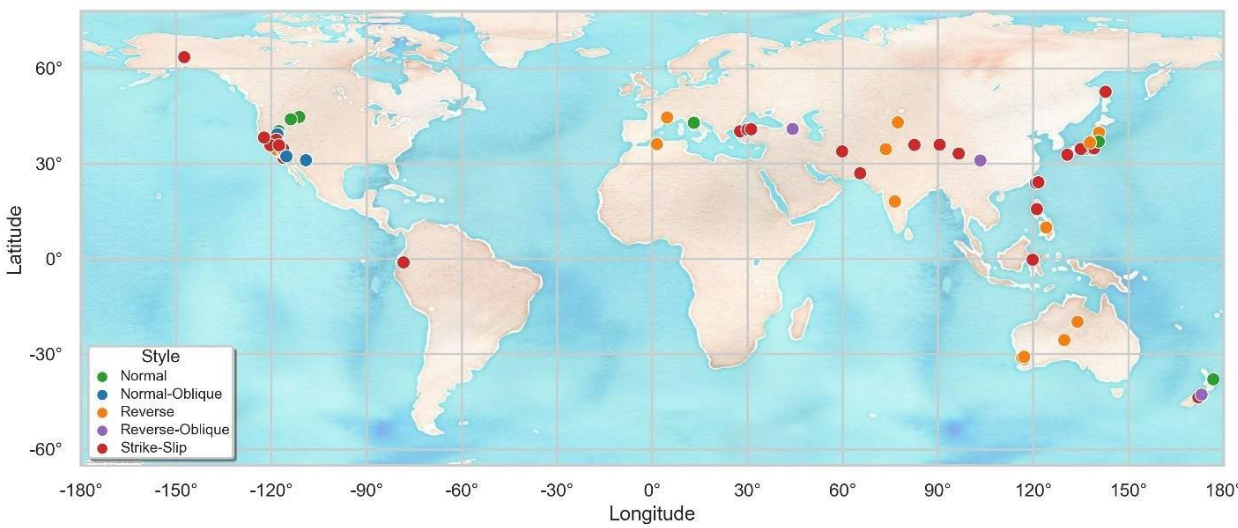

Figure 1.1. Epicentral locations of 71 of the 75 earthquakes in the FDHI Database (color-coded by style of faulting; see inset legend). Epicenters for the following events are not available: 1872 Owens Valley, California; 1912 Acambay, Mexico; 1986 Marryat Creek, Australia; and 2012 Pukatja, Australia.

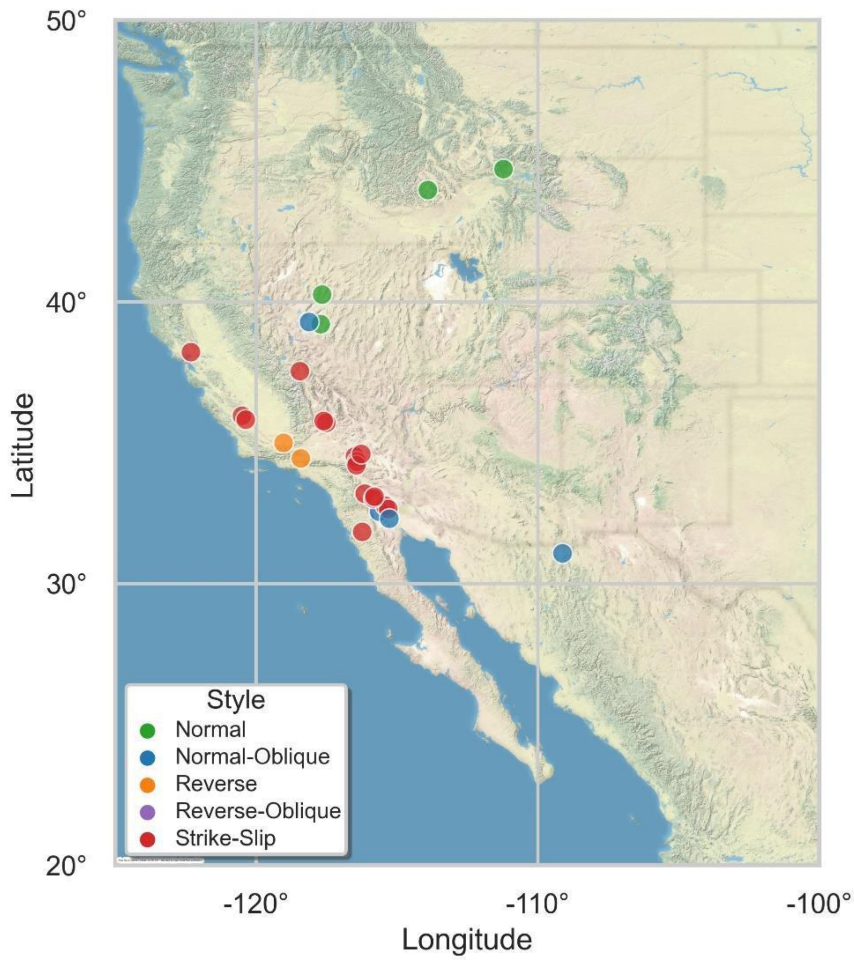

Figure 1.2. Epicentral locations of earthquakes in the FDHI Database in the conterminous United States and Mexico (color-coded by style of faulting; see inset legend). Epicenters for the 1872 Owens Valley, California and 1912 Acambay, Mexico earthquakes are not available.

Figure 1.4 shows the magnitude and style of faulting characteristics of the earthquakes in the database. All 66 events are ordered by date on the abscissa. Roughly 45% of the events are dominantly strike-slip, 20% are normal, and 35% are reverse. Overall, the events in the database span a magnitude range that corresponds to the hazard levels of interest for engineering design and analysis in active tectonic settings like California: more frequent smaller events (M ~6 to 6.5) that are more or less congruent with code-based hazard levels (e.g., ASCE 7-16 design response spectra), and larger (M ~7) events that are similar to the maximum considered earthquake hazard levels (e.g., ASCE 7-16 MCE_R level).

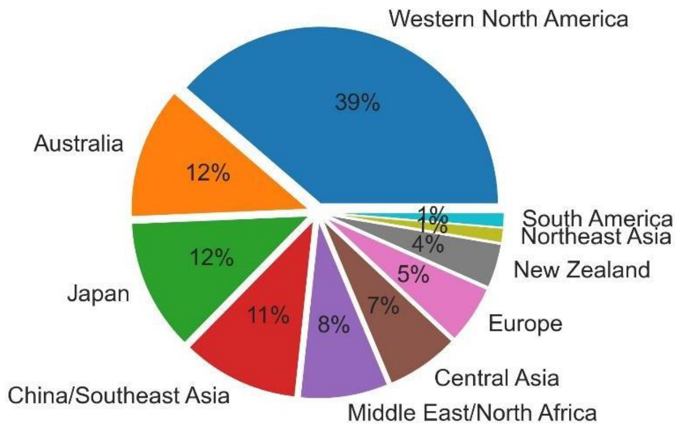

Figure 1.3. Regional distribution of earthquakes in the FDHI Database.

Event-specific metadata (including magnitude, magnitude type, hypocenter location, and style of faulting) are included for all earthquakes in the database. Dataset metadata (e.g., citation, mapping scale) are also included. The database includes over 87,000 individual point-in-space observations with geospatial control, including over 40,000 fault displacement measurements for a range of slip components (Figure 1.5). Surficial geologic unit classification (bedrock, young/old/undifferentiated alluvium; see Chapter 4.1 for definitions) is available for over 26,000 observation sites (Figure 1.5). The database also contains surface rupture maps for each earthquake with geospatial control on the rupture line vertices.

At the request of the model development teams, we also performed geologic interpretation of the rupture linework and displacement measurements to distinguish principal and distributed faulting (Chapter 2.5.3), aggregate the reported slip components into recommended net slip values for use in model development, and explicitly flag alternative measurements at the same location. Finally, as also requested by the model development teams, we developed an event-specific coordinate system (ECS) for each earthquake in the database. The ECS is a two-dimensional projection of the event data that accounts for curvature and discontinuities in the surface rupture trace. An example of the ECS is given in Figure 1.6, which also shows the mapped surface ruptures and interpreted principal/distributed classifications from the 1971 San Fernando (Sylmar) earthquake.

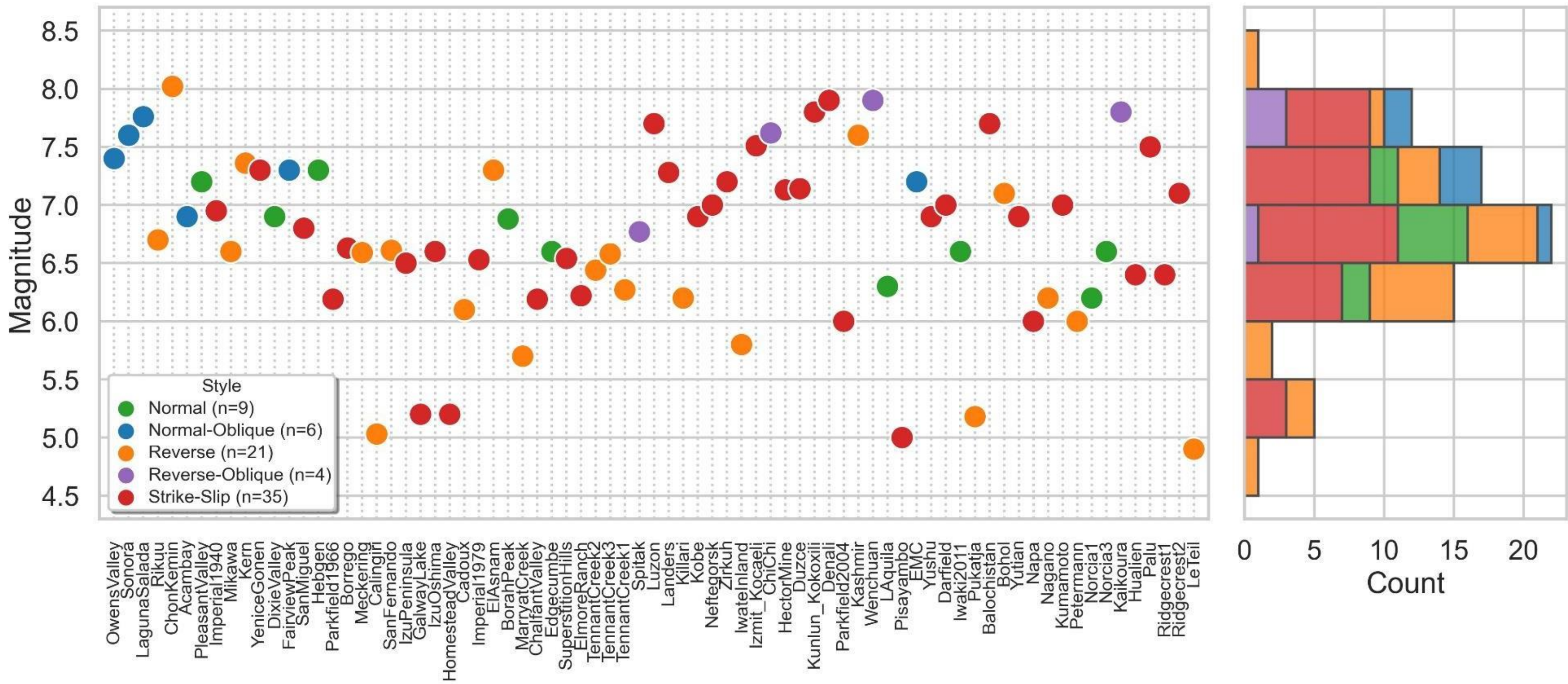

Figure 1.4. Magnitude and style of faulting of the 75 events in the FDHI Database.

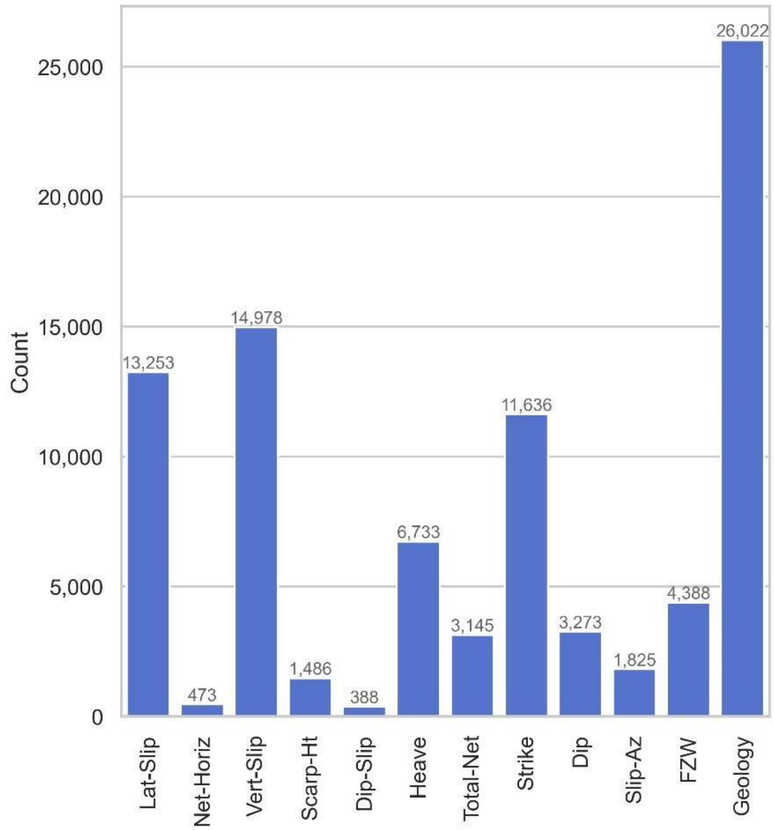

Figure 1.5. Number of measurements contained in the FDHI Database across all earthquakes and datasets. Slip components defined in Chapter 2.5.1 and in flatfiles in Appendix A.

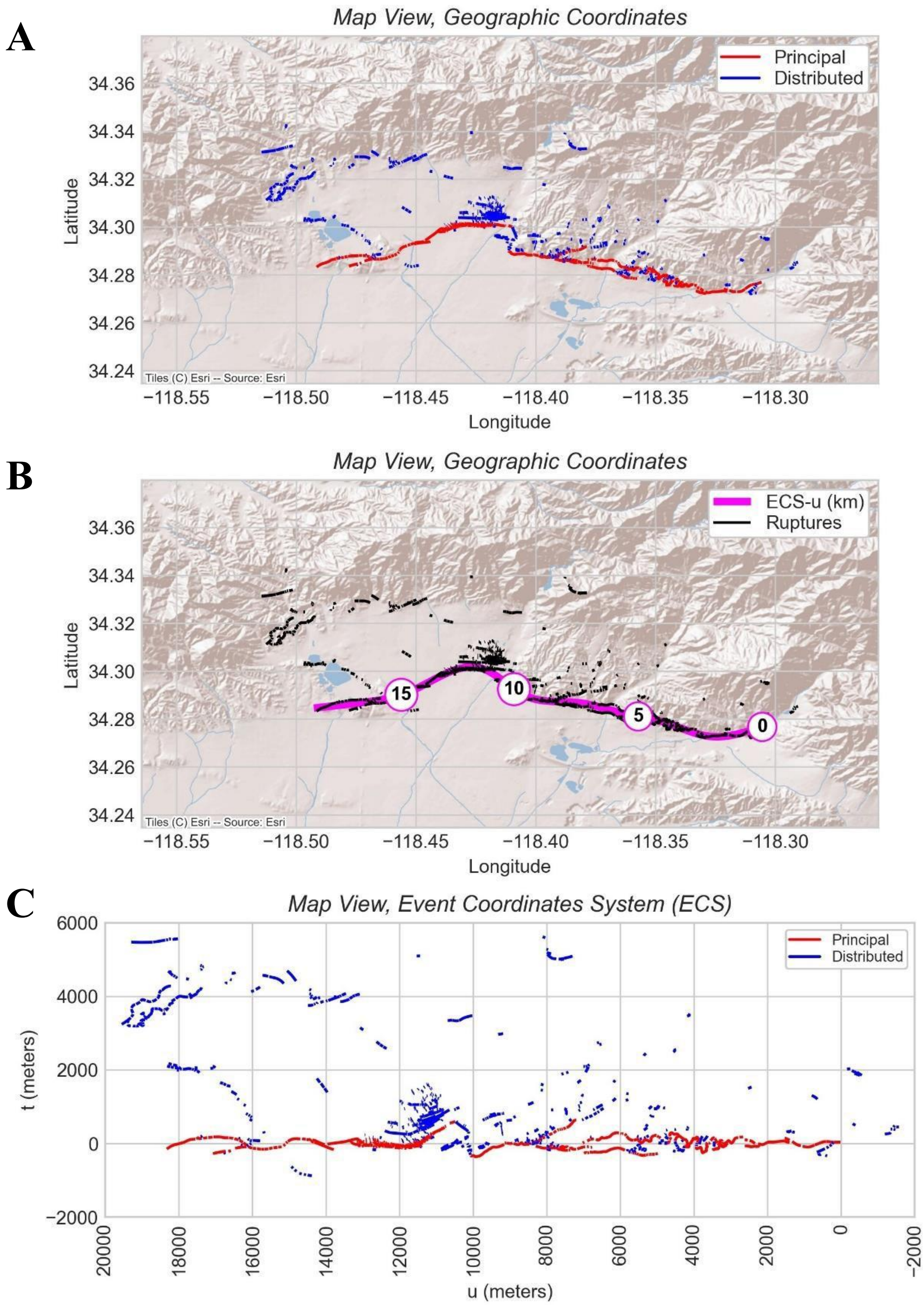

Figure 1.6. Surface rupture map from 1971 San Fernando (Sylmar) earthquake. EQ_ID = 25 in the FDHI Database. (A) Principal and distributed ruptures, geographic coordinates. (B) Ruptures and event-specific coordinate system (ECS) reference line, geographic coordinates; white circles are distance along reference line in kilometers. (C) Principal and distributed ruptures projected into ECS.

1.5 REPORT ORGANIZATON

The Chapters in this report document the development of the FDHI Database. (A separate report will document new models developed under the FDHI Project using this database). The process of building the database began with a systematic review of surface rupture characteristics, data collection tools, techniques, and reporting standards, and existing fault displacement and surface rupture compilations. We collaborated with the model developers to determine the initial database contents and then developed a custom relational database structure to accommodate the range of data types. We then reviewed the available published literature for geospatially-controlled measurements and rupture mapping from historical surface-rupturing earthquakes and performed first-order analysis and geologic interpretation of the raw datasets. All datasets were reviewed for quality and completeness before being imported into the database. Finally, we aggregated the database contents into flatfiles (*.csv format) for formal documentation and generated ESRI shapefiles (*.shp format) and Google Earth files (*.kmz format) for end-user convenience (Appendix A).

1.5.1 Definitions

Important terms are usually defined as they are introduced. In some cases, we defer detailed definitions to a specific chapter. For convenience, the following list summarizes some important terms and where they are defined in this report:

- Database-related terms (*relational database*, *flatfile*, and *metadata*) are defined in the footnotes in Chapter 1.2.
- *Principal* and *distributed* faulting are defined where they are first introduced in Chapter 2.5.3 are discussed in further detail in Chapter 4.3. The *total* and *cumulative* fault displacement measurement classifications are defined in Chapter 4.3.
- *Slip components* (e.g., vertical slip, fault-parallel slip) are defined in Chapter 2.5.1.

1.5.2 Chapters Overview

Chapter 2 of this report describes surface rupture characteristics with photographs of various types of complexities and reviews typical data sources and tools used to develop surface rupture maps and collect fault displacement measurements. Chapter 2 also provides a summary of key terms relating to surface rupture and fault displacements and their usage in this project.

Chapter 3 documents the data collection approach for this project. Chapter 3 includes event and dataset criteria, an overview of existing compilations, the standard workflow for developing data for each earthquake and dataset, and discussion of intentionally excluded data.

Chapter 4 describes the data analysis and interpretation applied to the collected data. The analyses include spatial analysis performed in GIS software to develop geologic information, elevation data and metrics, and the ECS. The interpretations include classifying or ranking ruptures and measurements generally as principal or distributed (additional classifications include cumulative and total, as described in Chapter 4.3), developing recommended net slip amplitudes for use in model development based on reported slip components, assigning recommended usage and quality codes to the measurement data, and explicitly identifying co-located alternative displacement measurements.

Chapter 5 describes technical aspects of the relational database development, including the database management system, database schema, and process of populating the database. More detail on the relational database is also documented in Appendix B.

Chapter 6 provides an overview of the flatfile documentation and contents. The flatfiles are contained in Appendix A of this report.

Chapter 7 discusses the QA/QC process applied throughout the database development and documentation.

Chapter 8 presents the conclusions of this report.

1.6 REFERENCES

American Society of Civil Engineers (ASCE) (2017). Minimum Design Loads and Associated Criteria for Buildings and Other Structures. ASCE Standard ASCE/SEI 7-16. American Society of Civil Engineers.

Ancheta, T. D., Darragh, R. B., Stewart, J. P., Seyhan, E., Silva,W. J., Chiou, B. S.-J., Wooddell, K. E., Graves, R. W., Kottke, A. R., Boore, D. M., Kishida, T., and Donahue, J. L., (2014). NGA-West2 database, *Earthquake Spectra,* **30**, 989–1005.

Baize, S. and Scotti, O. (2017). Fault Displacement Hazard Analysis Workshop in Menlo Park (USGS, California), 8-9/12/2016, Synthesis and Perspectives, *Institut Radioprotection S?reté Nucléaire*, 72 p.

Brandenberg, S. J., Wang, P., Nweke, C. C., Hudson, K., Mazzoni, S., Bozorgnia, Y., Goulet, C. A., Hudnut, K. W., Davis, C. A., Ahdi, S. K., Zareian, F., Fayaz, J., Koehler, R. D., Chupik, C., Pierce, I., Williams, A., Akciz, S., Hudson, M. B., Kishida, T., Brooks, B., Gold, R., Ponti, D., Scharer, K., McPhillips, D., DuRoss, C., Ericksen, T., Hernandez, J., Patton, J., Olson, B., Dawson, T., Treiman, J., Blake, K., Buchhuber, J., Madugo, C., Sun, J., Donnellan, A., Lyzenga, G., and Conway, E. (2019). Preliminary report on engineering and geological effects of the July 2019 Ridgecrest earthquake sequence. Report GEER-064, *Geotechnical Extreme Event Reconnaissance Association*.

Bozorgnia, Y., Abrahamson, N. A., Ahdi, S. K., Ancheta, T. D., Al Atik, L., Atchuleta, R. J., Atkinson, G.M., ... and Youngs, R. R. (in press). NGA-Subduction Research Program, *Earthquake Spectra*.

Bozorgnia, Y., Abrahamson, N., Arcos, B., Baize, S., Boncio, P., Chao, S.-H., Chen, R., Chiou, B., Dawson, T., Donahue, J., Goulet, C., Hanson, K., Kottke, A., Kuehn, N., Kuo, C.-H., Lavrentiadis, G., Madugo, D., Mazzoni, S., Milliner, C., Moss, R., Nurminen, F., Pace, B., Petersen, M., Sarmiento, A., Shen, A., Thomas, K., Thompson, S., Visini, F., Wang, Y., and Youngs, R. R. (2021). An Overview of the Fault Displacement Hazard Initiative Research Program. Presented at Seismological Society of America 2021 Annual Meeting, in *Seismological Research Letters*, **92**(2B), 1360-1361.

Bozorgnia, Y. and Stewart, J. P. (2020). Data Resources for NGA-Subduction Project. PEER Report 2020/02, *Pacific Earthquake Engineering Research Center*, University of California, Berkeley, CA.

Bozorgnia, Y., Abrahamson, N. A., Al Atik, L., Ancheta, T., D., Atkinson, G. M., Baker, J. W., Baltay, A., Boore, D. M., Campbell, K. W., Chiou, B. S. J., Darragh, R., Day, S., Donahue, J., Graves, R. W., Gregor, N., Hanks, T., Idriss, I. M., Kamai, R., Kishida, T., Kottke, A., Mahin, S. A., Rezaeian, S., Rowshandel, B., Seyhan, E., Shahi, S., Shantz, T., Silva, W., Spudich, P., Stewart, J. P., Watson-Lamprey, J., Wooddell, K., and Youngs, R. (2014). NGA-West2 Research Project, *Earthquake Spectra*, **30**(3), 973-987.

California Geological Survey (2018). Earthquake Fault Zones, A Guide for Government Agencies, Property Owners / Developers, and Geoscience Practitioners for Assessing Fault Rupture Hazards in California, Revised 2018, California Geological Survey Special Publication 42.

Chiou, B., Darragh, R., Gregor, N., and Silva, W. (2008). NGA project strong-motion database, *Earthquake Spectra*, **24**(1), 23-44.

Cluff, L. S., Page, R. A., Slemmons, D. B., and Crouse, C. B. (2003). Seismic hazard exposure for the Trans-Alaska pipeline, *In* Advancing Mitigation Technologies and Disaster Response for Lifeline Systems (pp. 535-546).

Goulet, C. A., Kishida, T., Ancheta, T. D., Cramer, C. H., Darragh, R. B., Silva, W. J., Hashash, Y. M. A., Stewart, J. P., Woodell, K. E., and Youngs, R. R. (2014). PEER NGA-East Database, PEER Report 2014/17, *Pacific Earthquake Engineering Research Center*, University of California, Berkeley, CA.

Kearse, J., Little, T. A., Van Dissen, R. J., Barnes, P. M., Langridge, R., Mountjoy, J., Ries, W., Villamor, P., Clark, K. J., Benson, A., Lamarche, G., Hills, M., and Hemphill-Haley, M. (2018). Onshore to offshore ground-surface and seabed rupture of the Jordan–Kekerengu–

Needles fault network during the 2016 Mw 7.8 Kaikōura earthquake, New Zealand, *Bulletin of the Seismological Society of America*, **108**(3B), 1573-1595.

Lee, G. C. and Loh, C. H. (1999). Preliminary report from MCEER-NCREE workshop on the 921 Taiwan earthquake, *Multidisciplinary Center for Earthquake Engineering Research*.

Moss, R. E. S. and Ross, Z. E. (2011). Probabilistic fault displacement hazard analysis for reverse faults, *Bulletin of the Seismological Society of America*, **101**(4), 1542-1553.

Petersen, M. D., Dawson, T. E., Chen, R., Cao, T., Wills, C. J., Schwartz, D. P., and Frankel, A. D. (2011). Fault displacement hazard for strike-slip faults, *Bulletin of the Seismological Society of America*, **101**(2), 805-825.

Proctor, R. J., Crook Jr., R., McKeown, M. H., and Moresco, R. L. (1972). Relation of known faults to surface ruptures, 1971 San Fernando earthquake, southern California, *Geological Society of America Bulletin*, **83**(6), 1601-1618.

Sarmiento, A., Baize, S., Boncio, P., Bozorgnia, Y., Dawson, T., Lavrentiadis, G., Madugo, D., Nurminen, F., Shen, A., and Thompson, S. (2021). A Next-Generation Fault Displacement and Surface Rupture Database. Presented at Seismological Society of America 2021 Annual Meeting, in *Seismological Research Letters*, **92**(2B), 1360.

Sarmiento, A., Dawson, T., Lavrentiadis, G., and Bozorgnia, Y. (2019a). Summary Report on the Fault Displacement Workshop Held on October 1, 2019, *Southern California Earthquake Center*, SCEC Award #19201.

Sarmiento, A., Abrahamson, N., Baize, S., Bozorgnia, Y, Chen, R., Coppersmith, K. J., Dawson, T. E., Donahue, J. L., Jacob, V., Ketabdar, M., Kottke, A. R., Kuehn, N., Lavrentiadis, G., Madugo, C., Mazzoni, S., Milliner , C., Shamsaabadi, A., Shantz, T., Shen, A., Thompson, S. C., and Youngs, R. R. (2019b). A New Model Database for Next-Generation Fault Displacement Hazard Analysis. Presented at Seismological Society of America 2019 Annual Meeting, Seattle, Washington, in *Seismological Research Letters*, **90**(2B), 1058.

Wells, D. L. and Coppersmith, K. J. (1994). New empirical relationships among magnitude, rupture length, rupture width, rupture area, and surface displacement, *Bulletin of the Seismological Society of America*, **84**(4), 974-1002.

Wesnousky, S. G. (2008). Displacement and geometrical characteristics of earthquake surface ruptures: Issues and implications for seismic-hazard analysis and the process of earthquake rupture, *Bulletin of the Seismological Society of America*, **98**(4), 1609-1632.

Youngs, R. R., Arabasz, W. J., Anderson, R. E., Ramelli, A. R., Ake, J. P., Slemmons, D. B., McCalpin, J. P., Doser, D. I., Fridrich, C. J., Swan III, F. H., Rogers, A. M., Yount, J. C., Anderson, L. W., Smith, K. D., Bruhn, R. L., Knuepfer, P. L. K., Smith, R. B., dePolo, C. M., O'Leary, D. W., Coppersmith, K. J., Pezzopane, S. K., Schwartz, D. P., Whitney, J.

W., Olig, S. S., and Toro, G. R. (2003). A methodology for probabilistic fault displacement hazard analysis (PFDHA), *Earthquake Spectra*, **19**(1), 191-219.

2 Surface Rupture Characteristics, Data Collection Methods, and Terminology

2.1 INTRODUCTION

The documentation of surface ruptures in an earthquake can vary significantly, owing to variations in mapping scale, rupture characteristics or expression, areas investigated, degree of preservation, level of effort, mapping standards, and the purpose of the rupture map. As a result, many scientists, engineers, and practitioners may be surprised by the variability of complexity and detail contained or absent in the database for individual earthquakes. Similarly, fault displacement measurements are also sometimes oversimplified, inconsistently documented, or incomplete for many reasons, and users of this database may also be surprised by the non-uniform spatial distribution of displacement measurements or the variability in alternative measurements at the same location. In this Chapter, we present examples through of photographs to show a range of surface rupture complexities and measurable, unmeasurable, or ambiguous features. We also provide an overview of the methods, tools, and techniques used in collecting surface rupture and fault displacement measurements after an earthquake. Finally, we define relevant geologic terms used in standard practice and the FDHI Database Project.

The goal of this Chapter is to give users of this database an understanding of what surface ruptures look like, how ruptures are represented on a map, and the strengths and limitations of the different methods, tools, and techniques that are used to document surface ruptures and fault displacements. An important conclusion of this Chapter is that variable documentation of the simplifications, assumptions, and terminology in rupture mapping and fault displacement measurement reporting is common in the original datasets we reviewed, and therefore the degree of simplification varies between events and sometimes within an event.

2.2 EXAMPLE MANIFESTATIONS OF SURFACE RUPTURE

Total surface rupture lengths are tens to hundreds of kilometers long, which presents many challenges in documenting the character and spatial distribution of the individual surface ruptures. Common challenges include inaccessible areas (e.g., private property, difficult terrain, offshore), deformation obscured by dense vegetation, snow, or landslides, post-earthquake ground surface modification (e.g., infrastructure repair work, weather/storm events), and resource limitations (e.g., time, budget, workforce). Distributed ruptures away from the principal fault and ruptures with small displacements suffer more of these limitations, as they are more easily overlooked by field reconnaissance teams and more susceptible to modification by surface processes. Although the quick turnaround time of high-resolution satellite-based data mitigates many of these challenges (Morelan and Hernandez, 2020; Milliner and Donnellan, 2020) for very recent and future earthquakes, the documentation of nearly all historical earthquakes was limited by these challenges.

In this Chapter, we present maps and photographs of surface rupture to reveal (un)intentional simplifications inherent in original datasets and the challenges in quantitatively capturing all deformation associated with a surface rupture. The maps demonstrate important differences in mapping scale that can arise from the data collection method or the intended use of the map. The photographs in this Chapter are an inexhaustive set of examples of surface rupture complexity at site-specific scales. Together, the maps and photographs are a useful introduction to help users of the FDHI Database visualize surface rupture complexity and understand the types of data included, data collection methods, and strengths and limitations of the methods.

Measuring fault displacement requires, at minimum, knowledge or inference of the ground surface and geometry of the physical features before the earthquake. Specifically, we must be able to identify physical features that were adjacent, or in some other known spatial configuration, before the earthquake and then measure their current separation (i.e., piercing points). Common piercing points include but are not limited to: geologic or geomorphic features such as channel margins or thalwegs, terrace risers, and alluvial fans; and cultural features such as roadways, vehicle tracks and fences. The photographs in this Chapter also provide some examples of measurable, unmeasurable, and ambiguous features. Furthermore, we show examples where incomplete documentation of surface rupture complexity can also cause ambiguity in reported displacement measurements.

2.2.1 Mapping Scale

Thorough and consistent documentation of surface ruptures is complicated by the fractal (scale-invariant) nature of faults (Turcotte, 1990). Site-specific factors, such as near-surface soil/rock conditions, also affect how ruptures manifest on the ground surface (e.g., Bray et al., 1994; Moss et al., 2013). Surface rupture characteristics vary widely from simple, discrete planar faulting to complex or diffuse networks of fissures or minute cracking. Mapping scale is particularly important for complex ruptures: small-scale maps have limited resolution that reduce detail, whereas large-scale maps can retain a high level of detail[4]. For example, Figure 2.1 shows a portion of the rupture mapping from the 1966 **M** 6.19 Parkfield, California earthquake at two different

[4] For example, a 1:500-scale map has more detail (larger scale) than a 1:50,000-scale map (smaller scale) (Avery and Berlin, 1992).

mapping scales that underscore the fractal nature of surface rupture. The full rupture was documented on a 1:24,000-scale topographic base map as mostly continuous curvilinear rupture traces, but the geologists also mapped minute fractures (~15 cm in length) at a very large scale in several locations. The site-specific mapping in Figure 2.1B is along an 8-m-long portion of the rupture. The purpose of site-specific mapping is usually to document a specific structural complexity or illustrate a representative level of complexity for a portion of the rupture.

Figure 2.1. Surface rupture datasets from 1966 **M** 6.19 Parkfield, California earthquake. (A) Ruptures mapped on 1:24,000-scale 7.5' quadrangle topographic map; magenta dot is location F10. (B) Fractures in asphalt road mapped from vertical photographs at location F10. Source: Brown et al. (1967), USGS Professional Paper 579.

Figure 2.2 is a 4-km-long section from the 2010 **M** 7.2 El Mayor-Cucapah, Mexico earthquake surface rupture at two different mapping scales. The Teran et al. (2015) mapping was completed at a 1:500 scale, and the Fletcher et al. (2014) mapping is a regional simplification at an unreported scale (likely ~1:50,000 or smaller). The Fletcher et al. (2014) compilation manually simplified the surface rupture based on the geometry and kinematics to investigate the fault rupture process in the earthquake.

Figure 2.3 shows a portion of the 2019 **M** 7.2 Ridgecrest, California earthquake at three different mapping scales. The Ponti et al. (2020) dataset in this area was developed from unmanned aerial vehicle (UAV) imagery at a very large scale (1:100 or larger), capturing small fractures (~2 m in length) that might not be of engineering significance; however, the mapping scale is less than 1:10,000 in other areas. The CGS lidar mapping (unpublished work) is based on a 1:1,000 scale. The differences in the ruptures mapped from these datasets are related to both the resolution of the source data and geologists' interpretations. The DuRoss et al. (2020) dataset was manually simplified from the Ponti et al. (2020) dataset for the purpose of developing fault displacement profiles. The scale of the DuRoss et al. (2020) dataset is not reported but is likely on the order of 1:24,000.

Mapping scale is generally controlled by the data collection method (Figure 2.3), intended usage of the map (Figure 2.2), or external limiting factors (e.g., inaccessible areas, resource limitations). Therefore, the level of detail in surface rupture maps can vary significantly between earthquakes, in different areas of the same earthquake, or even within the same area of an earthquake. This is an important limitation in the database that is inherited from the original datasets. Moreover, most surface rupture maps are not compiled at scales that are appropriate for site-specific engineering applications.

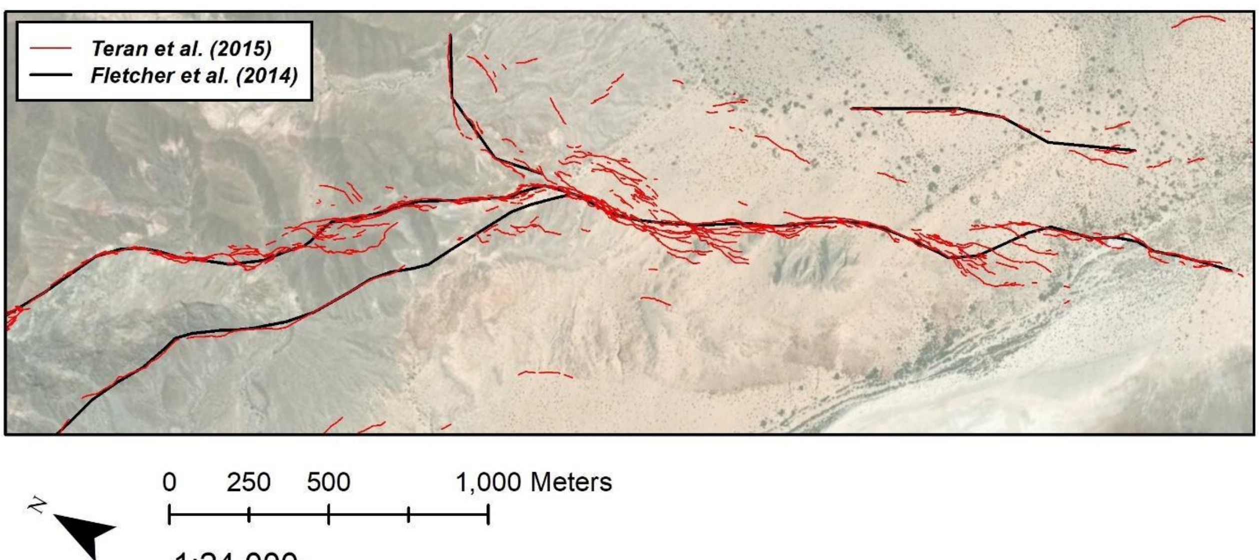

Figure 2.2. Surface rupture datasets from the 2010 **M** 7.2 El Mayor-Cucapah, Mexico (EMC) earthquake. Reported mapping scale from Teran et al. (2015) is 1:500; Fletcher et al. (2014) mapping scale not reported, but estimated to be ~1:50,000 or smaller. Area shown is near 32.548°N, 115.691°W.

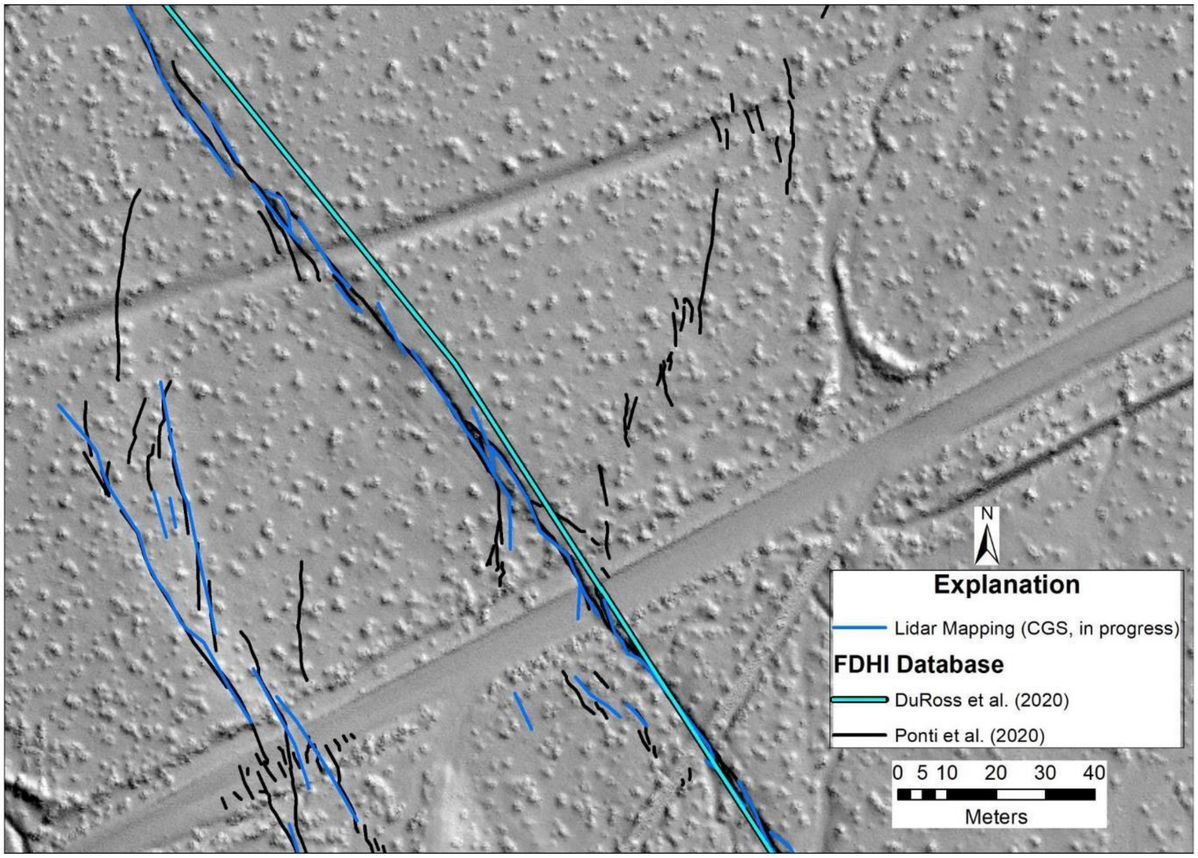

Figure 2.3. Surface rupture datasets from the 2019 **M** 7.2 Ridgecrest, California earthquake. Ponti et al. (2020) mapping scale is 1:100 in this area (varies elsewhere); unpublished lidar mapping by CGS (Dawson, T.), scale 1:1,000; and DuRoss et al. (2020) mapping scale not reported, but estimated to be ~1:24,000.

2.2.2 Single Discrete Surface Rupture

Conceptually, the simplest surface rupture pattern is a single, continuous, linear, and discrete fault, which is an infinitely thin feature that can be represented as a line on a map (sometimes informally referred to as a “knife-edge” rupture). The photographs in Figure 2.4 show examples of continuous, linear, and discrete surface ruptures from the 2019 **M** 7.1 Ridgecrest and 1906 **M** 7.9 San Francisco earthquakes in California (USGS, 2021).

The surface rupture characteristics in both photographs in Figure 2.4 are similar (continuous, linear, and discrete) and would be represented similarly on most surface rupture maps. There are subtle differences in the surface rupture characteristics that might be reflected on a site-specific scale map. For example, the surface soils in Figure 2.4B are displaced across a zone of deformation that is at least one-meter-wide. The zone of deformation is wider in the foreground of the picture, partly due to perspective but mainly due to a localized area of extension that forms a fissure. The alternating fissures and push-ups are a common manifestation of surface rupture in strike-slip earthquakes referred to as a "moletrack." The rupture continuity is also more variable in Figure 2.4B (such as above the woman's head in the photograph), and there are several short ruptures at a high angle to the main rupture with vertical displacement. A site-specific scale map of the area in Figure 2.4B might show the rupture as a zone (area in map view) and distinguish the fissure boundaries and high-angle splays.

The examples in Figure 2.4 are from right-lateral fault rupture in large earthquakes. It is unlikely that right-lateral displacements could be measured at either location, as distinctly displaced features (i.e., piercing points) are not visible in either photograph. (Note that the evaporite boundaries in Figure 2.4A are irregular and not reliable markers.) Alternatively, Figure 2.5 shows another example of a continuous, linear, and discrete surface rupture from the 2019 **M** 7.1 Ridgecrest, California earthquake that crosses a small channel margin, providing reliable piercing points for measuring right-lateral displacement.

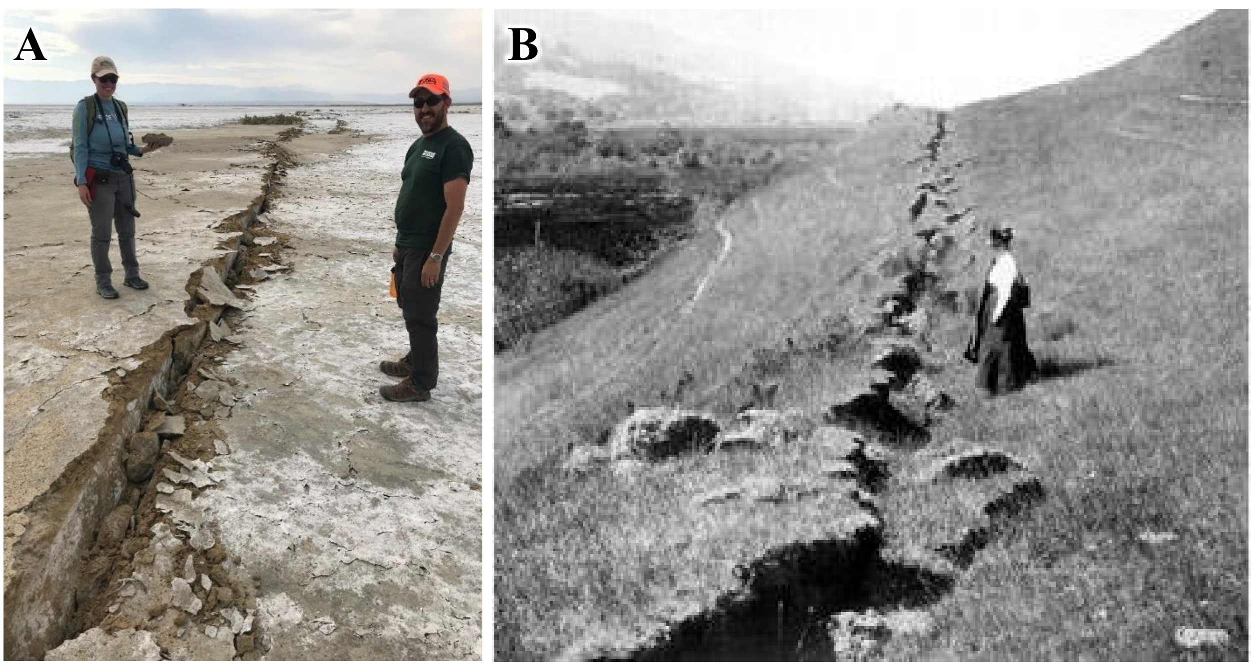

Figure 2.4. (A) Photograph along portion of 2019 Ridgecrest, California **M** 7.1 surface rupture, location not reported. (B) Photograph along portion of 1906 **M** 7.9 San Francisco, California surface rupture near 38.057312°N, 122.807878°W. Source: USGS Earthquake Photo Collections (USGS, 2021).

Figure 2.5. Photograph along portion of 2019 Ridgecrest, California **M** 7.1 surface rupture showing right-lateral displacement of a small channel margin (location not reported). Source: USGS Earthquake Photo Collections (USGS, 2021).

2.2.3 Distributed Ruptures and Deformation

Earthquakes can also produce multiple surface ruptures across zones hundreds of meters wide. Figure 2.6 is a photograph of the 1999 **M** 7.1 Hector Mine earthquake showing a fault zone roughly 25 meters in width (USGS, 2021). Several surface ruptures are visible in the photograph. Although many of the individual ruptures are continuous, linear, and discrete traces, the overall surface rupture at this location is relatively complex due to the amount and density of individual ruptures. Few, some, or all of the individual ruptures could be captured in a rupture map, depending on the scale or purpose of the map. Vertical slip can be measured along multiple locations of most of the ruptures visible in Figure 2.6, but piercing points for lateral slip measurements are not discernable in the photograph. Measurement reporting in rupture zones like this can vary, with individual measurements on separate ruptures (which may or may not be delineated on a rupture map) or slip measurements summed across closely-spaced ruptures. The latter case is not always distinguished in the original datasets.

Figure 2.6. Photograph along portion of 1999 Hector Mine, California **M** 7.1 surface rupture (location not reported). Source: USGS Earthquake Photo Collections (USGS, 2021).

In addition to discrete surface rupture traces, nonbrittle deformation in the form of warping, rotation, or tilting is also common in earthquakes. In the photograph in Figure 2.7, surface deformation is mainly accommodated by broad warping and multiple discontinuous fissures. The area across which warping or tilting of the ground surface occurs is typically poorly documented in rupture mapping: sometimes a trace is mapped at the base or center of the scarp, implying discrete rupture, or sometimes linework is omitted because a discrete rupture is absent. The discontinuous fissures are sometimes, but not always, included on rupture maps. Vertical slip is usually measured across the zone. Many engineered structures are sensitive to both the displacement amplitude and the width of the zone; however, the width of the zone is usually not reported, and measurement or rupture metadata might not distinguish between discrete surface rupture and broad warping.

Figure 2.7. Photograph along portion of 2016 Kaikoura, New Zealand **M** 7.8 surface rupture. Source: Madugo, C.

2.2.4 Site-Specific Complexity

Relatively simple rupture traces can transition into diffuse or discontinuous traces over short distances. Figure 2.8 is a photograph of surface rupture on the Kaikoura Fault northwest of Clarence, New Zealand from the 2016 Kaikoura **M** 7.6 earthquake. A robust and continuous subvertical rupture (fault scarp) is clear in the center of the photograph; however, the surface rupture expression suddenly changes from the distinct linear trace to a zone of deformation on the right side of the photograph. A rupture map might record individual ruptures in the zone of deformation or simply continue the linear trace from the left side of the picture. Several secondary ruptures are also visible in the hill above the main rupture. The secondary ruptures may or may not be included on a rupture map, depending on the scale or purpose of the map.

The range of surface rupture expressions in Figure 2.8 provides examples of simple and complicated locations for measuring fault displacement. The main rupture decays from a distinct linear trace (left) to a zone of distributed deformation (right). Multiple secondary ruptures are also evident in the hill above the main rupture. The uniformity of the vegetative grass highlights vertical displacements throughout the photograph area, and the topography provides some constraints on lateral displacements on the smaller, high-angle secondary faults (between the main rupture and the geologist in the photograph); therefore, reliable vertical displacements can be obtained on many of these faults. The offset fencing in the hills, near the geologist in the photograph, provides excellent piercing points for measurement of lateral displacement. Although it is difficult to see in the photograph, broken and offset fencing near the robust linear part of the main rupture can also be used to measure lateral and net displacements. Within the diffuse part of the main rupture, a good measurement of vertical displacement is probably possible while lateral displacement measurement opportunities might be limited. Most importantly, the relatively similar amplitude of vertical displacements across the main fault in this photograph span different fault zone widths: a subvertical discrete rupture on the left side of the picture, and a roughly two-meter-wide zone on the right side of the picture. Many engineered structures are sensitive to both the displacement amplitude and the width of the zone; however, width is usually not documented.

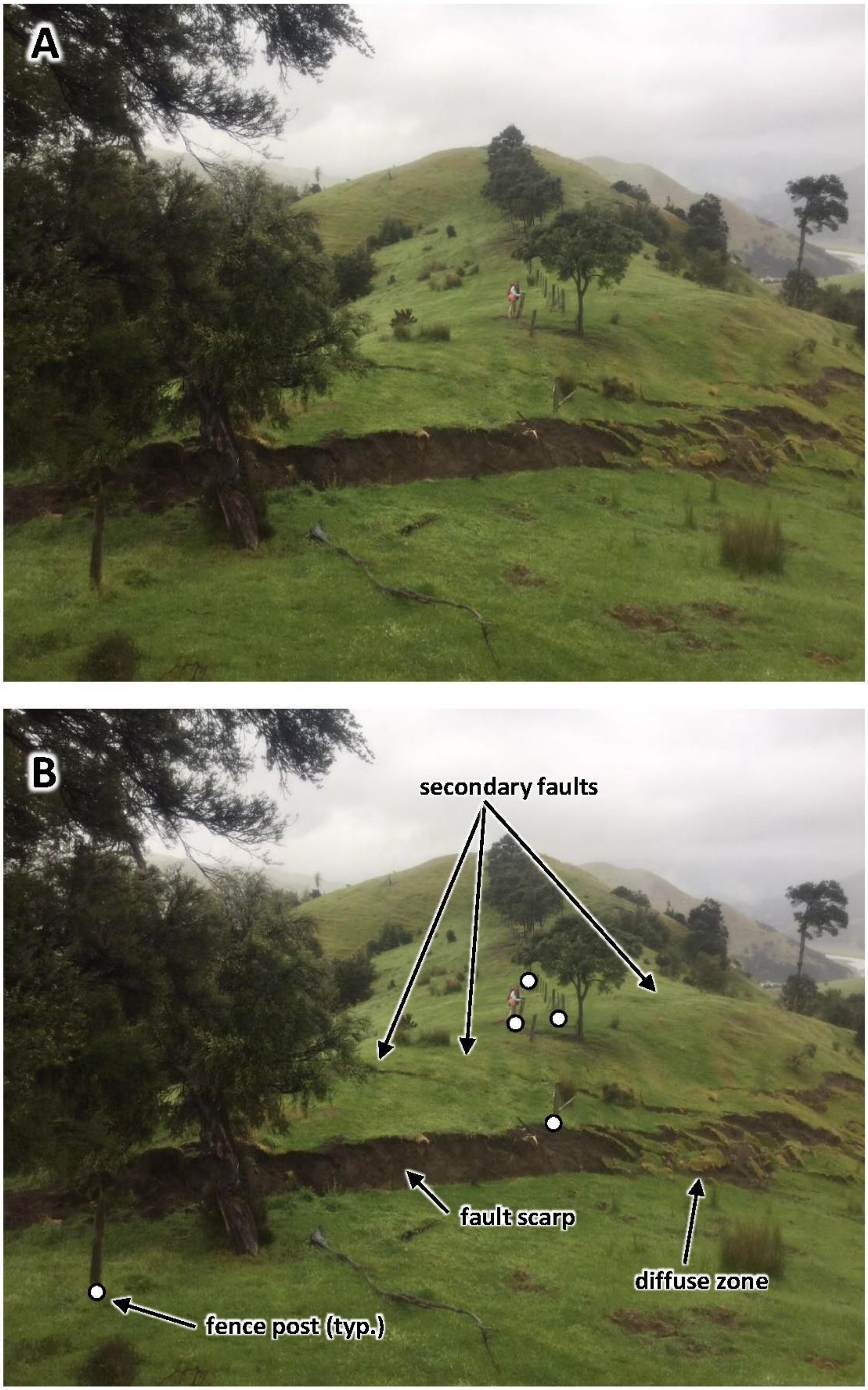

Figure 2.8. Photograph along portion of 2016 Kaikoura, New Zealand **M** 7.8 surface rupture. (A) Unannotated. (B) Annotated based on discussion in text. Source: Madugo, C.

The photograph in Figure 2.9 is also from the 2016 Kaikoura earthquake and is located within a few hundred meters of the picture in Figure 2.8. The rupture in Figure 2.9 manifests at the surface as two (sub)parallel principal faults forming a pop-up (or positive flower) structure with significant fissuring along the fault traces. The two rupture traces may or may not be shown on a smaller scale rupture map. Vertical slip can be measured on both sides of the structure; however, we have found that documentation of slip measurements on structures like this is sometimes ambiguous. Ideally, both rupture lines would be shown on a map, the measurement sites would correlate with the linework, and fault motion indicators (i.e., upside/downside for measurements or ruptures) would be reported. Due to positional location errors, measurement sites might not be precisely correlated with the linework; alternatively, the dataset originator might report two measurements at the center of the structure. In both cases, it can be challenging to discern the measured feature unless the dataset originator indicates the measurement is part of a pop-up structure. Further ambiguity can arise from the rupture mapping scale, as structures like this might be represented with one approximated rupture line. While there is significant fissuring on both sides of the pop-up structure, reporting standards vary: fissures may or may not be noted in measurement comments, and the width or depth of fissures is not always reported or identified as contributing to a reported net slip measurement.

Figure 2.9. Photograph along portion of 2016 Kaikoura, New Zealand **M** 7.8 surface rupture. Source: Madugo, C.

2.3 DATA COLLECTION METHODS

There are three general methods for mapping surface ruptures and measuring fault displacements: field-based observation, interpretation of remotely collected data, and automated or semi-automated analysis of pre- and post-earthquake digital data (Table 2.1). Typical data sources, tools and techniques, and advantages and disadvantages of the methods are discussed below.

Table 2.1. Generalized data source and analysis methods for surface rupture mapping and fault displacement measurements.

Type	Basis	Method
Field-based	Digital maps or imagery, printed maps, aerial photographs, GPS positioning	Ruptures and measurements are assessed on the ground or from low altitude aerial reconnaissance
Remote	Post-event aerial photographs, orthophotographs, satellite imagery, lidar	Ruptures and measurements are interpreted offsite
Automated/Semi-Automated	Geospatially-controlled and co-registered pre- and post-earthquake digital data	Rupture locations and measurements are calculated using differencing or change detection algorithms; results are interpreted for geologic consistency

2.3.1 Field-Based

Field-based methods include the conventional "boots on the ground" geologic mapping of surface ruptures on various media, such as digital or printed maps or aerial photographs. A key advantage of this method is the potential to document site-specific complexity if the mapping scale is sufficiently small. The related disadvantage is that artificial variability in fault trace complexity may be inadvertently documented if the scale of the base map changes along the length of the total surface rupture. Another key drawback of ground-based mapping is the potential to overlook surface ruptures outside the area surveyed. Reconnaissance air-based mapping is often used to guide ground teams to the spatial extent of surface ruptures. In areas with difficult terrain, restricted access, or when ground-based mapping is limited by personnel or time, air-based mapping might be the only method used.

A key advantage of field-based measurements is that it can be easier to confirm the measured displacements are only from the most recent earthquake in the field, as some offset geomorphic features may record displacements from multiple events. Fault displacements are measured with tools like measuring tapes, folding rulers, and hand levels or leveling staffs. These tools are usually better suited for discrete ruptures or distinct piercing points, but they are also used along warps and folds. Surveying methods and tools are also commonly used to construct profiles across (sub)vertical scarps (e.g., warps and folds) and along laterally-offset linear features. Surveying instruments, such as pole-mounted Global Navigation Satellite System (GNSS) receivers or total station theodolites, record the location and elevation of points along the profile. The data are collected in the field and analyzed or interpreted in the office. Measurement locations are either manually determined and annotated on various media (e.g., digital or printed maps or imagery) or automatically determined using portable GNSS devices such as handheld units, mobile phones, or tablet computers.

2.3.2 Remote

Remote methods require office-based geologic interpretation of remotely collected post-earthquake data. Typical data types include aerial photographs, orthophotographs, satellite imagery, unmanned aerial vehicle (UAV) photographs, or lidar collected after the earthquake. Surface ruptures and offset features are identified by geologic interpretation of the imagery or hillshades created from lidar-based digital elevation models. A key advantage of remote methods is the ability to quickly collect data over a large area, increasing the likelihood observations are collected before post-earthquake ground surface modification (e.g., infrastructure repairs, weather/storm events) obscures the rupture.

The ability to recognize ruptures and measure offset features is limited by the resolution of the imagery or elevation model, and vertical components of displacement cannot be measured from imagery. Misinterpretations can occur when mapping exclusively from remote data without any field verification, and the propensity for error is related to the dataset resolution, vegetation, pre-existing faulting, and the complexity of the rupture. For example, surface ruptures may be unobservable in lower resolution data, dense vegetation, or earthquakes with complex and diffuse ruptures, and offset features can be difficult to measure in dense vegetation or areas with diffuse ruptures. Pre-existing faults or lineaments that did not rupture in the earthquake of interest could be misinterpreted as fresh surface ruptures, and it can be difficult to discern displacements due exclusively to the most recent earthquake.

While misinterpretations can occur when mapping exclusively from remote data without any field verification, some physical settings are well-suited to remote interpretation. For example, maintained agricultural fields are usually flat with aligned rows of plants, and manmade structures like fences, walls, and roads provide excellent piercing points. Ideally, remote and field-based methods are used in tandem or iteratively to develop a verified surface rupture map and dataset of fault displacements.

2.3.3 Automated or Semi-Automated

Automated or semi-automated methods use differencing or change detection analysis and require geospatially-controlled and co-registered pre- and post-earthquake digital data. These methods include optical image correlation (also called pixel mapping) and differential lidar analysis. Mapping surface ruptures and measuring fault displacement are both possible, and a key advantage of these methods is the ability to collect and uniformly analyze data, with a high degree of spatial accuracy, over a large area. In particular, displacements can be measured across kilometer-scale apertures[5]. However, the results can be sensitive to the aperture over which displacement is measured (e.g., Gold et al., 2015; Zinke et al., 2014), and the threshold detection limits are a function of the spatial resolution of the pre- and post-earthquake datasets. Ideally, remote and field-based methods are used in conjunction with these methods to develop a verified surface rupture map and to understand how displacement measurements vary between different apertures or scales.

Surface rupture identification varies depending on the data and technique, but fully automated approaches generally extract points or cells of maximum pre- and post-earthquake positional differences for various gradients, such as displacement, strain, or rotation, (e.g., Howell et al., 2020; Milliner et al., 2016, 2021) and linearize or connect the cells using a greedy (spatial optimization) algorithm or similar approach (Milliner et al., in prep.). Semi-automated approaches, in which an analyst interprets and manually digitizes rupture linework from gradient maps, are more common (e.g., Milliner et al., 2015, 2016; Zinke et al., 2019; Nissen et al., 2014). This allows the analyst to apply geologic judgement to identify rupture ends, manually adjust areas with decorrelation artifacts, and manually differentiate areas of landsliding or lateral spreading. However, due to the data resolution and analysis procedures, closely-spaced parallel faults usually cannot be detected, and distinguishing between continuous linear ruptures, en-echelon rupture patterns, or non-brittle warping can be difficult.

Displacement measurement methods vary depending on the data and technique, but in general pre- and post-earthquake differences, such as displacement or strain, are calculated for each point or cell. Fault-normal profiles are constructed along the length of a defined rupture, and a functional form is fit across the profile to calculate the relative displacement on each side of the fault (e.g., Milliner et al., 2015, 2016; Gold et al., 2013). The length and width of the profiles varies depending on the data and technique. The key advantage to using these methods to measure fault displacement is that the total, or wide-aperture, fault displacement can be calculated, as well as the fault zone width and the accumulation of displacement across the zone. When sufficient elevation control is available, vertical displacement can also be calculated (Oskin et al., 2012; Nissen et al., 2014; Zinke et al., 2019). However, the results need to be reviewed to distinguish landsliding, lateral spreading, and natural or engineered landform changes from fault displacement (Nissen et al., 2014; Howell et al., 2020; Zinke et al., 2019).

[5] Measurement aperture is the length or area over which fault displacement is measured. Displacement outside the aperture window is not observed and therefore cannot be detected.

2.4 MEASUREMENT UNCERTAINTY

The epistemic uncertainty of fault displacement measurements is a function of several factors, including but not limited to degree of preservation, knowledge of pre-rupture geometry, the quality or reliability of the offset feature, measurement aperture, local variations in style of faulting, measurement tools, and time elapsed between the earthquake and the measurement. Brief examples of the factors are provided below. The accumulation of these factors inherently requires the use of more judgment in measuring displacements, and the effects of judgment and implicit biases (e.g., anchoring and confirmation biases) on measurement uncertainty are difficult to quantify (Arrowsmith and Rockwell, 2012).

- Degree of preservation is influenced by rupture characteristics (discrete vs. diffuse), site conditions (e.g., climate, vegetation, surface material properties), and amplitude of displacement (e.g., smaller displacements are more perishable).
- Offset features can be geologic, geomorphic, or cultural, and the quality of measurements across a feature is related to how the feature intersects the rupture (i.e., obliquity) and how confidently its pre-rupture configuration can be reconstructed. For example, cultural features such as fences, roads, and canals are often linear and more easily reconstructed, whereas sinuous channel or terrace margins can permit a range of pre-rupture configurations (e.g., Gold et al., 2011; Arrowsmith and Rockwell, 2012). The style of faulting can also affect how well offset features can be reconstructed; for example, fault-normal shortening (e.g., under-thrusting), can bury or obscure features. Confidence that the feature is offset by only one earthquake is also an important part of feature reliability.
- Measurement aperture can affect reported displacement measurements because some slip can be accommodated through continuous warping tens of meters beyond a discrete rupture trace (Rockwell et al., 2002).
- Localized changes in deformation mechanisms (e.g., displacement components or style of faulting) due to structural complexity or sudden changes in surface material properties can obscure or confuse displacement measurements. For example, rupture expression and displacements can be exaggerated or obfuscated by local refraction processes or when a rupture crosses from native soil onto hardscapes such as asphalt or concrete.
- Remote-based (Table 2.1) measurements are limited by the resolution of the dataset. Vegetation or atmospheric obstructions can limit imagery-based assessments.
- Measurements collected immediately after an earthquake are less likely to reflect afterslip or degradation.

In our experience compiling and analyzing the database, field- and remote-based (Table 2.1) displacement measurements are most often reported as a single preferred value. When uncertainties are documented, they are more commonly symmetrical (i.e., +/- value) and only rarely asymmetrical. Asymmetrical uncertainties are generally more robust because they reflect explicit evaluation of both the range of pre-rupture reconstructions and the most likely value (e.g., Gold et al., 2011; Scharer et al., 2014). Documentation on the meaning and application of uncertainties is also rare, in part because the preferred displacement and uncertainties do not represent a mean and standard deviation; however, it is typically assumed that uncertainties represent a minimum and maximum (Scharer et al., 2014). Conversely, measurements calculated using differencing or change detection algorithms (e.g., differential lidar, optical image correlation) are usually reported as mean values with a standard deviation or confidence interval (Milliner et al., 2016; Gold et al., 2015).

In addition to measurement uncertainty (i.e., the epistemic uncertainty discussed above), measurement errors can also occur. Gold et al. (2013) conducted a systematic evaluation of measurement errors using field- and remote-based methods at three locations in the 2010 **M** 7.2 El Mayor-Cucapah, Mexico earthquake. They conclude an uncertainty (two standard deviations or 2σ) of 11% to 17% is necessary to capture measurement errors.

2.5 TERMINOLOGY

The terminology used to describe surface rupture patterns and fault displacement measurements varies in professional literature and standard practice. In this Chapter, we identify relevant terms used by geologists and define how they are used in the FDHI Database Project.

2.5.1 Fault Displacements

Several terms are used by geologists to describe the magnitude, amplitude, or amount of ground surface movement across a surface rupture. For example, the terms *displacement*, *slip*, *separation*, and *offset* are inconsistently and interchangeably applied in professional literature and standard practice. For this project, we define *slip* as the actual relative displacement and *separation* as the apparent relative displacement. We use *offset* as a verb or adjective when describing the geomorphic or anthropogenic features displaced across a rupture. The terms *style*, *sense*, and *direction* all describe the relative movement of the ground surface across a surface rupture.

Surface ruptures generate three-dimensional ground surface displacements. As a result, several components of relative displacement (slip) can be measured (Figure 2.10). The slip components are also sometimes called slip vectors; however, recognizing that the term *vector* has a specific meaning in math and engineering (i.e., magnitude and azimuthal direction), we use *component* instead, because the azimuthal direction (i.e., rake) is rarely reported. The measured slip component is usually clearly documented in the original datasets, and we retained this information in the database. The style of slip (e.g., normal, reverse, left-lateral, right-lateral) is also usually reported in the original datasets and retained in the database.

Based on the geometric relationships in Figure 2.10, the net (three-dimensional) slip can be calculated from the net horizontal slip and dip slip measurements if it is not directly measured (Equations 2.1 through 2.3). In a pure strike-slip offset, the fault-parallel slip (FPS) is equivalent to the net slip (TDS). Similarly, in a pure normal or pure reverse offset, the dip slip (ADS) is equivalent to the net slip (TDS).

$$TDS = \sqrt{NHS^2 + VS^2} \tag{2.1}$$

$$NHS = \sqrt{FPS^2 + FNS^2} \tag{2.2}$$

$$ADS = \sqrt{FNS^2 + VS^2} \tag{2.3}$$

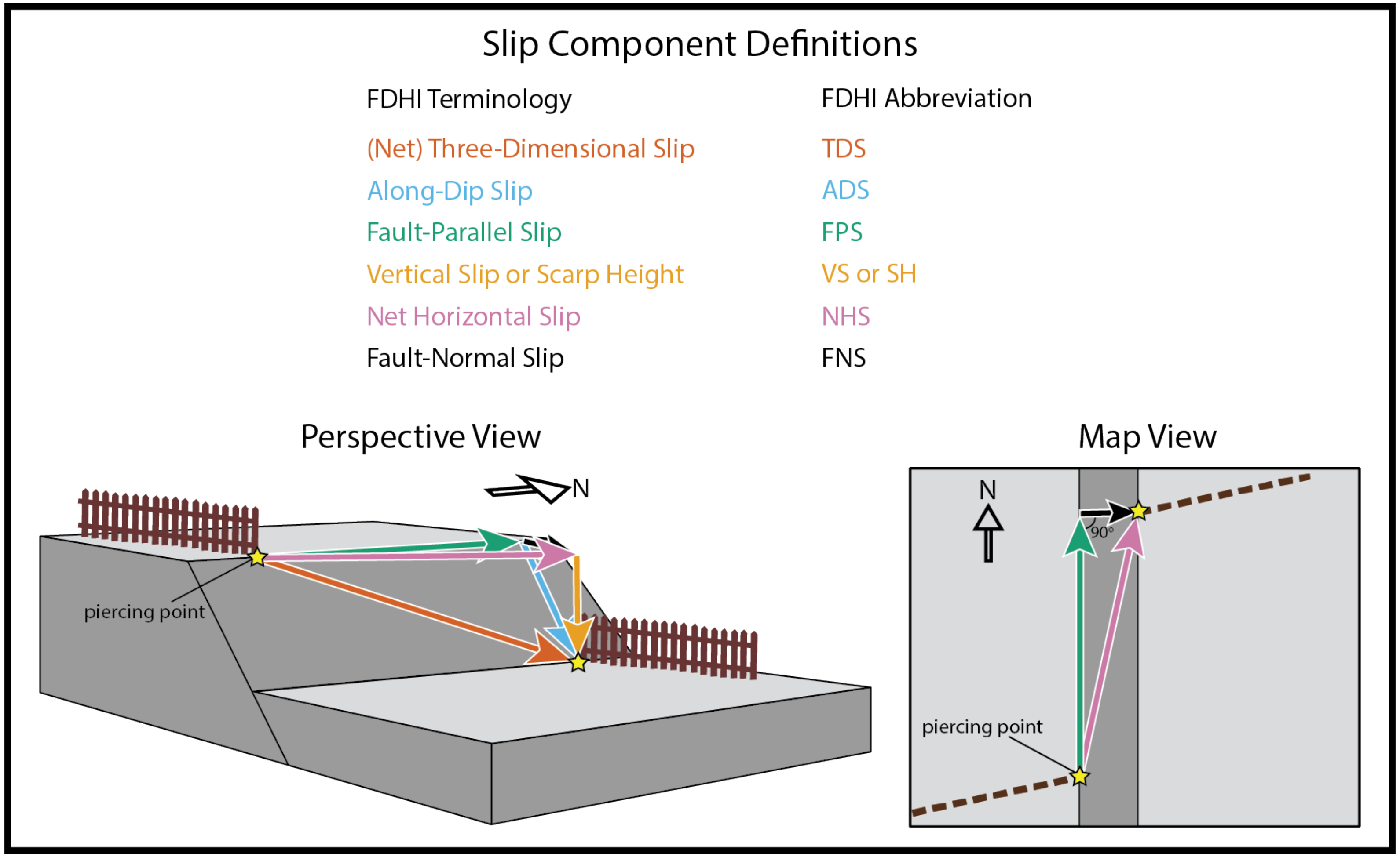

Figure 2.10. Fault displacement slip component definitions used in FDHI Database. Adapted from Ponti et al. (2020).

Vertical displacement measurements are sensitive to the slope of the ground surface before the earthquake (Caskey, 1995; Yang et al., 2015) (Figure 2.11). If the pre-earthquake ground surface was not flat, then vertical measurements that only consider the distance between the piercing points (orange arrow in Figure 2.10) are an apparent displacement (separation). The actual vertical component of the relative displacement (slip) is measured by projecting the original ground surface across the rupture (Figure 2.11). We refer to the actual vertical component of the relative displacement as *vertical slip* and the apparent vertical component of the relative displacement as *scarp height* (Figures 2.10 and 2.11). As shown in Figure 2.11, vertical slip and scarp height measurements can vary significantly depending on the slope and direction of the original ground surface. Fortunately, this distinction in vertical displacement measurements is usually documented in original datasets and retained in the database.

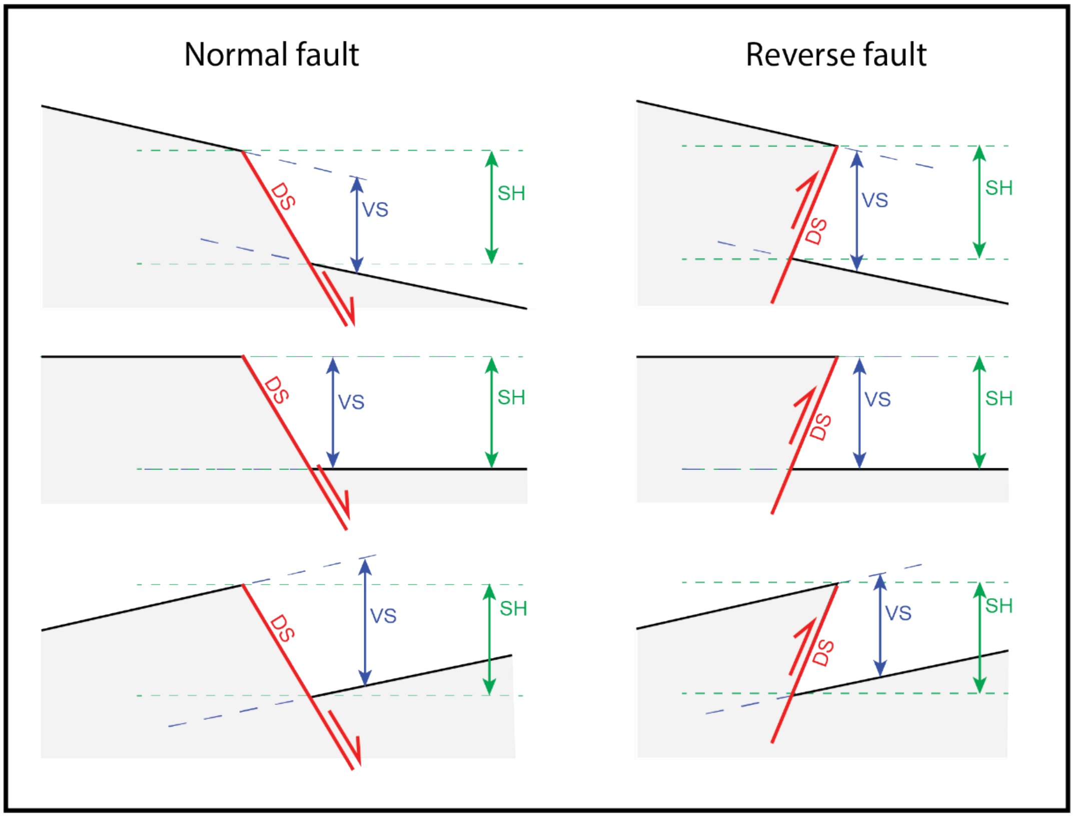

Figure 2.11. Schematic ground surface configurations and vertical fault displacement measurements for normal and reverse faults (profile view). DS = dip-slip; VS = vertical slip; SH = scarp height. Note that vertical slip and scarp height are vertical components of the slip vector in a Cartesian reference frame.

2.5.2 Discrete Slip and Continuous Deformation

Discrete expressions of surface rupture are clear locations of significant fault displacement (Figures 2.4 through 2.6). Measurements on discrete surface ruptures represent an infinitely narrow deformation zone width. conversely, broad warps represent continuous deformation across a wider zone (Figure 2.7). Although continuous deformation is easier to visualize with vertical displacement (Figure 2.7), lateral fault displacement also produces shear zones of continuous deformation that are evident when a continuous linear feature is offset (Figure 2.12). Measurements across broad warps or shears correspond to a specific deformation zone width and are measured within a specific aperture. In the schematic in Figure 2.12, all of the displacement (discrete slip plus continuous deformation) occurs between marker numbers 3 and 12, which represents the deformation zone width, and the surveyed length extends from marker numbers 1 to 14, representing the measurement aperture. While profile-based measurements are relatively common, measurement aperture and deformation zone width are rarely reported in the original datasets, and we include this information in the database when it is available. Fault zone width, which we interpret to represent the zone encompassing a network of closely-spaced ruptures, is sometimes reported and included in the database; however, the terms fault zone width and deformation zone width are often used ambiguously in professional literature and standard practice.

2.5.3 Principal (Primary) and Distributed (Secondary) Faulting

Surface ruptures are sometimes categorized as principal or distributed to reflect causative sources or relative significance of individual ruptures. The terms *principal* and *distributed* are sometimes used interchangeably with *primary* and *distributed*, respectively, in professional literature and standard practice. For this project, we use *primary* and *distributed*¸ and we follow the definitions in Coppersmith and Youngs (2000) and Youngs et al. (2003):

- **Principal faulting** is slip on the primary faults or tectonic/seismogenic features responsible for the earthquake.
- **Distributed faulting** is the secondary slip that occurs on other faults, splays, fractures, or shears near the principal fault.

As discussed in detail in Chapter 4.3 of this report, the FDHI Database includes classifications of rupture linework as principal or distributed, based on information reported in the original data sources or interpreted by the Database Team.

Fault displacement measurements can also be categorized as principal or distributed, based on the classification of their associated surface rupture (Youngs et al., 2003; Petersen et al., 2011, Nurminen et al., 2020). We introduce two additional measurement categories (cumulative and total) in this project to better distinguish measurements associated with multiple ruptures or wider measurement apertures. Cumulative measurements represent slips summed across multiple known principal ruptures, one principal rupture and one or more distributed ruptures, or principal rupture(s) plus continuous deformation (e.g., Figure 2.12). Total measurements represent wide-aperture slips calculated from the differencing or image correlation methods discussed in Chapter 2.3.3. Because total measurements capture the total displacement across a wide aperture, the measurement might not be associated with a single specific fault. The process of classifying fault displacement measurements as principal, distributed, cumulative, or total is discussed in Chapter 4.3 of this report.

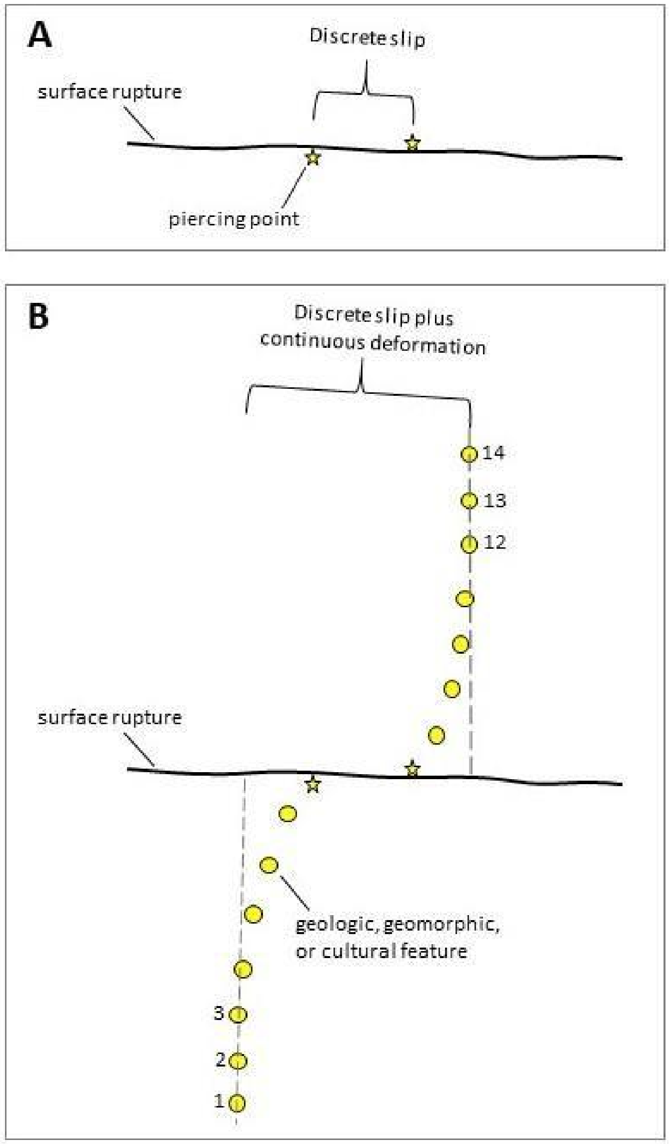

Figure 2.12. Plan-view schematics of right-laterally offset piercing points slip measurements (not to scale). (A) Narrow-aperture measurement captures discrete slip. (B) Wider aperture measurement discrete slip and continuous warping or deformation.

2.6 REFERENCES

Arrowsmith, J. R. and Rockwell, T. K. (2012). Repeatability, accuracy, and precision of surface slip measurements from high-resolution topographic data: Collaborative research with Arizona State University and San Diego State University, *Final Technical Report U.S. Geological Survey National Earthquake Hazards Reduction External Research Program*, USGS Award Number G11AP20029 (ASU) & G11AP20020 (SDSU).

Avery, T. E. and Berlin, G. L. (1992). Fundamentals of remote sensing and airphoto interpretation. Macmillan.

Bray, J. D., Seed, R. B., Cluff, L. S., and Seed, H. B. (1994). Earthquake fault rupture propagation through soil, *Journal of Geotechnical Engineering*, **120**(3), 543-561.

Brown, R. D. Jr. and Vedder, J. G. (1966). Surface tectonic fractures along the San Andreas Fault, The Parkfield-Cholame California earthquakes of June-August 1966, *U.S. Geological Survey Professional Paper 579*.

Caskey, S. J. (1995). Geometric relations of dip slip to a faulted ground surface: new nomograms for estimating components of fault displacement, *Journal of Structural Geology*, **17**(8), 1197-1202.

Coppersmith, K. J. and Youngs, R. R. (2000). Data needs for probabilistic fault displacement hazard analysis, *Journal of Geodynamics*, **29**(3-5), 329-343.

DuRoss, C. B., Gold, R. D., Dawson, T. E., Scharer, K. M., Kendrick, K. J., Akciz, S. O., Angster, S. J., Bachhuber, J., Bacon, S., Bennett, S. E. K., et al. (2020). Surface Displacement Distributions for the July 2019 Ridgecrest, California, Earthquake Ruptures, *Bulletin of the Seismological Society of America*, **110**(4), 1400-1418.

Fletcher, J. M., Teran, O. J., Rockwell, T. K., Oskin, M. E., Hudnut, K. W., Mueller, K. J., Spelz, R. M., Akciz, S. O., Masana, E., Faneros, G., Fielding, E. J., Leprince, S., Morelan, A. E., Stock, J., Lynch, D. K., Elliott, A. J., Gold, P., Liu-Zeng, J., Gonz?lez-Ortega, A., Hinojosa-Corona, A., and Gonz?lez-Garc?a, J. (2014). Assembly of a large earthquake from a complex fault system: Surface rupture kinematics of the 4 April 2010 El Mayor–Cucapah (Mexico) Mw 7.2 earthquake, *Geosphere*, **10**(4), 797-827.

Gold, R. D., Reitman, N. G., Briggs, R. W., Barnhart, W. D., Hayes, G. P., and Wilson, E. (2015). On-and off-fault deformation associated with the September 2013 Mw 7.7 Balochistan earthquake: Implications for geologic slip rate measurements, *Tectonophysics*, **660**, 65-78.

Gold, P. O., Oskin, M. E., Elliott, A. J., Hinojosa-Corona, A., Taylor, M. H., Kreylos, O., and Cowgill, E. (2013). Coseismic slip variation assessed from terrestrial LiDAR scans of the El Mayor–Cucapah surface rupture, *Earth and Planetary Science Letters*, **366**, 151-162.

Gold, R. D., Cowgill, E., Arrowsmith, J. R., Chen, X., Sharp, W. D., Cooper, K. M., and Wang, X. F. (2011). Faulted terrace risers place new constraints on the late Quaternary slip rate for the central Altyn Tagh fault, northwest Tibet, *Geological Society of America Bulletin*, **123**(5-6), 958-978.

Howell, A., Nissen, E., Stahl, T., Clark, K., Kearse, J., Van Dissen, R., Villamor, P., Langridge, R., and Jones, K. (2020). Three-dimensional surface displacements during the 2016 Mw 7.8 Kaikōura earthquake (New Zealand) from photogrammetry-derived point clouds, *Journal of Geophysical Research: Solid Earth*, **125**(1), e2019JB018739.

Milliner, C., and Donnellan, A. (2020). Using daily observations from Planet Labs satellite imagery to separate the surface deformation between the 4 July Mw 6.4 foreshock and 5 July Mw 7.1 mainshock during the 2019 Ridgecrest earthquake sequence, *Seismological Research Letters*, **91**(4), 1986-1997.

Milliner, C., Donnellan, A., Aati, S., Avouac, J. P., Zinke, R., Dolan, J. F., Wang, K., and Bürgmann, R. (2021). Bookshelf Kinematics and the Effect of Dilatation on Fault Zone Inelastic Deformation: Examples from Optical Image Correlation Measurements of the 2019 Ridgecrest Earthquake Sequence, *Journal of Geophysical Research: Solid Earth*, **126**(3), e2020JB020551.

Milliner, C. W. D., Dolan, J. F., Hollingsworth, J., Leprince, S., and Ayoub, F. (2016). Comparison of coseismic near-field and off-fault surface deformation patterns of the 1992 Mw 7.3 Landers and 1999 Mw 7.1 Hector Mine earthquakes: Implications for controls on the distribution of surface strain, *Geophysical Research Letters*, **43**(19), 10-115.

Milliner, C. W., Dolan, J. F., Hollingsworth, J., Leprince, S., Ayoub, F., and Sammis, C. G. (2015). Quantifying near-field and off-fault deformation patterns of the 1992 Mw 7.3 Landers earthquake, *Geochemistry, Geophysics, Geosystems*, **16**(5), 1577-1598.

Morelan, A. E. and Hernandez, J. L. (2020). Increasing Postearthquake Field Mapping Efficiency with Optical Image Correlation, *Bulletin of the Seismological Society of America*, **110**(4), 1419-1426.

Moss, R. E. S., Stanton, K. V., and Buelna, M. I. (2013). The impact of material stiffness on the likelihood of fault rupture propagating to the ground surface, *Seismological Research Letters*, **84**(3), 485-488.

Nissen, E., Maruyama, T., Arrowsmith, J. R., Elliott, J. R., Krishnan, A. K., Oskin, M. E., and Saripalli, S. (2014). Coseismic fault zone deformation revealed with differential lidar: Examples from Japanese Mw ∼7 intraplate earthquakes, *Earth and Planetary Science Letters*, **405**, 244-256.

Nurminen, F., Boncio, P., Visini, F., Pace, B., Valentini, A., Baize, S., and Scotti, O. (2020). Probability of occurrence and displacement regression of distributed surface rupturing for reverse earthquakes, *Frontiers in Earth Science*, **8**(581605).

Oskin, M. E., Arrowsmith, J. R., Corona, A. H., Elliott, A. J., Fletcher, J. M., Fielding, E. J., Gold, P. O., Garcia, J. J. G., Hudnut, K. W., Liu-Zeng, J., and Teran, O. J. (2012). Near-field deformation from the El Mayor–Cucapah earthquake revealed by differential LIDAR, *Science*, **335**(6069), 702-705.

Petersen, M. D., Dawson, T. E., Chen, R., Cao, T., Wills, C. J., Schwartz, D. P., and Frankel, A. D. (2011). Fault displacement hazard for strike-slip faults, *Bulletin of the Seismological Society of America*, **101**(2), 805-825.

Ponti, D. J., Blair, J. L., Rosa, C. M., Thomas, K., Pickering, A. J., Akciz, S., Angster, S., Avouac, J.-P., Bachhuber, J., Bacon, S., et al. (2020). Documentation of Surface Fault Rupture and Ground-Deformation Features Produced by the 4 and 5 July 2019 Mw 6.4 and Mw 7.1 Ridgecrest Earthquake Sequence, *Seismological Research Letters*, **91**(5), 2942-2959.

Rockwell, T. K., Lindvall, S., Dawson, T., Langridge, R., Lettis, W., and Klinger, Y. (2002). Lateral offsets on surveyed cultural features resulting from the 1999 Izmit and Duzce earthquakes, Turkey, *Bulletin of the Seismological Society of America*, **92**(1), 79-94.

Scharer, K. M., Salisbury, J. B., Arrowsmith, J. R., and Rockwell, T. K. (2014). Southern San Andreas fault evaluation field activity: Approaches to measuring small geomorphic offsets—Challenges and recommendations for active fault studies, *Seismological Research Letters*, **85**(1), 68-76.

Teran, O. J., Fletcher, J. M., Oskin, M. E., Rockwell, T. K., Hudnut, K. W., Spelz, R. M., Akciz, S. O., Hernandez-Flores, A. P., and Morelan, A. E. (2015). Geologic and structural controls on rupture zone fabric: A field-based study of the 2010 Mw 7.2 El Mayor–Cucapah earthquake surface rupture, *Geosphere*, **11**(3), 899-920.

Turcotte, D. L. (1990). Implications of chaos, scale-invariance, and fractal statistics in geology, *Global and Planetary Change*, **3**(3), 301-308.

United States Geological Survey (USGS) (2021). Earthquake Photo Collections. URL: https://www.usgs.gov/natural-hazards/earthquake-hazards/science/earthquake-photo-collections?qt-science_center_objects=0#qt-science_center_objects.

Yang, X., Li, W., and Qin, Z. (2015). Calculation of reverse-fault-related parameters using topographic profiles and fault bedding, *Geodesy and Geodynamics*, **6**(2), 106-112.

Youngs, R. R., Arabasz, W. J., Anderson, R. E., Ramelli, A. R., Ake, J. P., Slemmons, D. B., McCalpin, J. P., Doser, D. I., Fridrich, C. J., Swan III, F. H., Rogers, A. M., Yount, J. C., Anderson, L. W., Smith, K. D., Bruhn, R. L., Knuepfer, P. L. K., Smith, R. B., dePolo, C. M., O'Leary, D. W., Coppersmith, K. J., Pezzopane, S. K., Schwartz, D. P., Whitney, J. W., Olig, S. S., and Toro, G. R. (2003). A methodology for probabilistic fault displacement hazard analysis (PFDHA), *Earthquake Spectra*, **19**(1), 191-219.

Zinke, R., Hollingsworth, J., Dolan, J. F., and Van Dissen, R. (2019). Three-dimensional surface deformation in the 2016 Mw 7.8 Kaikōura, New Zealand, earthquake from optical image correlation: Implications for strain localization and long-term evolution of the Pacific-Australian plate boundary, *Geochemistry, Geophysics, Geosystems*, **20**(3), 1609-1628.

Zinke, R., Hollingsworth, J., and Dolan, J. F. (2014). Surface slip and off-fault deformation patterns in the 2013 Mw 7.7 Balochistan, Pakistan earthquake: Implications for controls on the distribution of near-surface coseismic slip, *Geochemistry, Geophysics, Geosystems*, **15**(12), 5034-5050.

3 Data Collection

This Chapter documents the data collection approach for the FDHI Database Project. The data collection process for the FDHI Database followed a systematic approach that entailed defining event and dataset selection criteria based on model developer needs, reviewing existing compilations, and developing and implementing a standard workflow to review and process data. Each candidate dataset was carefully reviewed for quality and compliance with the event and dataset selection criteria.

3.1 SELECTION CRITERIA

The event and dataset selection criteria for the FDHI Database were guided by model development needs and project timelines. Specific criteria for events and dataset contents are discussed in this Chapter. In general, we found the dataset criteria (i.e., dataset contents) to be more limiting than the event criteria. To support the model development project schedule, we enforced a database entry cut-off date of October 2020 by ceasing our data search and compilation efforts.

3.1.1 Event Criteria

The event selection criteria for the FDHI Database Project were broadly constrained to historical surface-rupturing crustal earthquakes. We considered global, shallow crustal events of all styles of faulting, all magnitudes, and both active and stable tectonic regimes. We limited our criteria to historical earthquakes to ensure the data capture single-event ruptures and displacements only. By constraining our criteria to events that produced surface rupture, we do not include information on earthquakes that did not reach the ground surface. The database does not include an exhaustive collection of global historical surface-rupturing earthquakes because most events do not meet the dataset criteria (Chapter 3.1.2). As a result, several significant historical surface-rupturing earthquakes are not in the database (Chapter 3.4).

3.1.2 Dataset Criteria

The dataset selection criteria generally relate to data content and quality. Only historical, inferred single-event measurement and rupture data from tectonic faulting are included (i.e., shaking related features and paleoseismic data were excluded). The minimum required content included geospatial control for fault displacement measurements and mapped ruptures. This is an important criterion because the new models will consider the spatial distribution for both displacement amplitudes and surface ruptures. We also specifically sought datasets that include measurements on distributed faults and datasets with detailed surface rupture mapping. Given the extensive areas involved in surface rupture of large earthquakes, some datasets are limited to specific portions of the rupture; therefore, we included multiple slip measurement datasets for the same event, when available, for more complete spatial coverage. In some cases, multiple slip measurements are available for the same site, and they are included in the database. All data were collected from published reports and journal papers and reviewed for quality (Chapter 3.3.2). We specifically excluded datasets with insufficient geospatial control, irrelevant content, or known errors or issues (Chapter 3.4).

As discussed in Chapter 3.2, the data for many older events are documented as displacement profiles, with limited or no information on measurement site location, distributed displacements, or mapped ruptures. Therefore, we found the geospatial control requirement to be the most limiting factor in including additional events. We also observed a general paucity of distributed rupture and displacement information reported in older events, which we infer to be a data completeness issue and not reflective of earthquake-specific characteristics.

3.2 EXISTING COMPILATIONS

Several previous studies have compiled observational data from historical surface-rupturing earthquakes (Table 3.1). The existing compilations vary in their content and completeness, generally due to limitations in available data and the intended usage of the compilation. There is also considerable event overlap between the compilations, owing to the limited number of historical surface-rupturing earthquakes. For example, the Baize et al. (2020) compilation includes the Takao et al. (2018) data, and the Nurminen et al. (2020) compilation includes the Boncio et al. (2018) data.

We reviewed the existing compilations to identify candidate events and datasets that met our selection criteria (Table 3.1). Our review was limited to published reports and journal papers, as we did not have access to proprietary compilations. In general, compilations with geospatial (two-dimensional) control for displacements and mapped ruptures were considered further for inclusion in the FDHI Database. Each candidate dataset was carefully reviewed for quality (i.e., completeness, accuracy, and consistency; Chapter 3.3.2), and a subset of events in the available compilations that did not meet our data quality requirements were not included in the database (Chapter 3.4).

Table 3.1. Review of existing compilations.

Compilers	No. of Events / Style[1]	Data Format	Reported Displacement	Displacement Spatial Control[3]	Surface Rupture Mapping	Rupture Spatial Control[3]	Meets Initial FDHI Database Selection Criteria
Wells & Coppersmith (1994)	244 / All	Tabulated	Max & mean	None	None	None	No
Pezzopane & Dawson (1996)	9 / NML & SS	Maps	Principal & distributed	2-D	Principal & distributed	2-D	Yes
Wesnousky (2008)	37 / All	Displacement profiles	Principal / main trace(s)	1-D	Principal	None	No
Petersen et al. (2011)	24 / SS	Displacement profiles, GIS	Principal & distributed	Varies, 1-D / 2-D	Varies	Varies, 2-D / none	Yes (subset)
Takao et al. (2018)	22 / SS & RV	GIS	Principal & distributed	2-D	Principal & distributed	2-D	Yes
Boncio et al. (2018)	11 / RV	Maps, GIS[2]	Distributed	2-D	Principal & distributed	2-D	Yes
Baize et al. (2020)	45 / All	GIS[2]	Principal & distributed	2-D	Varies	2-D	Yes
Nurminen et al. (2020)	15 / RV	GIS[2]	Distributed	2-D	Principal & distributed	2-D	Yes[4]

[1] Style of faulting abbreviations: SS = Strike-Slip; NML = Normal; RV = Reverse; OBL = Oblique.
[2] Includes tabulated data with geographic coordinates.
[3] One-dimensional (1-D) and two-dimensional (2-D).
[4] Compilation was released after database expansion cut-off date and is only partially included.

3.3 STANDARD WORKFLOW

We followed a standard workflow for events and datasets meeting the selection criteria to ensure the necessary data and metadata were collected, reviewed, and formatted for import into the relational database. In the following Chapters, we discuss the event metadata development and workflows for collecting the surface rupture, measurement, and geologic data and metadata.

3.3.1 Event Metadata

Earthquakes are identified in the FDHI Database by a unique integer called the earthquake identification number ("EQ_ID"). The earthquake identification number is based on the order the event was added to the database; therefore, the identification numbers are arbitrary and are not in event chronological order. Event metadata collected for the FDHI Database consisted of the common name, magnitude, magnitude type, style of faulting, region, and origin information (date in Coordinated Universal Time and hypocentral location). The seismic moment (in dyne-centimeters) was calculated based on the magnitude per Hanks and Kanamori (1979), except where it was directly reported. Earthquake metadata were assembled from the professional literature, including peer-reviewed journal publications and published reports. We preferentially selected metadata from the NGA-West2 database, which was subject to robust QA/QC process (Ancheta et al., 2013), when available; otherwise, we used an authoritative journal publication (preferred), the USGS database, or the local geoscience authority.

Table 3.2 lists the basic event metadata for all 75 earthquakes in the FDHI Database. This information, along with hypocentral locations and seismic moment, is also included in the flatfiles (Appendix A). The sources for the magnitude, style, and hypocenter metadata are also listed in Table 3.2.

Table 3.2. Event metadata.

EQ_ID	Name	Region	Date	Style[1]	Magnitude, Type[2]	Magnitude / Style Source	Hypocenter Source
1	Landers	California	6/28/1992	SS	7.28, Mw	NGA-West2	NGA-West2
2	HectorMine	California	10/16/1999	SS	7.13, Mw	NGA-West2	NGA-West2
3	EMC	Mexico	4/4/2010	NML-OBL	7.2, Mw	NGA-West2 / Teran et al. (2015)	NGA-West2
4	Balochistan	Pakistan	9/24/2013	SS	7.7, Mw	Gold et al. (2015)	USGS
5	Izmit_Kocaeli	Turkey	8/17/1999	SS	7.51, Mw	NGA-West2	NGA-West2
6	Borrego	California	4/9/1968	SS	6.63, Mw	NGA-West2	NGA-West2
7	Imperial1979	California	10/15/1979	SS	6.53, Mw	NGA-West2	NGA-West2
8	SuperstitionHills	California	11/24/1987	SS	6.54, Mw	NGA-West2	NGA-West2
9	Kobe	Japan	1/16/1995	SS	6.9, Mw	NGA-West2	NGA-West2
10	Denali	Alaska	11/3/2002	SS	7.9, Mw	NGA-West2	NGA-West2
11	Duzce	Turkey	11/12/1999	SS	7.14, Mw	NGA-West2	NGA-West2
12	Wenchuan	China	5/12/2008	RV-OBL	7.9, Mw	NGA-West2	NGA-West2
13	Napa	California	8/24/2014	SS	6.0, Mw	Ponti et al. (2019)	USGS
14	Yushu	China	4/13/2010	SS	6.9, Mwc	USGS	USGS
15	Hualien	Taiwan	2/6/2018	SS	6.4, Mw	Kuo et al. (2018)	USGS
16	ChiChi	Taiwan	9/20/1999	RV-OBL	7.62, Mw	NGA-West2	NGA-West2
17	Kumamoto	Japan	4/15/2016	SS	7, Mww	USGS	USGS
18	Nagano	Japan	11/22/2014	RV	6.2, Mww	USGS	USGS
19	Kashmir	Sub-Himalaya	10/8/2005	RV	7.6, Mw	Kaneda et al. (2008)	USGS
20	Kaikoura	New Zealand	11/13/2016	RV-OBL	7.8, Mw	Zinke et al. (2019)	USGS
21	Darfield	New Zealand	9/3/2010	SS	7.0, Mw	NGA-West2	NGA-West2
22	Parkfield2004	California	9/28/2004	SS	6.0, Mw	NGA-West2	NGA-West2
23	Norcia3	Italy	10/30/2016	NML	6.6, Mww	USGS	USGS
24	Hebgen	Montana	8/18/1959	NML	7.3, Mw	USGS	USGS

EQ_ID	Name	Region	Date	Style[1]	Magnitude, Type[2]	Magnitude / Style Source	Hypocenter Source
25	SanFernando	California	2/9/1971	RV	6.61, Mw	NGA-West2	NGA-West2
26	Bohol	Philippines	10/15/2013	RV	7.1, Mww	USGS	USGS
27	Acambay	Mexico	11/19/1912	NML-OBL	6.9, mB	Langridge et al. (2000)	n/a
28	Imperial1940	California	5/19/1940	SS	6.95, Mw	NGA-West2	NGA-West2
29	Parkfield1966	California	6/28/1966	SS	6.19, Mw	NGA-West2	NGA-West2
30	FairviewPeak	Nevada	12/16/1954	NML-OBL	7.3, Mw	USGS	USGS
31	DixieValley	Nevada	12/16/1954	NML	6.9, Mw	USGS	Baize et al. (2020)
32	GalwayLake	California	6/1/1975	SS	5.2, ML	Kanamori and Fuis (1976)	USGS
33	Sonora	Mexico	5/3/1887	NML-OBL	7.6, Mw	USGS	USGS
34	PleasantValley	Nevada	10/2/1915	NML	7.2, Mw	USGS	USGS
35	Kern	California	7/21/1952	RV	7.36, Mw	NGA-West2	NGA-West2
36	ChalfantValley	California	7/21/1986	SS	6.19, Mw	NGA-West2	NGA-West2
37	Zirkuh	Iran	5/10/1997	SS	7.2, Mw	Berberian et al. (1999)	Nemati (2015)
38	Petermann	Australia	5/20/2016	RV	6.0, Mw	Gold et al. (2019)	Geoscience Australia
39	OwensValley	California	3/26/1872	NML-OBL	7.4, Mw	USGS	n/a
40	LagunaSalada	Mexico	2/23/1892	NML-OBL	7.76, Mw	USGS	USGS
41	Iwaki2011	Japan	4/11/2011	NML	6.6, Mw	Toda and Tsutsumi (2013) / JMA	JMA
42	Ridgecrest1	California	7/4/2019	SS	6.4, Mw	USGS	USGS
43	Ridgecrest2	California	7/6/2019	SS	7.1, Mw	USGS	USGS
44	ElAsnam	Algeria	10/10/1980	RV	7.3, Mw	Hamdache et al. (2010) / Yielding et al. (1981)	Hamdache et al. (2010)
45	Cadoux	Australia	6/2/1979	RV	6.1, Mw	King et al. (2019)	King et al. (2019)
46	Calingiri	Australia	3/10/1970	RV	5.03, Mw	King et al. (2019)	King et al. (2019)
47	MarryatCreek	Australia	3/30/1986	RV	5.7, Mw	King et al. (2019)	King et al. (2019)
48	Meckering	Australia	10/14/1968	RV	6.59, Mw	King et al. (2019)	King et al. (2019)

EQ_ID	Name	Region	Date	Style[1]	Magnitude, Type[2]	Magnitude / Style Source	Hypocenter Source
49	Pukatja	Australia	3/23/2012	RV	5.18, Mw	King et al. (2019)	n/a
50	TennantCreek1	Australia	1/22/1988	RV	6.27, Mw	King et al. (2019)	King et al. (2019)
51	TennantCreek2	Australia	1/22/1988	RV	6.44, Mw	King et al. (2019)	King et al. (2019)
52	TennantCreek3	Australia	1/22/1988	RV	6.58, Mw	King et al. (2019)	King et al. (2019)
53	SanMiguel	Mexico	2/9/1956	SS	6.8, Ms	USGS / Doser (1992)	USGS
54	Yutian	China	2/12/2014	SS	6.9, Mw	Li et al. (2016)	USGS
55	Luzon	Philippines	7/16/1990	SS	7.7, Mwc	USGS	USGS
56	BorahPeak	Idaho	10/28/1983	NML	6.88, Mw	NGA-West2	NGA-West2
57	ElmoreRanch	California	11/24/1987	SS	6.22, Mw	NGA-West2	NGA-West2
58	Pisayambo	Ecuador	3/26/2010	SS	5.0, Mw	Champenois et al. (2017)	Champenois et al. (2017)
59	Rikuu	Japan	8/31/1896	RV	6.7, U	Baize et al. (2020)	Baize et al. (2020)
60	Mikawa	Japan	1/12/1945	RV	6.6, Mw	USGS / Baize et al. (2020)	USGS
61	IzuPeninsula	Japan	5/8/1974	SS	6.5, Ms	Baize et al. (2020)	Baize et al. (2020)
62	IzuOshima	Japan	1/14/1978	SS	6.6, Mwc	USGS / Baize et al. (2020)	Baize et al. (2020)
63	IwateInland	Japan	9/3/1998	RV	5.8, Mwc	USGS / Baize et al. (2020)	Baize et al. (2020)
64	Edgecumbe	New Zealand	3/2/1987	NML	6.6, Mw	NGA-West2	NGA-West2
65	Neftegorsk	Russia	5/27/1995	SS	7.0, Mwc	USGS	USGS
66	ChonKemin	Kyrgyzstan	1/3/1911	RV	8.02, Mw	Kulikova and Kruger (2015)	Kulikova and Kruger (2015)
67	Kunlun_Kokoxili	Northern Tibet	11/14/2001	SS	7.8, Mwc	USGS	USGS
68	LeTeil	France	11/11/2019	RV	4.9, Mww	Ritz et al. (2020) / USGS	Delouis et al. (2021)
69	Norcia1	Italy	8/24/2016	NML	6.2, Mww	USGS	USGS
70	HomesteadValley	California	3/15/1979	SS	5.2, ML	USGS	USGS
71	Palu	Indonesia	9/28/2018	SS	7.5, Mww	USGS	USGS
72	LAquila	Italy	4/6/2009	NML	6.3, Mw	NGA-West2	NGA-West2
73	Spitak	Armenia	12/7/1988	RV-OBL	6.77, Mw	NGA-West2	NGA-West2
74	Killari	India	9/29/1993	RV	6.2, Mwb	USGS	USGS
75	YeniceGonen	Turkey	3/18/1953	SS	7.3, Mw	USGS / Kür?er et al. (2019)	USGS

[1] Style of faulting abbreviations: SS = Strike-Slip; NML = Normal; RV = Reverse; OBL = Oblique

[2] Magnitude types from USGS (2021): Mw = moment magnitude, details not reported; Mwc = moment magnitude based on centroid moment tensor inversion of long-period surface waves; Mww = moment magnitude based on centroid moment tensor inversion of W-phase; mB = body-wave magnitude; ML = local magnitude; Ms = surface-wave magnitude; U = unspecified

3.3.2 Surface Rupture and Measurement Data and Metadata

The workflow for developing surface rupture and measurement information for each earthquake consisted of three steps: (1) literature review; (2) dataset processing; and (3) data quality evaluation. The first step served to identify available datasets that met the selection criteria, and the second step produced uniformly formatted datasets for import into the relational database. The third step documented our quality assessments of the data, which were ultimately used to provide data usage recommendation to the model development teams (Chapter 4.6). The goal of the workflow was to ensure all data were systematically collected and reviewed.

For each earthquake, we performed a literature review to collect candidate datasets with information bearing on surface rupture and fault displacement measurements. We began with existing compilations (Table 3.1) and the references therein and then supplemented event datasets with information from other sources when possible. Each candidate dataset was carefully reviewed for compliance with the selection criteria (particularly geospatial control, single-event data, and no known errors or issues). We reached out to dataset originators on several occasions to ask questions, confirm our intended usage of the data, or request digital source files for data presented in figures.

Multiple data sources were included for the same event in several cases, providing more complete spatial coverage of measurements and surface ruptures and/or technically defensible alternative measurements at the same location. Table 3.3 lists the measurement and surface rupture mapping sources included for all 75 events in the FDHI Database. To systematically track data sources, we assigned each dataset a unique identifier called the dataset identification number (DS_ID). The dataset identification number is based on the order the dataset was added to the database, and it is not related to a specific earthquake because some datasets present data for multiple earthquakes (e.g., existing compilations). In many cases, the most complete surface rupture maps and measurement datasets were generated by different researchers. In a few cases, multiple surface rupture datasets were available for the same earthquake. We manually combined supplementary surface rupture datasets to develop a single rupture dataset for more complete spatial coverage (Table 3.4). When alternative rupture datasets could not be combined, generally due to different mapping scales in overlapping areas, both rupture datasets are included in the database (e.g., 2010 El Mayor-Cucapah, Mexico; 2010 Darfield, New Zealand; and both 2019 Ridgecrest, California earthquakes). We provide recommendations to model development teams on alternative rupture datasets in Chapter 4.6.1. The information on all datasets used, based on dataset identification number (DS_ID) and citation, is included in the flatfile documentation in Appendix A.

Table 3.3. Measurement and surface rupture data sources included in the FDHI Database.

EQ_ID	Name	Measurements: [DS_ID][1] Source	Ruptures: [DS_ID][1] Source
1	Landers	[3] Milliner et al. (2016)	[6] Petersen et al. (2011)
		[6] Petersen et al. (2011)	
2	HectorMine	[2] Field et al. (2013)	[6] Petersen et al. (2011)
		[3] Milliner et al. (2016)	
		[6] Petersen et al. (2011)	
		[99] Chen et al. (2015)	
3	EMC	[18] Fletcher et al. (2014)	[17] Teran et al. (2015)
			[18] Fletcher et al. (2014)
4	Balochistan	[23] Gold et al. (2015)	[23] Gold et al. (2015)
		[75] Zinke et al. (2014)	
5	Izmit_Kocaeli	[6] Petersen et al. (2011)	[6] Petersen et al. (2011)
		[144] Rockwell et al. (2002)	
6	Borrego	[6] Petersen et al. (2011)	[6] Petersen et al. (2011)
7	Imperial1979	[6] Petersen et al. (2011)	[6] Petersen et al. (2011)
8	SuperstitionHills	[100] Sharp et al. (1989)	[100] Sharp et al. (1989)
9	Kobe	[6] Petersen et al. (2011)	[6] Petersen et al. (2011)
		[86] Baize et al. (2020)	
10	Denali	[39] Haeussler et al. (2004)	[24] Haeussler (2009)
		[40] Crone et al. (2004)	
		[90] Schwartz et al. (2012)	
11	Duzce	[37] Pucci et al. (2006)	[160] FDHI Manual Compilation[2] based on: Akyuz et al. (2002); pers. comm., Dawson, T.; and Duman et al. (2005)
		[38] Hartleb et al. (2002)	
		[43] Akyuz et al. (2002)	
		[144] Rockwell et al. (2002)	
12	Wenchuan	[44] Liu-Zeng et al. (2009)	[47] pers. comm., Liu-Zeng, J.
		[45] Liu-Zeng et al. (2010)	
		[46] Liu-Zeng et al. (2012)	
		[50] Xu et al. (2009)	
		[51] Tan et al. (2012)	
		[158] Nurminen et al. (2020)	
13	Napa	[56] Ponti et al. (2019)	[56] Ponti et al. (2019)
14	Yushu	[57] Li et al. (2012)	[57] Li et al. (2012)
		[58] Guo et al. (2012)	
15	Hualien	[61] Kuo et al. (2018)	[62] Huang et al. (2019)
		[62] Huang et al. (2019)	
16	ChiChi	[20] pers. comm., Kuo, Y.-T. and Yu, W.	[142] FDHI Manual Compilation[2] based on: Baize et al. (2020) & pers. comm., Kuo, Y.-T. and Yu, W.
		[65] Huang (1999)	
		[66] Lee et al. (2003)	
		[158] Nurminen et al. (2020)	
17	Kumamoto	[67] Shirahama et al. (2016)	[156] FDHI Manual Compilation[2] based on: Shirahama et al. (2016) and Goto et al. (2017)

EQ_ID	Name	Measurements: [DS_ID][1] Source	Ruptures: [DS_ID][1] Source
18	Nagano	[68] Okada et al. (2015)	[70] Ishimura et al. (2019)
		[69] Katsube et al. (2017)	
		[70] Ishimura et al. (2019)	
19	Kashmir	[71] Kaneda et al. (2008)	[71] Kaneda et al. (2008)
		[158] Nurminen et al. (2020)	
20	Kaikoura	[73] Zinke et al. (2019)	[107] FDHI Manual Compilation[2] based on: GNS Science and Zinke et al. (2019)
		[32] Kearse et al. (2018)	
		[33] Langridge et al. (2018)	
		[34] Williams et al. (2018)	
		[106] Howell et al. (2020)	
21	Darfield	[77] Litchfield et al. (2014)	[80] Villamor et al. (2012) & [103] Langridge et al. (2016)
		[78] Quigley et al. (2012)	
		[79] Elliott et al. (2012)	
22	Parkfield2004	[83] Rymer et al. (2006)	[83] Rymer et al. (2006)
23	Norcia3	[87] pers. comm., Boncio, P., based on: Brozzetti et al. (2019) and Villani et al. (2018)	[87] pers. comm., Boncio, P., based on: Civico et al. (2018); Brozzetti et al. (2019); and unpublished work
24	Hebgen	[84] Johnson et al. (2018)	[157] FDHI Manual Compilation[2] based on: Johnson et al. (2018) and USGS (1964)
		[86] Baize et al. (2020)	
25	SanFernando	[86] Baize et al. (2020)	[167] FDHI Manual Compilation[2] based on: California Geological Survey (2019) and USGS (1971)
		[2] Field et al. (2013)	
26	Bohol	[91] Rimando et al. (2019)	[91] Rimando et al. (2019)
27	Acambay	[93] Urbina and Camacho (1913)	[94] Langridge et al. (2000)
28	Imperial1940	[96] Rockwell and Klinger (2013)	[104] FDHI Manual Compilation[2] based on: California Geological Survey (2019); Rockwell and Klinger (2013); and Trifunac and Brune (1970)
		[162] pers. comm., Dawson, T.	
29	Parkfield1966	[108] Brown and Vedder (1966)	[108] Brown and Vedder (1966)
30	FairviewPeak	[98] Caskey et al. (1996)	[98] Caskey et al. (1996)
31	DixieValley	[98] Caskey et al. (1996)	[98] Caskey et al. (1996)
32	GalwayLake	[97] Hill and Beeby (1977)	[97] Hill and Beeby (1977)
33	Sonora	[110] Suter (2015)	[113] pers. comm., Suter, M.
		[111] Suter (2008a)	
		[112] Suter (2008b)	
34	PleasantValley	[117] Wallace et al. (1984)	[117] Wallace et al. (1984)
35	Kern	[122] Buwalda and St. Amand (1955)	[116] pers. comm., Thompson, S.
36	ChalfantValley	[125] Kahle et al. (1986)	[127] FDHI Manual Compilation[2] based on: Lienkaemper et al. (1987) and dePolo and Ramelli (1987)
		[126] Lienkaemper et al. (126)	

EQ_ID	Name	Measurements: [DS_ID][1] Source	Ruptures: [DS_ID][1] Source
37	Zirkuh	[124] Berberian et al. (1999)	[123] Francesca (2020)
38	Petermann	[120] Gold et al. (2019)	[120] Gold et al. (2019)
39	OwensValley	[129] Beanland and Clark (1994) [128] Haddon et al. (2016) [2] Field et al. (2013)	[129] Beanland and Clark (1994)
40	LagunaSalada	[130] Rockwell et al. (2015)	[130] Rockwell et al. (2015)
41	Iwaki2011	[131] Toda and Tsutsumi (2013) [140] Mizoguchi et al. (2012)	[141] FDHI Manual Compilation[2] based on: Toda and Tsutsumi (2013) and Mizoguchi et al. (2012)
42	Ridgecrest1	[132] DuRoss et al. (2020)	[132] DuRoss et al. (2020) [145] Ponti et al. (2020)
43	Ridgecrest2	[132] DuRoss et al. (2020)	[132] DuRoss et al. (2020) [145] Ponti et al. (2020)
44	ElAsnam	[134] Philip and Meghraoui (1983) [135] Yielding et al. (1981)	[134] Philip and Meghraoui (1983)
45	Cadoux	[136] King et al. (2019)	[136] King et al. (2019)
46	Calingiri	[136] King et al. (2019)	[136] King et al. (2019)
47	MarryatCreek	[136] King et al. (2019)	[136] King et al. (2019)
48	Meckering	[136] King et al. (2019)	[136] King et al. (2019)
49	Pukatja	[136] King et al. (2019)	[136] King et al. (2019)
50	TennantCreek1	[136] King et al. (2019)	[136] King et al. (2019)
51	TennantCreek2	[136] King et al. (2019)	[136] King et al. (2019)
52	TennantCreek3	[136] King et al. (2019)	[136] King et al. (2019)
53	SanMiguel	[139] Harvey (1985)	[139] Harvey (1985)
54	Yutian	[147] Li et al. (2016) [146] pers. comm., Liu-Zeng, J.	[146] pers. comm., Liu-Zeng, J.
55	Luzon	[148] Nakata et al. (1996)	[148] Nakata et al. (1996)
56	BorahPeak	[119] Crone et al. (1987) [149] Vincent (1995) [151] DuRoss et al. (2019)	[150] FDHI Manual Compilation[2] based on: Crone et al. (1987) and Vincent (1995)
57	ElmoreRanch	[100] Sharp et al. (1989)	[100] Sharp et al. (1989)
58	Pisayambo	[86] Baize et al. (2020)	[86] Baize et al. (2020)
59	Rikuu	[86] Baize et al. (2020)	[86] Baize et al. (2020)
60	Mikawa	[86] Baize et al. (2020)	[86] Baize et al. (2020)
61	IzuPeninsula	[86] Baize et al. (2020)	[86] Baize et al. (2020)
62	IzuOshima	[86] Baize et al. (2020)	[86] Baize et al. (2020)
63	IwateInland	[86] Baize et al. (2020)	[86] Baize et al. (2020)
64	Edgecumbe	[86] Baize et al. (2020)	[86] Baize et al. (2020)
65	Neftegorsk	[154] pers. comm., Pinegina, T., Kozhurin, A., & Arcos, B.	[154] pers. comm., Pinegina, T., Kozhurin, A., & Arcos, B.
66	ChonKemin	[152] Arrowsmith et al. (2017)	[152] Arrowsmith et al. (2017)
67	Kunlun_Kokoxili	[52] Xu et al. (2002) [92] Klinger et al. (2005)	[165] Fu et al. (2005)
68	LeTeil	[87] pers. comm., Baize, S.	[87] pers. comm., Baize, S.
69	Norcia1	[87] pers. comm., Boncio, P.	[87] pers. comm., Boncio, P.

EQ_ID	Name	Measurements: [DS_ID][1] Source	Ruptures: [DS_ID][1] Source
70	HomesteadValley	[168] Hill et al. (1980)	[168] Hill et al. (1980)
71	Palu	[169] Wu et al. (2021)	[171] Natawidjaja et al. (2021)
		[170] Jaya et al. (2019)	
		[171] Natawidjaja et al. (2021)	
72	LAquila	[87] pers. comm., Boncio, P.	[87] pers. comm., Boncio, P.
73	Spitak	[173] Nurminen et al. (2020)	[173] Nurminen et al. (2020)
74	Killari	[173] Nurminen et al. (2020)	[173] Nurminen et al. (2020)
		[174] Rajendran et al. (1996)	
75	YeniceGonen	[175] Kür?er et al. (2019)	[175] Kür?er et al. (2019)

[1] See Appendix A, Chapter 5 for full citations for each "DS_ID"

[2] See Table 3.4

Table 3.4. Events with surface rupture maps manually combined from multiple datasets.

EQ_ID	Name	Sources
11	Duzce	Akyuz et al. (2002); pers. comm., Akyuz, S. to Sarmiento, A., dated 28 Dec. 2018; pers. comm., Dawson, T. to Sarmiento, A., dated 18 Jul. 2018; Duman et al. (2005)
16	ChiChi	Baize et al. (2019); pers. comm., Kuo, Y.-T. & Yu, W. to Dawson, T., dated 29 Aug. 2018
17	Kumamoto	Shirahama et al. (2016); Baize et al. (2020); Goto et al. (2017)
20	Kaikoura	GNS Science (2018); Zinke et al. (2019)
24	Hebgen	Johnson et al. (2018); USGS (1964)
25	SanFernando	California Geological Survey (2019); USGS (1971)
28	Imperial1940	California Geological Survey (2019); Rockwell and Klinger (2013); Trifunac and Brune (1970)
36	ChalfantValley	Lienkaemper et al. (1987); dePolo et al. (1987)
41	Iwaki2011	Toda and Tsutsumi (2013); Mizoguchi et al. (2012)
56	BorahPeak	Crone et al. (1987); Vincent (1995)

Measurement and rupture data are provided in the professional literature in multiple formats. Measurement information is typically reported in tables that are embedded in the publication or attached as electronic supplements. The electronic supplements are usually data tabulated in *.csv format (or similar) or encoded for direct use in Geographic Information System (GIS) software as ESRI shapefiles or XML files (e.g., *.kml). Rupture linework is usually provided in GIS format (i.e., shapefiles or *.kml files). In some cases, measurement and rupture data were only provided as maps on figures or plates in the publication. For these datasets, we carefully georeferenced the maps using GIS software (Chapter 3.5), based on the map scale and projection, against appropriate base maps provided by ESRI (typically topographic maps). We then digitized the measurement locations or rupture linework and manually entered the relevant information in the shapefile attribute table.

Basic data cleaning and processing was performed on all original data to generate uniformly formatted ESRI shapefiles. We used the ESRI shapefile format because it was convenient and reliable for performing first-order geospatial analyses and geologic interpretation (Chapter 4) and standardizing data elements for importing into the relational database (Chapter 5). The shapefile format also allowed us to plot the data on base maps and visually inspect the data for quality assessments.

Processing of each measurement and rupture dataset ensured consistent formatting of reported data and metadata. For measurement data, the processing generally included the following: organizing reported measurement components (e.g., Figure 2.10) and uncertainties or ranges; identifying missing or duplicate data entries; adding measurement metadata; and adding event, dataset, site, and measurement identifier information (EQ_ID, DS_ID, PT_ID, and MEAS_ID, respectively). We used Microsoft Excel and Python ("pandas" library dataframes) to format measurement datasets and cull duplicated data. The processing for surface rupture datasets generally included: adding rupture metadata; adding event, dataset, and rupture identifier information (EQ_ID, DS_ID, and RUP_ID, respectively); and performing topological checks in GIS to cull duplicated linework. Processed measurement and rupture datasets were converted into ESRI shapefiles, taking care to properly project the data based on the original coordinate system.

Our data quality review considered three data quality metrics: completeness, accuracy, and consistency. Completeness refers to the spatial extent of the rupture mapping and displacement measurement data in the FDHI Database, relative to the known spatial extent of the surface rupture. We reviewed multiple data sources for each earthquake to develop the most complete dataset possible for each event. Accuracy relates to the reliability of the original data and includes both the spatial accuracy of the measurement location and the accuracy of the reported measurement. We also carefully reviewed the data for each earthquake for internal consistency within an individual data source and between multiple data sources.

The results of our data quality review are included in the database and were used to develop recommendations for the model development teams (Chapter 4.6). The database contains text descriptions of geographic areas that are incomplete, where applicable, to document our assessment of completeness. Co-located or alternative measurements within the same data source and/or from different sources (for the same event) are explicitly identified in the database as part of our consistency evaluation. Finally, through our accuracy assessment, we identified some individual measurements that might be incomplete and/or erroneous (from data sources that are otherwise reliable); these are still included in the database for completeness, but they are explicitly flagged for potential accuracy issues. We developed a quality code system to methodically track our assessments of measurement accuracy and consistency, as described in Chapter 4.6.2.

3.3.3 Geologic Data and Metadata

Geologic datasets were developed from published digital geologic maps to allow the model development teams to investigate geologic controls on fault displacements. These maps were typically regional-scale and published by state or national geoscience authorities in ESRI shapefile format (i.e., georeferenced). Minimal data cleaning and processing was required for the geologic datasets. We retained the unit lithologic and age descriptions as reported, and we added a generalized geology category consisting of bedrock, young alluvium (Holocene), old alluvium, and undifferentiated alluvium. Digital geologic data were available for most events in the database; however, we were unable to acquire information for earthquakes in Africa and some parts of Asia. The geospatial analyses that relate measurement and rupture data to geologic data are described in Chapter 4.1.

3.4 EXCLUDED DATA

Our standard workflow for developing surface rupture and measurement information included a data quality evaluation through which each candidate dataset was carefully reviewed for completeness, accuracy, consistency, and compliance with the event and dataset selection criteria. In this process, we identified and intentionally excluded published datasets with known quality issues and subsets of existing compilations that did not meet the project's quality standards.

We evaluated the existing compilations of fault displacement and surface rupture data in Table 3.1 in detail. Most of the event datasets that met the initial selection screening criteria in Table 3.1 were included in the FDHI Database; however, some of events did not meet the dataset selection criteria or data quality standards (Table 3.5). A subset of events reported in the existing compilations were given lower priority due to difficulty accessing original data or relatively limited number of observations and were not resolved prior to the database entry cut-off date. This subset included the following four earthquakes: 1988 Spitak, Armenia; 1944 Gerede-Bolu, Turkey; 1976 Motagua, Guatamala; 1954 Rainbow Mountain, Nevada.

Table 3.5. Events in existing compilations not included in FDHI Database due to selection criteria or data quality.

Event	Compiler	Comments
1869 Olinghouse, Nevada	Pezzopane & Dawson (1996)	Incomplete rupture mapping, no slip measurements
1903 Wonder, Nevada	Pezzopane & Dawson (1996)	No slip measurements
1932 Cedar Mountain, Nevada	Pezzopane & Dawson (1996)	Incomplete rupture mapping
1934 Excelsior Mountains, Nevada	Pezzopane & Dawson (1996)	No slip measurements
1934 Hansel Valley, Utah	Pezzopane & Dawson (1996)	No slip measurements
1950 Fort Sage, California	Pezzopane & Dawson (1996)	No slip measurements
1954 Stillwater, Nevada	Pezzopane & Dawson (1996)	Incomplete rupture mapping, few slip measurements
1980 Mammoth Lakes, California	Pezzopane & Dawson (1996)	Multi-event earthquake sequence
1993 Eureka Valley, California	Pezzopane & Dawson (1996)	Few slip measurements
1857 Fort Tejon, California	Petersen et al. (2011)	Incomplete rupture mapping
1930 Kita-Izu, Japan	Petersen et al. (2011)	No/incomplete geospatial control
1939 Erzincan, Turkey	Petersen et al. (2011)	No/incomplete geospatial control
1942 Irba-Niksar, Turkey	Petersen et al. (2011)	No/incomplete geospatial control
1943 Tosya, Turkey	Petersen et al. (2011)	No/incomplete geospatial control
1967 Mudurnu, Turkey	Petersen et al. (2011)	No/incomplete geospatial control
1981 Sirch, Iran	Petersen et al. (2011)	No/incomplete geospatial control
1998 Fandoqa, Iran	Petersen et al. (2011)	No/incomplete geospatial control
1938 Kussharo, Japan	Baize et al. (2020)	No rupture mapping

Event	Compiler	Comments
1891 Nobi, Japan	Baize et al. (2020)	Data quality concerns: duplicate sites (coordinates) with conflicting measurements and several sites have no data (meaning is ambiguous)
1927 North Tango, Japan	Baize et al. (2020)	Data quality concerns: duplicate sites (coordinates) with conflicting measurements and several sites have no data (meaning is ambiguous)
1930 North Izu, Japan	Baize et al. (2020)	Data quality concerns: duplicate sites (coordinates) with conflicting measurements and several sites have no data (meaning is ambiguous)
1943 Tottori, Japan	Baize et al. (2020)	Data quality concerns: duplicate sites (coordinates) with conflicting measurements and several sites have no data (meaning is ambiguous)
2000 Tottori Pref. West., Japan	Baize et al. (2020)	Incomplete rupture mapping, data quality concerns: duplicate sites (coordinates) with conflicting measurements and several sites have no data (meaning is ambiguous)
1944 La Laja, Argentina	Baize et al. (2020)	Few slip measurements
1959 Deshibori, Japan	Baize et al. (2020)	Few slip measurements
1918 Omachi, Japan	Baize et al. (2020)	Few slip measurements
1939 Oga, Japan	Baize et al. (2020)	Few slip measurements
2004 Niigata Pref. Chuetsu, Japan	Baize et al. (2020)	Few slip measurements
1984 Nagano Prefecture West., Japan	Baize et al. (2020)	No rupture mapping
2008 Iwate-Miyagi Inland, Japan	Baize et al. (2020)	Data quality concerns: rupture mapping and slip measurements contaminated with non-tectonic deformation (landslides)
1983 Coalinga/Nunez, California	Boncio et al. (2018)	Multi-event earthquake sequence
2016 Kumamoto, Japan	Lin et al. (2016)	Data quality concerns: publication was retracted; see Stein (2019) and Lin et al. (2019)
2014 Nagano, Japan	Lin et al. (2015)	Data quality concerns: appears to mix landslide and fault scarps; see Ishimura et al. (2019)
2008 Wenchuan, China	Lin et al. (2009)	Data quality concerns: slip measurements appear to be erroneous; see Feng et al. (2017)

Event	Compiler	Comments
2001 Kunlun/Kokoxili, Tibet	Lin et al. (2002)	Data quality concerns: slip measurements may be multi-event; see Xu et al. (2002)

3.5 SOFTWARE

The following software was used to manage the collected datasets:

- ESRI ArcMap and ArcGIS Desktop software version 10.7, Advanced license.
- Global Mapper version 19.

3.6 REFERENCES

Akyuz, H. S., Hartleb, R., Barka, A., Altunel, E., Sunal, G., Meyer, B. and Armijo, V. R. (2002). Surface rupture and slip distribution of the 12 November 1999 Duzce earthquake (M 7.1), North Anatolian fault, Bolu, Turkey, *Bulletin of the Seismological Society of America*, **92**(1), 61-66.

Ancheta, T. D., Darragh, R. B., Stewart, J. P., Seyhan, E., Silva, W. J., Chiou, B.-S. J., Wooddell, K. E., Graves R.W., Kottke, A. R., Boore, D. M., Kishida, T. and Donahue, J. L. (2013). PEER NGA-West2 Database, PEER Report 2013/03, *Pacific Earthquake Engineering Research Center*, University of California, Berkeley, CA.

Baize, S., Nurminen, F., Sarmiento, A., Dawson, T., Takao, M., Scotti, O., Azuma, T., Boncio, P., Champenois, J., Cinti, F. R., Civico, R., Costa, C., Guerrieri, L., Marti, E., McCalpin, J., Okumura, K., and Villamor, P. (2020). A worldwide and Unified Database of Surface Ruptures (SURE) for fault displacement hazard analyses, *Seismological Research Letters*, **91**(1), 499-520.

Berberian, M., Jackson, J. A., Qorashi, M., Khatib, M. M., Priestley, K., Talebian, M., and Ghafuri-Ashtiani, M. (1999). The 1997 May 10 Zirkuh (Qa'enat) earthquake (Mw 7.2): faulting along the Sistan suture zone of eastern Iran, *Geophysical Journal International*, **136**(3), 671-694.

Boncio, P., Liberi, F., Caldarella, M., and Nurminen, F. C. (2018). Width of surface rupture zone for thrust earthquakes: implications for earthquake fault zoning, *Natural Hazards and Earth System Sciences*, **18**(1), 241-256.

Brozzetti, F., Boncio, P., Cirillo, D., Ferrarini, F., Nardis, R., Testa, A., Liberi, F., and Lavecchia, G. (2019). High-resolution field mapping and analysis of the August–October 2016 coseismic surface faulting (central Italy earthquakes): Slip distribution, parameterization, and comparison with global earthquakes, *Tectonics*, **38**, 417–439.

California Geological Survey (2019). Alquist-Priolo (AP) Earthquake Fault Zones (EFZ) Geographic Information System (GIS) files, accessed December 2019.

Champenois, J., Baize, S., Vallée, M., Jomard, H., Alvarado, A., Espin, P., Ekström, G., and Audin, L. (2017). Evidences of surface rupture associated with a low-magnitude (M w 5.0) shallow earthquake in the Ecuadorian Andes, *Journal of Geophysical Research: Solid Earth*, **122**(10), 8446-8458.

Civico, R., Pucci, S., Villani, F., Pizzimenti, L., De Martini, P. M., Nappi, R., and Open EMERGEO Working group (2018). Surface ruptures following the 30 October 2016 Mw 6.5 Norcia earthquake, Central Italy, *Journal of Maps*, **14**(2), 151–160.

Crone, A. J., Machette, M. N., Bonilla, M. G., Lienkaemper, J. J., Pierce, K. L., Scott, W. E., and Bucknam, R. C. (1987). Surface faulting accompanying the Borah Peak earthquake and segmentation of the Lost River fault, central Idaho, *Bulletin of the Seismological Society of America*, **77**(3), 739-770.

Delouis, B., Oral, E., Menager, M., Ampuero, J. P., Trilla, A. G., Régnier, M., and Deschamps, A. (2021). Constraining the point source parameters of the 11 November 2019 Mw 4.9 Le Teil earthquake using multiple relocation approaches, first motion and full waveform inversions, *Comptes Rendus. Géoscience*, **353**(S1), 1-24.

dePolo, C. M. and Ramelli, A. R. (1987). Preliminary report on surface fractures along the White Mountains fault zone associated with the July 1986 Chalfant Valley earthquake sequence, *Bulletin of the Seismological Society of America*, **77**(1), 290-296.

Doser, D. I. (1992). Faulting processes of the 1956 San Miguel, Baja California, earthquake sequence, *Pure and Applied Geophysics*, **139**(1), 3-16.

Duman, T. Y., Emre, O., Dogan, A. and Ozalp, S. (2005). Step-over and bend structures along the 1999 Duzce earthquake surface rupture, North Anatolian fault, Turkey, *Bulletin of the Seismological Society of America*, **95**(4), 1250-1262.

Feng, G., Jónsson, S., and Klinger, Y. (2017). Which fault segments ruptured in the 2008 Wenchuan earthquake and which did not? New evidence from near-fault 3D surface displacements derived from SAR image offsets *Bulletin of the Seismological Society of America*, **107**(3), 1185-1200.

GNS Science (2018). "2016 Kaikoura Rupture" GIS download, accessed 9 October 2018.

Gold, R. D., Clark, D., Barnhart, W. D., King, T., Quigley, M., and Briggs, R. W. (2019). Surface rupture and distributed deformation revealed by optical satellite imagery: The intraplate 2016 Mw 6.0 Petermann Ranges earthquake, Australia, *Geophysical Research Letters*, **46**(17-18), 10394-10403.

Gold, R. D., Reitman, N. G., Briggs, R. W., Barnhart, W. D., Hayes, G. P., and Wilson, E. (2015). On-and off-fault deformation associated with the September 2013 Mw 7.7 Balochistan earthquake: Implications for geologic slip rate measurements, *Tectonophysics*, **660**, 65-78.

Goto, H., Tsutsumi, H., Toda, S., and Kumahara, Y. (2017). Geomorphic features of surface ruptures associated with the 2016 Kumamoto earthquake in and around the downtown of Kumamoto City, and implications on triggered slip along active faults, *Earth, Planets and Space*, **69**(1), 26.

Hamdache, M., Pel?ez, J. A., Talbi, A., and Casado, C. L. (2010). A unified catalog of main earthquakes for Northern Algeria from AD 856 to 2008, *Seismological Research Letters*, **81**(5), 732-739.

Hanks, T. C. and Kanamori, H. (1979). A moment magnitude scale, *Journal of Geophysical Research: Solid Earth*, **84**(B5), 2348-2350.

Ishimura, D., Toda, S., Mukoyama, S., Homma, S. I., Yamaguchi, K., and Takahashi, N. (2019). 3D Surface Displacement and Surface Ruptures Associated with the 2014 Mw 6.2 Nagano Earthquake Using Differential Lidar3D Surface Displacement and Surface Ruptures, *Bulletin of the Seismological Society of America*, **109**(2), 780-796.

Johnson, K. L., Nissen, E., and Lajoie, L. (2018). Surface Rupture Morphology and Vertical Slip Distribution of the 1959 Mw 7.2 Hebgen Lake (Montana) Earthquake From Airborne Lidar Topography, *Journal of Geophysical Research: Solid Earth*, **123**(9), 8229-8248.

Kanamori, H. and Fuis, G. (1976). Variation of P-wave velocity before and after the Galway Lake earthquake (ML= 5.2) and the Goat Mountain earthquakes (ML= 4.7, 4.7), 1975, in the Mojave desert, California, *Bulletin of the Seismological Society of America*, **66**(6), 2017-2037.

Kaneda, H., Nakata, T., Tsutsumi, H., Kondo, H., Sugito, N., Awata, Y., Akhtar, S. S., Majid, A., Khattak, W., Awan, A. A., Yeats, R. S., Hussain, A., Ashraf, M., Wesnousky, S. G., and Kausar, A. B. (2008). Surface rupture of the 2005 Kashmir, Pakistan, earthquake and its active tectonic implications, *Bulletin of the Seismological Society of America*, **98**(2), 521-557.

King, T. R., Quigley, M., and Clark, D. (2019). Surface-rupturing historical earthquakes in Australia and their environmental effects: new insights from re-analyses of observational data, *Geosciences*, **9**(10), 408.

Kulikova, G. and Krüger, F. (2015). Source process of the 1911 M 8.0 Chon-Kemin earthquake: Investigation results by analogue seismic records, *Geophysical Journal International*, **201**(3), 1891-1911.

Kür?er, A., Özalp, S., Özdemir, E., Uygun Güldoğan, ? ., and Duman, T. Y. (2019). Active tectonic and paleoseismologic characteristics of the Yenice-Gönen fault, NW Turkey, in light of the 18 March 1953 Yenice-Gönen Earthquake (Ms=7.2), *Bulletin of the Mineral Research and Exploration*, **159**(159), 29-62.

Kuo, Y. T., Wang, Y., Hollingsworth, J., Huang, S.-Y., Chuang, R. Y., Lu, C.-H., Hsu, Y.-C., Tung, H., Yen, J.-Y., and Chang, C.-P. (2018). Shallow fault rupture of the Milun fault in the 2018 M w 6.4 Hualien earthquake: A high-resolution approach from optical correlation of Pléiades satellite imagery, *Seismological Research Letters*, **90**(1), 97-107.

Langridge, R. M., Weldon, R. J., Moya, J. C., and Su?rez, G. (2000). Paleoseismology of the 1912 Acambay earthquake and the Acambay-Tixmadejé fault, Trans-Mexican volcanic belt, *Journal of Geophysical Research: Solid Earth*, **105**(B2), 3019-3037.

Li, H., Pan, J., Lin, A., Sun, Z., Liu, D., Zhang, J., Li, C., Liu, K., Chevalier, M.-L., Yun, K., and Gong, Z. (2016). Coseismic Surface Ruptures Associated with the 2014 Mw 6.9 Yutian Earthquake on the Altyn Tagh Fault, Tibetan Plateau, *Bulletin of the Seismological Society of America*, **106**(2), 595-608.

Lienkaemper, J. J., Pezzopane, S. K., Clark, M. M., and Rymer, M. J. (1987). Fault fractures formed in association with the 1986 Chalfant Valley, California, earthquake sequence: preliminary report, *Bulletin of the Seismological Society of America*, **77**(1), 297-305.

Lin, A., Satsukawa, T., Wang, M., Mohammadi Asl, Z., and Fueta, R. (2019). Retraction, *Science*, **364**(6439), 444.

Lin, A., Satsukawa, T., Wang, M., Mohammadi Asl, Z., Fueta, R., and Nakajima, F. (2016). Coseismic rupturing stopped by Aso volcano during the 2016 Mw 7.1 Kumamoto earthquake, Japan, *Science*, **354**(6314), 869-874.

Lin, A., Sano, M., Yan, B., and Wang, M. (2015). Co-seismic surface ruptures produced by the 2014 Mw 6.2 Nagano earthquake, along the Itoigawa–Shizuoka tectonic line, central Japan, *Tectonophysics*, **656**, 142-153.

Lin, A., Ren, Z., Jia, D., and Wu, X. (2009). Co-seismic thrusting rupture and slip distribution produced by the 2008 Mw 7.9 Wenchuan earthquake, China, *Tectonophysics*, **471**(3-4), 203-215.

Lin, A., Fu, B., Guo, J., Zeng, Q., Dang, G., He, W., and Zhao, Y. (2002). Co-seismic strike-slip and rupture length produced by the 2001 Ms 8.1 Central Kunlun earthquake, *Science*, **296**(5575), 2015-2017.

Mizoguchi, K., Uehara, S. I., and Ueta, K. (2012). Surface Fault Ruptures and Slip Distributions of the Mw 6.6 11 April 2011 Hamadoori, Fukushima Prefecture, Northeast Japan, Earthquake, *Bulletin of the Seismological Society of America*, **102**(5), 1949-1956.

Nemati, M. (2015). Slip distribution, aftershocks and co-seismic fault of some large Persian earthquakes, *Environmental Earth Sciences*, **73**(11), 7165-7181.

Nurminen, F., Boncio, P., Visini, F., Pace, B., Valentini, A., Baize, S., and Scotti, O. (2020). Probability of occurrence and displacement regression of distributed surface rupturing for reverse earthquakes, *Frontiers in Earth Science*, **8**(581605).

Petersen, M. D., Dawson, T. E., Chen, R., Cao, T., Wills, C. J., Schwartz, D. P., and Frankel, A. D. (2011). Fault displacement hazard for strike-slip faults, *Bulletin of the Seismological Society of America*, **101**(2), 805-825.

Pezzopane, S. K. and Dawson, T. E. (1996). Fault displacement hazard: A summary of issues and information. In *Seismotectonic Framework and Characterization of Faulting at Yucca Mountain, Nevada*, U.S. Geological Survey Administrative Report prepared for the U.S. Department of Energy, Chapter 9, 160 pp.

Ponti, D. J., Rosa, C. M., and Blair, J. L. (2019). The Mw 6.0 South Napa earthquake of August 24, 2014 – Observations of surface faulting and ground deformation, with recommendations for improving post-earthquake field investigations (No. 2019-1018). US Geological Survey.

Ritz, J. F., Baize, S., Ferry, M., Larroque, C., Audin, L., Delouis, B., and Mathot, E. (2020). Surface rupture and shallow fault reactivation during the 2019 Mw 4.9 Le Teil earthquake, France, *Communications Earth & Environment*, **1**(1), 1-11.

Rockwell, T. K. and Klinger, Y. (2013). Surface rupture and slip distribution of the 1940 Imperial Valley earthquake, Imperial fault, southern California: Implications for rupture segmentation and dynamics*, Bulletin of the Seismological Society of America*, **103**(2A), 629-640.

Shirahama, Y., Yoshimi, M., Awata, Y., Maruyama, T., Azuma, T., Miyashita, Y., Mori, H., Imanishi, K., Takeda, N., Ochi, T., Otsubo, M., Asahina, D., and Miyakawa, A. (2016). Characteristics of the surface ruptures associated with the 2016 Kumamoto earthquake sequence, central Kyushu, *Japan, Earth, Planets and Space*, **68**(1), 191.

Stein, R. S. (2019), Scientific fraud announced in two studies of the 2016 M=7.0 Kumamoto, Japan, earthquake, *Temblor*, http://doi.org/10.32858/temblor.018.

Takao, M., Kaneto, T., and Kurita, T. (2018). Outline of the PFDHA Method and Recent Studies on PFDHA in Japan. In *Best Practices in Physics-based Fault Rupture Models for Seismic Hazard Assessment of Nuclear Installations: Issues and Challenges Towards Full Seismic Risk Analysis*, 14 pp.

Teran, O. J., Fletcher, J. M., Oskin, M. E., Rockwell, T. K., Hudnut, K. W., Spelz, R. M., Akciz, S. O., Hernandez-Flores, A. P., and Morelan, A. E. (2015). Geologic and structural controls on rupture zone fabric: A field-based study of the 2010 Mw 7.2 El Mayor–Cucapah earthquake surface rupture, *Geosphere*, **11**(3), 899-920.

Trifunac, M. D. and Brune, J. N. (1970). Complexity of energy release during the Imperial Valley, California, earthquake of 1940, *Bulletin of the Seismological Society of America*, **60**(1), 137-160.

Toda, S. and Tsutsumi, H. (2013). Simultaneous reactivation of two, subparallel, inland normal faults during the Mw 6.6 11 April 2011 Iwaki earthquake triggered by the M w 9.0 Tohoku-oki, Japan, earthquake, *Bulletin of the Seismological Society of America*, **103**(2B), 1584-1602.

United States Geological Survey (USGS) (2021). Magnitude Types. URL: https://www.usgs.gov/natural-hazards/earthquake-hazards/science/magnitude-types?qt-science_center_objects=0#qt-science_center_objects.

USGS (1971). The San Fernando, California, earthquake of February 9, 1971: a preliminary report published jointly by the U.S. Geological Survey and the National Oceanic and Atmospheric Administration, *U.S. Geological Survey Professional Paper 733*.

USGS (1964). The Hebgen Lake, Montana, earthquake of August 17, 1959, *U.S. Geological Survey Professional Paper 435*.

Villani, F., Civico, R., Pucci, S., Pizzimenti, L., Nappi, R., De Martini, P. M., and Open EMERGEO Working Group (2018). A database of the coseismic effects following the 30 October 2016 Norcia earthquake in central Italy, *Scientific Data*, **5**, 180049.

Vincent, K.R. (1995). Implications for models of fault behavior from earthquake surface displacement along adjacent segments of the Lost River fault, Idaho, PhD. Dissertation, *University of Arizona*, 152 p.

Wells, D. L. and Coppersmith, K. J. (1994). New empirical relationships among magnitude, rupture length, rupture width, rupture area, and surface displacement, *Bulletin of the Seismological Society of America*, **84**(4), 974-1002.

Wesnousky, S. G. (2008). Displacement and geometrical characteristics of earthquake surface ruptures: Issues and implications for seismic-hazard analysis and the process of earthquake rupture, *Bulletin of the Seismological Society of America*, **98**(4), 1609-1632.

Xu, X., Chen, W., Ma, W., Yu, G., and Chen, G. (2002). Surface rupture of the Kunlunshan earthquake (Ms 8.1), northern Tibetan plateau, China, *Seismological Research Letters*, **73**(6), 884-892.

Yielding, G., Jackson, J. A., King, G. C. P., Sinvhal, H., Vita-Finzi, C., and Wood, R. M. (1981). Relations between surface deformation, fault geometry, seismicity, and rupture characteristics during the El Asnam (Algeria) earthquake of 10 October 1980, *Earth and Planetary Science Letters*, **56**, 287-304.

Zinke, R., Hollingsworth, J., Dolan, J. F., and Van Dissen, R. (2019). Three-dimensional surface deformation in the 2016 Mw 7.8 Kaikōura, New Zealand, earthquake from optical image correlation: Implications for strain localization and long-term evolution of the Pacific-Australian plate boundary, *Geochemistry, Geophysics, Geosystems*, **20**(3), 1609-1628.

4 Data Analysis

Analysis and geologic interpretation of the measurement and rupture data assembled from the professional literature was performed to meet model development needs. This Chapter documents the purposes and procedures of the analyses and interpretations. In brief, we completed geospatial analysis to develop geologic information, elevation data and metrics, and the event-specific coordinate systems (ECS) for each earthquake in the database. We also performed geologic evaluations of each dataset to classify (rank) measurements and ruptures and develop recommended net slip values and usage in model development. Incompatible measurement datasets and technically defensible alternative measurements are also explicitly flagged in the database.

4.1 GEOLOGY

Geologic data were included, when available, for each measurement site to allow the model development teams to investigate geologic controls on fault displacements. The geologic data included lithologic unit descriptions, unit age, general geology description, and distance to the closest mapped bedrock outcrop. The general geology description is six simple categories: bedrock, young alluvium (Holocene), old alluvium, undifferentiated alluvium, water, and glacier. The broad categories for alluvium include a range of sediments, such as fan, fluvial, colluvium, glacial, fluvio-glacial, lacustrine, and marine deposits. Young and old alluvial deposits are separated, when possible, to capture relative degrees of consolidation. The undifferentiated alluvium category is used when the source dataset does not provide age control. The bedrock distance parameter is the distance to the closest surface outcropping of bedrock, not the depth to bedrock. This parameter was included as a proxy for sediment thickness or basin depth (Milliner et al., 2015). The same geologic data are also reported for each rupture line vertex.

The geologic information for each measurement and rupture line vertex was calculated using built-in geospatial analysis tools in ArcGIS (see Chapter 4.7 for software versioning). We used our uniformly processed geologic datasets (Chapter 3.3.3) and measurement/rupture datasets (Chapter 3.3.2), in ESRI shapefile format, as inputs. The input datasets were projected from geographic coordinates into a projected coordinate system (in linear units) appropriate for the event location. The ArcGIS Identity Analysis Tool was used to calculate the geologic unit (including lithology, general geology, and unit age) of each measurement site or rupture line vertex. The ArcGIS Select Analysis and Near Analysis tools were used to calculate the distance between each measurement site (or rupture line vertex) and the closest mapped bedrock outcrop.

4.2 ELEVATION DATA AND METRICS

Elevation data and related metrics were computed for each measurement site to allow the model development teams to investigate topographic effects on fault displacements. We used the 1 arc-second (30 meter) resolution digital elevation model derived from the Shuttle Radar Topography Mission (STRM) data (Farr et al., 2007) for all events except Denali (EQ_ID = 10), which was located outside the SRTM data coverage. For Denali, we down-sampled a 5-meter resolution digital surface model derived from InSAR data (Alaska Geospatial Council, 2021) to 30-meter resolution. The data extraction, down-sampling, and analyses were performed in Python using the Geospatial Data Abstraction Library (GDAL) and Scientific Python library (Chapter 4.7).

The computed metrics quantify ground slope and surface irregularities or terrain texture (i.e., density of topographic peaks and troughs) in the vicinity of the measurement site. The following elevation data and metrics are included in the database:

- Elevation (meters)
- Ground slope (percent)
- Terrain class per Iwahashi et al. (2018): geomorphic terrain class based on ground slope and texture (Table 4.1)
- Prominence or relative elevation per Rai et al. (2017): difference between pixel elevation at site and mean elevation of all pixels in N-meter radius (where N = 125, 250, 500, and 1000)
- Terrain roughness: largest difference between pixel elevation at site and elevation of all adjacent pixels
- Topographic Position Index (TPI): difference between pixel elevation at site and mean elevation of all adjacent pixels
- Terrain Ruggedness Index (TRI) per Riley et al. (1999): total elevation change between pixel elevation at site and all adjacent pixel elevations

Table 4.1. Terrain classification code after Iwahashi et al. (2018).

Code	Geomorphic terrain description
1	steep mountain, rough
2	steep mountain, smooth
3	moderate mountain, rough
4	moderate mountain, smooth
5	hills, rough in small and large scales
6	hills, smooth in small scale, rough in large scale
7	upper large slope
8	middle large slope
9	dissected terrace, moderate plateau
10	slope in and around terrace or plateau
11	terrace, smooth plateau
12	alluvial fan, pediment, bajada, pediplain
13	alluvial plain, pediplain
14	alluvial or coastal plain, pediplain
15	alluvial or coastal plain (gentlest), lake plain, playa

4.3 RANK CLASSIFICATION

At the request of the model development teams, we interpreted the rupture linework and displacement measurements to distinguish principal and distributed faulting. Previous fault displacement models have treated principal and distributed faulting separately (Youngs et al., 2003; Petersen et al., 2011), and some model development teams are anticipated to continue this approach. The model developers recognized value in using expert geologic interpretation and judgment to distinguish principal and distributed ruptures and displacements. Including this information in the FDHI Database allows the model development teams to use the same interpretations of the data.

We follow Coppersmith and Youngs (2000) and Youngs et al. (2003) in defining principal surface ruptures as the primary faults or tectonic/seismogenic features responsible for the earthquake and distributed surface ruptures as the secondary faults, splays, fractures, or shears near the principal fault (Table 4.2). These criteria served as the basis for the Youngs et al. (2003) and Petersen et al. (2011) fault displacement models. An alternative ranking classification system by Baize et al. (2020) and Nurminen et al. (2020), which further subdivides principal and distributed ruptures, was not implemented for this project. In general, our principal surface ruptures typically correspond to Nurminen et al. (2020) Rank 1 and Rank 1.5, and our distributed ruptures correspond to their Ranks 2, 21, and 22.

Fault displacement measurements can also be categorized as principal or distributed, based on the classification of their associated surface rupture (Youngs et al., 2003; Petersen et al., 2011). To better distinguish measurements summed across multiple ruptures or measured across very wide apertures, we introduce two additional measurement rank classifications, cumulative and total, to respectively differentiate these measurements. Specifically, we use the cumulative classification for slip measurements summed across either (1) multiple principal ruptures, or (2) principal rupture(s) and one or more distributed ruptures. Total measurements represent wide-aperture slips calculated from the differencing or image correlation methods discussed in Chapter 2.3.3. The rank descriptions are summarized in Table 4.2. For distributed measurements in reverse, normal, and oblique style earthquakes, we also indicate if the site is located on the hanging wall or footwall.

Table 4.2. Rank classifications used in the FDHI Database.

Feature	Rank	Description
Rupture Line	Principal	Primary fault or tectonic/seismogenic feature responsible for the earthquake
	Distributed	Secondary features near the principal fault, such as other faults, splays, fractures, or shears
Measurement	Total	Wide-aperture displacements calculated from differencing or image correlation methods
	Cumulative	Displacement summed across multiple adjacent principal ruptures; or displacement summed across principal rupture(s) and adjacent distributed rupture(s); or displacement summed across principal rupture(s) and zone of continuous deformation
	Principal	Displacement on principal rupture
	Distributed	Displacement on distributed rupture

Surface rupture and measurement data reported in the professional literature often do not explicitly identify principal/primary or distributed/secondary faulting. As a result, we developed a workflow to manually assign principal, distributed, cumulative, and total rankings to all data in the FDHI Database (Figure 4.1). While we considered event characteristics such as style of faulting, dataset quality and completeness (e.g., mapping scale, known limitations such as inaccessible areas), and the original authors' interpretations in developing the rankings, the workflow relies largely on iterative application of geologic judgment. Figure 4.2 shows an example application of the workflow for part of the 1968 **M** 6.63 Borrego Mountain, California (EQ_ID = 6) earthquake.

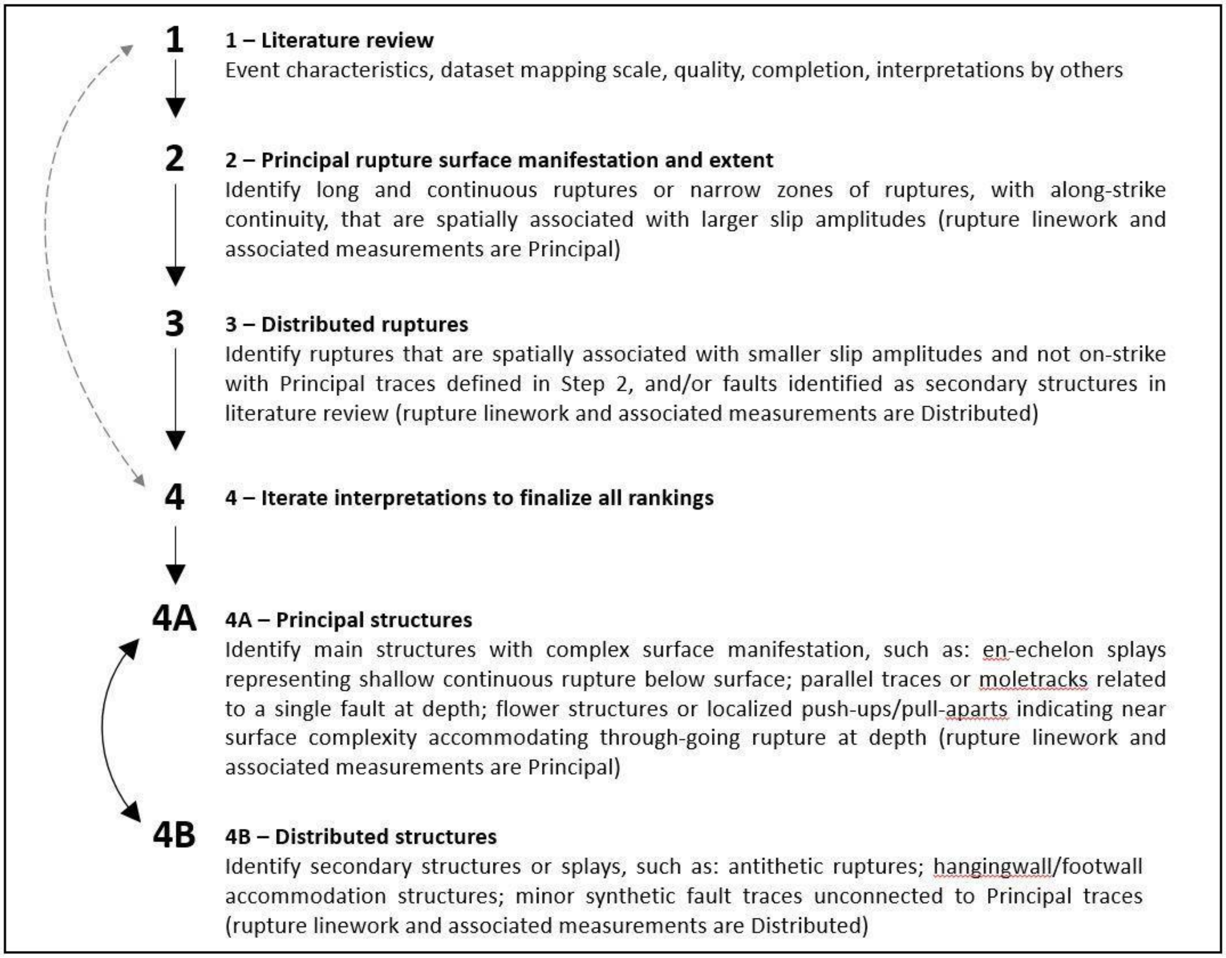

Figure 4.1. Flowchart for developing rank classifications based on geologic interpretation.

Principal surface rupture expression at the ground surface can vary significantly, as discussed in Chapter 2. Common patterns include the following: simple linear or curvilinear traces; segmented zones with en-echelon, anastomosing, or branching traces; moletrack zones; overlapping step-overs; flower or other slip-partitioning structures; and monoclinal warping or tilting. Examples of rank classifications for some of these patterns are shown in Figure 4.3 from the 1968 **M** 6.63 Borrego Mountain, California (EQ_ID = 6) and 1992 **M** 7.28 Landers, California (EQ_ID = 1) earthquakes. Although the classifications may be non-unique, they have been applied as consistently as possible across the contents of the database.

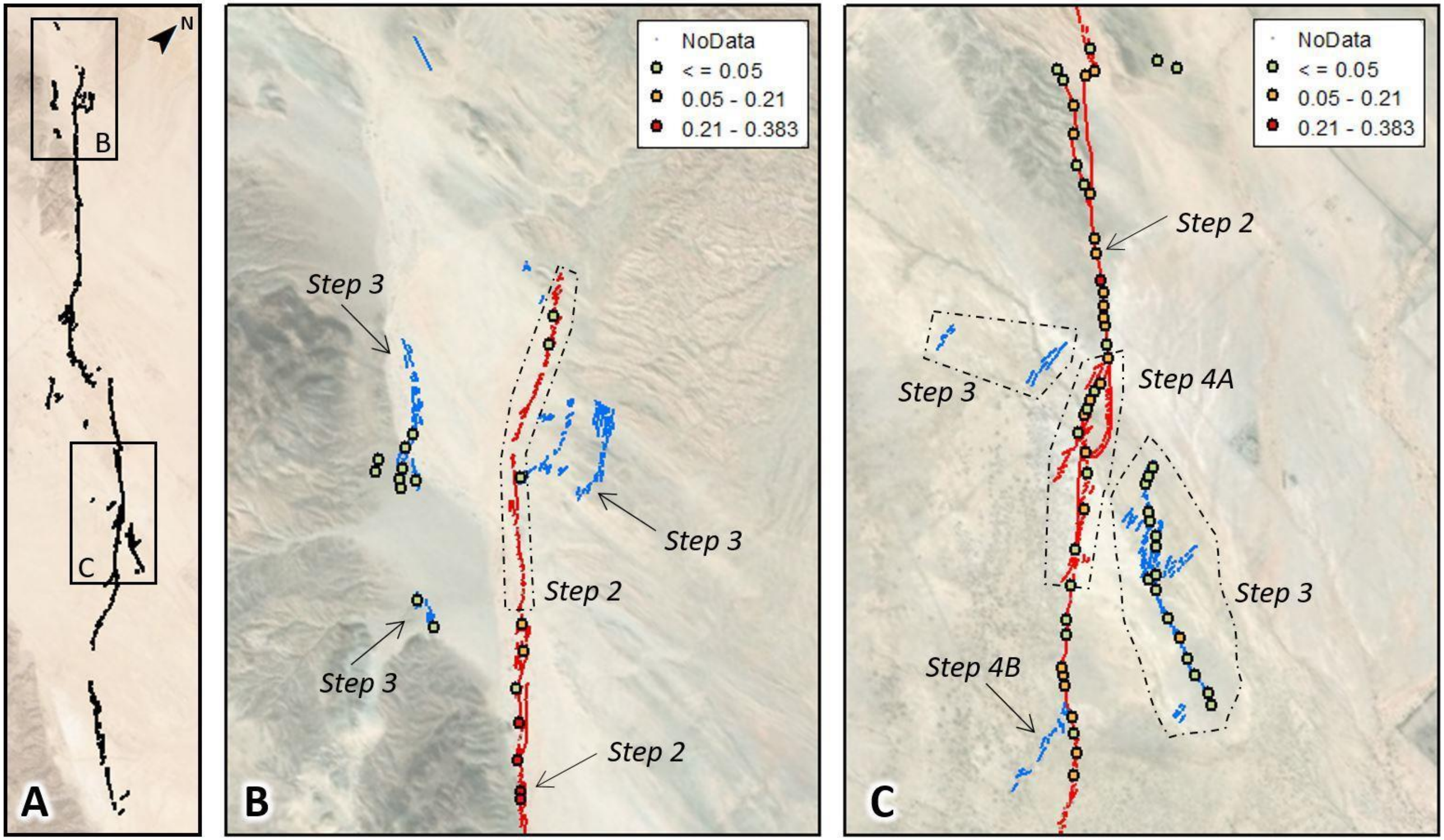

Figure 4.2. Example application of rank classification workflow applied to a portion of the 1968 **M** 6.63 Borrego Mountain, California earthquake; see Figure 4.1 for workflow steps and description. (A) Map of full surface rupture (black lines) at 1:350,000 scale. (B) and (C) Maps of rupture traces ranked in various steps as labeled; Red lines = principal ruptures; blue lines = distributed ruptures; filled circles are slip measurement sites, color-coding as shown in legend for recommended net displacement in meters. Arrows and black dashed polygons identify area considered in labeled workflow step. Map scale is 1:60,000.

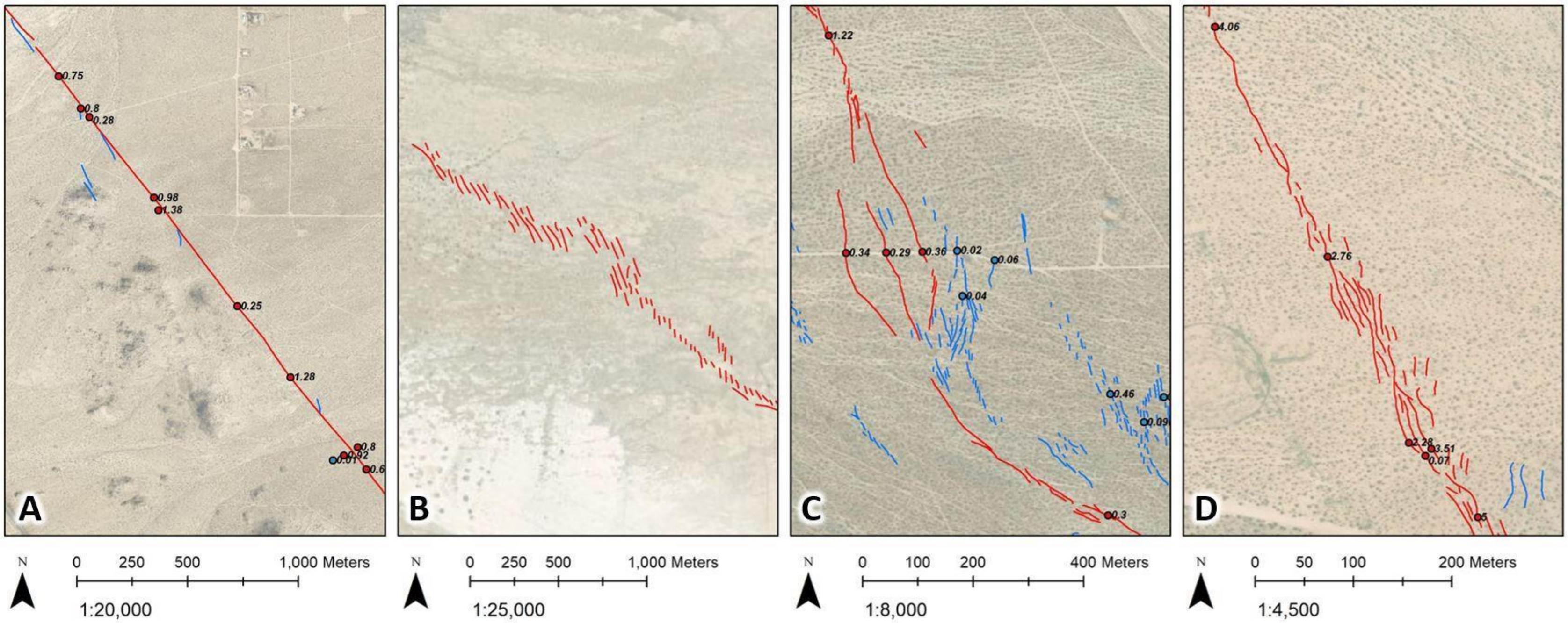

Figure 4.3. Example rank classifications for various surface rupture patterns. Red lines and circles are principal rank; blue lines and circles are distributed rank. Filled circles are slip measurement sites with recommended net displacement in meters. (A) Simple curvilinear principal fault trace from 1992 Landers, California **M** 7.28 earthquake. (B) Principal faulting as en-echelon overstepping array (R Riedel shears) from 1968 **M** 6.63 Borrego Mountain, California earthquake. (C) Tri-furcated/branching principal fault traces from Landers earthquake. (D) Anastomosing zone of principal faulting from Landers earthquake.

4.4 PAIRING MEASUREMENT SITES TO MAPPED RUPTURES

For end-user convenience, the closest mapped rupture to each measurement is explicitly identified in the database. Specifically, we report the rupture identifier ("RUP_ID") and distance to the rupture for each measurement, considering the classification of the measurement and rupture. The closest mapped principal rupture trace is reported for measurements classified as principal, cumulative, or total. For measurements classified as distributed, the closest mapped rupture, regardless of classification, is returned. The calculations were performed using built-in geospatial analysis tools in ArcGIS. The uniformly processed measurement and rupture datasets (Chapter 3.3.2), in ESRI shapefile format, were used as inputs, and the input datasets were projected from geographic coordinates into a projected coordinate system (in linear units) appropriate for the event location. The ArcGIS Select Analysis and Near Analysis tools were used to calculate the distance between each measurement site and the closest mapped rupture.

Measurement sites commonly are not perfectly co-located on a mapped rupture. In our experience compiling and analyzing the database, we found that spatial discrepancies were mainly related to the format in which the original data were provided in the professional literature. Data from older events were more likely to be documented on topographic maps with hand-drawn rupture linework and measurement sites, and the measurement sites and mapped ruptures are generally co-located. Conversely, in many modern datasets, measurement locations are recorded by handheld GPS devices, and rupture linework is collected on various media (e.g., printed maps, aerial photographs, digital base maps) at variable scales. Our experience is that dataset originators do not consistently check for spatial compatibility between the measurement site coordinates and mapped rupture linework. Furthermore, inconsistencies between measurement locations and mapped ruptures are also common when the rupture and measurement datasets were generated by different researchers (Chapter 3.3.2).

4.5 EVENT-SPECIFIC COORDINATE SYSTEM (ECS)

In the FDHI database, the locations of displacement points and rupture-line vertices are defined in terms of the latitude and longitude coordinates. However, in fault displacement hazard analyses, the along-strike and perpendicular-to-strike distance metrics are used to describe the location of fault displacements.

The objective of the event coordinate system (ECS) is to provide a unique value of the along-strike and perpendicular-to-strike distance metrics for every data point for the events in the database. A key challenge is that some of the ruptures have multiple parallel strands, complicating the selection of a single value for each distance metric. In the proposed approach, the along-strike and perpendicular-to-strike distance metrics are defined based on a reference axis for each event. This reference axis is not intended to match individual rupture strands, but instead provides a local coordinate system for the entire rupture profile. For instance, in the case of multiple sub-parallel ruptures strands, the reference axis will pass through the middle of the ruptures.

The location of the reference axis is estimated based on the location and amplitude of slip at the displacement measurement sites and the location of rupture-line vertices. With the reference axis determined, the u and t local axes are defined with respect to it. The u axis corresponds to the along-strike distance as measured from one arbitrary end of the rupture, and the t axis corresponds to the perpendicular-to-strike distance as measured from the reference axis.

An iterative process is used to estimate the location of the reference axis. At the start of each iteration, the location of the reference axis is expressed as a function of u:

$$f_{ref} = \begin{cases} x_{ref}(u) \\ y_{ref}(u) \end{cases} \tag{4.1}$$

where, $x_{ref}(u)$ and $y_{ref}(u)$ are the UTM coordinates. The starting solution for the reference axis corresponds to the first component of a principal component analysis of the displacement points and rupture-line vertices. In the subsequent iterations, the location of the reference axis is updated by minimizing the objective function g:

$$g = \sum_{i=1}^{n} wt_i \left[(x_{pt,i} - x_{ref}(u))^2 + (y_{pt,i} - y_{ref}(u))^2 \right] + \lambda \int_{u=0}^{L} \frac{\partial^2 x_{ref}}{\partial u} + \frac{\partial^2 y_{ref}}{\partial u^2} du \tag{4.2}$$

where x_{pt} and y_{pt} are ordinates of the displacement measurement sites and rupture-line vertices projected into Universal Transverse Mercator (UTM) coordinates. The first part of Equation 4.2 measures the weighted distance between the reference line and displacement measurement sites and rupture-line vertices, and the second part of the equation measures the curvature of the reference line scaled by the penalty factor, λ. The distance to the displacement measurement sites is weighted by the mean value of recommended net displacement, while the weights for the distance to the rupture-line vertices are equal to 0.01. Both the displacement measurement sites and rupture-line vertices are used in the calculation of the reference axis because the rupture lines commonly extend beyond the displacement measurement sites. With this weighting scheme, the reference axis is guided by the displacement measurement sites in areas of the surface rupture that are mapped by both displacement measurement sites and rupture vertices, whereas the reference axis is guided by the rupture-line vertices in parts of the surface rupture that are mapped only by rupture lines. Based on experts' review of preliminary results, the penalty factor, λ, is set to 0.1. Equation 4.2 ensures that the reference axis will pass close to the displacement points with the largest displacement values, as those points are assumed to be part of the main rupture, but also that the reference line remain smooth. The iterative procedure is terminated once the maximum distance between the current and the previous reference axis is less than 10 m. Once the reference axis is determined, the second version of generalized coordinate system (GC2; Spudich and Chiou, 2015) is applied to calculate the u and t coordinates of all the displacement measurement sites and rupture-line vertices in the event.

As an example of an ECS calculation, Figure 4.4 shows the reference axis and u and t local coordinate axes for the surface rupture of the 1992 **M** 7.28 Landers earthquake. Overall, the reference line maintains smoothness and passes through the middle of the displacement measurement sites. Furthermore, the reference axis is consistent with the mapped ends of the fault rupture.

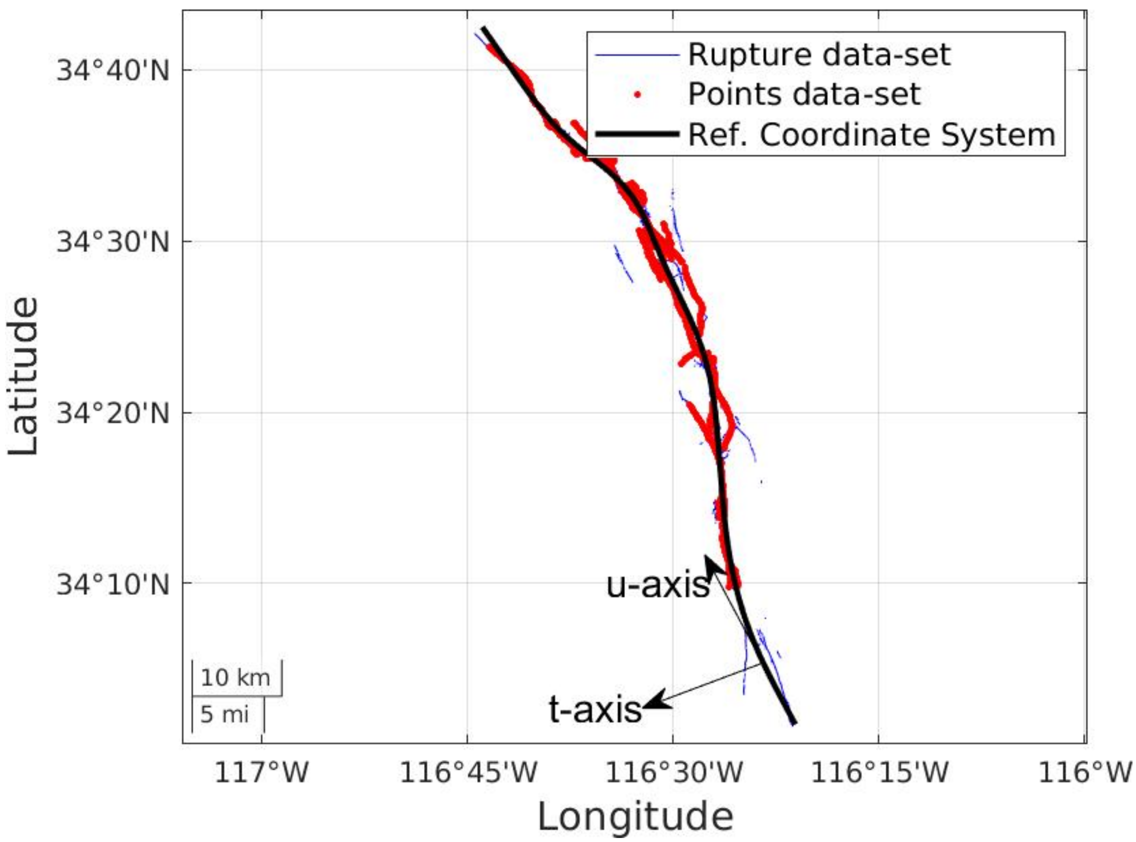

Figure 4.4. Event coordinate system for surface rupture of 1992 Landers, California **M** 7.28 earthquake (EQ_ID = 1).

4.6 RECOMMENDATIONS FOR MODEL DEVELOPERS

The FDHI Database was developed in collaboration with the model developers to ensure the content addressed model development needs. Below, we document differences in alternative rupture datasets that could impact the new models (Chapter 4.6.1), the development of recommended net slip values and usage flags for each measurement in the database (Chapter 4.6.2), specific events with potential foreshock or aftershock contamination (Chapter 4.6.3), and specific events with spatial completeness limitations (Chapter 4.6.4).

4.6.1 Surface Rupture Data

We collected the highest quality surface rupture data available for the earthquakes in the database through our literature review (Chapter 3). When multiple supplementary surface rupture datasets were available for the same event, we manually combined the datasets to develop a single composite rupture dataset (Chapter 3.3.2 and Table 3.4). In a few cases, the available rupture datasets are alternatives (not supplements) and could not be combined due to different mapping scales in areas of overlap. The alternative rupture datasets are included in the database for completeness, and we do not identify a preferred dataset as any preference would depend on specific modeling needs. Table 4.3 lists the events that have alternative surface rupture datasets and characteristics of the individual datasets.

Table 4.3. Events with alternative surface rupture mapping datasets in the FDHI Database.

EQ_ID	Name	DS_ID	Scale[1]	Completeness	Source
3	EMC	17	Larger (1:500) (more detail), uniform throughout	Incomplete in liquefaction area (i.e., southeast of 32.268°N, 115.324°W)	Teran et al. (2015)
		18	Smaller (less detail), uniform throughout	Complete	Fletcher et al. (2014)
21	Darfield	80	Larger (more detail), uniform throughout	Complete	Villamor et al. (2012)
		103	Smaller (1:250,000) (less detail), uniform throughout	Complete	Langridge et al. (2016)
42	Ridgecrest1	132	Smaller (less detail), uniform throughout	Complete	DuRoss et al. (2020)
		145	Larger (more detail), varies throughout	Complete	Ponti et al. (2020)
43	Ridgecrest2	132	Smaller (less detail), uniform throughout	Complete	DuRoss et al. (2020)
		145	Larger (more detail), varies throughout	Complete	Ponti et al. (2020)

[1] Actual scale listed if reported in original source. Larger/smaller convention per Avery and Berlin (1992).

4.6.2 Fault Displacement Measurement Data

At the request of the model development teams, we provided recommended net slip values and usage flags for each measurement in the database. To complete this effort, we used custom measurement quality codes, a measurement technique compatibility identifier, and a measurement co-location identifier to guide our recommendations. Every measurement in the FDHI Database was evaluated in detail through this process.

We developed recommended net slip values for each measurement in the database. Fault displacement measurements are usually reported in the literature as a specific slip component, such as lateral slip or scarp height (Chapter 2.4.1). The individual slip component measurements as reported by the dataset originators are in the FDHI Database; however, to support model development, we also aggregated the reported slip components into recommended net slip values. Including this information in the FDHI Database allows the model development teams to develop displacement models for the same displacement metric, based on the same input data.

When dataset originators directly report a net (three-dimensional) slip component (TDS in Figure 2.10), we use this as the recommended net slip value; otherwise, the recommended net slip was calculated from the reported slip components for each measurement using basic trigonometric relationships (Figure 2.10 and Equations 2.1 through 2.3). In our experience, the dip angle and dip-slip component (ADS in Figure 2.10) were rarely reported in the source data, and the fault-normal component (FNS in Figure 2.10) was only occasionally reported; therefore, most of the calculated recommended net slip values imply a vertical fault (i.e., 90° dip). To systematically track the basis for the recommended net slip values, we list the reported slip components used in the calculation in a field called "recommended_net_vector_basis" in the database (cf. flatfile documentation in Appendix A). We also calculated upper and lower bounds of recommended net slips based on the bounding range calculated from the reported slip components.

We also created measurement quality codes to methodically document our assessments of the accuracy and consistency of every recommended net slip value in the database as part of our data quality review. The quality codes identify measurements with location errors or unreported slip components (relating to accuracy, as defined in Chapter 3.3.2) and sites that have alternative measurements (relating to consistency, as defined in Chapter 3.3.2). To track our consistency assessments, we also created a unique location identifier ("location_id") for each earthquake and a compatibility or grouping identifier ("group_id"). Alternative measurements known or inferred to be at the same location have the same "location_id" (which is unique for each earthquake). The "group_id" field is used to explicitly separate the data in each earthquake into recommended sets that are internally compatible. The most common example is differentiating between wide-aperture measurements (e.g., based on optical image correlation) and field measurements collected on a discrete rupture. Other examples of incompatible measurements include events with datasets that mix vertical slip and scarp height, and measurement techniques that might unintentionally include slip from multiple events. Table 4.4 lists the groupings for each earthquake in the database.

Although all the information used to define the groupings is included in the database (e.g., individual slip components, measurement technique), we found that aggregating the relevant information into one field was a useful step towards developing recommended data usage flags for the model developers.

Table 4.4. Measurement technique groupings ("group_id" column) in the FDHI Database.

EQ_ID	Name	group_id	Measurement Technique
1	Landers	1_01	field-based measurements
1	Landers	1_02	optical image correlation
2	HectorMine	2_01	field-based measurements
2	HectorMine	2_02	optical image correlation
2	HectorMine	2_03	post-event lidar measurements (acquired ~10 yrs after earthquake)
3	EMC	3_01	field-based measurements
4	Balochistan	4_01	post-event high-resolution satellite imagery measurements
4	Balochistan	4_02	optical image correlation, densely spaced (~0.5 km average spacing)
4	Balochistan	4_03	optical image correlation, broadly spaced (~5.5 km average spacing)
5	Izmit_Kocaeli	5_01	field-based measurements
6	Borrego	6_01	field-based measurements
7	Imperial1979	7_01	field-based measurements
8	SuperstitionHills	8_01	field-based measurements
9	Kobe	9_01	field-based measurements
10	Denali	10_01	field-based measurements
11	Duzce	11_01	field-based measurements
12	Wenchuan	12_01	field-based measurements, based on vertical offset
12	Wenchuan	12_02	field-based measurements, based on scarp height
13	Napa	13_01	field-based measurements
14	Yushu	14_01	field-based measurements
15	Hualien	15_01	field-based measurements
15	Hualien	15_02	optical image correlation
16	ChiChi	16_01	field-based measurements
17	Kumamoto	17_01	field-based measurements
18	Nagano	18_01	field-based measurements
19	Kashmir	19_01	field-based measurements
20	Kaikoura	20_01	field-based measurements
20	Kaikoura	20_02	optical image correlation
21	Darfield	21_01	field-based measurements; post-event lidar measurements; post-event high-resolution satellite imagery measurements
22	Parkfield2004	22_01	field-based measurements

EQ_ID	Name	group_id	Measurement Technique
23	Norcia3	23_01	field-based measurements
24	Hebgen	24_01	post-event lidar measurements (acquired ~50 yrs after earthquake), based on vertical offset
24	Hebgen	24_02	field-based measurements, based on scarp height
25	SanFernando	25_01	field-based measurements
26	Bohol	26_01	field-based measurements
27	Acambay	27_01	field-based measurements (acquired ~125 yrs after earthquake)
28	Imperial1940	28_01	field-based measurements
29	Parkfield1966	29_01	field-based measurements
30	FairviewPeak	30_01	field-based measurements
31	DixieValley	31_01	field-based measurements
32	GalwayLake	32_01	field-based measurements
33	Sonora	33_01	field-based measurements (acquired ~125 yrs after earthquake)
34	PleasantValley	34_01	field-based measurements
35	Kern	35_01	field-based measurements
36	ChalfantValley	36_01	field-based measurements
37	Zirkuh	37_01	field-based measurements
38	Petermann	38_01	field-based measurements
38	Petermann	38_02	optical image correlation
39	OwensValley	39_01	field-based measurements (acquired ~100 yrs after earthquake)
39	OwensValley	39_02	post-event lidar measurements (acquired ~125 yrs after earthquake, with some field verification)
40	LagunaSalada	40_01	field-based measurements (acquired ~125 yrs after earthquake)
41	Iwaki2011	41_01	field-based measurements
42	Ridgecrest1	42_01	field-based measurements
43	Ridgecrest2	43_01	field-based measurements
44	ElAsnam	44_01	field-based measurements
45	Cadoux	45_01	field-based measurements
46	Calingiri	46_01	field-based measurements
47	MarryatCreek	47_01	field-based measurements
48	Meckering	48_01	field-based measurements
49	Pukatja	49_01	field-based measurements
50	TennantCreek1	50_01	field-based measurements
51	TennantCreek2	51_01	field-based measurements
52	TennantCreek3	52_01	field-based measurements
53	SanMiguel	53_01	field-based measurements
54	Yutian	54_01	field-based measurements
55	Luzon	55_01	field-based measurements
56	BorahPeak	56_01	field-based measurements
56	BorahPeak	56_02	post-event lidar measurements (acquired ~40 yrs after earthquake)

EQ_ID	Name	group_id	Measurement Technique
57	ElmoreRanch	57_01	field-based measurements
58	Pisayambo	58_01	field-based measurements
58	Pisayambo	58_02	InSAR slip inversion
59	Rikuu	59_01	field-based measurements
60	Mikawa	60_01	field-based measurements
61	IzuPeninsula	61_01	field-based measurements
62	IzuOshima	62_01	field-based measurements
63	IwateInland	63_01	field-based measurements
64	Edgecumbe	64_01	field-based measurements
65	Neftegorsk	65_01	field-based measurements
66	ChonKemin	66_01	field-based measurements (acquired ~100 yrs after earthquake)
67	Kunlun_Kokoxili	67_01	field-based measurements
67	Kunlun_Kokoxili	67_02	post-event high-resolution satellite imagery measurements
68	LeTeil	68_01	field-based measurements
68	LeTeil	68_02	InSAR slip inversion
69	Norcia1	69_01	field-based measurements
70	HomesteadValley	70_01	field-based measurements
71	Palu	71_01	field-based measurements
72	LAquila	72_01	field-based measurements
73	Spitak	73_01	field-based measurements
74	Killari	74_01	field-based measurements
75	YeniceGonen	75_01	field-based measurements

Recommended usage flags are included in the FDHI Database for each recommended net slip value. The flags are based on the quality codes and therefore are based on our assessment of the accuracy and consistency of the measurement. Table 4.5 lists the quality codes and the associated usage flag. We use three recommended usage flags: Keep, Check, and Toss. Recommended net slip values labeled as "Keep" are high quality data and can be used with confidence, provided that the model developer considers the rank (Chapter 4.3) and "group_id" associated with the recommended net slip value. Values labeled as "Toss" are low quality data that are erroneous or incomplete and should not be used for recommended net slip values; however, these measurement sites have other useful information (e.g., strike, dip), so they are preserved in the database. Finally, values labeled as "Check" might have quality issues related to consistency (i.e., alternative measurements) or accuracy (i.e., location errors or incomplete measurements), as documented in the quality code (Table 4.5). Model developers can use the quality codes to decide if values labeled as "Check" are appropriate for their models, again considering the rank and grouping associated with the recommended net slip value.

Table 4.5. Recommended net slip value quality codes used in the FDHI Database.

Quality Code	Explanation	Recommendation[1]	Model Development Usage Flag[1]
1	No known errors or issues (can be any rank or group_id)	Reliable data	Keep
2000	Multiple measurements (same rank and same group_id) available at same location_id (confident[2])	Review available alternative data	Check
2001	Multiple measurements (same rank and same group_id) available at same location_id (inferred[2])	Review available alternative data	Check
3000	Incomplete measurement, lateral slip component might be missing	Use with caution	Check
3001	Incomplete measurement, vertical slip component might be missing	Use with caution	Check
3002	Measurement might be minimum	Use with caution	Check
3003	Measurement might be maximum	Use with caution	Check
3004	Dataset originator quality is low	Use with caution	Check
3005	Deformation might not be tectonic	Use with caution	Check
3006	Incomplete measurement, extensional slip component might be missing	Use with caution	Check
4000	Location might be erroneous	Use with caution	Check
4001	Measurement might be erroneous	Use with caution	Check
5000	Measurement technique might mis-estimate vertical slip component	Use with caution	Check
9000	Other measurement at location_id is more complete	Unreliable data	Toss
9001	No measurement data	Unreliable data	Toss
9002	Incomplete measurement, significant lateral slip unaccounted for	Unreliable data	Toss
9003	Incomplete measurement, significant vertical slip unaccounted for	Unreliable data	Toss
9004	Measurement likely erroneous	Unreliable data	Toss
9005	Location likely erroneous	Unreliable data	Toss
9006	Deformation likely not tectonic	Unreliable data	Toss

[1] Applies to recommended net slip value; included in database for model developers.
[2] Measurements identified as co-located based on documentation from dataset originators (confident) or our evaluation of the reported slip components and site locations (inferred).

4.6.3 Foreshocks and Aftershocks

Spatiotemporal clustering of surface-rupturing earthquakes can cause difficulty in differentiating ruptures and displacements between events. We explicitly identify surface rupture and/or fault displacement data in the FDHI Database that might reflect deformation from an earthquake sequence ("multi_event_flag") or from an aftershock ("aftershock_flag"), where such information is available. Two events in the database have areas that might have ruptured in an aftershock (1992 Landers, California and 2010 Yushu, China), and one event has data that captures both foreshocks and the mainshock (2016 Norcia, Italy). These events are listed in Table 4.6. Maps differentiating areas that might have ruptured in the mainshock and aftershock for the Landers, Yushu, and Kumamoto events are shown on Figure 4.5.

Table 4.6. Events in FDHI Database with potential foreshock or aftershock deformation.

EQ_ID	Name	Foreshock/Aftershock Notes
1	Landers	Southern-most portion (south of Pinto Mountain Fault) may have ruptured in aftershock; see Figure 4.5A (Hough et al., 1993)
14	Yushu	Northwestern portion may have ruptured in aftershock; see Figure 4.5B (Li et al., 2012)
23	Norcia3	Some measurements reflect unknown displacement from foreshocks (pers. comm., Boncio. P., based on: Brozzetti et al., 2019 and Villani et al., 2018b)

The 2016 Norcia, Italy **M** 6.6 earthquake (EQ_ID = 23) has more fault displacement measurements (n=5,718) than any other event in the FDHI Database. However, measurements from this event include an unspecified amount of displacement produced by foreshocks in areas that re-ruptured in the mainshock. The mainshock occurred on October 30, 2016 and was preceded by two surface-rupturing foreshocks on August 24, 2016 and October 26, 2016. The first foreshock (**M** 6.0 August 24, 2016) ruptured the southern portion of the mainshock rupture area, and the October 26, 2016 **M** 5.9 foreshock ruptured the northern portion. While some studies document fault displacements or displacement profiles of the August 24, 2016 foreshock (e.g., Villani et al., 2018a; Brozzetti et al., 2019), the contribution from foreshocks is not separated in the curated dataset used in the FDHI Database (Boncio, P., pers. comm.). The curated dataset was developed from extensive data quality reviews and was recommended by the model developers and SURE project colleagues as the authoritative dataset for this event. Model development teams and end users should be aware that the Norcia earthquake data in the FDHI Database is not strictly single-event, but rather includes an undetermined amount of deformation from **M** 6.0 and **M** 5.9 foreshocks.

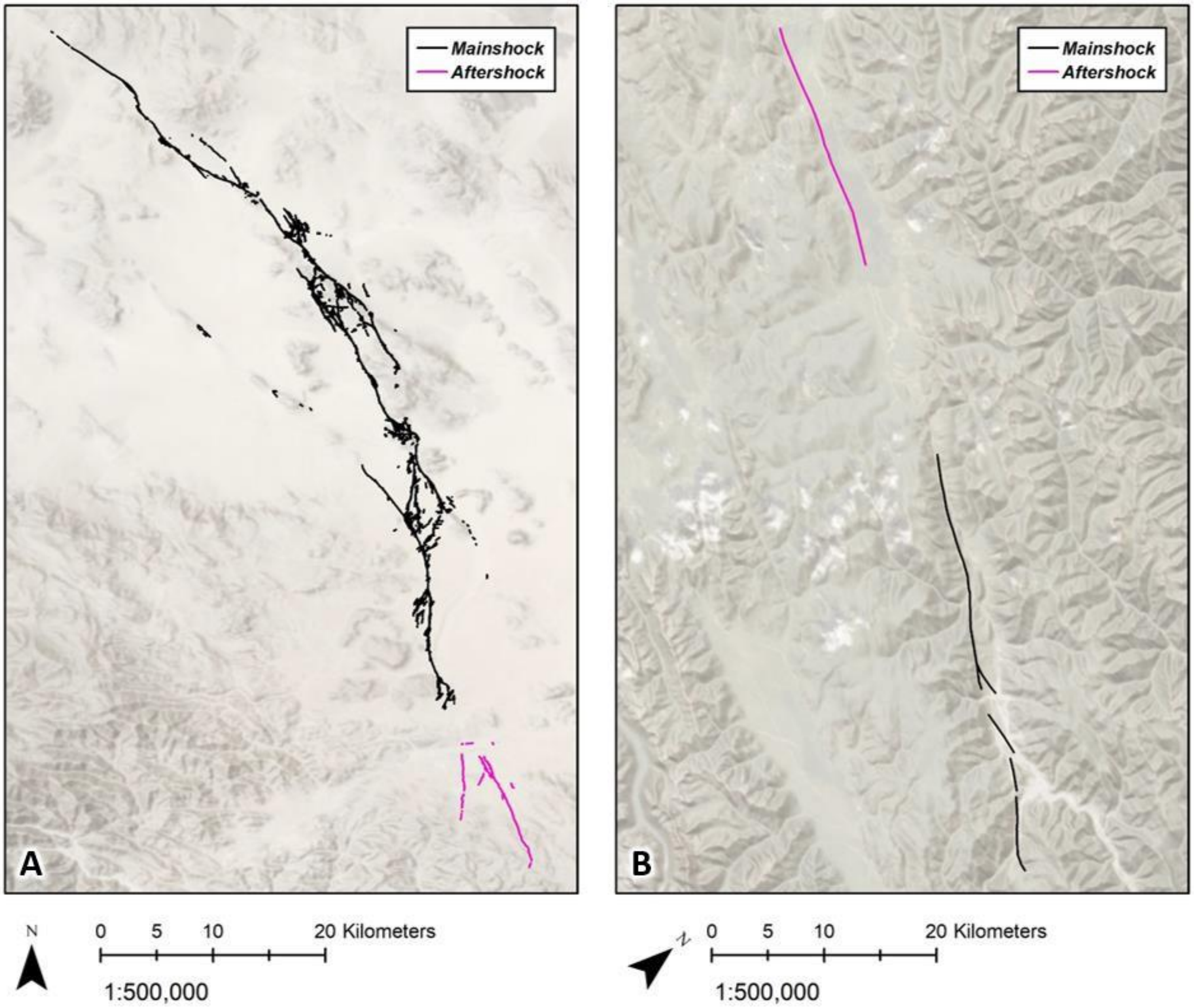

Figure 4.5. Spatial distribution of mainshock (black) and aftershock (magenta) surface ruptures in (A) 1992 **M** 7.28 Landers, California earthquake (EQ_ID = 1) and (B) 2010 **M** 6.9 Yushu, China earthquake (EQ_ID = 14).

Finally, we note two earthquake sequences in California (1987 Superstition Hills-Elmore Ranch and 2019 Ridgecrest) where the surface rupture and fault displacement data were successfully separated into individual events. The 1987 **M** 6.22 Elmore Ranch (EQ_ID = 57) earthquake ruptured several southwest-trending left-lateral faults and was shortly followed by the **M** 6.54 Superstition Hills earthquake (EQ_ID = 8), which ruptured a southeast-trending right-lateral fault system. The first event occurred at approximately six o'clock in the evening local time, and field investigation teams were not able to evaluate surface rutpures before the second event occurred roughly 12 hours later. Surface ruptures from the 1987 Superstition Hills-Elmore Ranch sequence are commonly differentiated based on fault strike and style of faulting (Sharp et al., 1989) (Figure 4.6.). Similarly, the 2019 Ridgrecrest earthquake sequence included two surface-rutpuring earthquakes that occurred 34 hours apart. Rapid response by field investiagtion and geodesy teams allowed surface ruptures and fault displacements from the **M** 6.4 foreshock (EQ_ID = 42) to be documented prior to the **M** 7.1 mainshock (EQ_ID = 43), allowing the data from the sequence to be reliably separated into individual events (DuRoss et al., 2020; Milliner and Donnellan, 2020) (Figure 4.7).

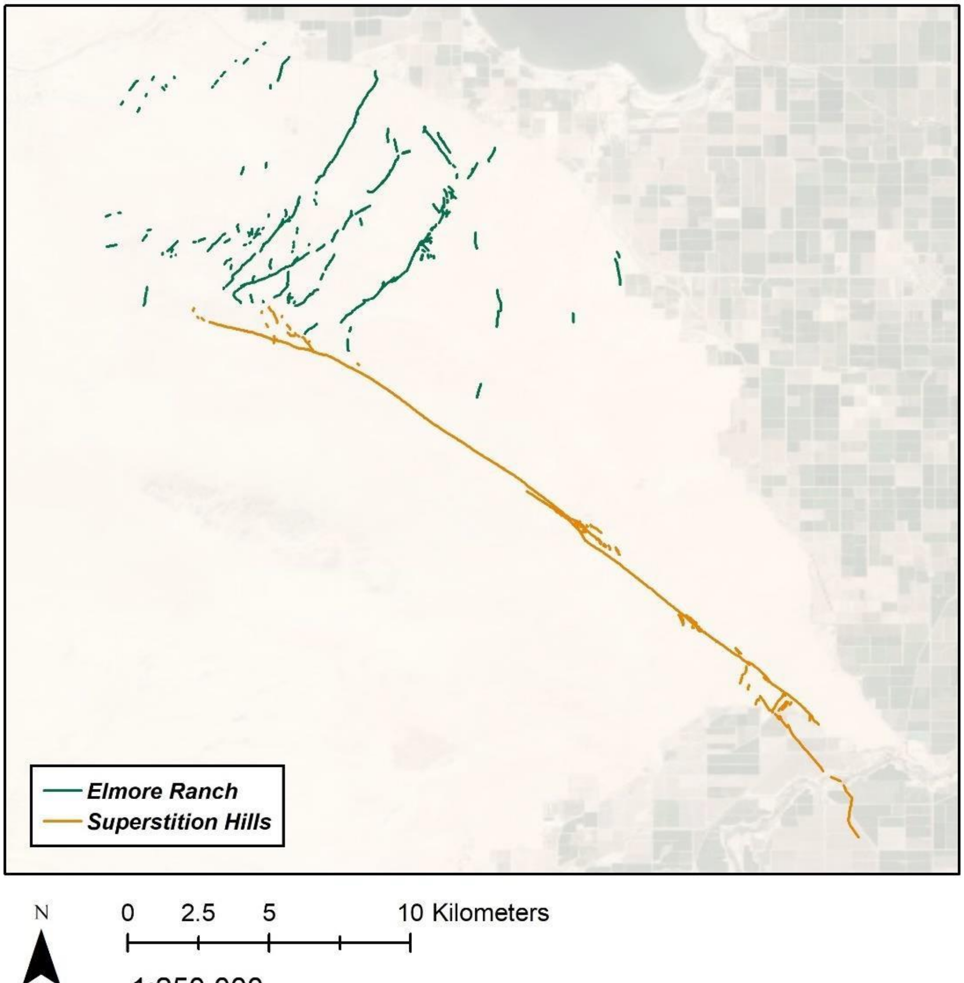

Figure 4.6. Surface ruptures from 1987 Superstition Hills-Elmore Ranch, California earthquake sequence. Green lines: **M** 6.22 Elmore Ranch earthquake (EQ_ID = 57). Orange lines: **M** 6.54 Superstition Hills earthquake (EQ_ID = 8).

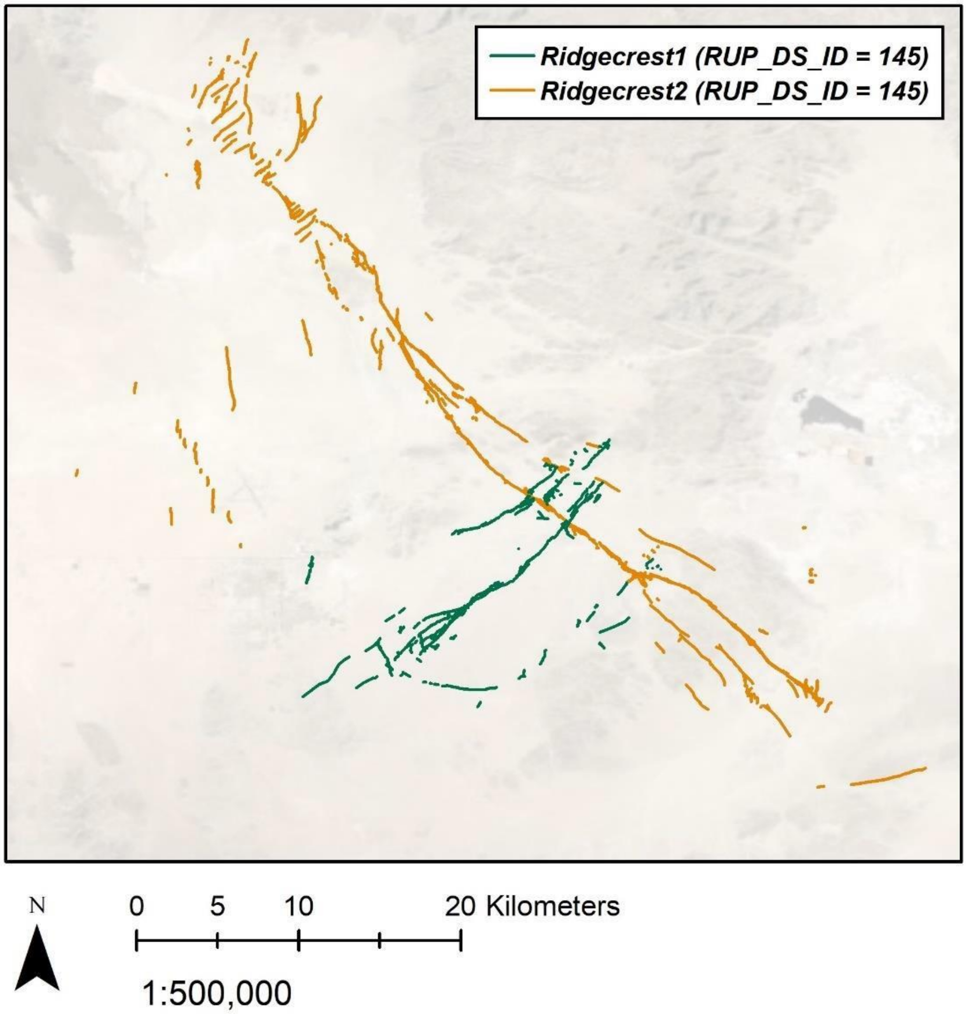

Figure 4.7. Surface ruptures from 2019 Ridgecrest, California earthquake sequence. Green lines: **M** 6.4 Ridgecrest1 earthquake (EQ_ID = 42). Orange lines: **M** 7.1 Ridgecrest2 earthquake (EQ_ID = 43). See Chapter 4.6.1 and Table 4.3 for discussion on alternative surface rupture datasets for the Ridgecrest earthquakes.

4.6.4 Spatial Completeness Limitations

As discussed in Chapter 2, logistical constraints can preclude full documentation of surface ruptures and fault displacement measurements in an earthquake. The level of detail in rupture mapping can vary in different areas of the rupture, and the spatial distribution of measurement sites is nonuniform. As part of our data quality review, we evaluated the completeness of the data for each earthquake in the FDHI Database relative to the known spatial extent of the surface rupture. While most of the events in the FDHI Database generally have complete spatial coverage of surface ruptures and measurements (notwithstanding variations in mapping scale and nonuniform spacing of measurement sites), a subset of events listed in Table 4.7 have incomplete data in specific areas. Two earthquakes (1992 Landers, California and 2010 Yushu, China) have known slip gaps near areas that may have ruptured in aftershocks (Figure 4.5 and Table 4.6).

Table 4.7. Events in FDHI Database with known spatial completeness limitations.

EQ_ID	Name	Spatial Completeness Notes
1	Landers	Surface rupture mapping and measurements are complete; known slip gap near 34.147°N, 116.416°W
3	EMC	Extensive liquefaction southeast of 32.268°N, 115.324°W; no measurements in liquefaction area; no surface rupture mapping in "DS_ID = 17" in liquefaction area, but "DS_ID = 18" surface rupture mapping is complete[1]
5	Izmit_Kocaeli	Surface rupture mapping is complete, but no measurements in Sea of Marmara and Lake Sapanca
9	Kobe	Surface rupture mapping and measurements on Awaji Island are complete; possible undocumented rupture offshore (to northwest in Akashi Strait)
12	Wenchuan	Possible undocumented rupture to southwest
13	Napa	Surface rupture mapping is complete, but no measurements south of 38.225°N, 122.311°W (in Napa River estuary)
14	Yushu	Surface rupture mapping and measurements are complete; known slip gap near 33.135°N, 96.667°E
15	Hualien	Surface rupture mapping and measurements on island of Taiwan are complete; undocumented rupture offshore to northeast, and possible undocumented offshore to southeast
20	Kaikoura	Surface rupture mapping is complete; measurements in "group_id = 20_01" are concentrated in onshore Northern Domain and on Hundalee Fault[2]
26	Bohol	Surface rupture mapping on Bohol Island is complete; possible undocumented rupture offshore (to southwest in Cebu Strait); measurements are concentrated at northeastern area of rupture
27	Acambay	Surface rupture mapping is complete; measurements are concentrated at southeastern area of rupture
56	BorahPeak	Surface rupture mapping is complete; measurements in "group_id = 56_02" are concentrated in Thousand Springs-Mackay Fault area[2]
61	IzuPeninsula	Surface rupture mapping and measurements on Honshu Island are complete; possible undocumented rupture offshore (to southeast)
62	IzuOshima	Surface rupture mapping and measurements on Honshu Island are complete; possible undocumented rupture offshore (to southeast)
71	Palu	Surface rupture mapping is complete in onshore and offshore portion south of Tanimbaya Peninsula; possible undocumented rupture to north-northwest; no measurements offshore

[1] The two alternative surface rupture maps for the 2010 El Mayor-Cucapah (EMC) earthquake are differentiated by the dataset identification number (DS_ID); see Chapter 4.6.1 for discussion.
[2] The grouping identifier ("group_id") is used to explicitly separate the data in each earthquake into internally compatible sets based on measurement technique and aperture; see Chapter 4.6.2 for discussion.

4.7 SOFTWARE

The following software was used in the data analysis:

- ESRI ArcMap and ArcGIS Desktop software version 10.7, Advanced license
- Geospatial Data Abstraction Library (GDAL) version 3.2.1
- Scientific Python (SciPy) version 1.6.1

4.8 REFERENCES

Alaska Geospatial Council (2021). Alaska IFSAR Data and Status Web App. URL: http://agc.dnr.alaska.gov/elevation.html.

Avery, T. E. and Berlin, G. L. (1992). Fundamentals of remote sensing and airphoto interpretation. Macmillan.

Baize, S., Nurminen, F., Sarmiento, A., Dawson, T., Takao, M., Scotti, O., Azuma, T., Boncio, P., Champenois, J., Cinti, F. R., Civico, R., Costa, C., Guerrieri, L., Marti, E., McCalpin, J., Okumura, K., and Villamor, P. (2020). A worldwide and Unified Database of Surface Ruptures (SURE) for fault displacement hazard analyses, *Seismological Research Letters*, **91**(1), 499-520.

Brozzetti, F., Boncio, P., Cirillo, D., Ferrarini, F., Nardis, R., Testa, A., Liberi, F., and Lavecchia, G. (2019). High-resolution field mapping and analysis of the August–October 2016 coseismic surface faulting (central Italy earthquakes): Slip distribution, parameterization, and comparison with global earthquakes, *Tectonics*, **38**, 417–439.

Coppersmith, K. J. and Youngs, R. R. (2000). Data needs for probabilistic fault displacement hazard analysis, *Journal of Geodynamics*, **29**(3-5), 329-343.

DuRoss, C. B., Gold, R. D., Dawson, T. E., Scharer, K. M., Kendrick, K. J., Akciz, S. O., Angster, S. J., Bachhuber, J., Bacon, S., Bennett, S. E. K., et al. (2020). Surface Displacement Distributions for the July 2019 Ridgecrest, California, Earthquake Ruptures, *Bulletin of the Seismological Society of America*, **110**(4), 1400-1418.

Farr, T. G., Rosen, P. A., Caro, E., Crippen, R., Duren, R., Hensley, S., Kobrick, M., Paller, M., Rodriguez, E., Roth, L., Seal, D., Shaffer, S., Shimada, J., Umland, J., Werner, M., Oskin, M., Burbank, D., and Alsdorf, D. (2007). The shuttle radar topography mission, *Reviews of Geophysics*, **45**(2).

Fletcher, J. M., Teran, O. J., Rockwell, T. K., Oskin, M. E., Hudnut, K. W., Mueller, K. J., Spelz, R. M., Akciz, S. O., Masana, E., Faneros, G., Fielding, E. J., Leprince, S., Morelan, A. E., Stock, J., Lynch, D. K., Elliott, A. J., Gold, P., Liu-Zeng, J., Gonz?lez-Ortega, A., Hinojosa-Corona, A., and Gonz?lez-Garc?a, J. (2014). Assembly of a large earthquake from a complex fault system: Surface rupture kinematics of the 4 April 2010 El Mayor–Cucapah (Mexico) Mw 7.2 earthquake, *Geosphere*, **10**(4), 797-827.

Hough, S. E., Mori, J., Sembera, E., Glassmoyer, G., Mueller, C., and Lydeen, S. (1993). Southern surface rupture associated with the 1992 M7.4 Landers Earthquake: Did it all happen during the mainshock?, *Geophysical Research Letters*, **20**(23), 2615-2618.

Iwahashi, J., Kamiya, I., Matsuoka, M., and Yamazaki, D. (2018). Global terrain classification using 280 m DEMs: segmentation, clustering, and reclassification, *Progress in Earth and Planetary Science*, **5**(1), 1-31.

Langridge, R. M., Ries, W. F., Litchfield, N. J., Villamor, P., Van Dissen, R. J., Barrell, D. J. A., Rattenbury, M. S., Heron, D. W., Haubrock, S., Townsend, D. B., Lee, J. M., Berryman, K. R., Nicol, A., Cox, S.C., and Stirling, M. W. (2016). The New Zealand Active Faults Database, *New Zealand Journal of Geology and Geophysics*, **59**(1), 86-96.

Li, C. Y., Pang, J. Z., and Zhang, Z. Q. (2012). Characteristics, geometry, and segmentation of the surface rupture associated with the 14 April 2010 Yushu earthquake, eastern Tibet, China, *Bulletin of the Seismological Society of America*, **102**(4), 1618-1638.

Milliner, C. and Donnellan, A. (2020). Using Daily Observations from Planet Labs Satellite Imagery to Separate the Surface Deformation between the 4 July Mw 6.4 Foreshock and 5 July Mw 7.1 Mainshock during the 2019 Ridgecrest Earthquake Sequence, *Seismological Research Letters*, **91**(4), 1986-1997.

Milliner, C. W., Dolan, J. F., Hollingsworth, J., Leprince, S., Ayoub, F., and Sammis, C. G. (2015). Quantifying near-field and off-fault deformation patterns of the 1992 Mw 7.3 Landers earthquake, *Geochemistry, Geophysics, Geosystems*, **16**(5), 1577-1598.

Nurminen, F., Boncio, P., Visini, F., Pace, B., Valentini, A., Baize, S., and Scotti, O. (2020). Probability of occurrence and displacement regression of distributed surface rupturing for reverse earthquakes, *Frontiers in Earth Science*, **8**(581605).

Petersen, M. D., Dawson, T. E., Chen, R., Cao, T., Wills, C. J., Schwartz, D. P., and Frankel, A. D. (2011). Fault displacement hazard for strike-slip faults, *Bulletin of the Seismological Society of America*, **101**(2), 805-825.

Ponti, D. J., Blair, J. L., Rosa, C. M., Thomas, K., Pickering, A. J., Akciz, S., Angster, S., Avouac, J.-P., Bachhuber, J., Bacon, S., et al. (2020). Documentation of Surface Fault Rupture and Ground-Deformation Features Produced by the 4 and 5 July 2019 Mw 6.4 and Mw 7.1 Ridgecrest Earthquake Sequence, *Seismological Research Letters*, **91**(5), 2942-2959.

Rai, M., Rodriguez-Marek, A., and Chiou, B. S. (2017). Empirical terrain-based topographic modification factors for use in ground motion prediction, *Earthquake Spectra*, **33**(1), 157-177.

Riley, S. J., DeGloria, S. D., and Elliot, R. (1999). A terrain ruggedness index that quantifies topographic heterogeneity, *Intermountain Journal of Sciences*, **5**(1-4), 23-27.

Sharp, R. V., Budding, K. E., Boatwright, J., Ader, M. J., Bonilla, M. G., Clark, M. M., Fumal, T. E., Harms, K. K., Lienkaemper, J. J., Morton, D. M., O'Neill, B. J., Ostergren, C. L., Ponti, D. J., Rymer, M. J., Saxton, J. L., and Sims, J. D. (1989). Surface faulting along the Superstition Hills fault zone and nearby faults associated with the earthquakes of 24 November 1987, *Bulletin of the Seismological Society of America*, **79**(2), 252-281.

Spudich, P., and Chiou, B. (2015). Strike-parallel and strike-normal coordinate system around geometrically complicated rupture traces: Use by NGA-West2 and further improvements. US Department of the Interior, US Geological Survey.

Teran, O. J., Fletcher, J. M., Oskin, M. E., Rockwell, T. K., Hudnut, K. W., Spelz, R. M., Akciz, S. O., Hernandez-Flores, A. P., and Morelan, A. E. (2015). Geologic and structural controls on rupture zone fabric: A field-based study of the 2010 Mw 7.2 El Mayor–Cucapah earthquake surface rupture, *Geosphere*, **11**(3), 899-920.

Villamor, P., Litchfield, N., Barrell, D., Van Dissen, R., Hornblow, S., Quigley, M., Levick, S., Ries, W., Duffy, B., Begg, J., Townsend, D., Stahl, T., Bilderback, E., Noble, D., Furlong, K., and Grant, H. (2012). Map of the 2010 Greendale Fault surface rupture, Canterbury, New Zealand: application to land use planning, *New Zealand Journal of Geology and Geophysics*, **55**(3), 223-230.

Villani, F., Pucci, S., Civico, R., De Martini, P. M., Cinti, F. R., and Pantosti, D. (2018a). Surface faulting of the 30 October 2016 Mw 6.5 central Italy earthquake: Detailed analysis of a complex coseismic rupture, *Tectonics*, **37**, 3378–3410.

Villani, F., Civico, R., Pucci, S., Pizzimenti, L., Nappi, R., De Martini, P. M., and Open EMERGEO Working Group (2018b). A database of the coseismic effects following the 30 October 2016 Norcia earthquake in central Italy, *Scientific Data*, **5**, 180049.

Youngs, R. R., Arabasz, W. J., Anderson, R. E., Ramelli, A. R., Ake, J. P., Slemmons, D. B., McCalpin, J. P., Doser, D. I., Fridrich, C. J., Swan III, F. H., Rogers, A. M., Yount, J. C., Anderson, L. W., Smith, K. D., Bruhn, R. L., Knuepfer, P. L. K., Smith, R. B., dePolo, C. M., O’Leary, D. W., Coppersmith, K. J., Pezzopane, S. K., Schwartz, D. P., Whitney, J. W., Olig, S. S., and Toro, G. R. (2003). A methodology for probabilistic fault displacement hazard analysis (PFDHA), *Earthquake Spectra*, **19**(1), 191-219.

5 Relational Database Development

5.1 INTRODUCTION

A custom relational database was created to systematically manage the event, measurement, and rupture data and related metadata that were assembled and developed for this project. Relational databases use a defined schema to store different data types in individual tables, relate the data between tables using key fields, and hold the information and schema in a single file. Alternative data repository formats are typically collections of separate spreadsheets with limited or no cross-referencing. The relational database structure improves efficiency, quality control, and expandability, relative to spreadsheet formats, by minimizing errors due to repetition, enforcing data entry constraints, and enforcing defined relationships between tables. Relational databases are relatively new to the geotechnical engineering community, but they are well-established in the information technology and petroleum industries (Hoffman, 2003; Brandenberg et al., 2018; Mazzoni et al., 2020).

Relational database management systems can be server-based (client-server model) or embedded (serverless). For this project, we sought an open-source management system with a wide range of programming language support (e.g., Matlab toolbox, Python or R libraries) that was compatible with multiple computer operating systems (Windows, Macintosh, and Linux). We also decided a serverless management system was more appropriate because the database would not require multiple users to simultaneously update or query data entries. Based on these criteria, the SQLite database engine (Hipp, 2020) was selected as the relational database management system. Specific software versioning is reported in Chapter 5.3 and Appendix B.

This Chapter provides an overview of the relational database structure (or schema) and contents. More details bearing on the individual tables and schema are provided in Appendix B. The contents of the database have been aggregated into flatfiles for formal documentation and end-user convenience (Chapter 6 and Appendix A). We recommend most users of the FDHI Database use the flatfiles.

5.2 DATABASE STRUCTURE AND CONTENTS

The process of designing the relational database began with a systematic review of surface rupture characteristics, data collection tools, techniques, and reporting standards (Chapter 2), and existing fault displacement and surface rupture compilations (Chapter 3). We collaborated with the model developers to determine the initial database contents and then developed a custom schema to accommodate the range of data types. As the project progressed, additional data and interpretations requested by the model development teams were readily accommodated by the custom and flexible database schema.

Several different types of data are available to document historical surface-rupturing earthquakes. For this project, we broadly grouped the data types into four categories: earthquake information, rupture information, measurement information, and the event-specific coordinate system (ECS) model (Figure 5.1). Each category contains information such as metadata, geospatial data, direct observations, analysis outputs, or interpretations, as described in Chapters 3 and 4 of this report.

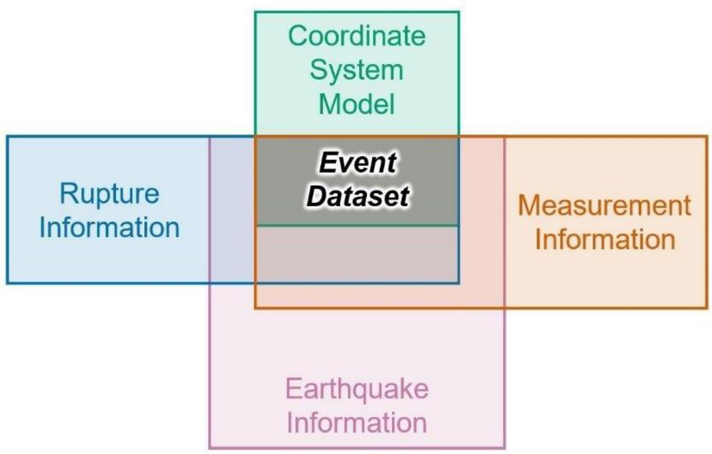

Figure 5.1. Schematic showing four data-type categories that collectively describe an earthquake (event) dataset.

The core database structure is shown in the relational schema diagram in Figure 5.2. Four database tables are emphasized by the yellow shading in the diagram, corresponding to the four data type categories from Figure 5.1. Placeholder table names ("RUP_otherTables" and "PT_otherTables") are shown in Figure 5.2 to illustrate the general relationship between the core database structure and the other individual observation or interpretation database. Table 5.1 summarizes the relationship between the data type categories and the core database schema. The entire database contains 37 individual tables. Appendix B contains additional documentation on the database schema, including lists of every table and column in the database and access to a digital version of the full schema.

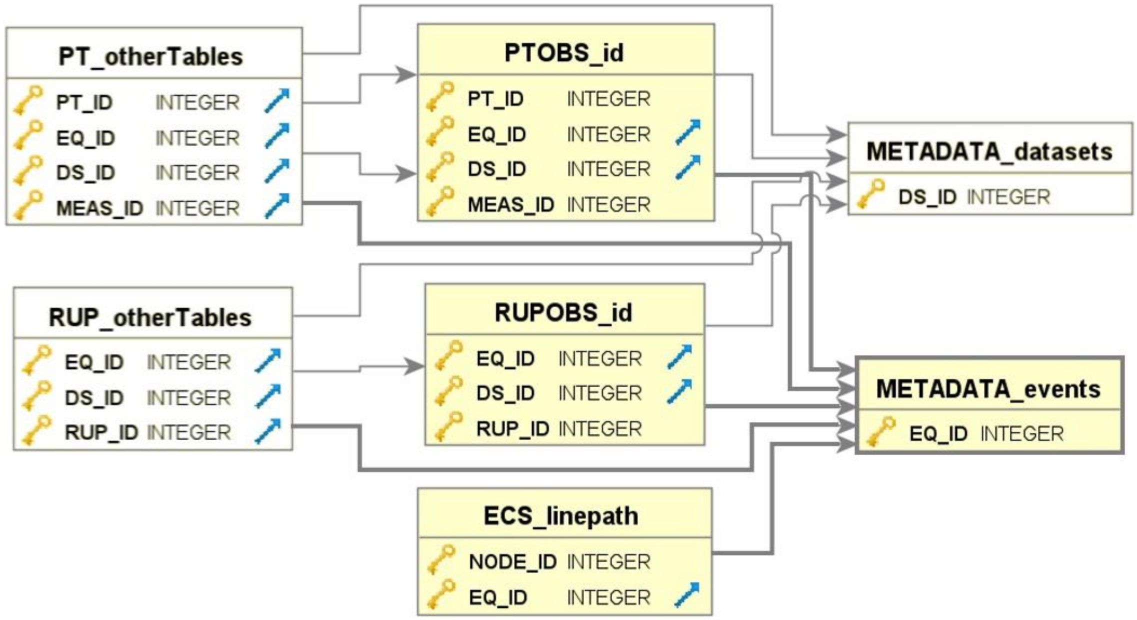

Figure 5.2. Relational schema diagram showing the core FDHI Database structure. Gold key symbol and blue arrow symbol represent primary and foreign keys, respectively.

Table 5.1. Parent tables in FDHI Database.

Data Category	Database Table Name	Table Type	Table Purpose/Contents
Earthquake Information	METADATA_events	Parent	Assign event identifier (EQ_ID); store event metadata
Measurement Information	PTOBS_id	Child & Parent	Assign measurement identifiers (PT_ID & MEAS_ID)
Rupture Information	RUPOBS_id	Child & Parent	Assign rupture line identifier (RUP_ID)
Coordinate System Model	ECS_linepath	Child	Store geographic coordinates for ECS reference line

The database contains metadata and geospatially-controlled surface rupture and fault displacement data from 75 global historical earthquakes. The process of developing the event metadata and surface rupture/fault displacement data and metadata is described in Chapter 3.3. Similarly, Chapter 4 documents the data analyses and interpretations performed to support the model development. Table 5.2 is a general summary of the database contents.

Table 5.2. Generalized list database contents.

Data Category	Contents[1]
Earthquake Information	EQ_ID, name, region, date, style, magnitude, magnitude type, seismic moment, hypocenter
Measurement Information	PT_ID, MEAS_ID, location_id, group_id, geographic coordinates, elevation data and metrics, slip measurements, site geology, classification/rank, recommended net slip values, recommended net slip quality code and suggested usage
Rupture Information	RUP_ID, NODE_ID, geographic coordinates, site geology, mapping accuracy/confidence, classification/rank
Coordinate System Model	reference line geographic coordinates, ECS ordinates for measurement sites, ECS ordinates for rupture line vertices

[1] Simplified listing of contents

5.3 SOFTWARE

Figure 5.2 was made using "DbVisualizer" (https://www.dbvis.com/). The following software versions were used to build, populate, and query the FDHI Database:

- SQLite database engine version 3.14.2 (Hipp, 2020; https://www.sqlite.org)
- Python version 2.7.15 (https://www.python.org)
- Python "sqlite3" module version 2.6.0 (https://docs.python.org)
- Python "pandas" library version 0.18.1 (https://pandas.pydata.org/)

5.4 REFERENCES

Brandenberg, S. J., Kwak, D. Y., Zimmaro, P., Bozorgnia, Y., Kramer, S. L., and Stewart, J. P. (2018). Next-Generation Liquefaction (NGL) case history database structure. In *Geotechnical Earthquake Engineering and Soil Dynamics V: Liquefaction Triggering, Consequences, and Mitigation*, American Society of Civil Engineers, 426-433.

Hipp, R. D. (2020). SQLite. Retrieved from https://www.sqlite.org/index.html.

Hoffman, D. R. (2003). *Effective Database Design for Geoscience Professionals*. PennWell Books.

Mazzoni S., Kishida T., Ahdi S.K., Contreras V., Darragh R.B., Chiou B.S.-J., Kuehn N., Bozorgnia Y., Stewart J.P. (2020). Chapter 2: Relational Database, in Data Resources for NGA-Subduction Project, PEER Report No. 2020/02, *Pacific Earthquake Engineering Research Cente*r, University of California, Berkeley, CA.

6 Flatfile Documentation

The relational database contents have been aggregated into flatfiles for documentation and usability. The database contains fault displacement measurements, surface rupture maps, and associated metadata (including event information, analysis results, and geologic interpretations) , and this information is contained across 37 tables and 365 columns in one relational database file. As described in Chapter 5, we broadly grouped the content into four categories: earthquake information, measurement information, rupture information, and the event-specific coordinate system (ECS) model. We provide three flatfiles in *.csv format for the three latter information categories: (1) a measurements flatfile; (2) a ruptures flatfile; and (3) an ECS model flatfile. Earthquake information is contained in all three flatfiles.

The flatfiles are the formal documentation of the database contents. We used our knowledge of the database schema to produce the flatfiles and check for errors and inconsistencies. We recommend most users of the FDHI Database (including model developers, geoscience researchers, and industry professionals) use the flatfiles to access the contents of the database. For further convenience, these flatfiles are also provided as ESRI shapefiles for use in various Geographic Information System (GIS) software. Appendix A provides information on the flatfile contents and contains the flatfiles (in *.csv and ESRI shapefile formats) as electronic supplements.

7 Quality Assurance and Quality Control

The FDHI Database development included a robust quality assurance (QA) and quality control (QC) effort to ensure the database contents were carefully assessed for quality and content for use in the development of the new fault displacement models. For this project, we consider evaluations of data quality (i.e., completeness, accuracy, and consistency; Chapter 3.3.2) to address QA, and data requests and reviews by the model development teams as relating to QC. The key components of the QA/QC effort included collaborating with the model developers to define the database contents, using a structured relational database, developing standard workflows to review and process datasets, performing analysis and interpretation of the data, and engaging the model developers in a participatory peer review of interim database versions. The QA/QC measures applied to the FDHI Database have resulted in a more reliable, stable, and useful product.

Our standard workflow for developing surface rupture, measurement, and event information for each earthquake (Chapter 3.3) was designed to support QA. Each candidate dataset was carefully reviewed for data quality and compliance with the event and dataset selection criteria (Chapter 3.1). The Database Team met regularly (approximately bi-weekly for two years) to review and discuss individual datasets and earthquake characteristics. The work developing the rank classifications (Chapter 4.3) and recommended net slip values and quality codes (Chapter 4.6.2) resulted in a comprehensive QA effort in which every entry of each dataset was evaluated in detail. We assigned quality codes to each measurement to identify good/reliable data, alternative data, potentially incomplete or erroneous data, and unreliable data (Table 4.2). In developing the rank classifications, different members of the Database Team independently developed rankings for the same event or subsets of the same event, and the results were compared and discussed. In general, there was high reliability and repeatability of the rankings; in some complex ruptures, the variations captured technically defensible alternative interpretations, and we coordinated to develop a preferred interpretation.

The database was created primarily for model developers to use in developing new fault displacement models; therefore, our QC efforts focused on ensuring the database content addressed model development needs. We held monthly meetings with the model developers for almost two years and attended several model development working group meetings in that time. The event and dataset criteria (Chapter 3.1) were established based on the modeling needs, and specific analysis and geologic interpretation (Chapter 4) of the raw data were also performed to support model development. Participatory reviews of interim internal database versions by the modeling teams helped identify content important to the model development (QC) and data elements that needed further review (QA). Finally, using a relational database structure also supports the QA/QC effort by minimizing errors due to repetition, enforcing data entry constraints, and maintaining important references between data elements.

8 Conclusions

We have assembled a geospatially-controlled relational database of surface rupture maps, measurements, and associated metadata for 75 historical earthquakes of **M** 4.9 to 8.0 for all styles of faulting. All information is contained in a structured relational database, and the contents have been aggregated into flatfiles (*.csv format), ESRI shapefiles, and Google Earth files for formal documentation and end-user convenience (Appendix A). The work was completed as part of the Fault Displacement Hazard Initiative (FDHI) Project to support the development of next-generation fault displacement models, and the FDHI Database was developed in collaboration with the model developers. The new fault displacement models are anticipated to provide improved estimates of the amplitude and spatial distribution of principal and distributed displacements for future surface-rupturing earthquakes. While several fault displacement models are currently used in standard practice, there are significant differences in their input datasets, estimated displacement metrics, modeling techniques, and treatment of uncertainty. The FDHI Project will help mitigate these critical issues by using a common database and producing independent models in a coordinated research program. The new models will be useful for engineering design and analysis of critical infrastructure located on or near active fault zones and will be applicable for both deterministic and probabilistic fault displacement hazard analysis.

The data quality review, analysis, and geologic interpretation efforts completed in this project are a unique feature of the FDHI Database and have resulted in a reliable and stable product for model development teams and the geoscience community. The data were collected through an extensive literature review and were systematically assessed for completeness, accuracy, and consistency. Multiple source datasets are included for the same earthquake, where available, allowing database users to make comparisons in a common framework. The database also includes geologic data and terrain metrics, which have not been included in previous databases, allowing model developers to investigate geologic and topographic controls on fault displacements. The development and application of a new event-specific coordinate system (ECS) algorithm herein supplements geographic coordinates with strike-parallel and strike-normal ordinates for all surface rupture linework and measurement locations. All surface ruptures in the database are classified as principal or distributed rank based on detailed geologic evaluations. We introduce two additional measurement rank classifications (cumulative and total) in this project to better distinguish measurements associated with multiple ruptures or wide measurement apertures. While the classification scheme may be non-unique, it has been applied as consistently as possible across the contents of the database. Hanging wall and footwall flags are included for distributed measurements in reverse, normal, and oblique style earthquakes. We also provide preferred and bounding (e.g., maximum and minimum) recommended net slip values calculated from the reported slip components. The basis for the calculations is tracked in the database, and each value is assigned a quality code. Finally, the structured relational database created for this project was designed to be expandable and extensible as additional earthquake data become available, new measurement techniques develop, and user needs evolve.

NATURAL HAZARDS RISKS AND RESILIENCY RESEARCH CENTER (NHR3)

UCLA

Final Report on Task 5: Fault Displacement Model

Cal Poly

Caltech

SCEC
AN NSF+USGS CENTER

UC Irvine

UCLA

UC Santa Barbara

USC

UCLA–PG&E Fault Displacement Model

Nicolas Kuehn, Ph.D.
University of California, Los Angeles

Albert Kottke, Ph.D., P.E.
Chris Madugo, Ph.D.
Pacific Gas and Electric Company
Oakland, CA

Alexandra Sarmiento, P.E., C.E.G.
Yousef Bozorgnia, Ph.D., P.E.
University of California, Los Angeles

A report on research conducted with support from Pacific Gas & Electric Company, California High-Speed Rail Authority, California Department of Transportation, Southern California Gas Company, Los Angeles Department of Water and Power, and California Energy Commission

Report GIRS-2022-06

DOI: 10.34948/N3X59H

University of California, Los Angeles (headquarters)

Natural Hazards Risk & Resiliency Research Center

B. John Garrick Institute for the Risk Sciences

UCLA–PG&E Fault Displacement Model

Nicolas Kuehn, Ph.D.
University of California, Los Angeles

Albert Kotke, Ph.D., P.E.
Chris Madugo, Ph.D.
Pacific Gas and Electric Company
Oakland, CA

Alexandra Sarmiento, P.E., C.E.G.
Yousef Bozorgnia, Ph.D., P.E.
University of California, Los Angeles

A report on research conducted with support from Pacific Gas & Electric Company, California High-Speed Rail Authority, California Department of Transportaton, Southern California Gas Company, Los Angeles Department of Water and Power, and California Energy Commission.

Report GIRS-2022-06

Natural Hazards Risk and Resiliency Research Center
B. John Garrick Insttute for the Risk Sciences
University of California, Los Angeles (Headquarters)

September 2022

ABSTRACT

This report presents the development and results of a new fault displacement model. The work was completed as part of the Fault Displacement Hazard Initatve (FDHI) Project, which is a mult-year and community-based research project coordinated by the University of California. The new model predicts the total discrete net displacement across simple and complex fault surface ruptures as a functon of magnitude, style of faultng, and positon along the rupture length. The model is applicable to shallow crustal earthquakes for all styles of faultng. The model formulatons are based on 73 earthquakes in the FDHI Project database with varying magnitude ranges: strike-slip (**M** 6.0 to 7.9), reverse (**M** 4.9 to 8.0), and normal (**M** 6.0 to 7.6). When applied outside these magnitude ranges, the model predictons are associated with an increased epistemic uncertainty. We used a novel aggregaton process to combine measurements across (sub)parallel principal and distributed fault ruptures at a site and applied it to all events in the database. Event-specific random effects are used to capture aleatory variability in both the magnitude and locaton scaling. The model parameters are estmated by a Bayesian robust regression via Markov Chain Monte Carlo sampling. An important feature of the new model is a set of alternatve model coefficients (samples from the posterior distributon) that capture epistemic uncertainty in the model and underlying data. Our approach robustly captures uncertainty and variability, making the model well-suited for use in probabilistc fault displacement hazard analyses. The newly developed model is compared against existng models and is found to perform well with reduced estmates of displacement for large magnitudes at high confidence intervals. The model and documentaton are available through the Natural Hazards Risk and Resiliency Research Center (NHR3) website (https://www.risksciences.ucla.edu/nhr3).

ACKNOWLEDGMENTS

Support for this project was provided by the Pacific Gas & Electric Company, California High-Speed Rail Authority, California Department of Transportaton, Southern California Gas Company, Los Angeles Department of Water and Power, and California Energy Commission. The California Geological Survey, United States Geological Survey, Southern California Earthquake Center, California Insttute of Technology, and Lets Consultants Internatonal were partners in this project.

The support of these organizatons is gratefully appreciated. The opinions, findings, conclusions or recommendatons expressed in this publicaton are those of the authors and do not necessarily reflect the views of the study sponsors, the Natural Hazards Risk and Resiliency Research Center (NHR3), or the Regents of the University of California.

Our new model was developed through the Fault Displacement Hazard Initatve (FDHI) research program and benefited from constructve interactons with over two dozen researchers and practcing professionals. The authors are grateful for the guidance and feedback provided by the FDHI project partcipants. To support our comparisons to existng models, Drs. Rui Chen, Robb Moss, and Grigorios Lavrentadis kindly provided calculatons for the Petersen et al. (2011), Moss and Ross (2011), and Youngs et al. (2003) models, respectvely. Geologic evaluatons of fault zone complexity by Keene Karlsson are also greatly appreciated.

CONTENTS

LIST OF FIGURES

LIST OF TABLES

1 INTRODUCTION

The Fault Displacement Hazard Initatve (FDHI) Project is a mult-year, community-based research program coordinated by the University of California. The objectves of the project are to develop (i) a modern fault rupture and displacement database, (ii) a set of next-generaton fault displacement models, and (iii) engineering guidelines for fault displacement analysis. Our new fault displacement model, abbreviated as "KEA22," is one of four new fault displacement models developed through the FDHI Project. Collectvely, the new models are antcipated to provide improved estmates of probabilistc and deterministc fault displacement hazard by using a comprehensive modern database, compatble displacement metrics and predictor variables, and sophistcated statstcal modeling.

Quantfying fault rupture hazard is necessary for the seismic design of infrastructure proximal to actve surface-rupturing faults. For example, site-specific engineering solutons can be developed to allow structures to accommodate fault displacement when surface rupture hazard cannot be mitgated by avoidance, such as lifeline systems (e.g., the Trans-Alaska Pipeline; Cluff et al. 2003); and nonlinear response history analysis of structures can incorporate fling-step amplitudes consistent with the ground moton hazard level. While several fault displacement models are currently used in standard practce (e.g. Moss and Ross, 2011; Nurminen et al., 2020; Petersen et al., 2011; Wells and Coppersmith, 1994; Wesnousky, 2008; Youngs et al., 2003), these models have significant differences in their input datasets, estmated displacement metrics, modeling techniques, and treatment of uncertainty. Accordingly, it is difficult to make meaningful comparisons of the results from different models and correctly apply alternatve models in hazard assessments. The new models developed through the FDHI Project will help mitgate these issues by using a common database and producing compatble alternatve displacement models.

Our new fault displacement model predicts the total discrete net displacement across complex fault surface ruptures, which we refer to as "aggregated net displacement." The predicted displacement is a functon of moment magnitude and normalized positon along the rupture. While the same methodology and functonal form are used for all styles of faultng, separate regression parameters are developed for each style. We apply a robust regression to avoid model bias from the outlier low displacement values that are ubiquitous in slip profiles. Bayesian regression analysis is used to estmate the distributon of the regression parameters to capture epistemic uncertainty in the slip profile shape and amplitude, and event terms are used to capture aleatory variability in the profile shape and amplitude. Our approach robustly captures uncertainty and variability, making our model well-suited for use in probabilistc fault displacement hazard analysis (PFDHA).

This model addresses displacement amplitude only. A complete evaluaton of fault displacement hazard includes surface rupture likelihood models and an earthquake magnitude-frequency model. The later is a site-specific issue that is handled in the seismic source characterizaton. There are two types of conditonal probability models that address surface rupture likelihood: (i) probability of rupture in the event, given magnitude and style of faultng, and (ii) probability of rupture at the site, given rupture occurs anywhere in the event. While the current scope of the FDHI Project is focused predictve models for displacement amplitude, new models for the conditonal probability of rupture at site are antcipated in a future phase of the project. It is noted that the database developed for the FDHI Project only contains informaton on surface-rupturing earthquakes and therefore is not suitable for developing models on the conditonal probability of rupture in an event.

The Chapters in this report document the development of our new fault displacement model. The process began with evaluatng the FDHI Database contents and selectng a large subset of the published database with minimal modificatons (Dataset). Next, we investgated alternatve displacement metrics and modeling approaches (Displacement Metric and Geologic Complexity Evaluatons). The final model, including functonal form, performance, and recommended implementaton are discussed in Model, Model Performance, and Model Implementaton. The model performance is further documented in Comparisons to Existng Models, where we present results for a set of deterministc test cases. Because our model predicts the total discrete net displacement across complex fault surface ruptures, we provide preliminary guidance on Parttoning Aggregated Slip onto Principal and Distributed Sources. Finally, the Summary and Future Work Chapter concludes the report.

2 DATASET

We used a subset of the FDHI Database (Sarmiento et al., 2021) to develop our new fault displacement model. This chapter provides an overview of the FDHI Database and documents our data selecton process. The distributon of the final event and data subset used in the model development is also presented.

21 FDHI DATABASE

The FDHI database is a new geospatally-controlled database containing data relatng to fault ruptures and displacements from historical surface-rupturing earthquakes. The database was developed in collaboraton with earthquake geologists, model developers, engineering community end-users, and project sponsors through the FDHI Project. The primary goal of the database was to support the development of new fault displacement models by systematcally collectng, reviewing, and organizing relevant data in a database. The new database provides a common set of inputs that can be used by all model development teams in the FDHI Project to allow a more systematc comparison of model performance.

Surface rupture maps and fault displacement measurements from 75 global surface-rupturing earthquakes are reported in the FDHI Database (Figure 2.1). The events occurred between 1872 and 2019 and range from **M** 4.9 to 8.0. Only historical events in shallow crustal tectonic environments were considered. Roughly 45% of the events are dominantly strike-slip, ∼20% are normal, and ∼35% are reverse. Nearly 40% of the earthquakes in the database are from Western North America, which includes California, Nevada, Idaho, Montana, Alaska, and Mexico. The database contains over 87,000 individual point-in-space observatons with geospatal control, including over 40,000 individual fault displacement measurements for various slip components (e.g., lateral slip, vertcal slip, net slip). Surficial geologic unit classificaton (bedrock, young/old/undifferentated alluvium) is available for over 26,000 observaton sites.

The FDHI Database also contains additonal metadata requested by the model development teams. For example, an event-specific coordinate system (ECS) was developed for each earthquake in the database as an alternatve to lattude and longitude coordinates. The ECS is a two-dimensional projecton of the event data that accounts for curvature and discontnuites in the surface rupture trace, effectvely transforming event data to an along-strike dimension. Geologic analyses and interpretatons were also performed to support model development.

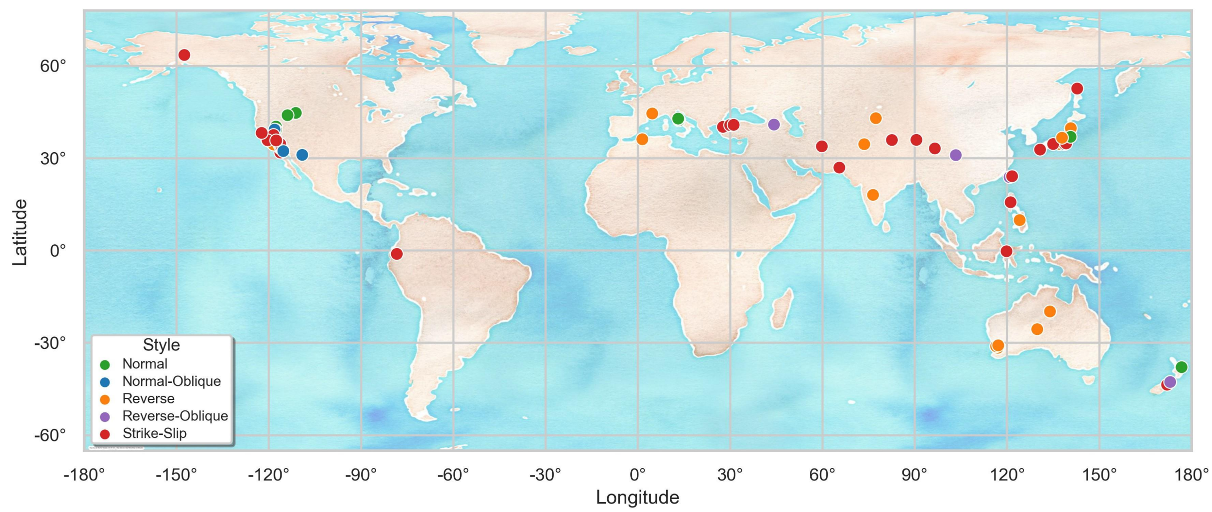

Figure 2.1. Epicentral locatons of 71 of the 75 earthquakes in the FDHI Database (color-coded by style of faultng; see inset legend). Epicenters for the following events are not available: 1872 Owens Valley, California; 1912 Acambay, Mexico; 1986 Marryat Creek, Australia; and 2012 Pukatja, Australia. *Source*: Sarmiento et al. (2021).

These included (i) classifying rupture linework and displacement measurements as principal or distributed, (ii) developing recommended net slip values from reported slip components (i.e., the vector sum of horizontal and vertcal components), (iii) explicitly flagging alternatve measurements known or inferred to be at the same locaton, and (iv) flagging potentially incomplete measurements using a quality code.

2.2 DATA SELECTION

The UCLA/PG&E fault displacement model was developed using a large subset of the published FDHI Database with minimal modificatons. The subset selecton was based on the predicted displacement metric (Displacement Metric), model formulaton (Model), and event-specific seismological or geological characteristcs. We performed a five-step screening process to select an appropriate subset of the FDHI Database (Figure 2.2).

The screening to retain the appropriate subset was relatvely simple because the FDHI Database was developed in collaboraton with the model developers. The first four steps are basic algorithmic filters. As our fault displacement model predicts aggregated discrete net displacements along a normalized rupture length, we used the *recommended net slip preferred* displacement values in the database (Figure 2.2, Step 1). We only retained nonzero values because we use a logarithmic functonal model form and $\ln(x)$ is not analytc at $x = 0$ (Step 2). To extract the appropriate subset of data, we selected measurements corresponding to a *rank* of Cumulatve, Principal, or Distributed (Step 3; Table 2.1). Measurements with a *rank* of Total were excluded because they contain a significant amount of contnuous deformaton and our model aims to predict aggregated discrete displacements. We excluded all measurements with quality codes corresponding to unreliable data (i.e., those with the “Toss” *recommended usage flag* in

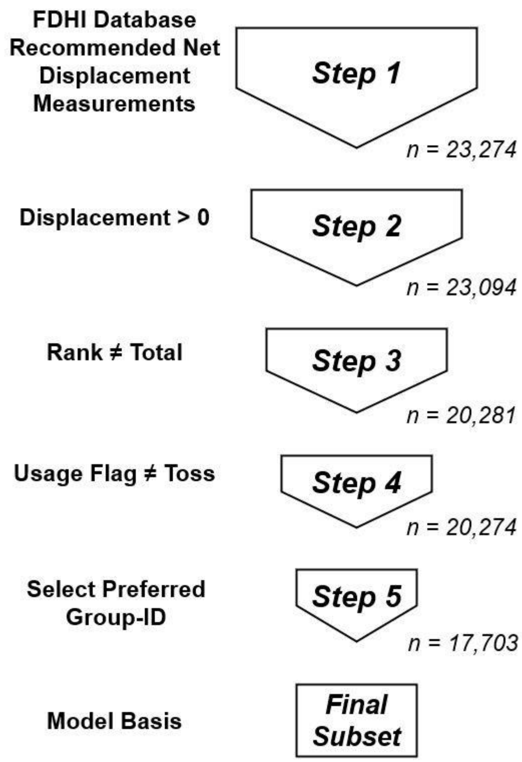

Figure 2.2. Data selecton flowchart.

the FDHI Database; Step 4). While we also considered excluding quality codes corresponding to the "Check" *recommended usage flag*, such strict criteria removed approximately 25% of the available measurements and did not significantly improve the model performance; therefore, we elected to retain these data.

Our final data selecton screening (Figure 2.2, Step 5) used geologic judgment to determine the most appropriate event dataset when alternatve event datasets were available. Multple tools and techniques are available to measure fault displacements, and the results from different methods are not always comparable. For example, displacements interpreted from post-event lidar datasets can be less reliable than field-based measurements if single-event piercing points are ambiguous. Measurements of vertcal displacement are sensitve to the pre-earthquake ground slope angle and directon, which is not considered in scarp height measurements. Recognizing that incompatble measurement methods should be readily distnguished, the FDHI Database assigned a *group identfier* to each measurement and documented the basis for each grouping.

We used the *group identfier* in the FDHI Database to identfy alternatve datasets that remained afer our inital screenings (Figure 2.2, Steps 1 through 4). While the Step 3 screening removed most alternatve datasets (i.e., those derived from automated change detecton analyses, which corresponded to a *rank* of Total), five earthquakes with alternatve datasets remained afer the Step 4 screening. Table 2.2 summarizes the remaining events with alternatve datasets. In general, we first prioritzed field-based measurements over lidar-based; we then favored vertcal measurements based on vertcal separaton (which considers topography) over scarp height.

Table 2.1. Measurement Rank Classificatons in FDHI Database.

Rank	Descripton	Model Usage
Total	Wide-aperture displacements containing discrete slip on one or more faults and contnuous deformaton	Excluded
Cumulatve	Displacement summed across one or more adjacent principal and/or distributed ruptures; or displacement summed across principal rupture(s) and narrow zone of contnuous deformaton	Included
Principal	Displacement on principal rupture[1]	Included
Distributed	Displacement on distributed rupture[2]	Included

[1] Primary faults or tectonic features responsible for the earthquake

[2] Secondary faults, splays, fractures, or shears near a principal fault

For the 1940 **M** 6.95 Imperial Valley earthquake, we separated the Cumulatve-*rank* measurements into a separate and excluded *group identfier*. These data consist of a dense collecton of over 600 measurements spanning less than 25% of the full rupture, whereas the Group 28_01 data contain 27 measurements well-spaced along the rupture length. When included in the model, the Group 28_02 data exerted a strong control on the predicted displacements beyond the data extent and produced significant misfits to the Group 28_01 data, especially at the ends of the ruptures. Therefore, we elected to separate and exclude the Group 28_02 data (Table 2.2).

We made minimal modificatons to the final database subset developed from the screening in Figure 2.2. First, we separated the 1940 **M** 6.95 Imperial Valley data into two separate *group identfiers*, as discussed above. Second, we excluded the 2010 **M** 7.2 El Mayor-Cucapah, Mexico (EMC) normal-oblique earthquake because the spatal distributon of measurements along the rupture was concentrated at the northern end, and a stable estmate of the displacement profile shape parameter could not be determined No displacement measurements were available in the southern $\sim 50\%$ of the rupture where extensive liquefacton occurred. Lastly, we excluded the 2010 **M** 5.0 Pisayambo, Ecuador strike-slip earthquake because the documented fault displacements were unusually large (Champenois et al., 2017). The maximum displacement in the Pisayambo earthquake was a significant outlier with respect to other small magnitude strike-slip events, and efforts to include the earthquake had a strong and adverse impact on the model performance. We speculate that the large coseismic displacements could be due to site-specific conditons such as actve regional volcanism, steep topography, shallow hypocenter, and/or post-glacial rebound.

Table 2.2. Subset of Measurement Groupings in FDHI Database.

EQ_ID	Name	Group ID	Measurement Basis	Model Usage
2	HectorMine	2_01	field-based measurements	Included
2	HectorMine	2_03	post-event lidar measurements (acquired 10 yrs afer earthquake)	Excluded
12	Wenchuan	12_01	field-based measurements, based on vertcal offset	Included
12	Wenchuan	12_02	field-based measurements, based on scarp height	Excluded
24	Hebgen	24_01	post-event lidar measurements (acquired 50 yrs afer earthquake), based on vertcal offset	Excluded
24	Hebgen	24_02	field-based measurements, based on scarp height	Included
28	Imperial1940	28_01	field-based measurements	Included
28	Imperial1940	28_02	post-event air photo measurements	Excluded
39	OwensValley	39_01	field-based measurements (acquired 100 yrs afer earthquake)	Included
39	OwensValley	39_02	post-event lidar measurements (acquired 125 yrs afer earthquake, with some field verificaton)	Excluded
56	BorahPeak	56_01	field-based measurements	Included
56	BorahPeak	56_02	post-event lidar measurements (acquired 40 yrs afer earthquake)	Excluded

23 DATA DISTRIBUTION

Figure 2.3 shows the earthquake magnitude distributons of the selected data as scater plots with marginal histograms. The earthquakes are identfied by the name used in the FDHI Database and are ordered by date on the abscissa. The strike-slip subset is the most robust with 35 events in total, including 20 events in the **M** 6.5 to 7.5 range. The normal subset is the least robust, with only 14 events constrained to **M** 6.0 to 8.0. The reverse subset contains 25 events spanning **M** 4.9 to 8.0. Nine of the reverse events (Meckering, Calingiri, Cadoux, Marryat Creek, Tennant Creek 1/2/3, Pukatja, and Petermann) are from Australia, which is a stable contnental region. While ground moton atenuaton propertes are known to vary between stable contnental and actve crustal setngs (e.g. Goulet et al., 2018), it is unknown if fault displacements are sensitve to tectonic setng.

The distributon of displacement measurement locatons in our selected subset as a functon of rank and normalized positon along the rupture is shown on Figure 2.4. The normalized positon is folded at the midpoint for the purposes of the histograms because the ECS directon is arbitrary; however, the model development (see Model) considered the full normalized positon from zero to one. Cumulatve-*rank* measurements are relatvely rare in

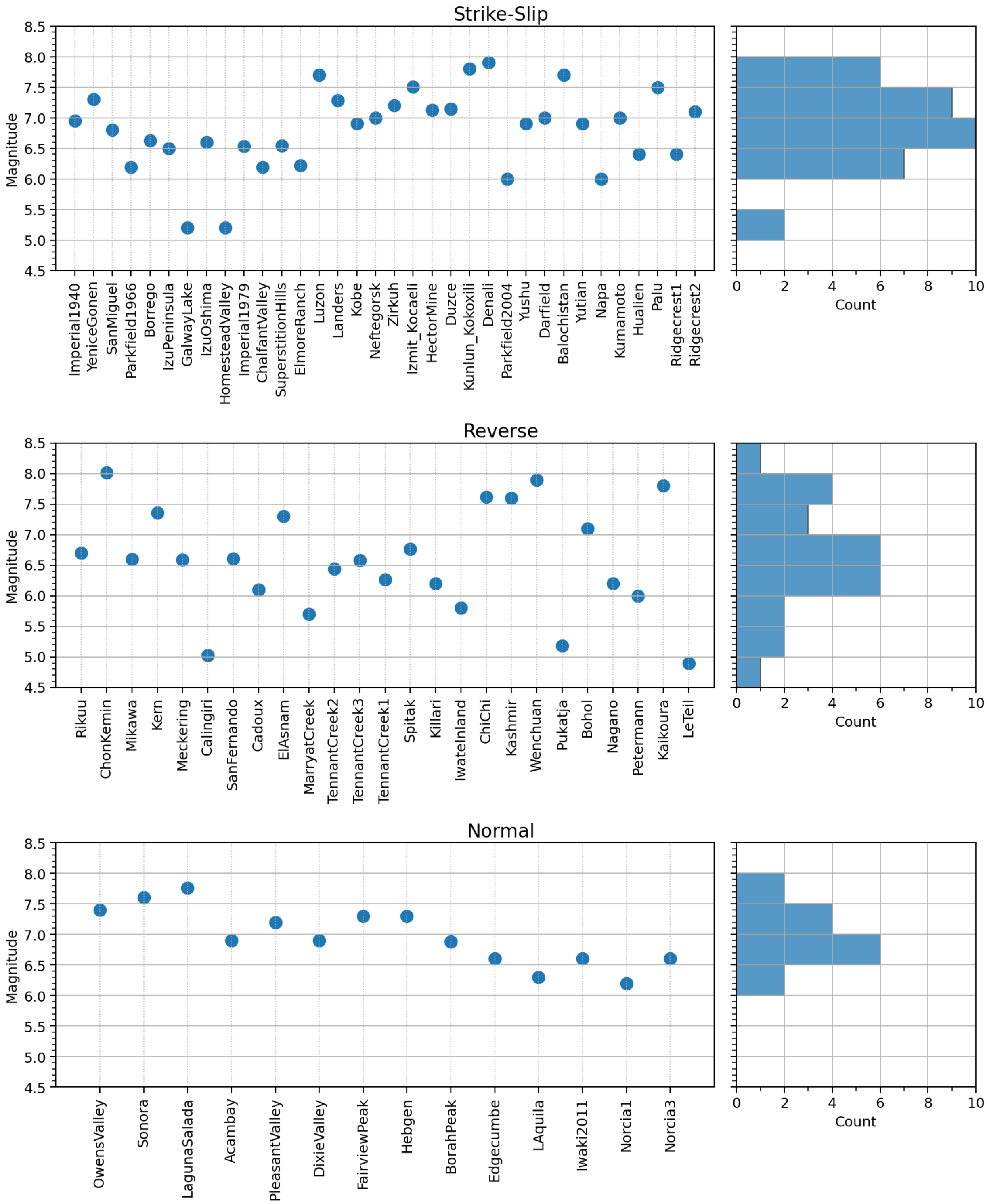

Figure 2.3. Earthquake magnitude distributon of data used in model development. (Top) Strike-slip events. (Middle) Reverse and reverse-oblique events. (Botom) Normal and normal-oblique events.

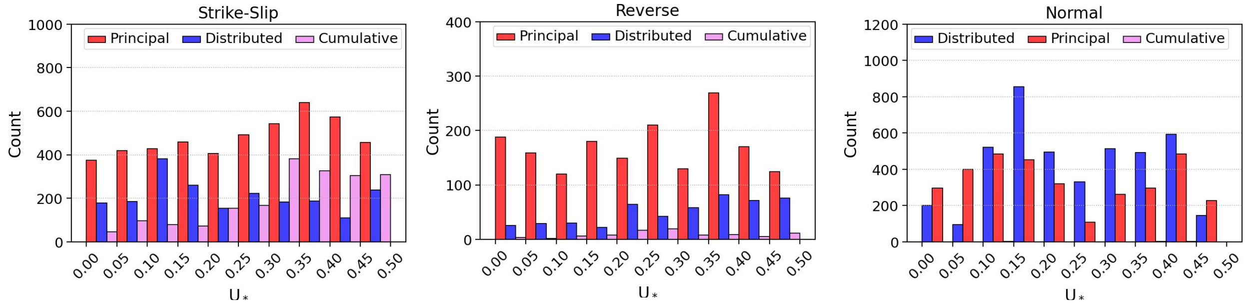

Figure 2.4. Distributon of displacement measurements along normalized rupture length U_* based on rank. (Lef) Strike-slip events. (Middle) Reverse and reverse-oblique events. (Right) Normal and normal-oblique events.

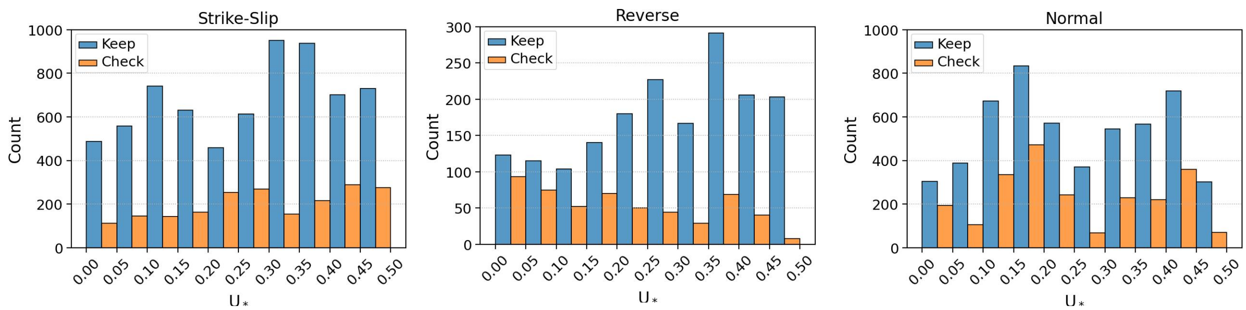

Figure 2.5. Distributon of displacement measurements along normalized rupture length U_* based on quality codes. (Lef) Strike-slip events. (Middle) Reverse and reverse-oblique events. (Right) Normal and normal-oblique events.

our selected subset of reverse ($n = 88$) and normal ($n = 3$) events and are lef-skewed with a peak near 45% for strike-slip events. In general, the distributon of Principal-*rank* measurement locatons along the folded rupture length is close to uniform (but slightly lef-skewed) for strike-slip and reverse events and bimodal for normal events with peaks near 10% and 40%. The distributon of Distributed-*rank* measurement locatons is slightly right-skewed for Strike-Slip events with a peak near 10%; slightly lef-skewed for Reverse events with the mass of the distributon at 20% and greater; and bimodal for Normal events with peaks near 15% and 40%. It is noted that the normal events dataset is dominated by the Norcia3 earthquake, which has over 5,700 observatons.

Similar histograms on Figure 2.5 show the distributon of displacement measurement locatons based on the *quality code* in the FDHI Database. High quality, reliable data are labeled "Keep," and medium or uncertain quality are labeled "Check." Data labeled as unreliable were excluded from our selected subset. In general, the bulk of the measurements are high quality for all styles of faultng. The distributon of high quality data for strike-slip and normal events is bimodal and the reverse data are lef-skewed. Medium quality data are slightly lef-skewed for strike-slip events, right-skewed for reverse events, and bimodel for normal events. As discussed above, the Norcia3 earthquake dominates the normal events subset and therefore exerts a strong control on the distributons in Figures 2.4 and 2.5.

3 DISPLACEMENT METRIC

Fault displacement models predict or estmate a specific displacement metric. Displacement metrics can vary based on slip component and source type (e.g., principal or distributed faultng). An understanding of different displacement metrics is critcal to compare results from different models or use alternatve models to capture epistemic uncertainty. In this chapter, we provide an overview of common displacement metrics and discuss the aggregated net displacement metric used in our model.

3.1 DEFINITIONS

Surface ruptures generate three-dimensional ground surface displacements that can be idealized with three slip components or vectors: two horizontal [(i) lateral or fault parallel and (ii) heave or fault normal] and one vertcal. The net displacement is the vector sum of the three slip vectors. A vertcal strike-slip fault will only produce displacement in the lateral directon, and a pure dip-slip fault will only produce displacements in the fault normal (heave) and vertcal directons. Local variatons in fault geometry and/or obliquity in the source mechanism commonly generate fault displacements between these two end member cases, making net slip a more complete metric. However, most surface ruptures have a dominant component that is consistent with the style of faultng of the source mechanism, and some models use lateral or vertcal slip instead of net slip as the displacement metric (e.g. Moss and Ross, 2011; Petersen et al., 2011; Youngs et al., 2003). The omited components are assumed or implied to be due to local variatons in fault geometry and outside the scope of the models.

Youngs et al. (2003) identfied important differences in principal and distributed fault sources and developed separate fault displacement models based on source type. Following Coppersmith and Youngs (2000), Youngs et al. defined principal surface ruptures as the primary faults or tectonic/seismogenic features responsible for the earthquake and distributed surface ruptures as secondary faults, splays, fractures, or shears near the principal fault. They showed principal faults accommodate significantly higher displacements and are more contnuous than distributed faults, which are more spatally diffuse and can occur several kilometers away from the principal source. Based the different driving mechanisms and surface manifestatons, Youngs et al. (2003) developed separate datasets and fault displacement models for the two source types. Subsequent models by Petersen et al. (2011) and Nurminen et al. (2020) followed similar source type distnctons.

Recent technological advances allow for surface deformaton to be measured across kilometer-scale apertures. Total (wide-aperture) displacements are calculated using high resoluton pre- and post-event imagery or elevaton data (e.g., optcal image correlaton or differental lidar). These datasets provide a new source type that is the sum of all discrete displacements on both principal and distributed faults plus contnuous inelastc deformaton (e.g., warping, block rotatons, cracking) (Milliner et al., 2015). While these analyses are becoming standard practce as the availability of high resoluton satellite imagery and elevaton (lidar) data contnues to improve (e.g. Milliner and Donnellan, 2020; Scot et al., 2018), the majority of the fault displacement measurements currently available are stll discrete (on-fault) measurements on individual principal or distributed fault sources.

Table 3.1 lists several fault displacement models that are regularly used in engineering practce, as well as new models in development through the FDHI Project. The models predict a range of displacement metrics (i.e., slip component and source type). Comparisons between models or end-user applicatons of multple models using logic trees should consider the displacement metric for which the model was developed. Most of the new models developed through the FDHI Project predict similar displacement metrics (i.e., aggregated net). The term “aggregated” is used for displacements that are summed across (sub)parallel faults.

Table 3.1. Displacement Metrics for New & Existng Models.

Model	Status	Style	Slip Component	Source Type
Wells and Coppersmith (1994)	Existng	Any	Varies by style	Principal
Wesnousky (2008)	Existng	Any	Varies by style	Principal
Youngs et al. (2003)	Existng	Normal	Vertcal	Principal, Distributed[1]
Petersen et al. (2011)	Existng	Strike-slip	Lateral[2]	Principal, Distributed[1]
Moss and Ross (2011)	Existng	Reverse	Vertcal	Principal
Lavrentadis and Abrahamson (2019)	Existng	Any	Net	Principal
Nurminen et al. (2020)	Existng	Reverse	Vertcal	Distributed
Milliner et al.	In Progress[3]	Any	Net	Total (wide-aperture)
Visini et al.	In Progress[3]	Reverse, Normal	Vertcal	Distributed
CalPoly/NCREE/LCI	In Progress[4]	Reverse, Normal	Vertcal	Principal
CGS/Caltrans	In Progress[4]	Strike-slip	Net	Aggregated on Principal
Updated Wavenumber	In Progress[4]	Any	Net	Aggregated on Principal & Distributed
UCLA/PG&E (this study)	In Progress[4]	Any	Net	Aggregated on Principal & Distributed

[1] Authors provide separate models for principal and distributed source types
[2] Error in published paper states net displacement
[3] Part of FDHI Project (partcipant)
[4] Part of FDHI Project (modeler)

3.2 MOTIVATION FOR AGGREGATING DISPLACEMENTS

Surface rupture characteristcs vary widely from simple, discrete planar faultng to complex or diffuse networks of (sub)parallel faults, fissures, or minute cracks (Figure 3.1). Locatons of complexites are controlled by site-specific and fault system-specific factors (e.g. Aydin and Du, 1995; Dolan and Haravitch, 2014; Teran et al., 2015), and distributed ruptures and related co-seismic deformaton (such as warping and tltng) can occur across zones hundreds of meters in width. This broadening of the fault zone can result in lower observed displacements on individual ruptures and large along-strike variability in displacement amplitudes. Moreover, ruptures can step or jump across unfaulted ground or change from simple planar features to complex zones over short (meter-scale) distances, further exacerbatng along-strike variability in fault displacements. Models developed without accountng for fault complexity or displacement transfer between segments will therefore have large along-strike fault displacement variability and high standard deviatons, which may be challenging to apply in engineering design.

We considered two approaches to handling fault complexity in the model development: (i) identfy zones of complexity and develop model(s) to estmate displacement reducton within the zones; or (ii) aggregate displacements across fault strike. The first approach directly includes site-specific geologic complexity factors and provides a “site-specific” displacement. The second approach sums all discrete displacements (Principal and Distributed *rank*) on (sub)parallel faults at a specific along-strike positon. When sufficient displacement measurements are available and aggregated across the zone, the variability is reduced and should approach the displacement in a simple rupture if contnuous inelastc deformaton between the (sub)parallel faults is minimal. However, subsequent parttoning of the aggregated slip is required for site-specific analysis. We ultmately developed our model using the second approach.

Developing predictve displacement models that incorporate site-specific geologic complexity is challenging for two reasons. First, the complexity factor(s) causing displacement variability need to be parametricized in the model. Second, applying such a model requires antcipatng the study site is (not) within a zone of complexity. We atempted to correlate areas of low displacement amplitudes with zones of complexity for most of the earthquakes in the database with sufficient informaton (e.g., detailed surface rupture maps and adequate spatal coverage of displacement measurements). Specifically, we sought to develop complexity predictor variables based on automated techniques (e.g., topographic analysis, fault segment detecton) or manual geologic analysis. While geologic explanatons for observed complexites could be identfied *a posteriori* for many (but not all) occurrences in the database, we found the forward-predicton of the locatons of the complexites to be a significant barrier in applying a complexity predictor variable in our model. As a result, we pursued the aggregated displacement approach, as described in the remaining sectons of this chapter. For completeness, our efforts to predict fault zone complexites are documented in an appendix to this report (see Geologic Complexity Evaluatons).

The aggregated displacement approach has several advantages over existng models and potental site-specific complexity models. First, the aggregated displacement metric beter captures the total discrete slip across zones of complexites or distributed faultng. This reduces apparent along-strike variability caused by site-specific complexites and beter captures the total surface displacement, thereby reducing the shallow slip deficit (e.g. Brooks et al., 2017; Dolan and Haravitch, 2014; Fialko et al., 2005; Xu et al., 2016). This in turn improves the performance of magnitude-displacement correlaton because moment magnitude is related to seismic moment (e.g., $M_0 = \mu AD$). Second, aggregatng displacements across principal and distributed fault sources mitgates the need for separate variables that account for site or fault system factors that control displacement parttoning. Such variables are subjectve and difficult to systematcally quantfy. Lastly, summing measured displacements on (sub)parallel faults can be handled through a simple algorithm, and remaining outlier low displacement values can be handled with a robust regression in the model development.

Figure 3.1. Surface rupture photographs from USGS Earthquake Photo Collectons (U.S. Geological Survey, 2021). (Lef) Simple discrete surface rupture from 2019 **M** 7.1 Ridgecrest, California earthquake. (Right) Zone of distributed surface ruptures from 1999 **M** 7.1 Hector Mine, California earthquake.

3.3 DISPLACEMENT AGGREGATION METHODOLOGY

We developed an algorithm to aggregate displacements across fault strike to capture the total discrete net displacement across complex fault surface ruptures. Because measurement locatons are not spatally uniform, the algorithm uses an hourglass-shaped search window to capture additonal measurements in the fault-normal directon. In general, the search window is subdivided into fault-parallel bins and is centered on an origin net displacement measurement. The narrow search zone near the fault is to limit potental for aggregatng additonal along-strike informaton. As the distance increases, the search window increases at the same rate. *Rank*-dependent average net displacements are determined for each bin (e.g., $\bar{d}_b^p$) and then summed for every bin. The aggregated net displacement (D_{agg}) is then the sum of the contributng net displacements and the origin net displacement, such that

$$D_{agg} = D_0 + \sum_{b=1}^{n_{bins}} (\bar{d}_b^c + \bar{d}_b^p + \bar{d}_b^d) \tag{3.1}$$

where D_0 is the origin net displacement, and the contributng net displacements are based on *rank*: d^c, d^p, and d^d for Cumulatve, Principal, and Distributed, respectvely.

The algorithm uses the event-specific coordinate system (ECS) in the FDHI Database, which is an along-strike projecton of the rupture and displacement data. The *u* coordinate in the ECS represents the nominal length along strike, and the *t* coordinate represents the fault-normal distance. The hourglass search window is centered on the *u,t* coordinate of the origin net displacement D_0 (Figure 3.2). The triangular porton is constructed at a 45° angle and extends ± 50 m from the origin along both the *u* and *t* axes to form an isosceles right triangle. The rectangular porton is 100 m in width and extends ± 5 km from the origin along the *t* axis. The hourglass is subdivided into 10 m fault-parallel bins.

We minimize double-countng measurements in the hourglass in two ways. First, each measurement in the FDHI Database is associated with a rupture, and we retain only one measurement per rupture in the hourglass search window (e.g., $\tilde{d}_{rup}^{rank}$). Second, we use the bins to average displacements at a given distance (e.g., $\bar{d}_{bin}^{rank}$), minimizing double-countng of displacements on en echelon faults in shear zones. For ruptures with multple contributng measurements, we use the bin closest to the hourglass centerline. If the measurements span the centerline, then we linearly interpolate the displacement for that rupture (Figure 3.3a); otherwise, we use the median of the contributng measurements (Figures 3.3b and 3.3c). When multple measurements of the same *rank* but from different ruptures occur in the same bin, we use the mean bin displacement (Figure 3.3d):

$$\bar{d}_{bin}^{rank} = \frac{1}{n_{rups}} \sum_{r=1}^{n_{rups}} \tilde{d}_r^{rank} \tag{3.2}$$

where $\tilde{d}_r^{rank}$ is either the median or interpolated displacement for a rupture *r*.

The aggregaton analysis was performed using every Cumulatve and Principal *rank* net displacement value in our selected subset of the FDHI Database (see Data Selecton) as an origin

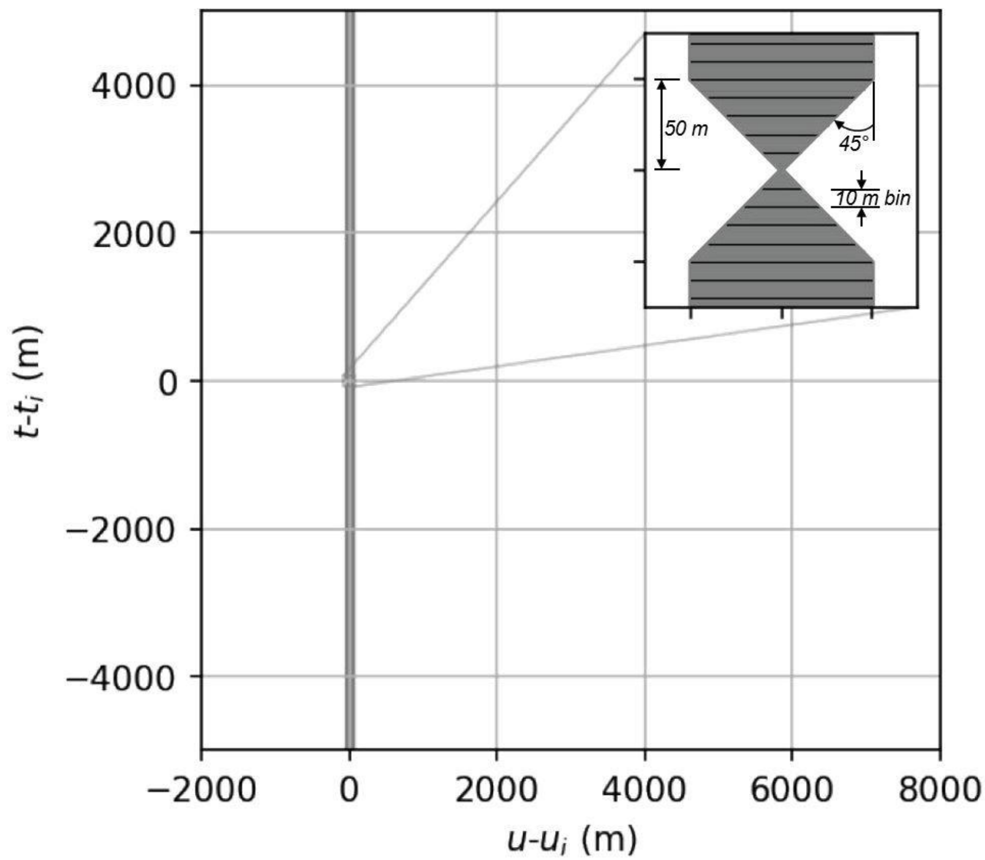

Figure 3.2. Aggregaton algorithm search window geometry.

measurement. As a result, the same measurement can be used in more than one search window. We distnguish this from double-countng because the contributng measurements in each bin (e.g., $\bar{d}_{bin}^{rank}$) are essentally used as estmates for displacements that presumably occurred but were not reported, thereby widening the measurement aperture to beter capture the total discrete net displacement across complex fault zones. Because our model is developed for a normalized positon along the *u* axis (see Model), including origin measurements located at $t' = 0$ smooths peaks and troughs common in displacement profiles that we infer are partally due to insufficiently accountng for coseismic displacements on (sub)parallel faults.

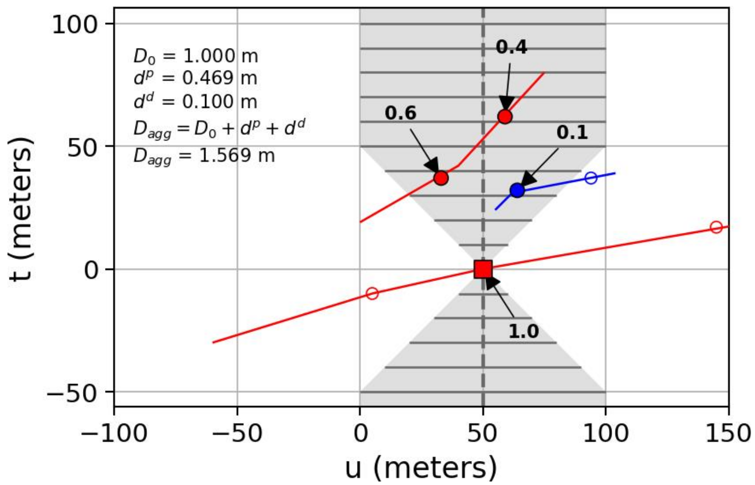

(a) One principal rupture with multple measurements spanning centerline.

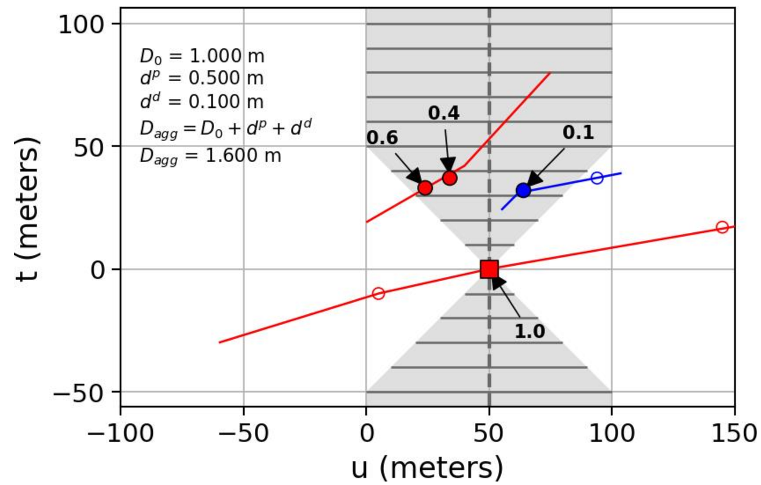

(b) One principal rupture with multple measurements in the same bin.

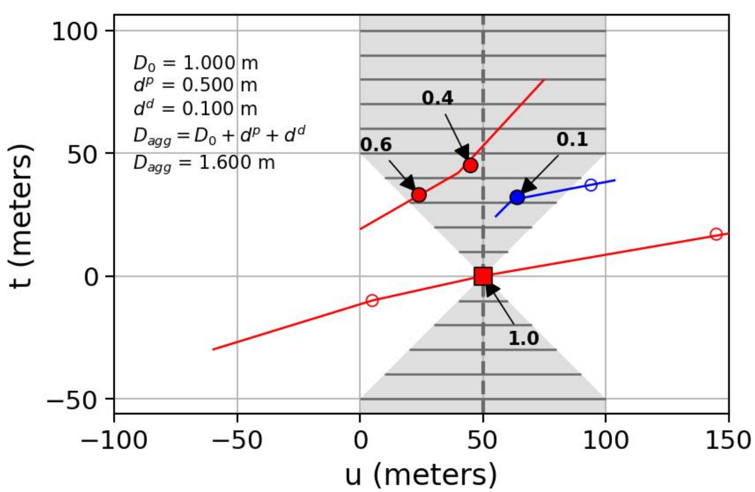

(c) One principal rupture with multple measurements in different bins.

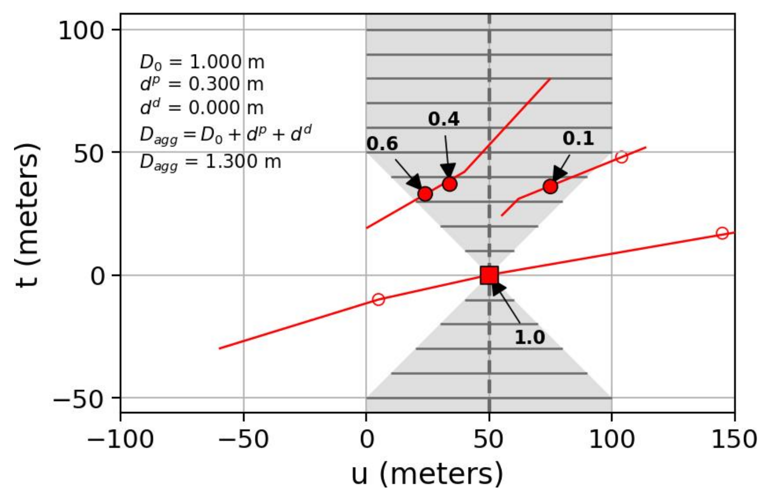

(d) Multple principal ruptures.

Figure 3.3. Example applicatons of aggregaton algorithm. Red and blue lines represent principal and distributed ruptures, respectvely. Red and blue circles represent principal and distributed measurements, respectvely; hollow circles are outside hourglass search window and not included in the aggregaton. Red square is origin measurement. Dashed vertcal gray line is hourglass centerline.

3.4 DISPLACEMENT AGGREGATION RESULTS

The results of the aggregaton analysis are best evaluated for earthquakes with complex surface faultng, copious field-based measurements, and total (wide-aperture) displacements. However, there are few events in the FDHI Database that meet all three criteria. There are only six earthquakes our selected subset of the FDHI Database with wide-aperture measurements, and half have diffuse or undermapped surface ruptures (e.g., Hualien and Petermann) or limited field measurements (e.g., Kaikoura). In cases where the surface ruptures are diffuse, the total (wide-aperture) displacements are likely controlled by contnuous inelastc deformaton that is not captured in our aggregaton of discrete displacements. Field measurements are unavailable for over 50% of the Kaikoura earthquake, limitng the impact of aggregated displacements.

The aggregaton results for the 1992 **M** 7.28 Landers, California earthquake are used to demonstrate the performance of the aggregaton algorithm. The Landers event is the most complete dataset in the FDHI Database. The earthquake generated a complex surface rupture that was mapped in detail with abundant field measurements, and total (wide-aperture) displacement data are also available.

We use four types of plots to illustrate the Landers results. First, we show displacement profiles with the individual and aggregated net displacements (Figure 3.4). The mapped surface ruptures and measurement locatons in *u,t* coordinates are also shown to help identfy areas of complex surface faultng and the spatal distributon of measurement sites. Second, we show net displacement density curves based on *rank*, which are calculated using a standard (Gaussian) kernal density estmator on the natural logarithm of the displacements (marginal plot in top right of Figure 3.4). Third, we show cumulatve distributons of the net displacements based on *rank* (Figure 3.5). Lastly, we use a scater plot of origin versus aggregated displacements to compare the origin amplitude and aggregated amplitude (Figure 3.6).

The analysis for the Landers earthquake produced aggregated net displacements that are in good agreement with the total (wide-aperture) displacements. The amplitude of the total displacements in the top panel of Figure 3.4 compare well to the aggregated displacements, which were developed using the Principal and Distributed *rank* measurements. The center of the aggregated displacement density curve is shifed higher than the Principal-*rank* curve, and its peak is consistent with upper peak of the Total-*rank* curve. The total and aggregated cumulatve displacement distributon curves in Figure 3.5 are similar, suggestng the aggregaton algorithm is reasonably approximatng the total (wide-aperture) displacements. The median aggregated net displacement ($\sim$1.3 m) is approximately 85% higher than the Principal-*rank* value ($\sim$0.7 m). The maximum aggregated-to-origin rato is approximately 100 and decreases to about 1.5 as the origin amplitude increases (Figure 3.6), suggestng fault zone widths are narrower for higher on-fault displacements.

The aggregaton results for all events used in our model development are summarized on Figure 3.7. The figure shows the number of measurements for each *rank* ploted against the rato of the median aggregated net displacement versus median Principal-*rank* net displacement. There is a weak trend in which more measurements correspond to higher ratos. The trend is relatvely weak because fault complexity (i.e., measurements on parallel ruptures) has a greater influence on the aggregaton than the number of observatons alone. The median rato for the

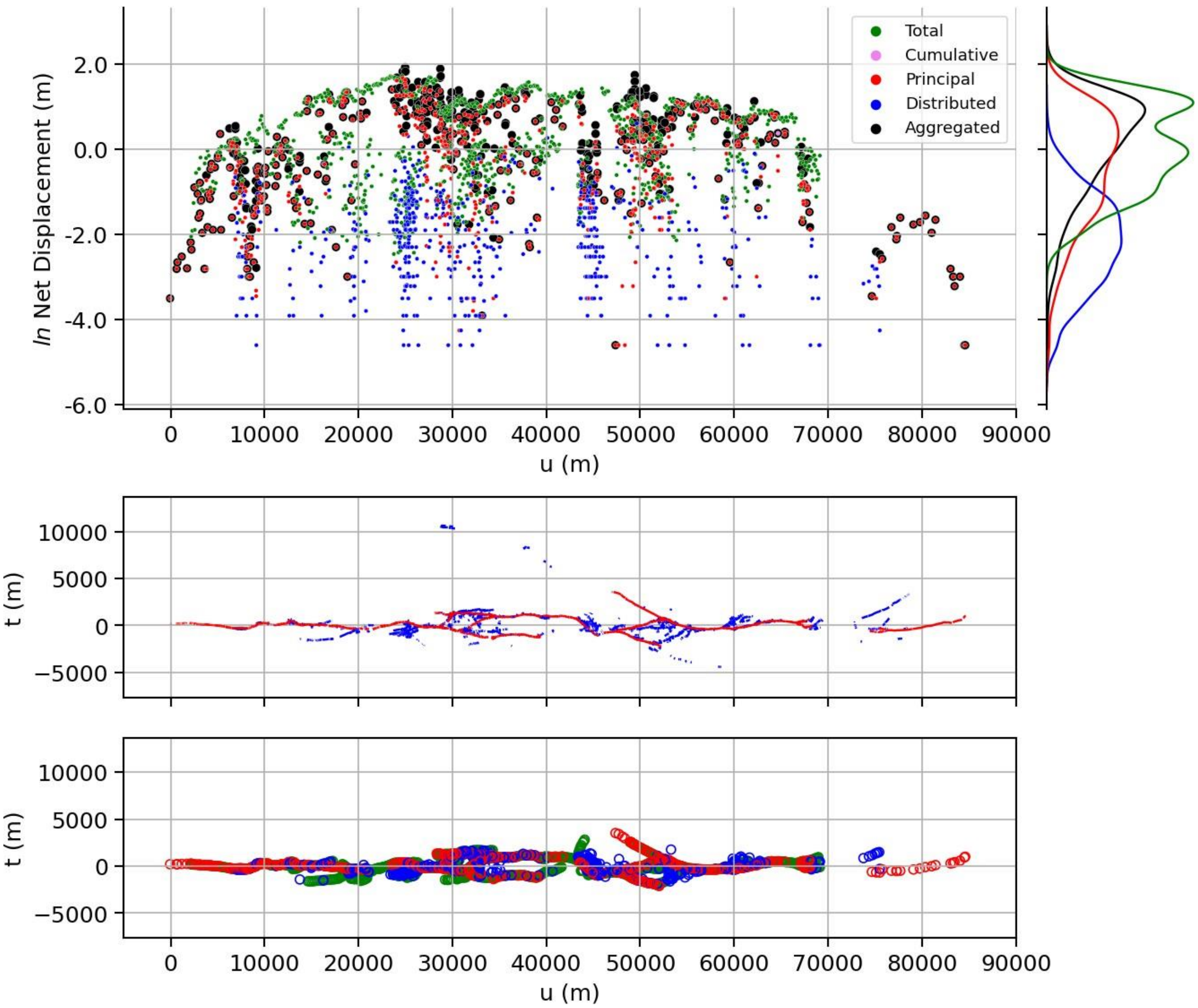

Figure 3.4. Aggregated net displacement (D_{agg}) results for 1992 **M** 7.28 Landers, California earthquake. (Top) Natural log (ln) of net displacement values color-coded by *rank* as shown in legend. (Middle) Mapped surface ruptures projected into *u,t* coordinates. Red and blue lines are principal and distributed ruptures, respectvely. (Botom) Net displacement measurement locatons projected into *u,t* coordinates; color-coding matches top panel.

Darfield event (Figure 3.7, botom plot) is slightly less than unity because the Cumulatve-*rank* measurements control the aggregaton. For this event, the rato of the median aggregated versus median Cumulatve-*rank* net displacement is larger than one.

The relatve contributons of each origin measurement to the aggregated net displacement are shown on Figures 3.8, 3.9, and 3.10, for all strike-slip, reverse, and normal events, respectvely. Measurements in which the origin contributon is 100% reflect less complex surface faultng paterns or a lack of measurements on (sub)parallel faults. Events with significant contributons from other cumulatve, principal, or distributed measurements reflect complex surface ruptures with abundant measurements. The events with higher median ratos on Figure 3.7 correspond with the more complex aggregatons on Figures 3.8, 3.9, and 3.10 (e.g., Landers, EMC, Norcia3).

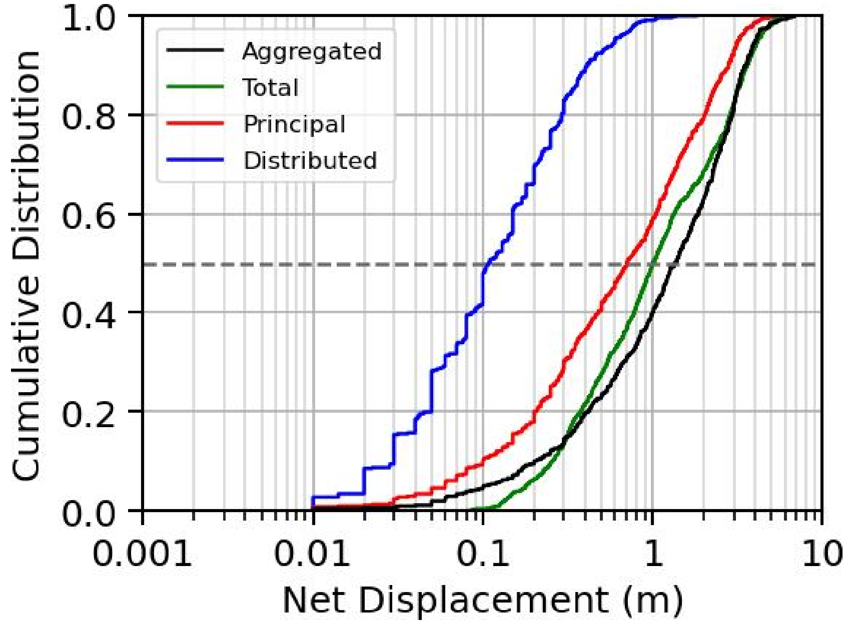

Figure 3.5. Cumulatve distributon of displacement values for 1992 **M** 7.28 Landers, California earthquake.

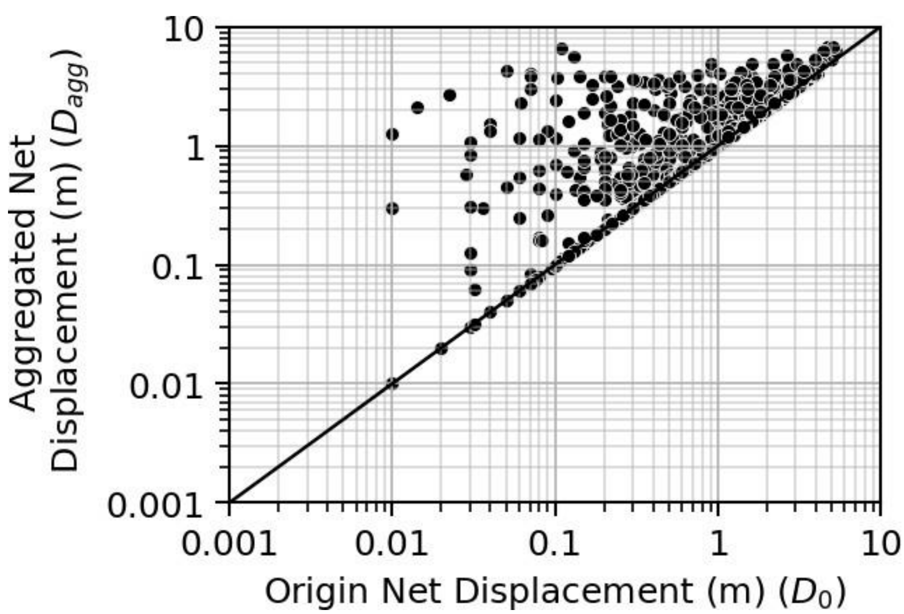

Figure 3.6. Comparison of aggregated and origin net displacements for 1992 **M** 7.28 Landers, California earthquake.

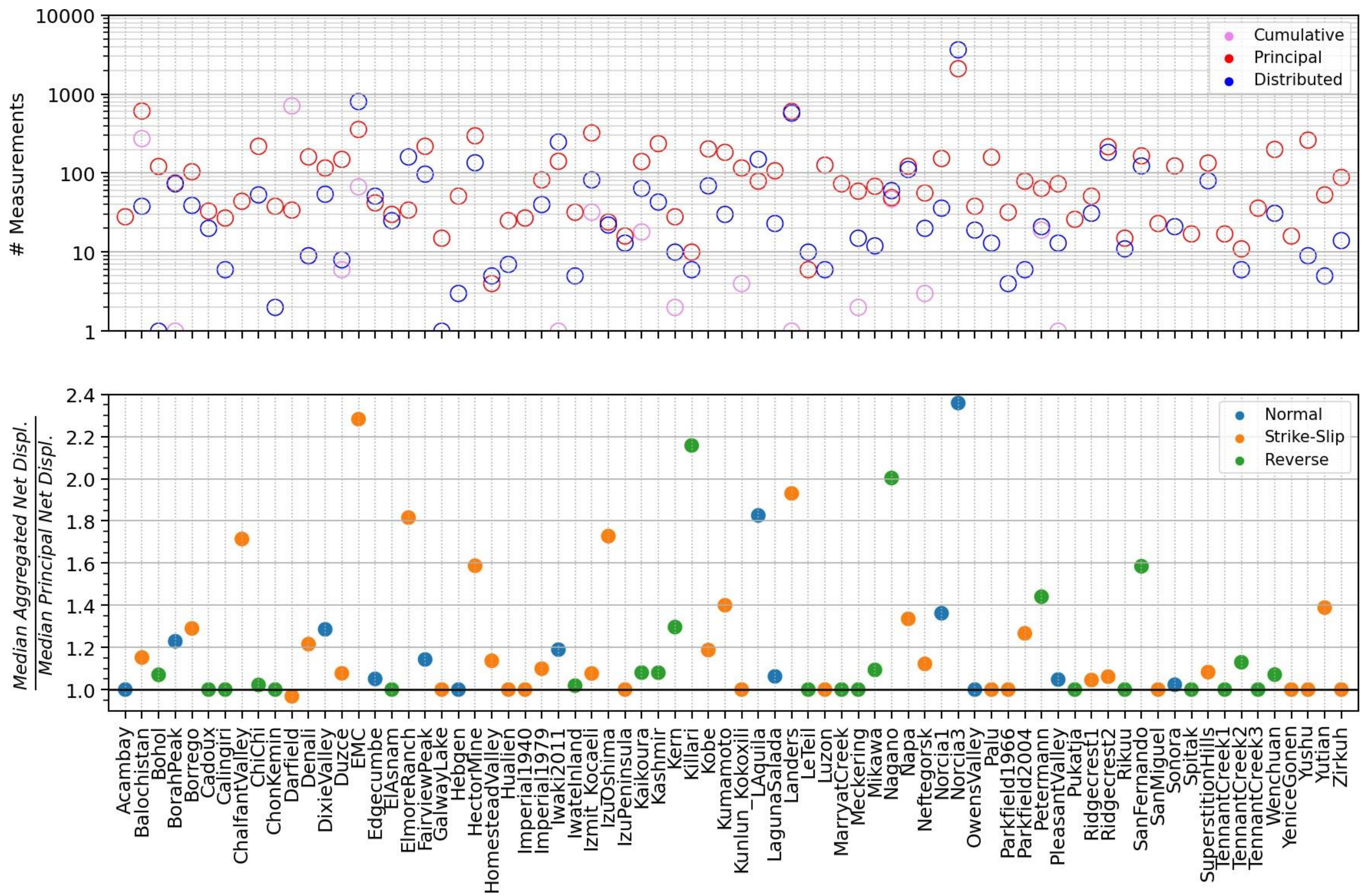

Figure 3.7. Aggregaton results for all events. (Top) Number of observatons for each earthquake based on *rank*. (Botom) Rato of median aggregated net displacement to median Principal-*rank* displacement for each earthquake.

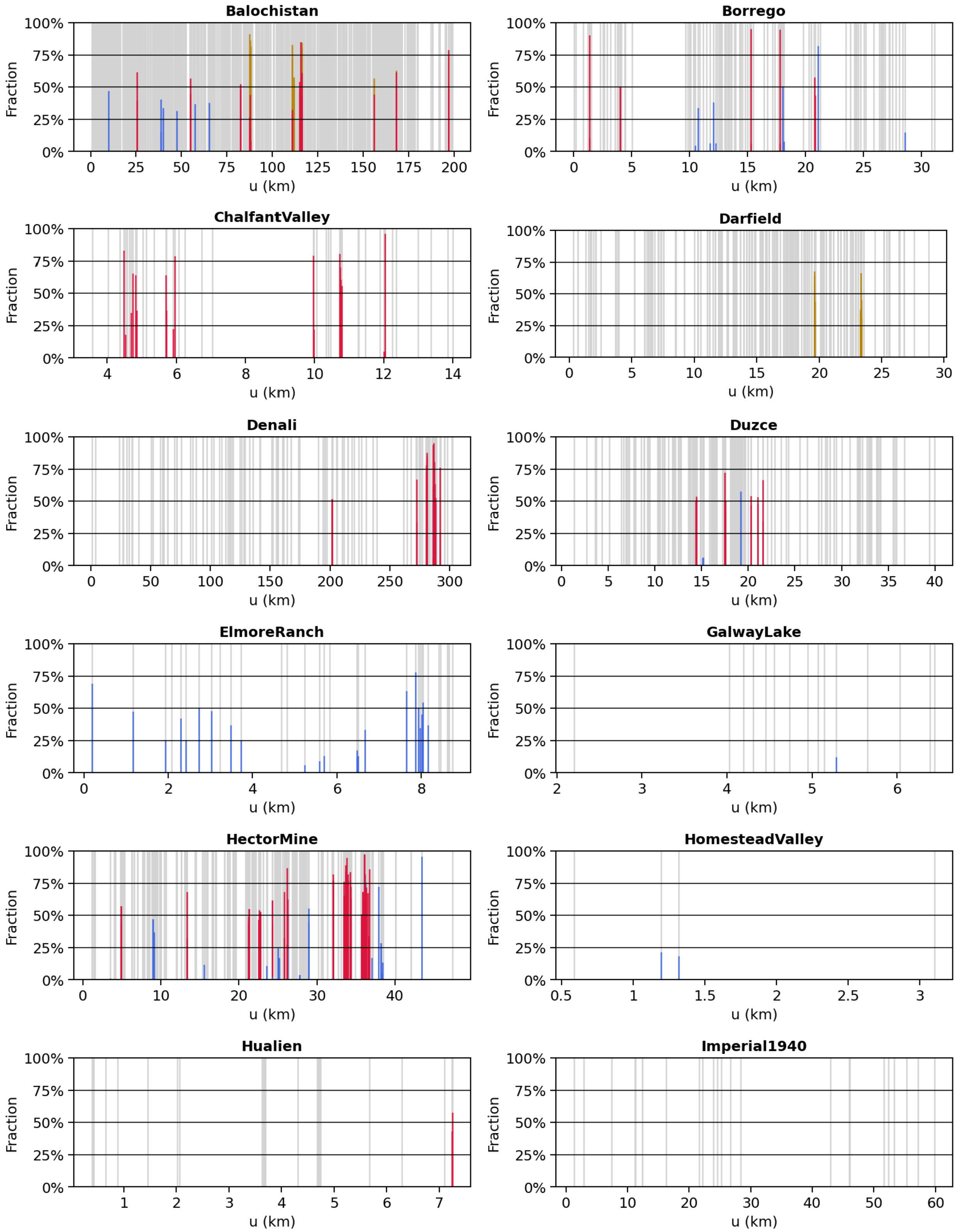

Figure 3.8. Aggregaton results for strike-slip events. Fractonal contributons of seed net displacement (gray vertcal bars), distributed (blue), principal (red), and cumulatve (orange).

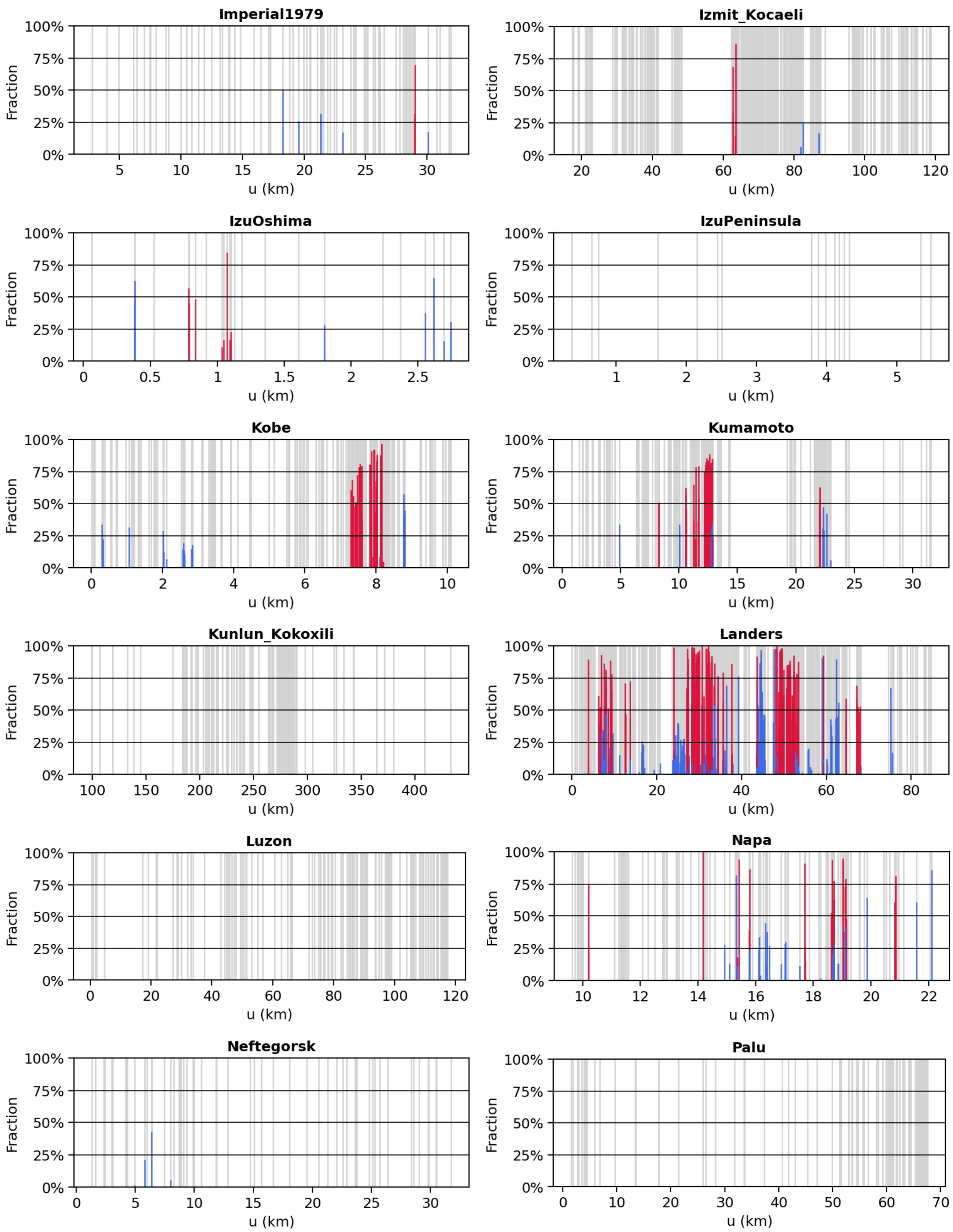

Figure 3.8. Aggregaton results for strike-slip events (contnued). Fractonal contributons of seed net displacement (gray vertcal bars), distributed (blue), principal (red), and cumulatve (orange).

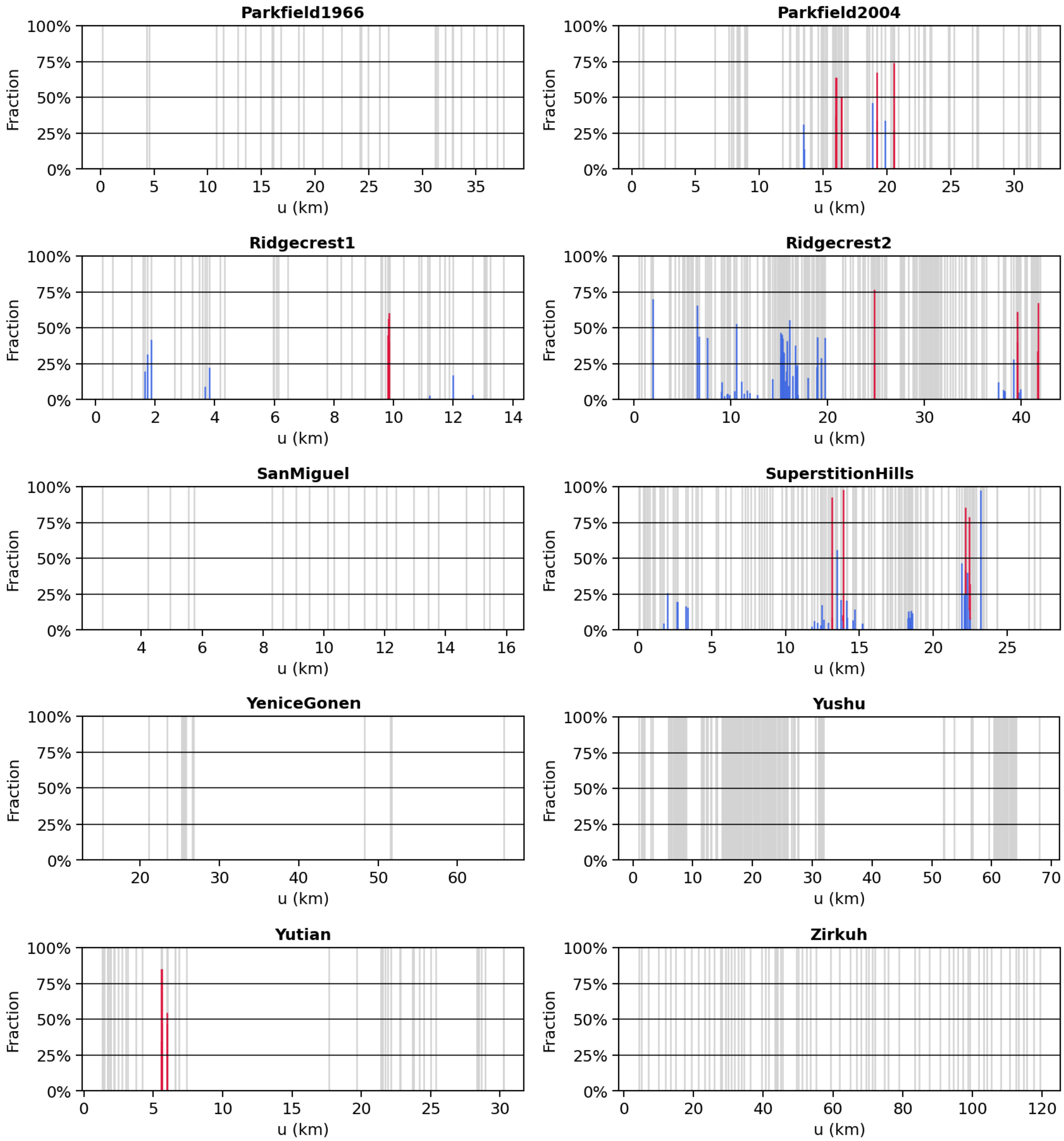

Figure 3.8. Aggregaton results for strike-slip events (contnued). Fractonal contributons of seed net displacement (gray vertcal bars), distributed (blue), principal (red), and cumulatve (orange).

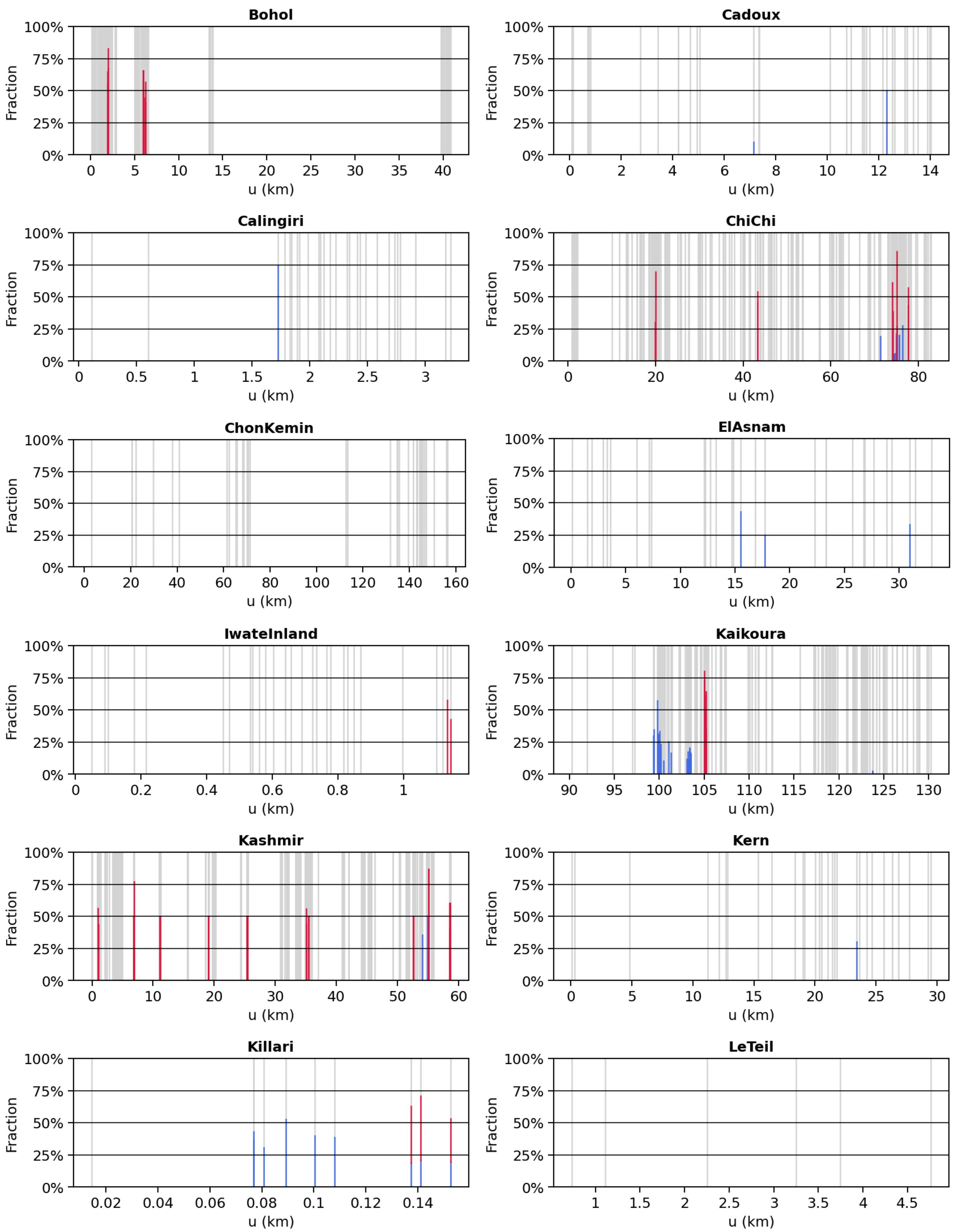

Figure 3.9. Aggregaton results for reverse events. Fractonal contributons of seed net displacement (gray vertcal bars), distributed (blue), principal (red), and cumulatve (orange).

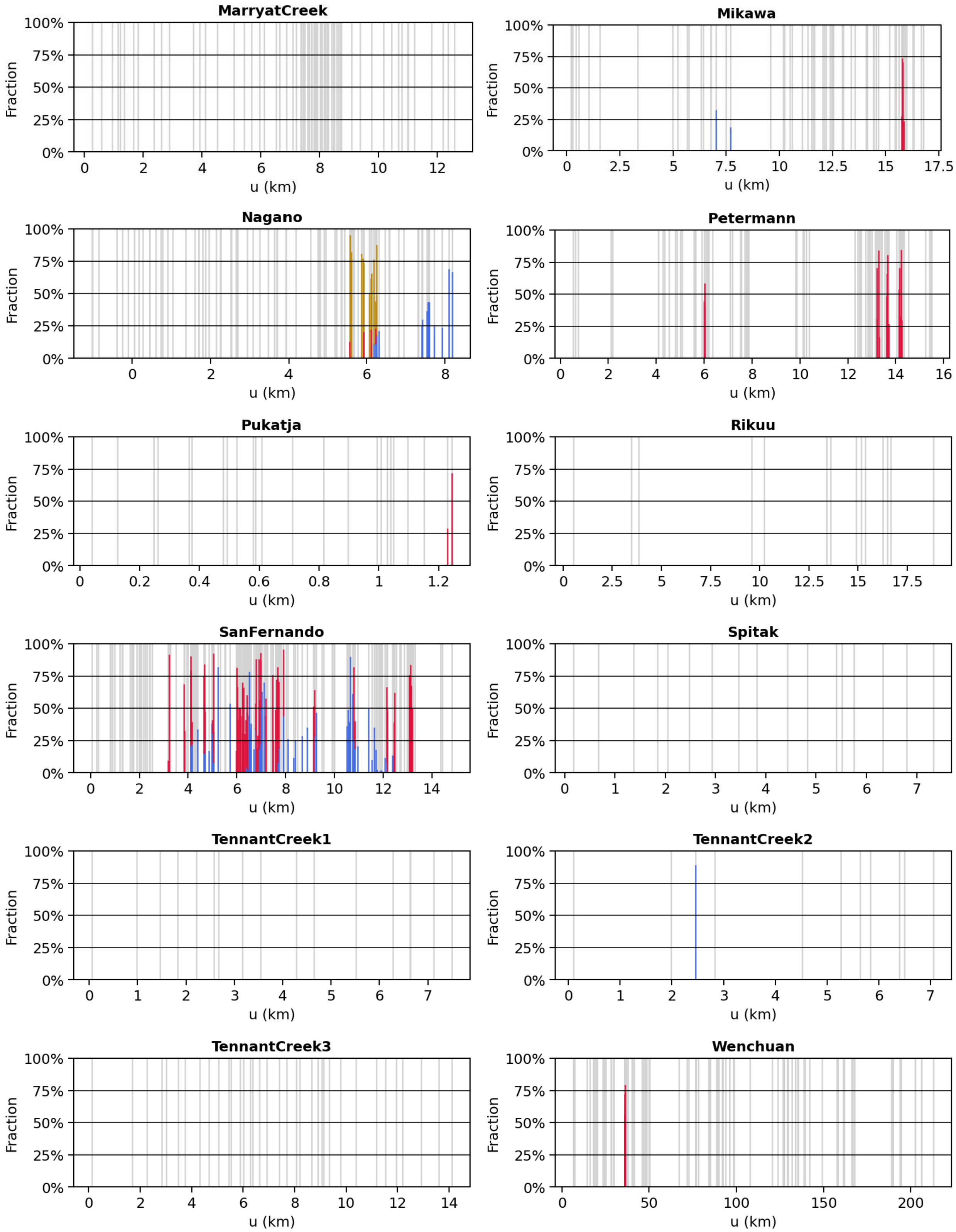

Figure 3.9. Aggregaton results for reverse events (contnued). Fractonal contributons of seed net displacement (gray vertcal bars), distributed (blue), principal (red), and cumulatve (orange).

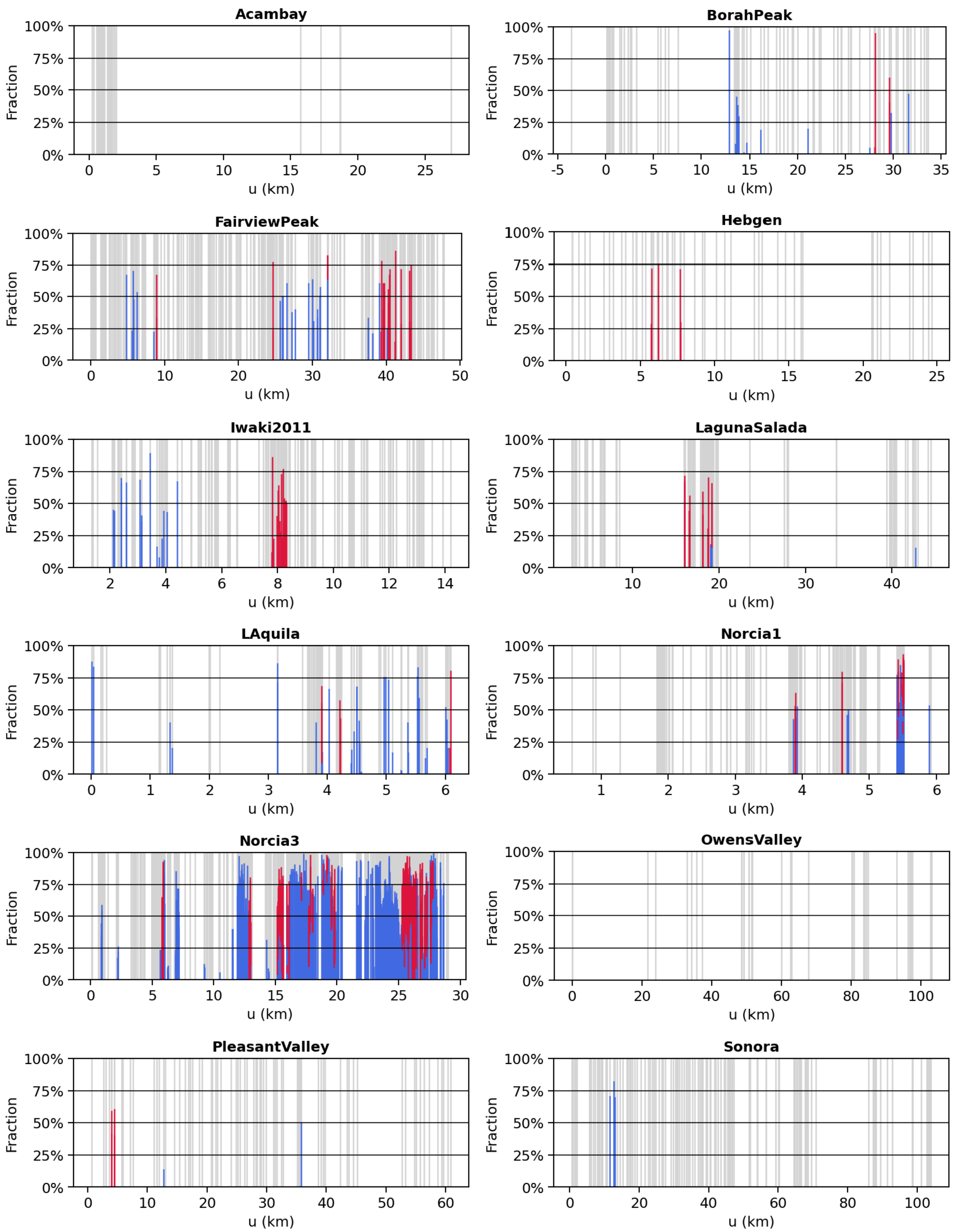

Figure 3.10. Aggregaton results for normal events. Fractonal contributons of seed net displacement (gray vertcal bars), distributed (blue), principal (red), and cumulatve (orange).

4 MODEL

In this chapter, we describe the model that describes the dependence of (aggregated) displacement D on the predictor variables. Predictor variables are moment magnitude $\mathbf{M}$ and normalized positon along the rupture, $U_* = x/L$, where L is the rupture length, and x is the positon along the rupture.

The model describes a conditonal probability distributon of S given the predictor variables, $P(D|U_*, \mathbf{M})$. We model the displacement distributon as a lognormal distributon, similar to ground-moton models

$$Y = \ln D \sim N(\mu, \sigma) \tag{4.1}$$

where the median and standard deviaton are functons of $\mathbf{M}$ and U_*, $\mu = f(\mathbf{M}, U_*)$ and $\sigma = g(\mathbf{M}, U_*)$. Our target variable is the logarithmic displacement, $Y = \ln D$. This means that we can model the likelihood as a normal distributon; however, to account for low displacement values, which can occur at model complexites, we use a Student-T distributon for the likelihood, which implements a form of Bayesian robust regression (Gelman et al., 2013). The Student-T distributon is only used for model fitng to account for outliers; in a forward applicaton, the lognormal distributon should be used to calculate exceedance probabilites and fractles of the displacement distributon.

The model parameters are estmated using Bayesian inference (e.g. Gelman et al., 2013; Spiegelhalter and Rice, 2009), which means we estmate the *posterior* distributon of the parameters given the data. The posterior distributon is proportonal to the product of the *prior* distributon and the likelihood

$$P(\vec{\theta}|D) \propto P(\vec{\theta})\, P(D|\vec{\theta}) \tag{4.2}$$

The likelihood for an individual observaton i describes the probability of observing a data point given the model and the values of the model parameters. In our case, this is the Student-T distributon.

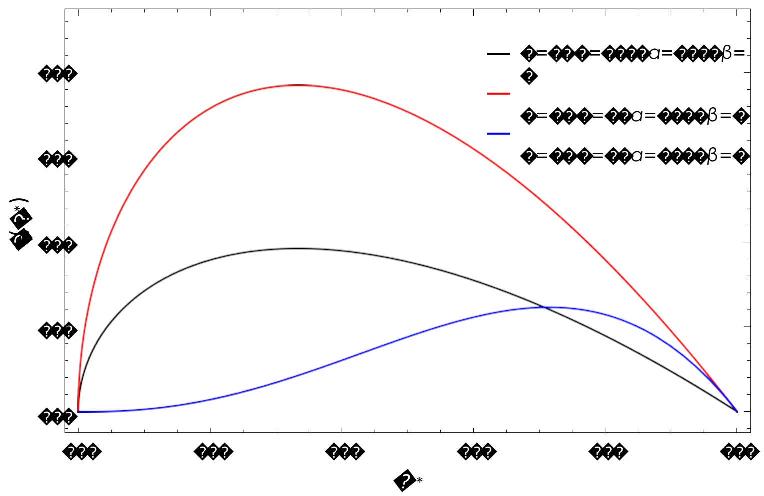

Figure 4.1. Functon $f_u(U_*)$ for different combinatons of its parameters.

41 MEDIAN PREDICTION

411 Dependence on x/L

The basic functonal form of the model to describe the dependence of the logarithmic displacement on U_* is derived from the probability density functon (PDF) of the Beta distributon. It has the following form

$$f_u(U_*) = a + \gamma\, U_*^{\alpha} (1 - U_*)^{\beta} \tag{4.3}$$

For $c > 0$, $\alpha > 0$, $\beta > 0$, $f_u(U_*)$ exhibits a convex shape, where the minimum value $\min(f_u(U_*)) = a$ is reached for $U_* = 0, 1$ (and thus $f_u(0) = f_u(1)$), and the maximum value is

$$\max(f_u(U_*)) = a + \gamma \left(\frac{\alpha}{\alpha + \beta}\right)^{\alpha} \left(\frac{\beta}{\alpha + \beta}\right)^{\beta} \tag{4.4}$$

which is reached for $U_{*,max} = \frac{\alpha}{\alpha+\beta}$. The parameter c determines the shape of the functon, and the relatve height between maximum $\max(f_u(U_*))$ and minimum a. Figure 4.1 shows $f_u(U_*)$ for different parameter combinatons of a, γ, α, β. In the model, we constrain α and β to lie between 0 and 1, to avoid a "flatening out" at the end of he ruptures. $f_u(U_*)$ allows for a shape of the median displacement along the fault that is similar to the quadratc and bilinear models of Petersen et al. (2011).

412 Dependence on Magnitude

The maximum $\max(f_u(U_*))$ is modeled as a functon of magnitude; this is the predicted mode of functon $f_u(U_*)$, and we call it *peak median displacement*. In general, m should increase with magnitude **M**. Similar to ground-moton models, we find that at large magnitudes the displacement dependence flatens out, so we use a bilinear functon for the magnitude dependency. The functonal form uses the logistc hinge functon, which is a bilinear functon

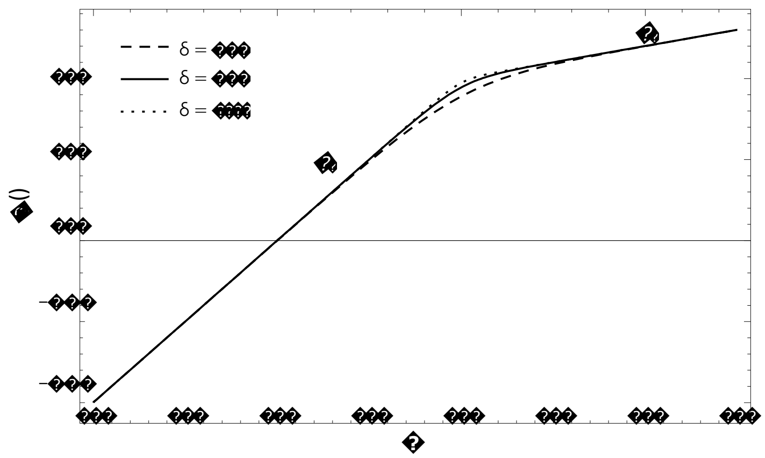

Figure 4.2. Logistc hinge functon, used to model the magnitude scaling of the displacement model.

with a smooth transiton:

$$\max(f_u(U_*)) = f_M(\mathbf{M}) = c_1 + c_3(\mathbf{M} - M_b) + (c_2 - c_3)\delta \ln\left[1 + \exp\left(\frac{\mathbf{M} - M_b}{\delta}\right)\right] \tag{4.5}$$

where M_b is the magnitude break point, c_1 is the value of the functon at the break point, c_2 and c_3 are the slope below and above the break point, and δ controls the smoothness of the transiton, with lower values of δ leading to a sharper transiton. Figure 4.2 shows an example scaling of the logistc hinge functon $f_M(\mathbf{M})$.

413 Event-specific Effects

We include event-specific effects that account for between-event variability in the peak median displacement for events of the same magnitude, as well as for the shape of the displacement profile across the rupture. These event-specific terms are modeled as random effects. The random effect for the maximum is modeled as normal distributon

$$\delta m \sim N(0, \sigma_m) \tag{4.6}$$

To model between-event variability of the shape, we model the parameter c as a random effect. Since γ needs to be positve to generate physically meaningful shapes of the displacement profiles, we model it with a truncated normal distributon

$$\gamma \sim N(\mu_\gamma, \sigma_\gamma)\ T(0, \infty) \tag{4.7}$$

This is equivalent to the following form

$$\begin{aligned} \gamma &= \mu_\gamma + \delta\gamma \\ \delta\gamma &\sim N(0, \sigma_\gamma)\ T(-\mu_\gamma, \infty) \end{aligned} \tag{4.8}$$

The random effect δm is applied to all faultng styles. However, we found that strike-slip events have a similar shape which does not require a random effect for γ, so $\delta\gamma$ applies only to the models for normal and reverse faultng. The γ term describes the strength of the along-fault curvature (i.e., $U_*^{\alpha}(1-U_*)^{\beta}$) and as γ approaches zero the shape tends to a constant value over the normalized slip.

For normal and strike-slip events, we observe less variability in the peak median displacement at large magnitudes than at small magnitudes, so for these faultng styles the standard deviaton σ_m is magnitude dependent. We describe the model for σ_m in Secton 4.2.

414 Full Median Model

Combining the dependence on magnitude **M** and normalized positon on the fault U_* with the random effects, the median for each event can be calculated as

$$
\begin{aligned}
\mu = {} & c_1 + c_3(M - M_b) + (c_2 - c_3)\delta \ln\left[1 + \exp\left(\frac{M - M_b}{\delta}\right)\right] \\
& - (\mu_Y + \delta\gamma)\left(\frac{\alpha}{\alpha+\beta}\right)^{\alpha}\left(\frac{\beta}{\alpha+\beta}\right)^{\beta} + (\mu_Y + \delta\gamma)\, U_*^{\alpha}(1 - U_*)^{\beta} \\
& + \delta m
\end{aligned}
\tag{4.9}
$$

In a forward predicton, the event terms δm and $\delta\gamma$ are unknown and need to be integrated out.

Influence of Event Term $\delta\gamma$

The event term δm is additve in Equaton (4.9), and thus hs the effect of changing the overall slip level by the same amount across the rupture. By contrast, the event term $\delta\gamma$ changes the shape of the slip profile across the rupture, and leads to a different slip adjustment for different values of U_*.

To account for the variability in $\delta\gamma$, one can use Monte Carlo integraton. In this case, one samples different values of $\delta\gamma$ according to Equaton (4.8), calculate predictons for each sample, and then assess mean/median and standard deviaton from the resultng predictons. Results of this procedure are shown in Figure 4.3, which shows the median and 5%/95% fractles of predictons based on 10,000 samples of $\delta\gamma$. Compared to predictons with a fixed μ_Y, the median predictons change, and there is large variability at the ends of the rupture. The difference in median predictons, as well as the standard deviaton $\sigma_{Y,med}$ due to variability in $\delta\gamma$ are both also shown in Figure 4.3. These are independent of magnitude, and can thus be calculated once. Then, the median model becomes

$$
\begin{aligned}
\mu = {} & c_1 + c_3(M - M_b) + (c_2 - c_3)\delta \ln\left[1 + \exp\left(\frac{M - M_b}{\delta}\right)\right] \\
& - \mu_Y\left(\frac{\alpha}{\alpha+\beta}\right)^{\alpha}\left(\frac{\beta}{\alpha+\beta}\right)^{\beta} + \mu_Y\, U_*^{\alpha}(1 - U_*)^{\beta} \\
& + \delta m + \Delta \mathrm{med}_Y
\end{aligned}
\tag{4.10}
$$

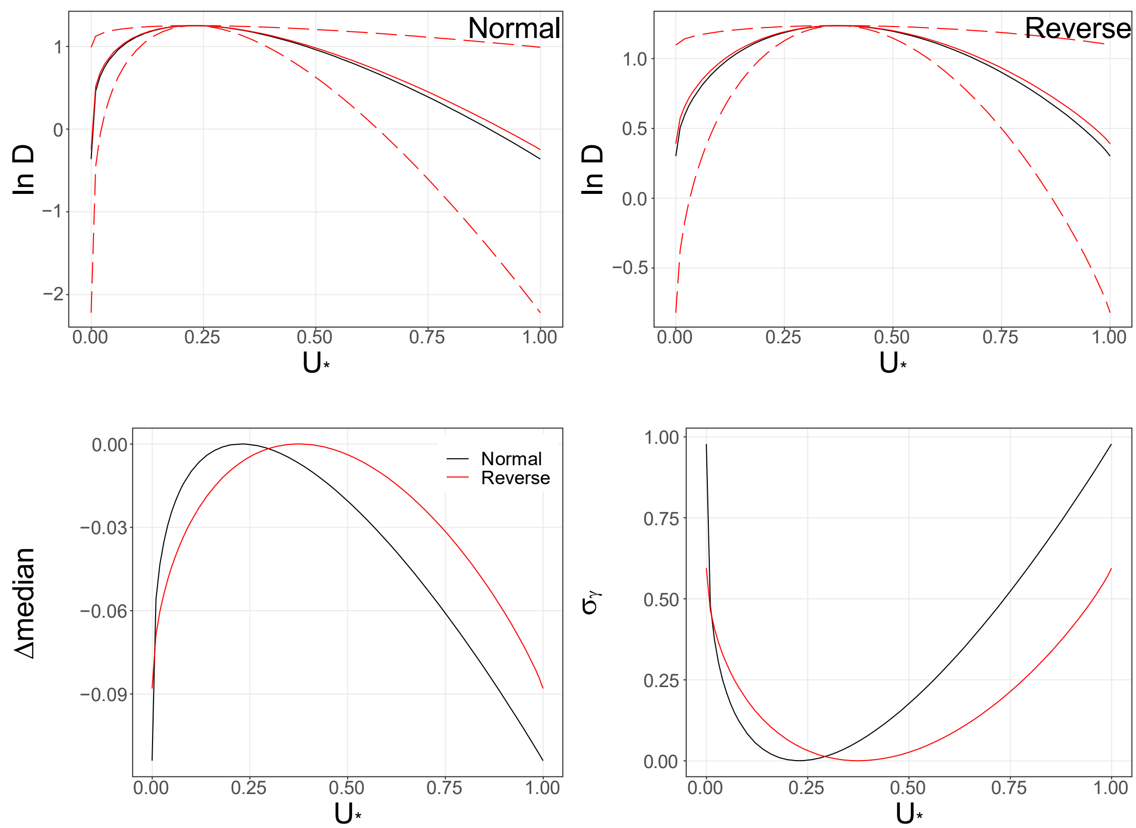

Figure 4.3. Influence of varying even term $\delta\gamma$ for reverse and normal models. Black line shows predicton with μ_{γ}, red lines show range of predictons based on 10000 samples of $\delta\gamma$. Botom lef plot shows the difference in median predictons (black line minus red line in the top two plots). Botom right plot shows the standard deviaton of the 10000 predictons. The magnitude is $\mathbf{M} = 8$.

We have calculated values of $\Delta \mathrm{med}_Y$ and $\sigma_{Y,med}$ for each of the posterior samples of the normal and reverse model, for values $U_* = 0., 0.01, 0.02, \ldots, 1$. For other values of U_*, one can use linear interpolaton.

42 STANDARD DEVIATION MODELS

There are three standard deviatons in the model: the standard deviaton for the observatons σ_u conditonal on the event-specific effects δm and $\delta\gamma$, and the standard deviatons for the random effects δm and δc, σ_m and σ_Y respectvely. The standard deviatons σ_u and σ_m deviatons can depend on the predictor variables for different styles of faultng. The standard deviaton σ_Y leads to a variability $\sigma_{Y,med}$ which depends on U_* (Figure 4.3).

Figure 4.4 shows the event terms δm for the different faultng styles. For strike-slip and normal faultng events, the variability of the event terms δm at large magnitudes ($\mathbf{M} > 7$) is small compared to the variability at magnitudes of around $\mathbf{M} \approx 6$. Hence, for these two faultng styles we model the standard deviaton σ_m as magnitude dependent. For strike-slip events, the two events at $\mathbf{M} = 5.2$ (Galway Lake and Homestead Valley) exhibit very different displacement values, which leads to large differences in the event terms. Thus, we model the standard deviaton σ_m as

$$\sigma_m(\mathbf{M}) = \begin{cases} s_{m,s1} + s_{m,s2}(\mathbf{M} - s_{m,s3}) - s_{m,s2}\,\delta \ln\left[1 + \exp\left(\frac{\mathbf{M} - s_{m,s3}}{\delta}\right)\right] & \text{strike-slip} \\ s_{m,n1} - s_{m,n2}\frac{1}{1+\exp[-s_{m,n3}(\mathbf{M}-7)]} & \text{normal} \\ s_{m,r} & \text{reverse} \end{cases} \tag{4.11}$$

For strike-slip events, the standard deviaton σ_m is modeled as a bi-linear functon which increases with lower magnitudes and has a slope of zero at large magnitudes (meaning σ_m is constant at large magnitudes). For normal faultng events, the standard deviaton is constant at small magnitudes, and constant at large magnitudes, with a smooth transiton modeled by the logistc sigmoid functon. Due to the lack of data for normal faultng events with $\mathbf{M} < 6$, it is not clear whether the standard deviaton should increase. We deemed it "conservatve" to not extrapolate the value of σ_m towards larger values at smaller magnitudes.

Figure 4.5 shows the 68% fractle of positve residuals along the rupture, calculate in bins of width 0.025. Focusing on positve residuals means we are not concerned about low-displacement outliers affectng the plot. For both strike-slip and reverse faultng events, the range of residuals at the end of the rupture ($U_* = 0$ and $U_* = 1$) is larger than in the center, while the range for normal events is more constant along the rupture. Hence, we model the standard deviaton of the observaton level σ_u for strike-slip and reverse events with a quadratc functon

$$\sigma_u = g(U_*) = \begin{cases} s_{s1} + s_{s2}(U_* - x)^2 & \text{strike-slip} \\ s_{r1} + s_{r2}(U_* - x)^2 & \text{reverse} \\ s_n & \text{normal} \end{cases} \tag{4.12}$$

x is the minimum of the functon $g(U_*)$ for strike-slip and reverse events. We constrain x to coincide with the peak median displacement along the rupture $f_u(U_*)$, so $x = \frac{\alpha}{\alpha+\beta}$ The s_x are parameters to be estmated during the regression.

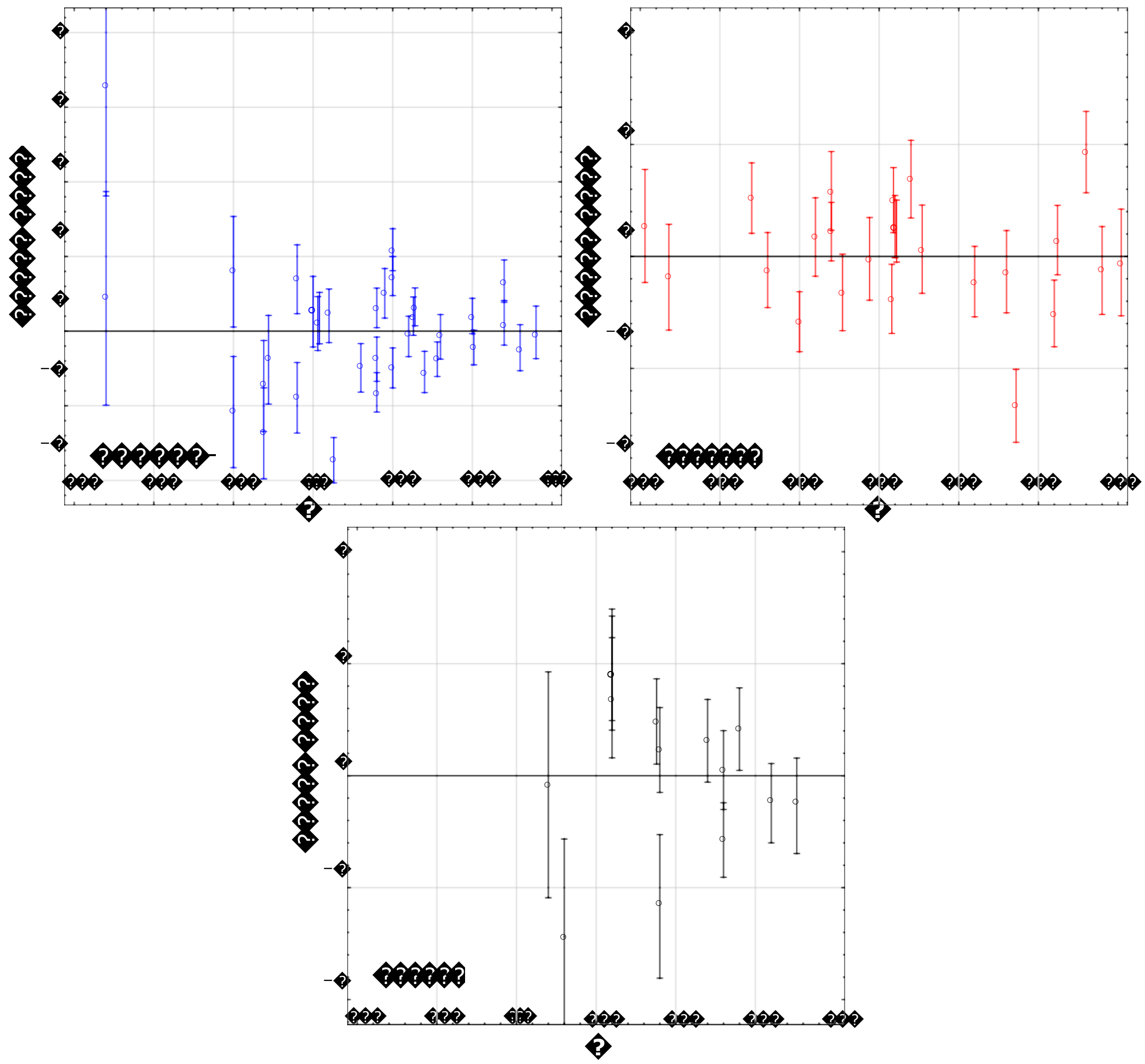

Figure 4.4. Event terms associated with the peak median displacement for different styles of faultng. The uncertainty intervals are the 5% and 95% fractles of the posterior distributon of the event terms.

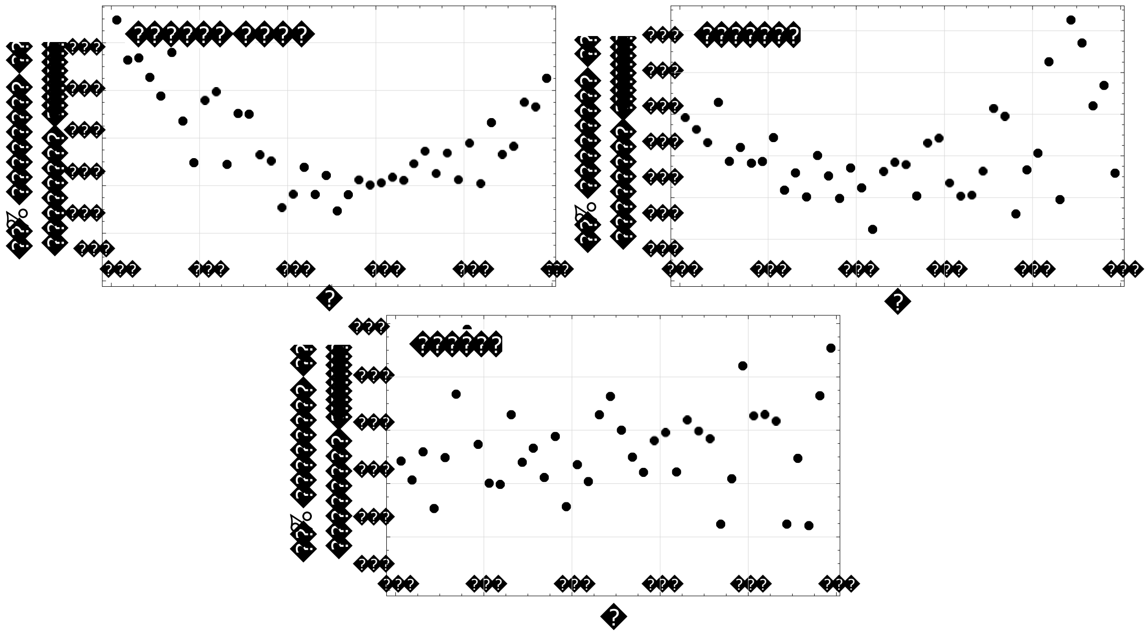

Figure 4.5. 68% fractle of all positve residuals to the median predicton, for different faultng styles.

43 OBSERVATION LIKELIHOOD

The observaton likelihood is modeled as a Student-T distributon. The Student-T distributon has heavier tails than the normal distributon, and thus can assign higher density to outlier values. This makes the Student-T a popular choice for Bayesian robust regression, as it is less susceptble to outliers. Figure 4.6 shows the aggregated displacement againstU_* for the Superstton Hills earthquake. As one can see, the overall shape is nicely parabolic, but there are some parts of the rupture with anomalously low displacement value.

The low displacement values are treated as outliers, and are accommodated via a Bayesian robust regression (Gelman et al., 2013). In this case, the observaton likelihood is a Student-T distributon, which has heavier tails than the normal distributon, and is thus less susceptble to outliers. The observatonal model is as follows

$$\ln D \sim S_T(\mu, \sigma_u, \nu(U_*)) \tag{4.13}$$

where μ is the mean/median of the distributon and is modeled via $f(\mathbf{M}, U_*)$, σ_u is the standard deviaton modeled via $\sigma_u = g(U_*)$, and ν is the degrees-of-freedom parameter. For large values of ν ($\nu \to \infty$) the Student-t distributon approaches the normal distributon. ν is a parameter of the model that is estmated.

Since the low-displacement outliers are unevenly distributed across the rupture, the value of ν changes along the rupture. We partton each rupture into 40 bins of length 0.025, and estmate a different value of ν for each bin and event. Thus, we can identfy parts of the rupture with more outliers by the value of ν.

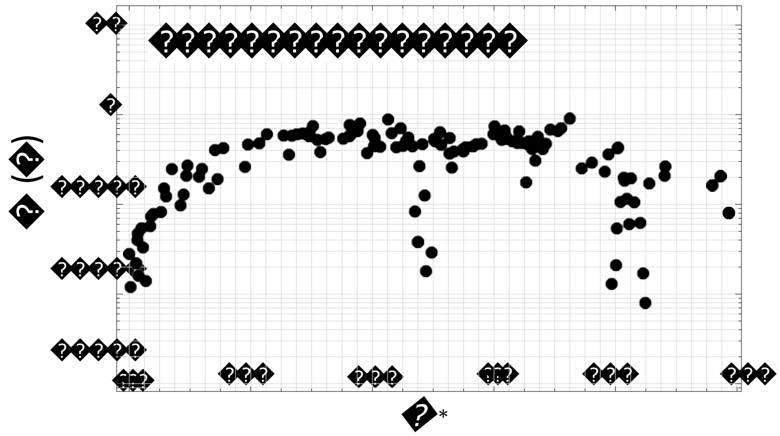

Figure 4.6. Aggregated displacement vs. U_* for Superstton Hills.

44 MODEL ESTIMATION

The model parameters $\vec{\theta}$ are estmated using Bayesian inference (Gelman et al., 2013; Spiegelhalter and Rice, 2009), which means we estmate the *posterior* distributon of the parameters given the data. The posterior distributon is proportonal to the product of the *prior* distributon and the likelihood

$$P(\vec{\theta}|D) \propto P(\vec{\theta})\ P(D|\vec{\theta}) \tag{4.14}$$

The likelihood is described in Secton 4.3 (cf. Equaton (4.13)), and is a Student-T distributon, with median $\mu(\mathbf{M}, U_*)$, standard deviaton $\sigma(\mathbf{M}, u_*)$, and degrees-of-freedom $\nu(U_*)$.

The model parameters to be estmated comprise the parameters of the median functon (c_1, c_2, c_3, α, β), the hyper-parameters controlling the distributon of the random effects (μ_Y, σ_Y, s_{mx} for the standard deviaton σ_m), the random effects $\delta\gamma$ and δm, and the coefficients for the standard deviaton σ (s_x). The prior distributons for the random effects are a truncated normal distributon for $\delta\gamma$ and a normal distributon for δm (cf. Secton 4.1.3). For the other parameters, we use weakly informatve prior distributons[1], which help to stabilize the regression. The prior

[1]See https://github.com/stan-dev/stan/wiki/Prior-Choice-Recommendations for some generic advice of different levels of priors.

distributons are

$$
\begin{aligned}
\alpha, \beta &\sim \text{Beta}(2, 2) \\
c_1, c_2 &\sim N(0, 10) \\
c_3 &\sim N(1, 0.5) \\
\mu_Y &\sim N(5, 10)\ T(0, \infty) \\
\sigma_Y &\sim N(0, 2)\ T(0, \infty) \\
s_{s1}, s_{r1}, s_n &\sim N(0, 1)\ T(0, \infty) \\
s_{s2}, s_{r2} &\sim N(0, 2)\ T(0, \infty) \\
s_{m,s1}, s_{m,s2}, s_{n,s1}, s_{m,n2}, s_{m,r} &\sim N(0, 1)\ T(0, \infty) \\
s_{m,s3} &\sim N(7, 0.5)\ T(0, \infty) \\
s_{n,s3} &\sim N(10, 10)\ T(0, \infty) \\
\nu &\sim \text{Gamma}(2, 0.1)
\end{aligned}
\tag{4.15}
$$

The models are estmated separately for the different faultng styles (strike-slip, reverse, normal), with the appropriate adjustments for missing random effects or different functonal forms for the standard deviatons. The model parameters are estmated via Markov Chain Monte Carlo (MCMC) sampling, using the program Stan (Carpenter et al., 2017; Stan Development Team, 2022). The regressions are carried out in the computer environment R (R Core Team, 2021) with the package cmdstanr (Gabry and Č eˇsnovar, 2021). For each faultng style, we run 4 chains with 1000 warm-up iteratons and 500 sampling iteratons each. Hence, in total we obtain 2000 samples from the posterior distributon, which can be used to assess the epistemic uncertainty associated with the model. Convergence of the chains is evaluated via the $\hat{R}$ (R-hat) statstc (Vehtari et al., 2020).

45 WITHIN-MODEL EPISTEMIC UNCERTAINTY

Apart from predictons for the median and standard deviaton, we also provide estmates of within-model epistemic uncertainty. Epistemic uncertainty refers to the uncertainty that can potentally be reduced with increasing knowledge and/or data (e.g. Bommer, 2003). It is important to account for epistemic uncertainty in a hazard analysis, since data is ofen sparse, ofen for scenarios that are important such as large magnitudes.

In the context of model predictons, there are two important types of model predictons: between-model and within-model uncertainty. Between-model uncertainty is associated with differences in model predictons due to distnct models, with different functonal forms, and possibly different developing teams. An example from fault-displacement model development are the different models presented in Petersen et al. (2011) (bilinear, quadratc, and elliptcal). For ground-moton models, examples are the NGA-West 2 models (Bozorgnia et al., 2014; Gregor et al., 2014), mainly based on Californian data, the models presented in Douglas et al. (2014) for Europe/Middle East, or the NGA-East project (Goulet et al., 2018, 2021). Between-model uncertainty captures different choices in the data selecton and/or model development process, as well as differences in underlying assumptons for the model. By contrast, within-model uncertainty is due to uncertainty in the estmated model parameters is influenced by how well constrained model parameters are by the available data, and is associated with model predictons of a single model. An example from ground-moton models is Al-Atk and Youngs (2014) for the NGA-West 2 models. Between and within-model uncertainty should be seen as complimentary; it can depend on the scenario which is larger/more important.

By the nature of this work, we can only quantfy within-model uncertainty, while the different models developed within FDHI address between-model uncertainty. Since we estmate the parameters of the model via Bayesian inference, epistemic uncertainty is assessed by the posterior distributon of the parameters $p(\vec{\theta}|D)$.

In general, in a hazard analysis aleatory variability and epistemic uncertainty are treated differently: aleatory variability is integrated out, while epistemic uncertainty is not. Thus, aleatory variability results in a hazard curve, while epistemic uncertainty results in a distributon of hazard curves (though in the end, when using the mean hazard one implicitly integrates out epistemic uncertainty).

A useful quantty to illustrate some of the concepts in this context is the posterior predictve distributon. The posterior predictve distributon describes the full distributon for a new observaton, and combines aleatory variability (randomness in the process) and epistemic uncertainty (how well the model can quantfy its predictons). The posterior predictve distributon for a new observaton $\tilde{y}$ at magnitude $\tilde{\mathbf{M}}$ and positon along the rupture $\tilde{U}_*$ is defined as (Gelman et al., 2013)

$$p(\tilde{y}\,|\,\tilde{\mathbf{M}},\tilde{U}_*,D) = \int p(\tilde{y}\,|\,\tilde{\mathbf{M}},\tilde{U}_*,\vec{\theta})\; p(\vec{\theta}|D)\; d\vec{\theta} \tag{4.16}$$

meaning it is calculated by integratng out the uncertainty of the parameters, i.e. by integratng over the posterior distributon of the parameters. The posterior predictve distributon can be approximated by

$$p(\tilde{y}\,|\,\tilde{\mathbf{M}},\tilde{U}_*,D) \approx \frac{1}{M}\sum_{i=1}^{M} p(\tilde{y}\,|\,\tilde{\mathbf{M}},\tilde{U}_*,\vec{\theta}_i) \tag{4.17}$$

where $\vec{\theta}_i \sim p(\vec{\theta}|D)$ is a sample from the posterior distributon. For our model, the results consist of 2000 samples from the posterior distributon, obtained via MCMC. Thus, one can directly use Equaton (4.17) to calculate the posterior predictve distributon.

5 MODEL IMPLEMENTATION

This chapter provides some guidance on implementng the model. An implementaton in R (R Core Team, 2021) can be found at https://github.com/NHR3-UCLA/KKMSB22_Displacement_Model.

The forward model is a lognormal distributon for aggregated principal displacement D, so model implementaton comes down to calculatng median and standard deviaton for a given set of predictor variables **M** and U_*. The median and standard deviaton fully describe the distributon, and thus exceedance probabilites or fractles can be calculated.

The functon for the median predicton is given in Equaton (4.9), with coefficients c_1, c_2, c_3 α, β, μ_Y as well as $M_b = 7$ and $\delta = 0.1$. For each style of faultng, there is a different set of coefficient.

The standard deviaton quantfies the aleatory variability. It consists of the variability in observatons across the rupture (σ_u, calculated as in Equaton (4.12)), the variability in event terms δm (σ_m, given by Equaton (4.11)), and the event terms $\delta\gamma$ (for reverse and normal events, σ_Y). Since the event term δm is additve, the variances σ_u^2 and σ_m^2 can be added to give the total variance. This does not work for event terms $\delta\gamma$, as this term controls the shape of the slip profile. Hence, for this term we resort to Monte Carlo integraton. We sample event terms $\delta\gamma$, calculate the median predicton for each sample, and then calculate mean and standard deviaton of the resultng predictons. Then, the total variance can be calculated as

$$\sigma_T^2 = \sigma_m^2 + \sigma_u^2 + \sigma_{Y,med}^2 \tag{5.1}$$

where $\sigma_{Y,med}$ is the standard deviaton in median predictons due to variability of $\delta\gamma$.

Overall, the calculaton of the slip distributon for a partcular set of predictor variables is as follows:

1. Select the set of coefficients (normal, reverse, strike-slip).
2. Calculate σ_m and σ_u.
3. If the style of faultng is reverse or normal,
    (a) Calculate Δmed_Y and $\sigma_{Y,med}$ by interpolaton along U_*.

(b) Calculate the median predicton μ according to Equaton (4.10).

(c) Calculate the total standard deviaton via Equaton (5.1).

4. If the style of faultng is strike-slip:

(a) Calculate the median predicton μ according to Equaton (4.9).

(b) Calculate the total standard deviaton as $\sigma_T = \sqrt{\sigma_m^2 + \sigma_u^2}$

5. Return μ and σ_T.

We provide 2000 sets of coefficients for each style-of-faultng model, which are sampled from the posterior distributon. These are used to capture the epistemic uncertainty in the model coefficients (i.e., the within-model epistemic uncertainty). If no epistemic uncertainty is desired, one can use a point estmate for each coefficient such as the mean or median. If epistemic uncertainty is to be included in the analysis, one should repeat the calculatons for each of the 2000 sets of coefficients (or a subset). The reducton in the number of sets from 2000 can be adjusted based on the acceptable level of accuracy. In general, we recommend that at least 100 samples be used. This gives a set of lognormal distributons, which can be used to calculate exceedance probabilites for the different posterior samples. This allows one to assess epistemic uncertainty in exceedance probabilites, and thus in hazard curves.

Figure 5.1 shows a comparison of median predictons and total standard deviatons $\sigma_T = \sqrt{\sigma_m^2 + \sigma_u^2}$. These are calculated using the mean or median coefficients (i.e. we calculate the mean/median, and then calculate the median predicton and standard deviatons), as well as via the mean/median of the posterior predictons (i.e. we calculate median predicton and standard deviatons for each of the posterior samples, and then compute the mean/median). In general, we find that there are almost no differences in the median predictons (also across the different models), and the differences in standard deviatons are minor in most cases. There are some differences in the strike-model for $\mathbf{M} = 6.5$. In general, the full model includes the epistemic uncertainty due to the 2000 samples, and any point estmate leads to loss of informaton. If a point estmate is really desired, then we recommend using the median of the posterior distributon.

The model is not symmetric with respect to U_*, which means that one should calculate predictons for U_* and $1 - U_*$ and give each of them equal weight. Note that both the median and the standard deviaton σ are affected.

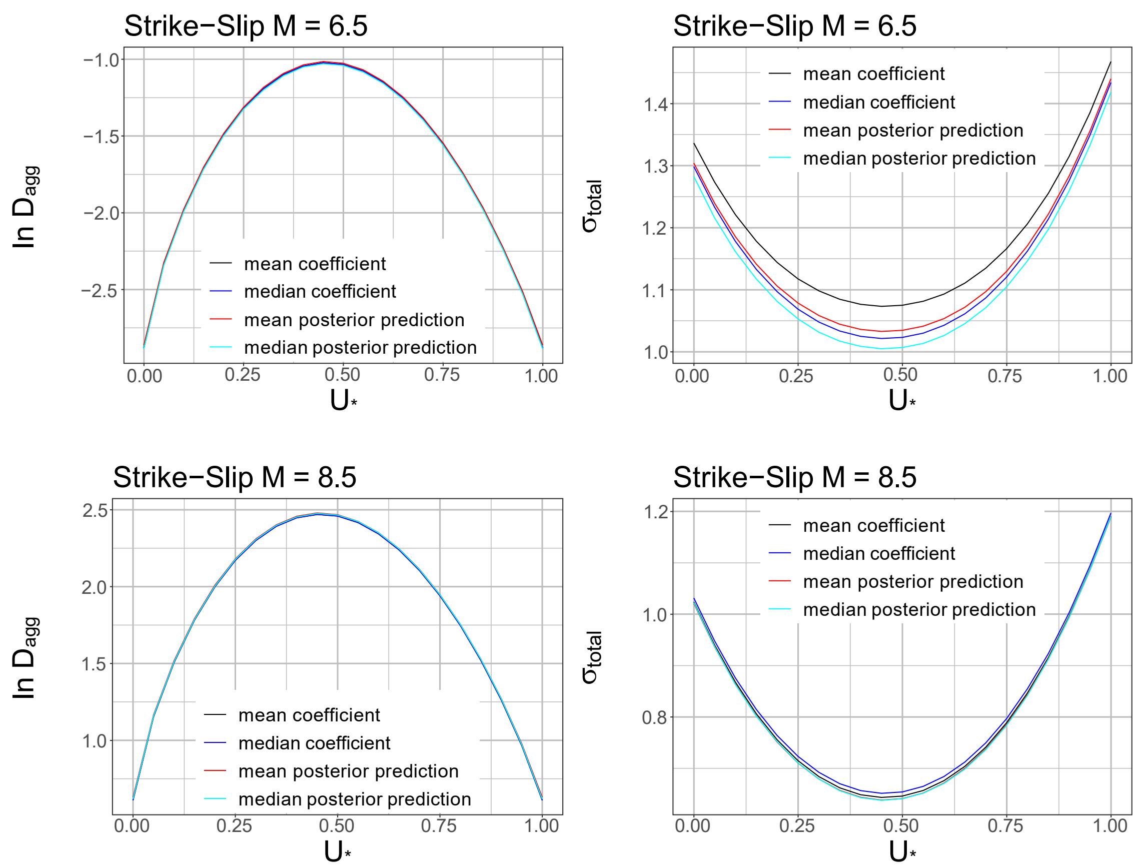

Figure 5.1. Comparison of median predictons and standard deviatons, computed using the mean/median coefficients, and calculated by taking the mean/median of posterior predictons.

6 MODEL PERFORMANCE

In this chapter, we provide results of the model that show the scaling with magnitude **M** and positon along the rupture U_*, the standard deviatons, and residuals. Comparisons with existng models, such as Petersen et al. (2011), are presented in Chapter 7.

6.1 OBSERVATION LEVEL

This secton describes results with respect to individual observatons. Thus, we conditon on the event-specific terms, which are included in the calculaton of predictons.

Figure 6.1 shows residuals of the model, calculated as

$$\text{resid} = Y - \mu = \ln D - \mu \tag{6.1}$$

where μ is the predicted median logarithmic displacement (including event specific effects). μ is calculated as the mean of the posterior predictons, meaning we calculate the predicton μ_p for each posterior sample p, and then calculate the mean of the 2000 predictons. Similar to Figure 4.5, one can see the larger range of residuals at the end of the rupture for strike-slip and reverse events. One can also see the skewed nature of the residuals, with larger negatve values corresponding to low-slip outliers.

The models for the standard deviaton σ_u are ploted in Figure 6.2. Shown are the mean, median, and 5%/95% fractles of the uncertainty distributon, calculated from the 2000 posterior samples. For the strike-slip and reverse models σ_u is modeled as a quadratc functon, which leads to lower values in the center, but larger variability at the end of the ruptures.

Figure 6.3 shows the predicted average for the Superstton Hills event, together with the observed aggregated displacement values. The predictons incorporate the event-specific effect δm for Superstton Hills. Shown are the mean, median, and 5%/95% fractles of the predictve distributon, which is calculated from the 2000 posterior samples. The right part of Figure 6.3 shows the values of the degrees-of-freedom ν of the Student-T distributon, which was used as the observaton likelihood. For larger values of ν, the Student-T distributon approaches the normal distributon. The ν values are estmated for small bins along the rupture, with a prior that is a Gamma distributon $\nu \sim \text{Gamma}(2, 0.1)$, which has a mean of 20 (Jua´rez and Steel, 2010). One can see in Figure 6.3 that most of the estmated ν values have a mean of 20 wth wide

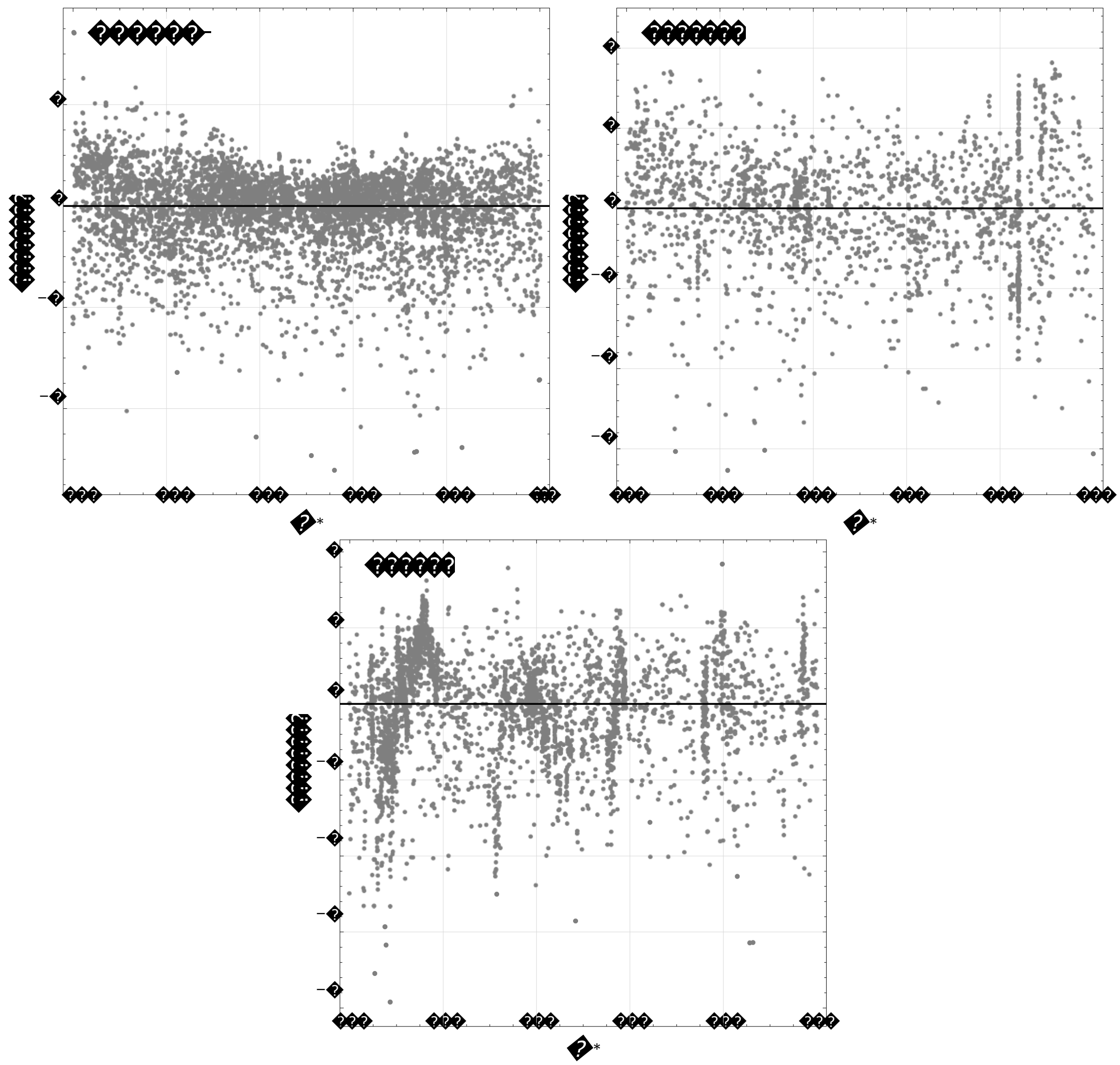

Figure 6.1. Residuals of all events against the models for the different styles of faultng.

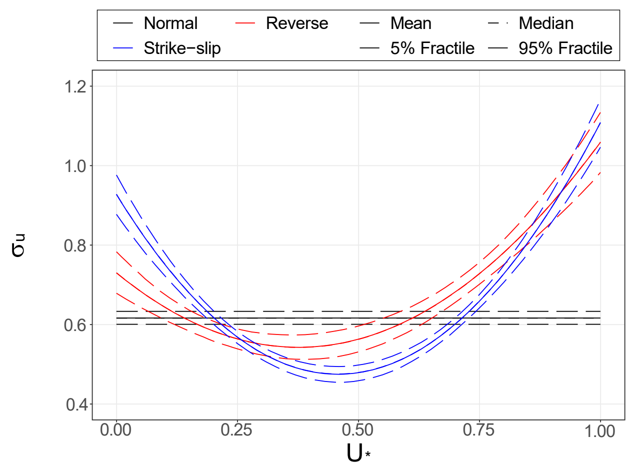

Figure 6.2. Models of $\sigma_u = g(U_*)$ against positon along the rupture U_*, for different faultng styles.

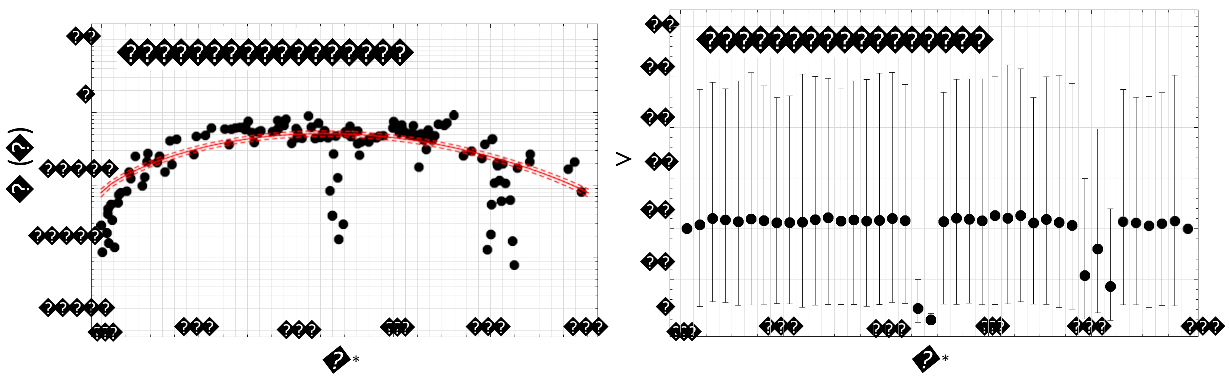

Figure 6.3. Slip for Superstton Hills, and ν of Student T distributon. Uncertainty bands are the 5% and 95% fractles of the posterior distributon.

uncertainty intervals, meaning that in this case the normal distributon is adequate to describe the data. However, for the range where significant outliers are present ($0.45 < U_* < 0.5$ and $0.775 < U_* < 0.825$), the values of ν decrease strongly, indicatng heavier tails of the observaton likelihood which takes care of the outlier values. Similar plots like Figure 6.3 for the other events can be found in Appendix B (Plots of Event Data and Predictons).

62 MAGNITUDE SCALING

Figure 6.4 shows the scaling of f_M (**M**) with magnitude for the different faultng styles. Recall that that f_M **M** $= \max(f_u(U_*))$, meaning it represents the mode of the predicted median slip across the rupture (peak median displacement). Based on Figure 6.4, reverse events are associated with larger slip predictons at low magnitudes (**M** < 6.5) compared to normal and strike-slip events. The magnitude scaling of strike-slip and normal faultng events shows a pronounce change in

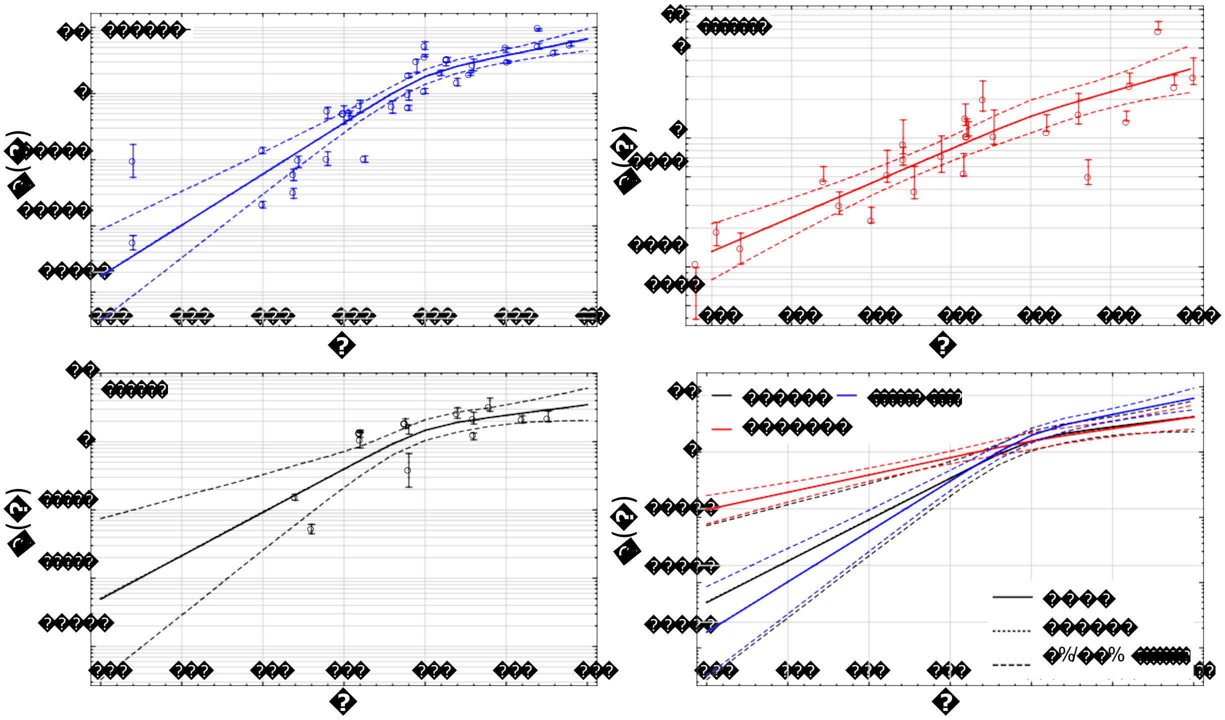

Figure 6.4. Magnitude scaling functon for the peak median displacement.

scaling, with a flater slope at large magnitudes (**M** > 7). The reverse events exhibit a flater slope at low magnitudes, and show a comparably lesser change in scaling.

The dashed lines in Figure 6.4 show the 5% ad 95% fractles of the epistemic uncertainty associated with f_M (**M**). For each posterior sample, we calculate a predicton, and then calculate the corresponding fractle. For magnitudes above or below the largest/smallest observed event, the fractle ranges become larger, indicatng larger epistemic uncertainty associated with extrapolaton. This is especially apparent for low magnitudes and the normal faultng style model, as the lowest magnitude in this case is **M** $= 6.2$, and thus the model is no well constrained at low magnitudes.

Figure 6.4 also displays the event-specific predictons of f_M (**M**), i.e. the predictons including the event-specific effect $\delta\mathrm{m}$ (cf. Equaton 4.9). The event terms $\delta\mathrm{m}$ themselves are shown in Figure 6.5, together with the model for σ_m. In general, the event terms are well centered and captured by the σ_m-model, but we can also see that the models are not well constrained for low magnitudes (n partcular for strike-slip and normal), due to lack of data. For the strike-slip model, there are two events at **M** $= 5.2$ (Homestead Valley and Galway Lake) with very different event terms and event-specific predictons. In partcular, the Homestead Valley earthquake has a very large event term. This drives the large value of σ_m at low magnitudes. It is a model choice to account for Homestead Valley via the σ_m-model, but we have to acknowledge that this part of the model is not well constrained. There is the queston whether Homestead Valley is an outlier event (or whether Galway Lake is an outlier), and whether the large standard deviaton is justfied based on two (not very well recorded) events. On the other hand, one should not ignore the differences in slip between the two events. In the end, this issue can only be resolved with more data. We advise to be careful when applying the strike-slip model to low magnitudes.

Similar to the strike-slip model, the normal model is not well constrained by data at low magnitudes. Here, we do not have data at all. Hence, we also advise cauton when applying the model at low magnitudes.

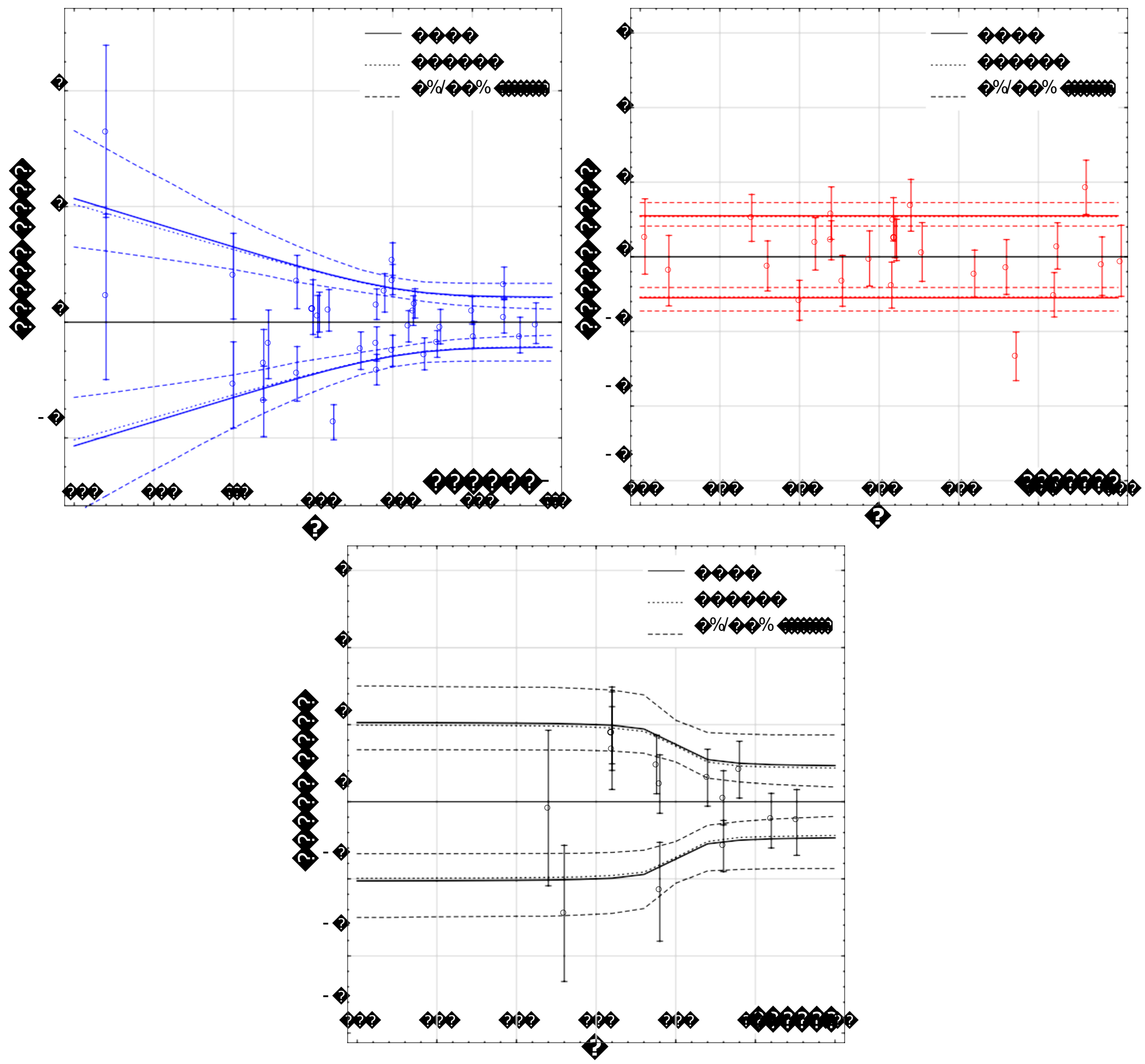

Figure 6.5. Standard deviaton σ_m and event terms δm for different styles of faultng.

6.3 MODEL PREDICTIONS

This secton documents unconditonal predictons of the model, i.e. predictons that do not include event-specific effects like $\delta\gamma$ and δm. Model predictons for **M** 5.5, 6.5, 7.2, 7,7, and 8.5 earthquakes are shown on Figures 6.6 through 6.8 for strike-slip, reverse, and normal styles of faultng, respectvely. Predictons are shown including epistemic uncertainty, thus corresponding to the full predictve distributon, and without epistemic uncertainty, using the median coefficients. The mean, median, and 5%, 16%, 84% and 95% fractles of the displacement distributon are shown.

Predictons for the case without epistemic uncertainty are calculated as follows:

1. Calculate the median of each parameter from the 2000 posterior samples.
2. With the medians, calculate median predicton μ, σ_m, σ_u, and $\sigma_{Y,med}$, and compute $\sigma^2_T = \sigma_m^2 + \sigma_u^2 + \sigma_{Y,med}^2$
3. Calculate fractles of lognormal distributon $\mathrm{LN}(\mu, \sigma_T)$.

For the predictons including epistemic uncertainty, we calculate median predictons and standard deviaton values for each of the 2000 samples. We then compute the median μ_S and standard deviaton σ_S of the set of median predictons, as well as the median of the set of calculated standard deviatons $\sigma_{T,m}$. We then calculate the fractles of a lognormal distributon $\mathrm{LN}(\mu_S, \sqrt{\sigma^2_{T,m} + \sigma_S^2})$.

The results are shown in Figures 6.6 to 6.8. In general, we can see that including epistemic uncertainty leads to a wider range of fractles, in partcular for magnitudes that are outside the data range (such as **M** $= 8.5$, or **M** $= 5.5$ for the normal model). As mentoned before, the normal and reverse model show stronger asymmetry than the strike-slip model. Due to the large variability at the end of the rupture, mainly due to $\delta\gamma$, we also see an increase in the larger fractles at U_* values close to one.

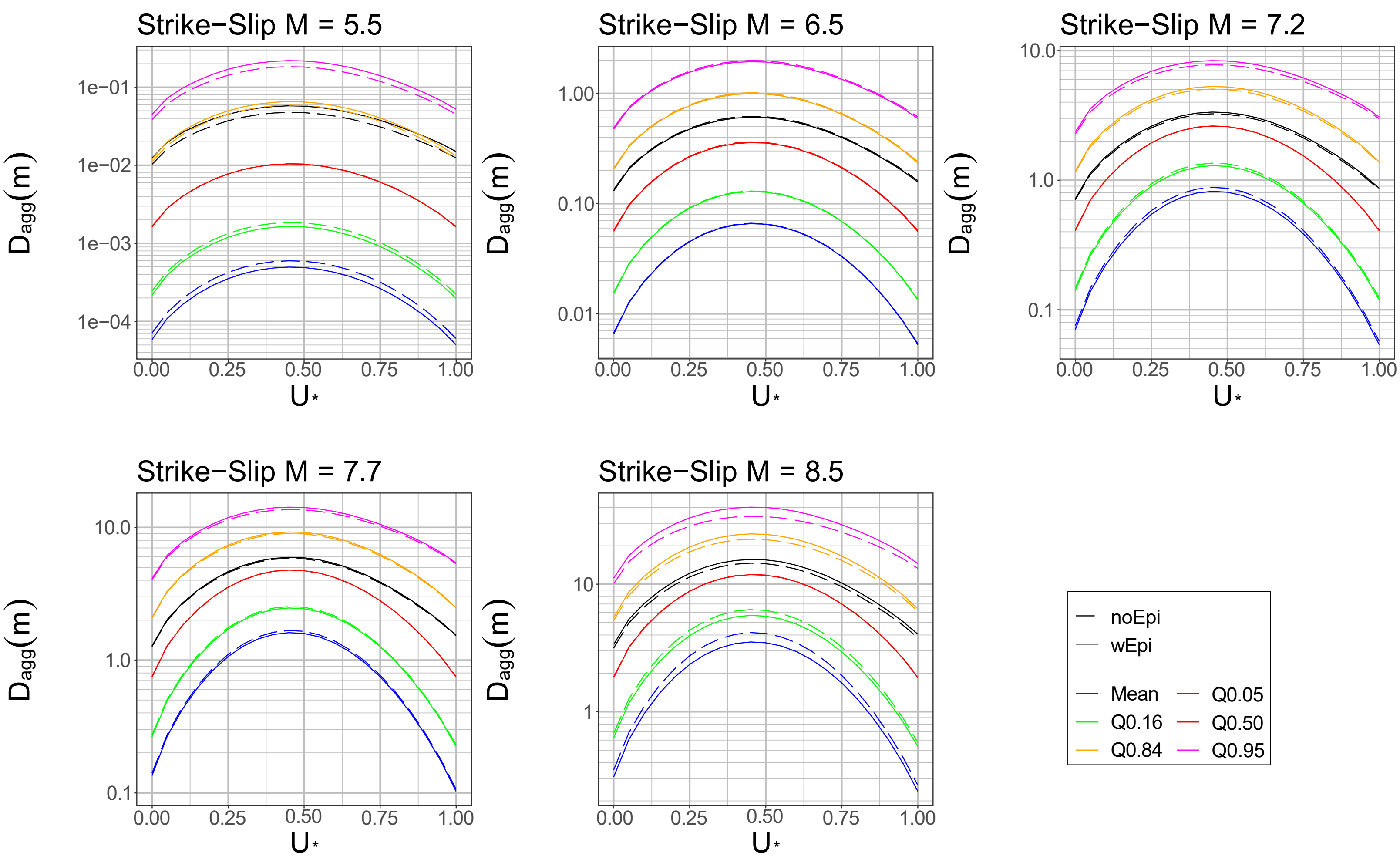

Figure 6.6. Predicted aggregated displacements (D_{agg}) as a functon of normalized positon along rupture (U_*) for strike-slip events for various earthquake magnitudes. Mean displacement and 5th, 16th, 50th, 84th, and 95th fractles are shown.

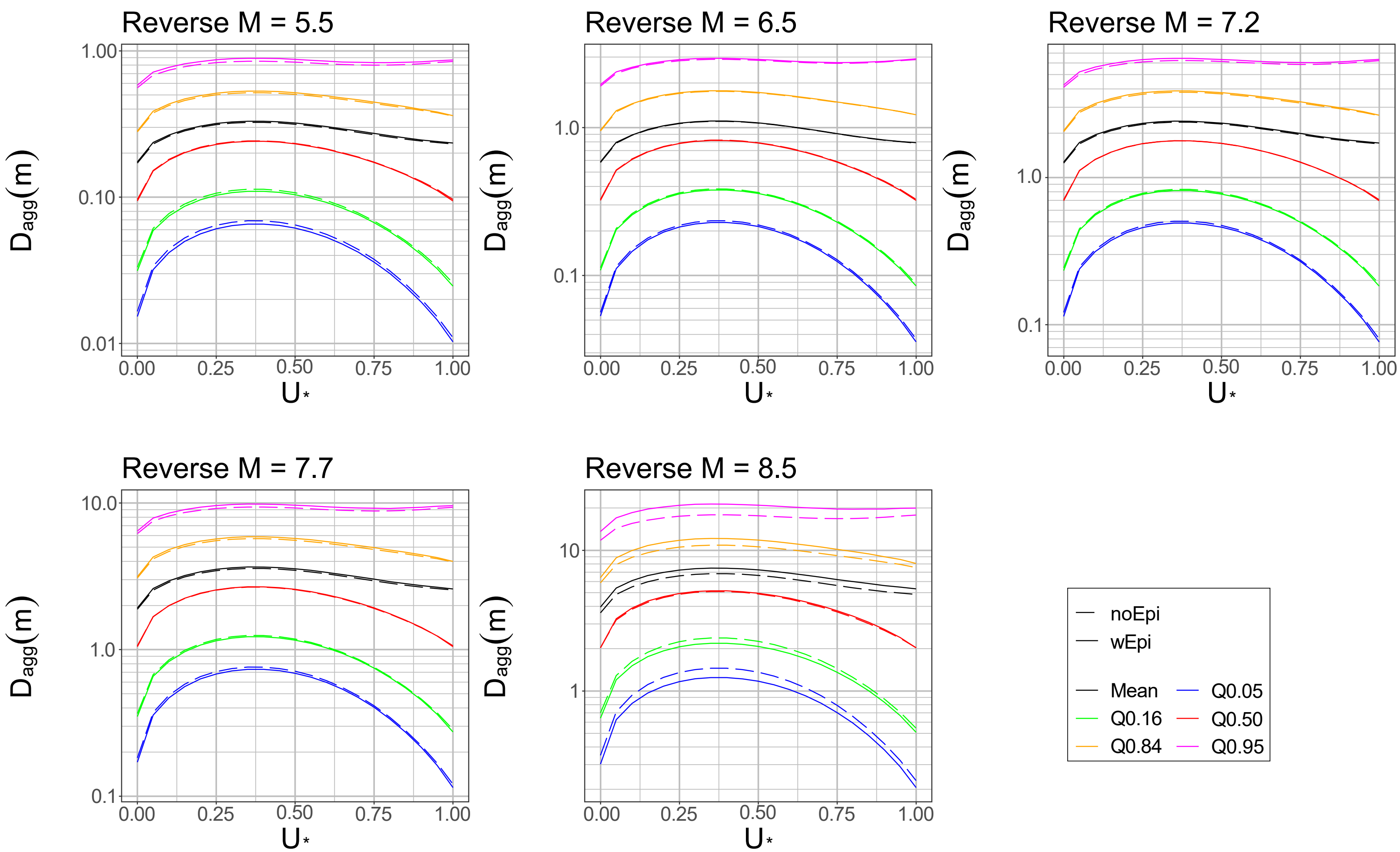

Figure 6.7. Predicted aggregated displacements (D_{agg}) as a functon of normalized positon along rupture (U_*) for reverse events for various earthquake magnitudes. Mean displacement and 5th, 16th, 50th, 84th, and 95th fractles are shown.

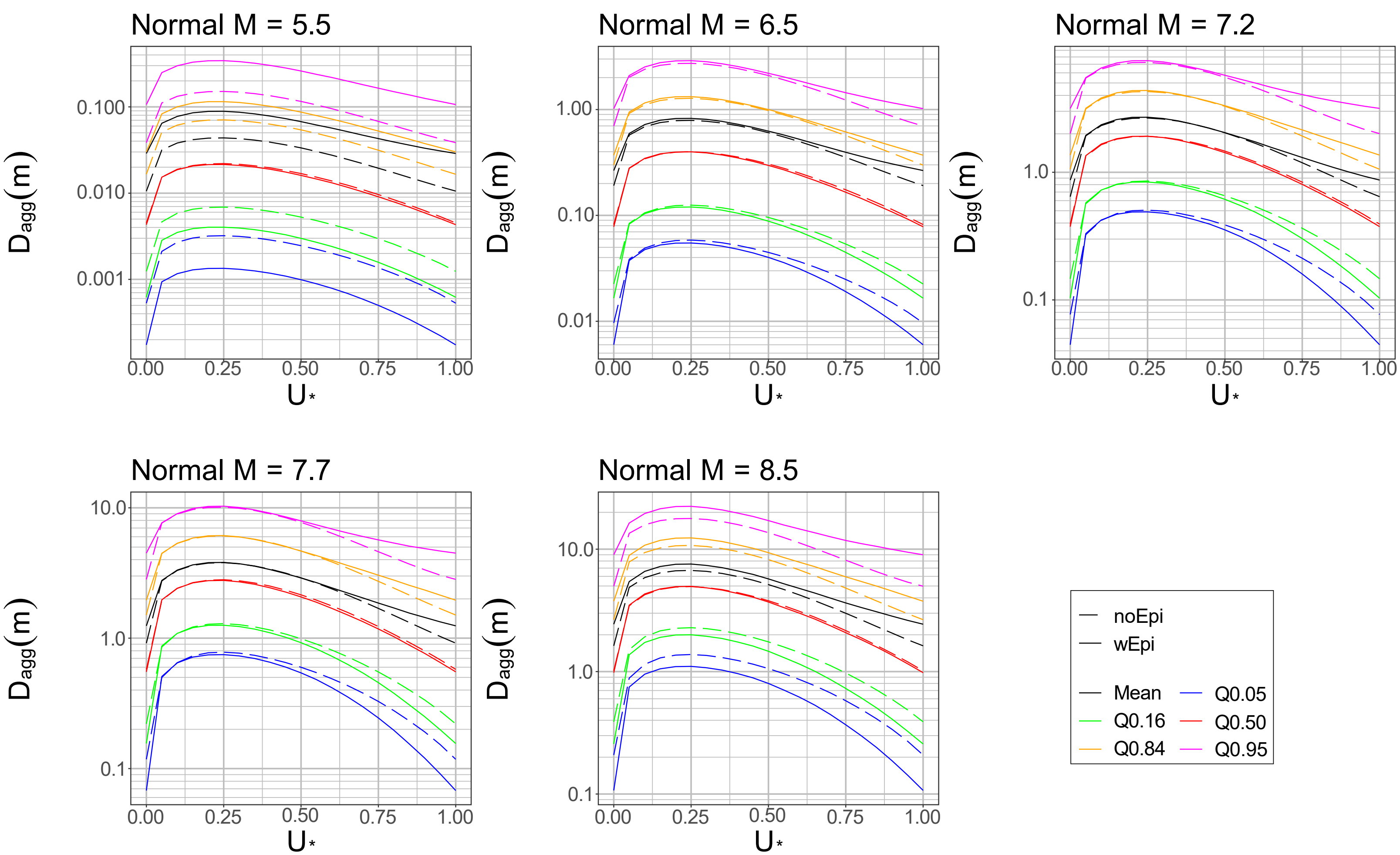

Figure 6.8. Predicted aggregated displacements (D_{agg}) as a functon of normalized positon along rupture (U_*) for normal events for various earthquake magnitudes. Mean displacement and 5th, 16th, 50th, 84th, and 95th fractles are shown.

7 COMPARISONS TO EXISTING MODELS

Several fault displacement models are currently used in standard practce. In this Chapter, we compare results between our new model and a subset of the available models in Table 3.1. Specifically, our comparison includes models by Petersen et al. (2011), Moss and Ross (2011), and Youngs et al. (2003) because these models incorporate displacement variability along the rupture length (i.e., locaton scaling) and are therefore more comparable to our new model. The comparisons are made for a set of deterministc cases by calculatng predicted displacement means and fractles.

The suite of deterministc cases evaluated herein considered all styles of faultng and representatve ranges of earthquake magnitudes, normalized locatons along the rupture, and percentles of the predicted displacement distributons (Table 7.1). The comparisons and related discussions are separated in this Chapter based on style of faultng because the existng models were developed for specific styles, and the our new model also style-dependent. The magnitude range was selected to capture events roughly corresponding to the hazard levels of interest for engineering design and analysis in actve tectonic setngs like California (e.g., **M** $\sim$6.5 and $\sim$7.2 events are ofen high contributors to PGA hazard deaggregatons for ASCE 7-16 design and MCE_R level response spectra, respectvely), as well as events at and beyond the data limits (e.g., **M** 5.5 and 8.5). The selected normalized positons along rupture are adequate to reconstruct profile shapes for comparisons of peak amplitudes and locatons, as well as the displacement decay at rupture ends. Finally, the displacement distributons evaluated for the deterministc cases capture the mean, median, and ± 1 and ± 1.6 standard deviatons.

The compared models vary in their applicable tectonic conditons, input and predicted parameters, functonal form, and treatment of uncertainty. However, all the models consider style of faultng, earthquake magnitude (or normalized displacement as a proxy for magnitude), and relatve locaton along rupture, allowing for meaningful comparisons between our new model and existng models. Table 7.2 lists the applicable style of faultng, magnitude range, slip component, and source type for each model. Predicted parameters, input parameters, and the generalized form for each model are listed in Table 7.3.

The KEA22 results presented in this Chapter include full epistemic uncertainty and aleatory variability. Epistemic uncertainty is captured as follows (cf. Model Implementaton):

1. We used the average median value from 2,000 samples of all coefficient posterior distributons.

Table 7.1. Deterministc cases evaluated herein.

Parameter	Values
Style of faultng	Strike-Slip, Reverse, Normal
Moment magnitude	5.5, 6.5, 7.2, 7.7, 8.5
Normalized positon along rupture	0.05, 0.15, 0.30, 0.40, 0.50, 0.60, 0.70, 0.85, 0.95
Predicted displacement	Mean, fractles: 5th, 16th, 50th, 84th, 95th

2. We computed the variance of the 2,000 median values (σ^2_{med}) and added it to the total model variance (e.g., $\sigma^2_T = \sigma^2_u + \sigma^2_m + \sigma^2_{Y,med} + \sigma^2_{med}$).

3. We equally weighted the results for complementary rupture positons (e.g., U_* = 0.3 and 0.7) because the asymmetry cannot be predicted *a priori*.

Aleatory variability is captured with the standard deviatons for magnitude scaling (σ_m) and locaton scaling (σ and σ_Y).

The existng models handle epistemic uncertainty and aleatory variability differently, as discussed below.

Table 7.2. Summary of applicability criteria for models.

Model	Abbreviaton	Style	Magnitude Range	Slip Component	Source Type
This Model	KEA22	Strike-Slip	6.0– 8.0[(1)]	Net	Aggregated
		Reverse	5.0– 8.0[(1)]		
		Normal	6.0– 8.0[(1)]		
Petersen et al. (2011)	PEA11	Strike-Slip	Not reported	Lateral	Principal
Moss and Ross (2011)	MR11	Reverse	5.5 – 8.0	Vertcal	Principal
Youngs et al. (2003)	YEA03	Normal	Not reported	Vertcal	Principal

[(1)] Recommended range based on data; may be extrapolated to smaller or larger magnitudes, but between event variability σ_m is larger at small magnitudes (cf. Figure 6.5 and Standard Deviaton Models), and epistemic uncertainty in magnitude scaling coefficients should be included (cf. Figure 6.4 and Within-Model Epistemic Uncertainty).

Table 7.3. Summary of model parameters.

Parameter	This Model	PEA11	MR11	YEA03
Predicted displacement (D) variable	$D_{agg} = f(\mathbf{M}, U_*)$	$D = f(m, l/L)$ or $D/D_{ave} = f(l/L)$	$D/AD = f(x/L)$ or $D/MD = f(x/L)$	$D/AD = f(x/L)$ or $D/MD = f(x/L)$
Moment magnitude	$\mathbf{M}$	m [(1)]	–	–
Normalized positon along rupture, range	U_* [0, 1]	l/L [0, 0.5]	x/L [0, 0.5]	x/L [0, 0.5]
Average displacement	–	D_{ave} [(1)]	AD [(2)]	AD [(2)]
Maximum displacement	–	–	MD [(2)]	MD [(2)]

[(1)] Optonal, models with and without normalizaton provided
[(2)] Model requires normalizaton by average or maximum displacement

7.1 STRIKE-SLIP MODELS

Petersen et al. (2011), denoted as PEA11 herein, present a complete methodology to calculate probabilistc fault displacement for principal and distributed displacements on strike-slip fault systems. Our comparison here focuses on their predictons for principal lateral fault displacement amplitude, D, which they model as a lognormal distributon.

PEA11 provide three alternatve locaton scaling models to provide within-model epistemic uncertainty on the along-strike displacement variability. All regressions are conditoned on the normalized rupture length l/L, and the range is folded to the interval $[0, 0.5]$ because the rupture directon is not known *a priori*. All three locaton scaling models were evaluated: (i) a bilinear profile with constant displacement at the center of the rupture and strong displacement decay at the rupture ends, (ii) an elliptcal profile with peak displacement at the center of the rupture, and (iii) a quadratc profile with peak displacement offset from the center of the rupture. For brevity, we only show the results from the elliptcal model.

PEA11 also provide two magnitude scaling models. The models conditoned on either: (i) the earthquake magnitude, m, or (ii) the average displacement, D_{ave}. In developing their regressions directly conditoned on magnitude, they used the strike-slip D_{ave} magnitude – average displacement relatonship from Wells and Coppersmith (1994). Therefore, the two regressions provide the same result if the Wells and Coppersmith (1994) $\log_{10}(\mathrm{D}_{ave})$ regression is used to obtain D_{ave}. The PEA11 results shown herein used the first formulaton with direct dependence on magnitude (i.e., without normalizaton).

The PEA11 model does not capture epistemic uncertainty in magnitude scaling, and our implementaton here only uses the elliptcal model and therefore does not include epistemic uncertainty in locaton scaling. The standard deviaton provided in PEA11 is a total standard deviaton, but it can be readily separated into locaton and magnitude scaling components using the Wells and Coppersmith (1994) $\log_{10}(\mathrm{D}_{ave})$ standard deviaton.

The following discussion focuses on median magnitude scaling comparisons and model predictons for various magnitudes and normalized rupture positons. Plots for mean predictons and a range of fractles are provided for completeness but are not discussed for brevity. Results from the PEA11 bilinear and quadratc models were also compared but are not included for brevity. The results from the bilinear and quadratc models are sufficiently similar to the elliptcal model for the purposes of this comparison, and our general conclusions are applicable to all of the PEA11 locaton scaling models.

Figure 7.1 compares the magnitude scaling functons used in our model and the PEA11 elliptcal model. The results are shown for the rupture ends and midpoint for various fractles. In general, our new model produces lower median displacements at the rupture midpoint for magnitudes **M** $\lesssim 6.6$, higher median displacements for $6.6 \lesssim$ **M** $\gtrsim 8.1$, and similar displacements at larger magnitudes. Our mean predictons for the rupture midpoint are similar for $6.7 \lesssim$ **M** $\gtrsim 7.4$ and lower otherwise.

Figures 7.2 through 7.6 compare the predictons from our model with the PEA11 elliptcal model for a range of magnitudes, various normalized positons along the rupture length (x/L), and various fractles. Differences in our median model predictons, relatve to the PEA11 model, are mainly due to our inclusion of a magnitude break-point (e.g., Figure 7.1) and are most apparent at smaller and larger magnitudes. At smaller magnitudes (**M** $\lesssim 6$), our median predictons are lower by roughly a factor of 5. Our median predictons for **M** ± 6.5 magnitude earthquakes are in good agreement with the PEA11 model, producing values with a factor of 1.5 or beter. For larger earthquake magnitudes (**M** $\sim$ 7 to $\sim$ 8), our median predictons are higher by a factor of roughly 1.5 to 3. Finally, for **M** 8.5, our median predictons are with a factor of 1.5 of the PEA11 values.

In general, the predictons from our new model compare well with the PEA11 model. We use a different magnitude scaling functon (Figure 7.1), which causes most of key the differences in the predicted displacements. Our magnitude scaling model is bilinear with a smooth hinge at (**M** 7), whereas the PEA11 model uses a log-linear magnitude scaling functon from Wells and Coppersmith (1994). We note that the updated version of the PEA11 model, developed through the FDHI project, also applies a bilinear magnitude scaling model. (It is noted that because PEA11 provides users with a functonal form conditoned on the average displacement, other magnitude scaling functons could be used.) Our predictons are generally within a factor of 3 of the PEA11 elliptcal model for the mean and 5th through 95th fractles, and most magnitudes and rupture positons are within a factor 2 or beter. However, significant differences are observed for small magnitudes (**M** $\lesssim 6$), where our predictons are lower due to our bilinear magnitude scaling model.

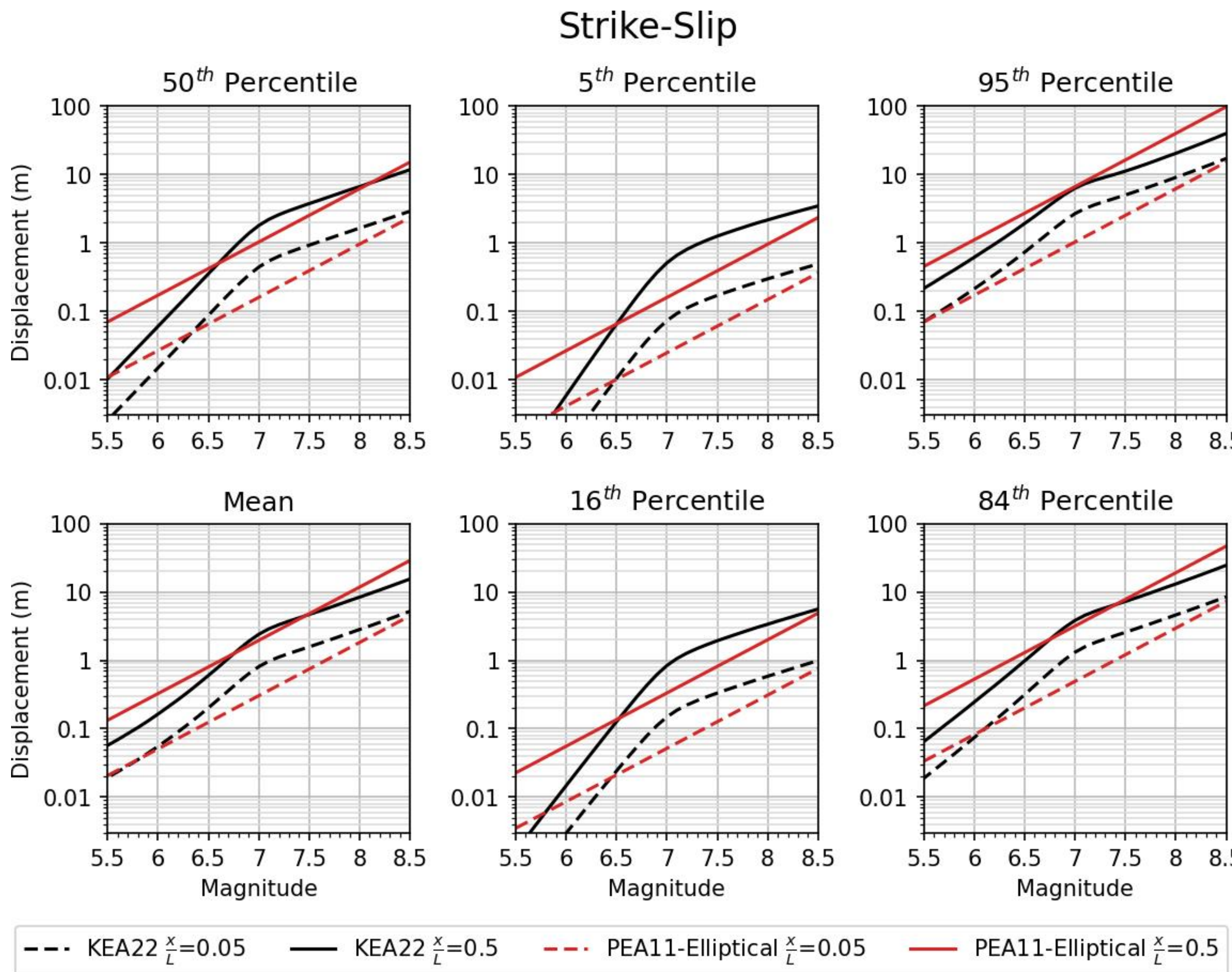

Figure 7.1. Comparison of magnitude scaling models for strike-slip events near end of rupture ($x/L = 0.05$) and midpoint ($x/L = 0.5$) at various fractles. "PEA11" in legend is Petersen et al. (2011). We thank Dr. Rui Chen for calculatng the "PEA11" displacements shown here.

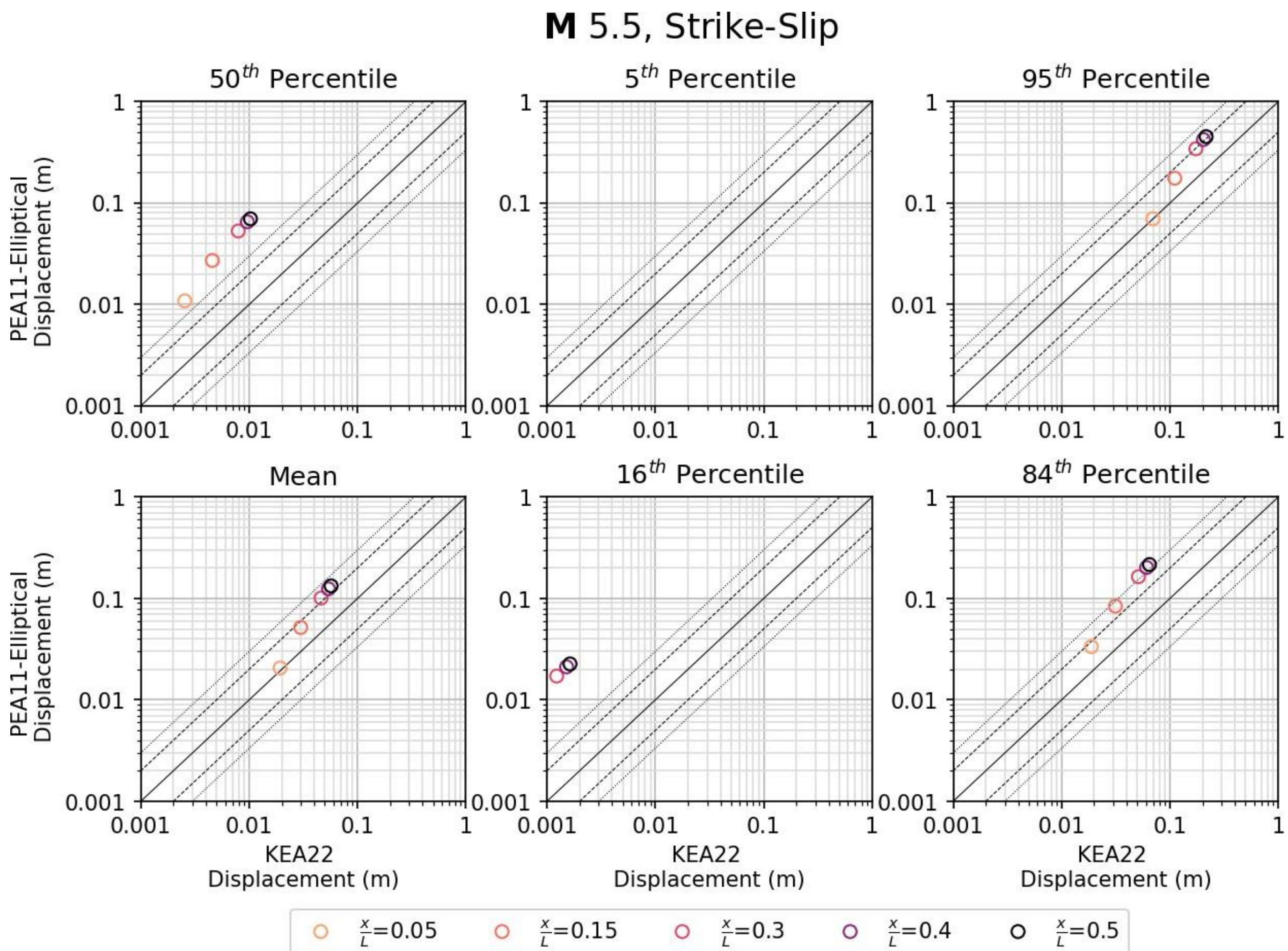

Figure 7.2. Comparison of predicted displacements fractles for various normalized positons along rupture, x/L, for **M** 5.5 strike-slip earthquakes. Note that KEA22 5 predictons for 5th percentile are less than 0.001 m. Solid line is identty (1:1) line; dashed lines are factor of two; doted lines are factor of three. "PEA11" is Petersen et al. (2011) model. We thank Dr. Rui Chen for calculatng the "PEA11" displacements shown here.

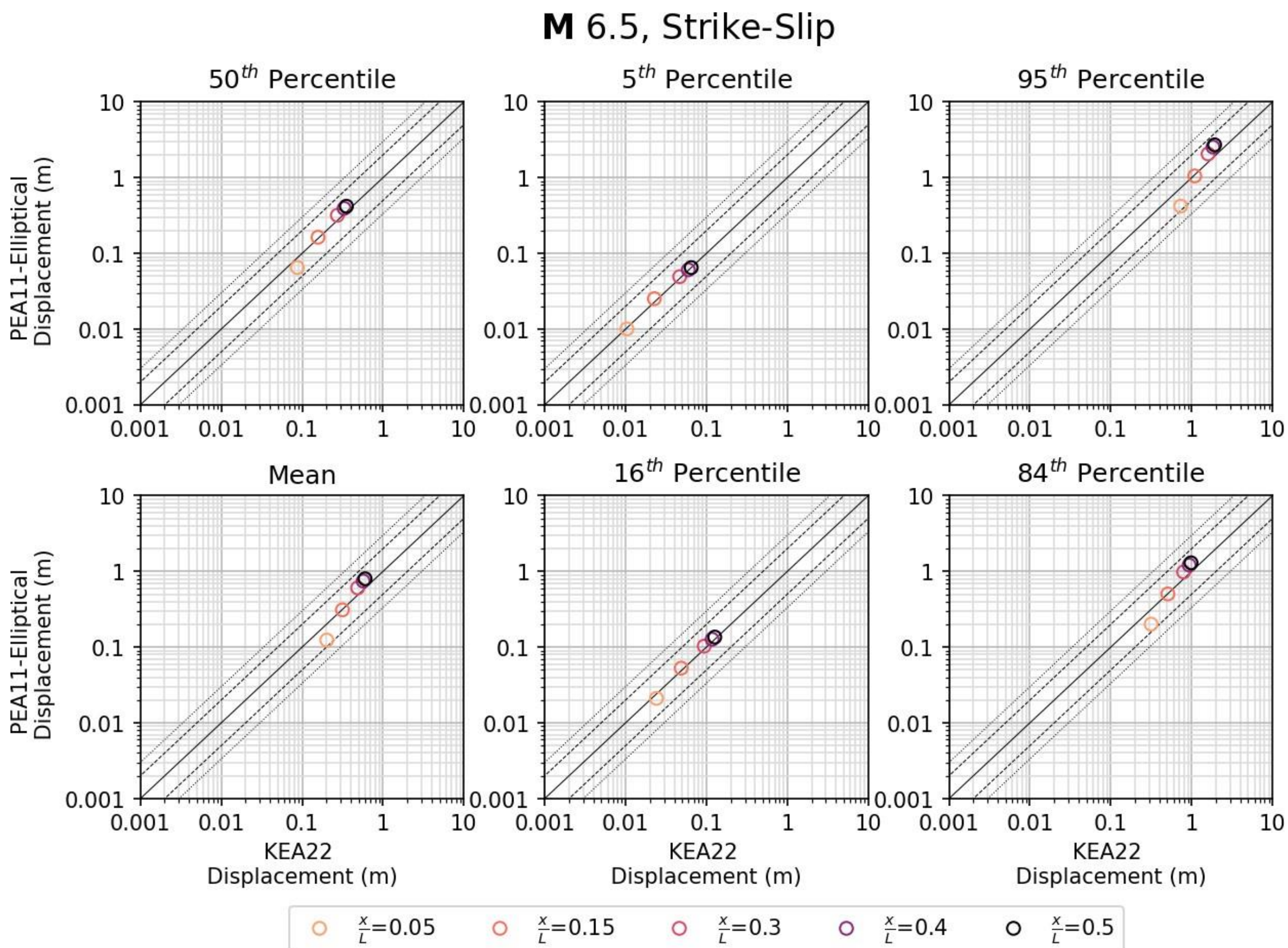

Figure 7.3. Comparison of predicted displacements fractles for various normalized positons along rupture, x/L, for **M** 6.5 strike-slip earthquakes. Solid line is identty (1:1) line; dashed lines are factor of two; doted lines are factor of three. “PEA11” is Petersen et al. (2011) model. We thank Dr. Rui Chen for calculatng the “PEA11” displacements shown here.

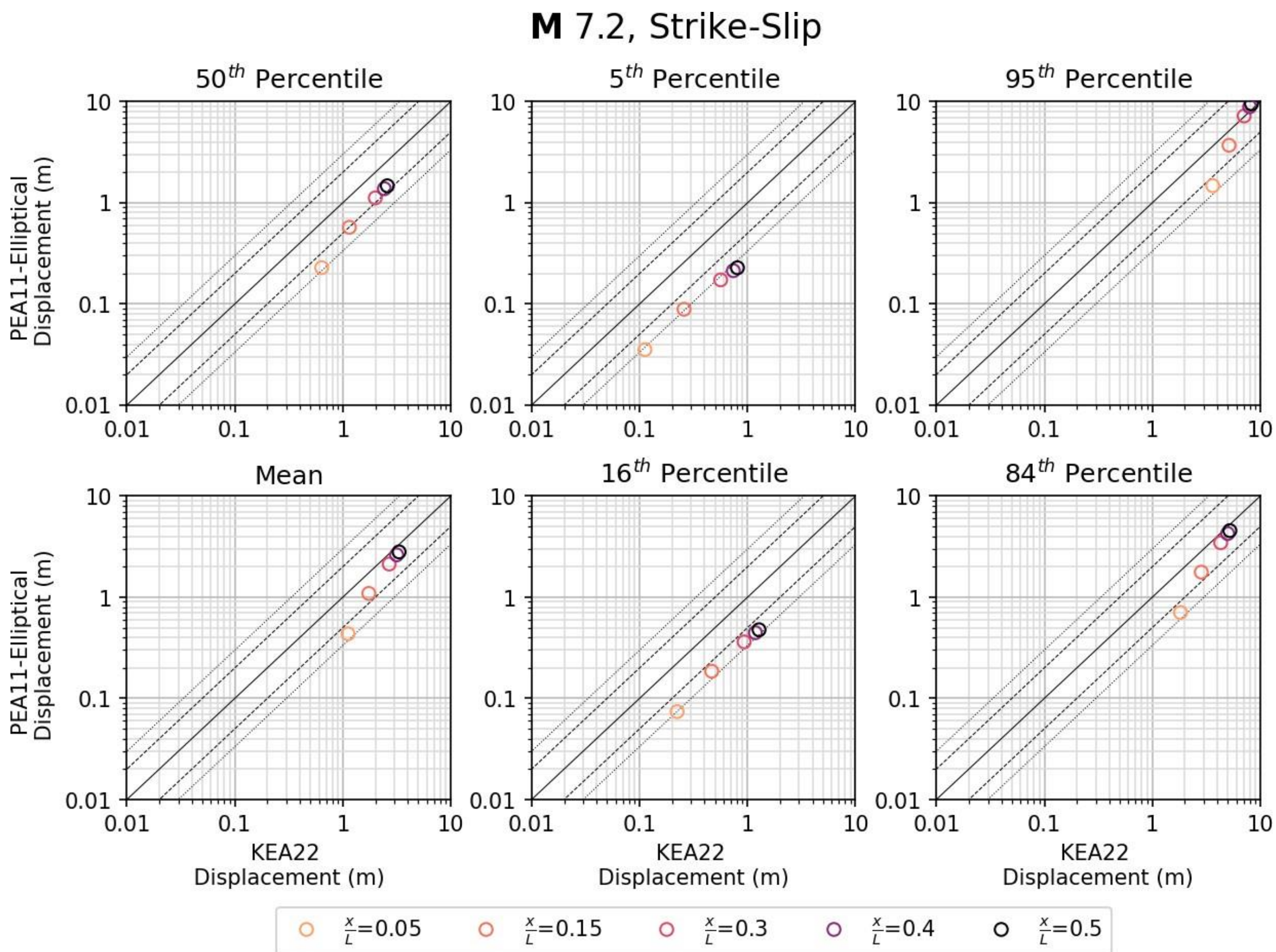

Figure 7.4. Comparison of predicted displacements fractles for various normalized positons along rupture, x/L, for **M** 7.2 strike-slip earthquakes. Solid line is identty (1:1) line; dashed lines are factor of two; doted lines are factor of three. “PEA11” is Petersen et al. (2011) model. We thank Dr. Rui Chen for calculatng the “PEA11” displacements shown here.

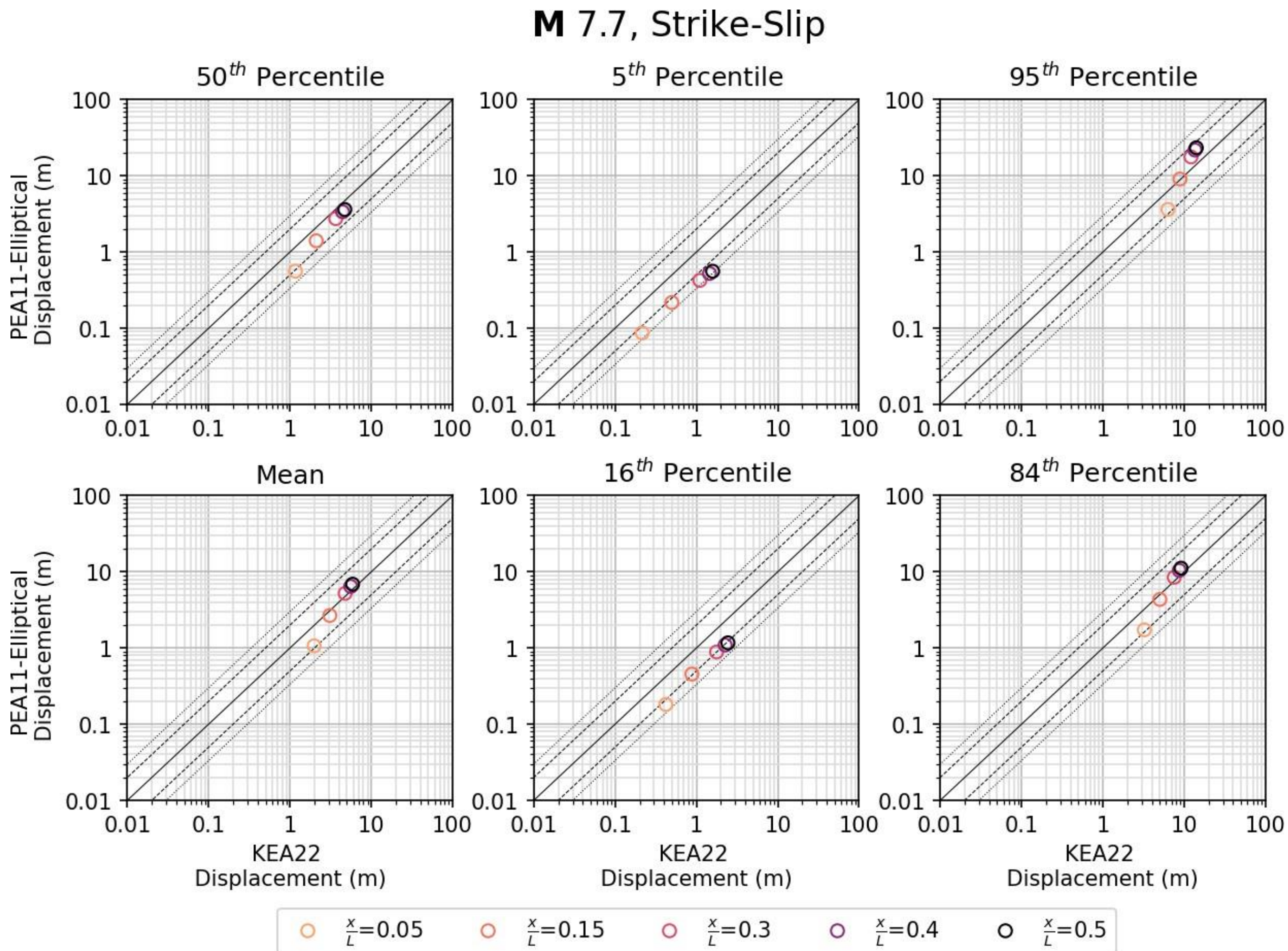

Figure 7.5. Comparison of predicted displacements fractles for various normalized positons along rupture, x/L, for **M** 7.2 strike-slip earthquakes. Solid line is identty (1:1) line; dashed lines are factor of two; doted lines are factor of three. “PEA11” is Petersen et al. (2011) model. We thank Dr. Rui Chen for calculatng the “PEA11” displacements shown here.

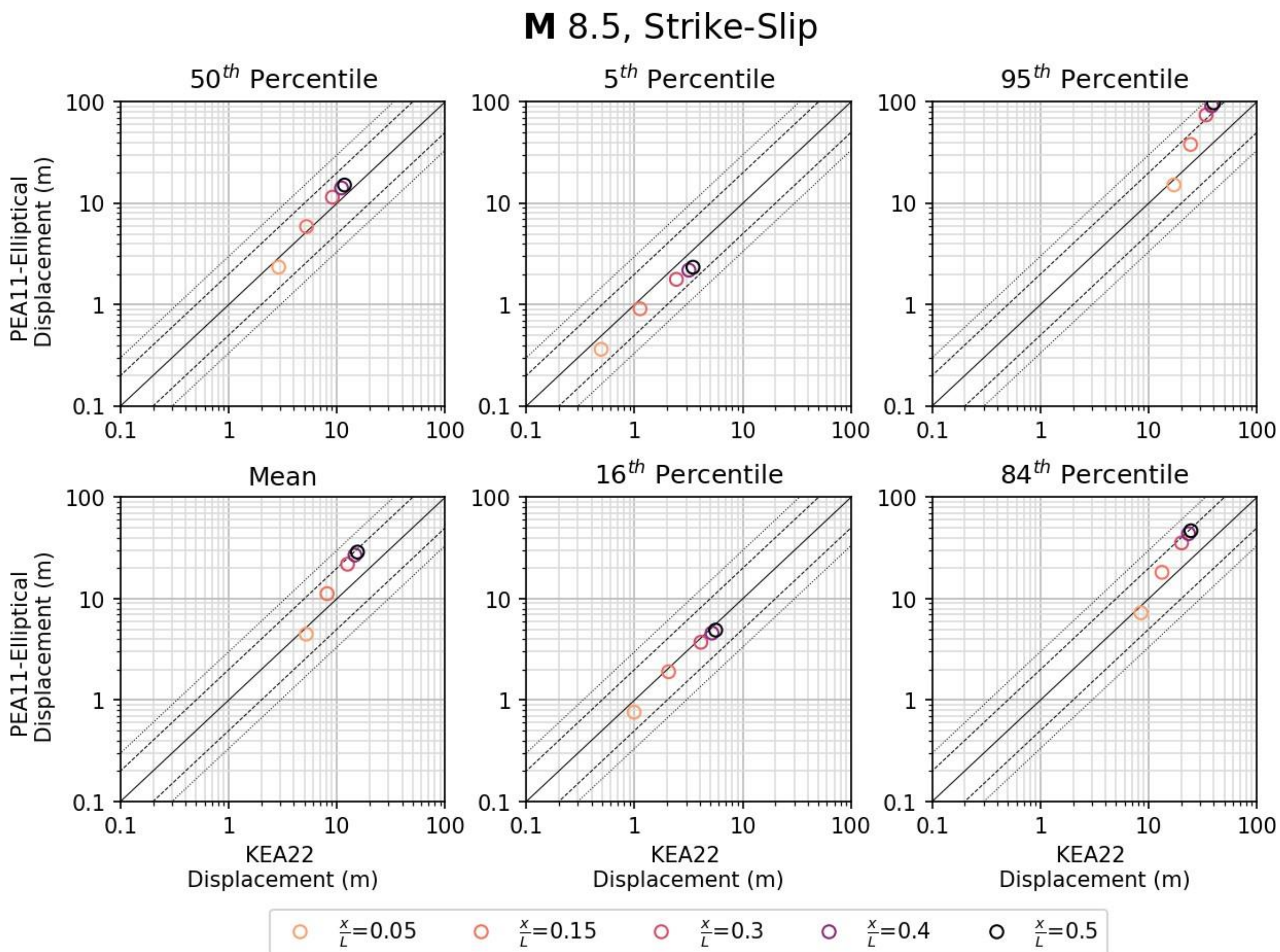

Figure 7.6. Comparison of predicted displacements fractles for various normalized positons along rupture, x/L, for **M** 7.2 strike-slip earthquakes. Solid line is identty (1:1) line; dashed lines are factor of two; doted lines are factor of three. "PEA11" is Petersen et al. (2011) model. We thank Dr. Rui Chen for calculatng the "PEA11" displacements shown here.

7.2 REVERSE MODELS

Moss and Ross (2011), denoted as MR11 herein, provides a complete methodology to calculate probabilistc fault displacement for principal displacements on reverse fault systems. Our comparison here focuses on their predictons for principal vertcal fault displacement, D.

MR11 provide three alternatve locaton scaling models to provide within-model epistemic uncertainty on the along-strike displacement variability: (i) conditoned on the average displacement, AD, using a Weibull distributon, (ii) conditoned on the average displacement, AD, using a Gamma distributon, and (iii) conditoned on the maximum displacement, MD, using a Beta distributon. All regressions are conditoned on the normalized rupture length x/L, and the range is folded to the interval $[0, 0.5]$ because the rupture directon is not known *a priori*. The model conditoned on maximum displacement was used for the comparisons here for two reasons. First, Dr. Robb Moss noted this was his preferred model. Second, the use of maximum displacement, rather than average displacement, is more consistent with our magnitude scaling model.

MR11 also provide recommended magnitude scaling models for the average and maximum displacement conditons. Both models are updated versions of the log-linear magnitude – displacement regressions in Wells and Coppersmith (1994). The maximum displacement values used in these comparisons were calculated using the updated regression in MR11.

The MR11 model does not directly capture epistemic uncertainty in magnitude nor locaton scaling, but different implementatons can capture such uncertaintes. Here, our comparisons do not include epistemic uncertainty. The range implied by the Gamma distributon is the aleatory variability in the locaton. Based on discussions with Dr. Robb Moss, multplying the D/MD Gamma distributon with the MD lognormal distributon results in a distributon that approaches lognormal. He provided us with a standard deviaton that was first transformed to approximate a normal distributon and then converted to lognormal. This standard deviaton represents the aleatory variability in the locaton scaling. We also included the standard deviaton in the MR11 maximum displacement model in our comparisons here..

Figure 7.7 compares the magnitude scaling functons used in our model and the MR11 model. The results are shown for the rupture ends and midpoint for various fractles. Our new model produces nearly identcal median displacements at magnitudes **M** $\lesssim 7.2$. Our predicted median displacements are less at larger magnitudes due to our inclusion of a magnitude break-point at **M** 7.

Figures 7.8 through 7.11 compare the predictons from our model with the MR11 model for a range of magnitudes, various normalized positons along the rupture length (x/L), and various fractles. Our median predictons are generally within a factor of 0.5 or beter of the MR11 model for all magnitudes and rupture positons considered. It is noted that comparisons for **M** 8.5 events are not available because it is outside the recommended range of the MR11 model (Table 7.2). Our mean predictons are systematcally lower by roughly a factor of 2 of the MR11 predictons. For the lower fractles, our predictons are also systematcally higher but within a factor of 2 (16^{th}) or 3 (5^{th}) for all magnitudes and rupture positons. Finally, our predicton displacements for higher fractles (84^{th} and 95^{th}) are lower but within a factor of about 2.5.

In general, the predictons from our new model compare very well with the MR11 model. There are two key reasons for the similarites. First, although we use a bilinear magnitude scaling model with a smooth hinge at (**M** 7) and MR11 uses log-linear magnitude scaling functon, we found the magnitude scaling for reverse events to be close to log-linear. Second, MR11 did not incorporate magnitude-dependent variability, and we also found the between-event variability (σ_m) for reverse earthquakes to be independent of magnitude (cf. Figure 6.5). As a result, both models are similar, and we infer the relatvely simple magnitude scaling model with a constant standard deviaton is less sensitve to new data.

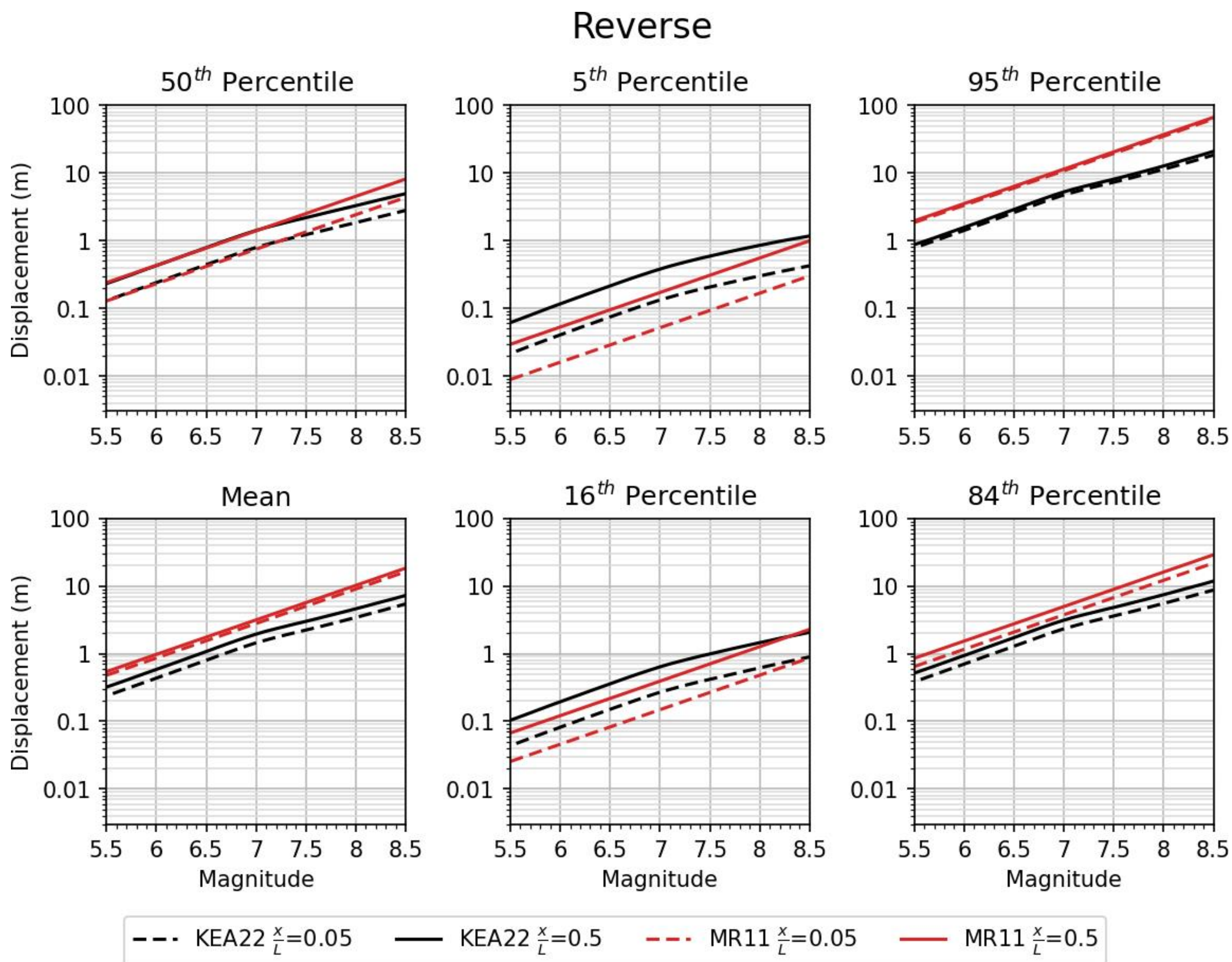

Figure 7.7. Comparison of magnitude scaling models for reverse events near end of rupture ($x/L = 0.05$) and midpoint ($x/L = 0.5$) at various fractles. "MR11" in legend is Moss and Ross (2011). We thank Dr. Robb Moss for calculatng the "MR11" displacements shown here.

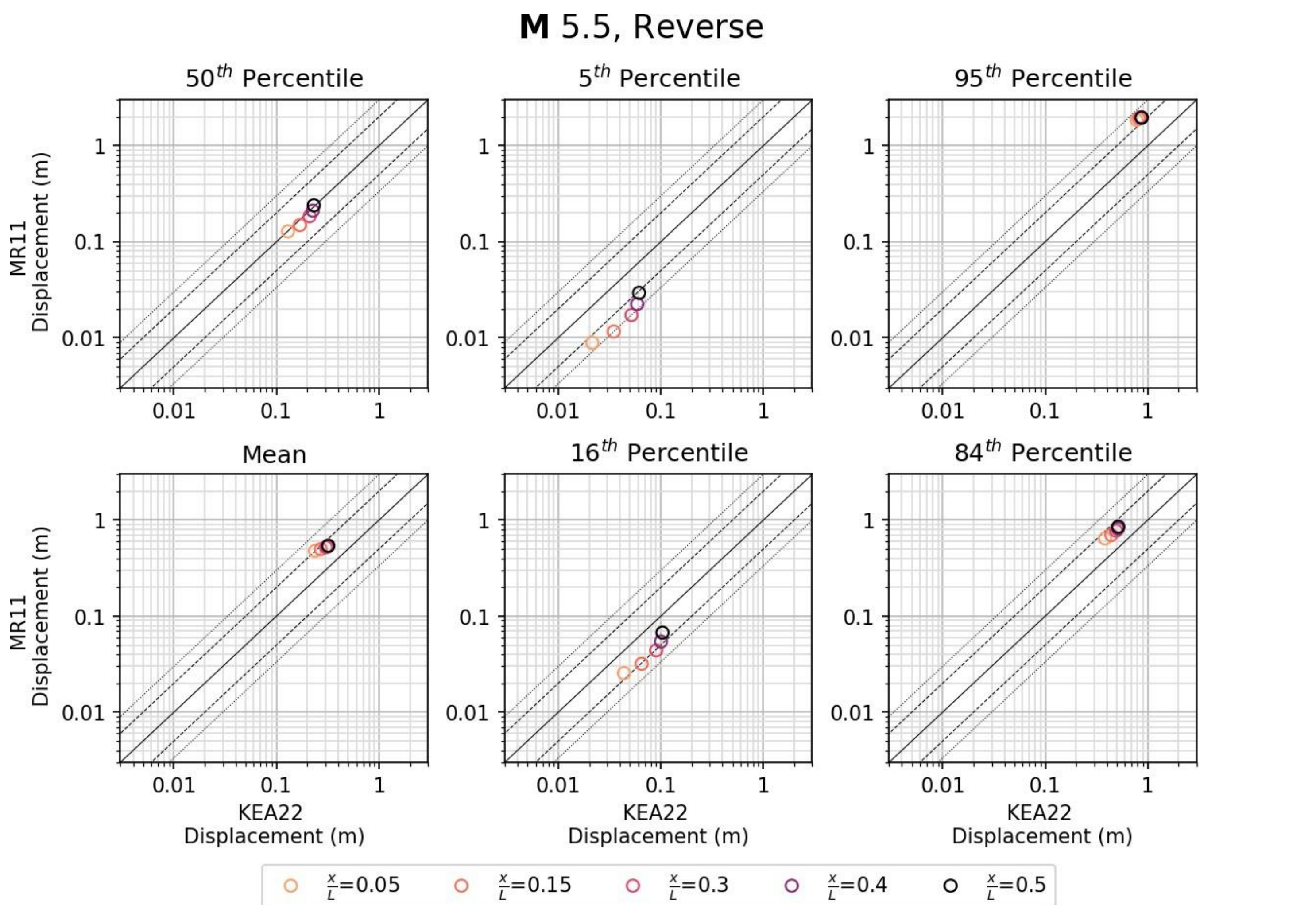

Figure 7.8. Comparison of predicted displacements fractles for various normalized positons along rupture, x/L, for **M** 5.5 reverse earthquakes. Solid line is identty (1:1) line; dashed lines are factor of two; doted lines are factor of three. “MR11” is Moss and Ross (2011). We thank Dr. Robb Moss for calculatng the “MR11” displacements shown here.

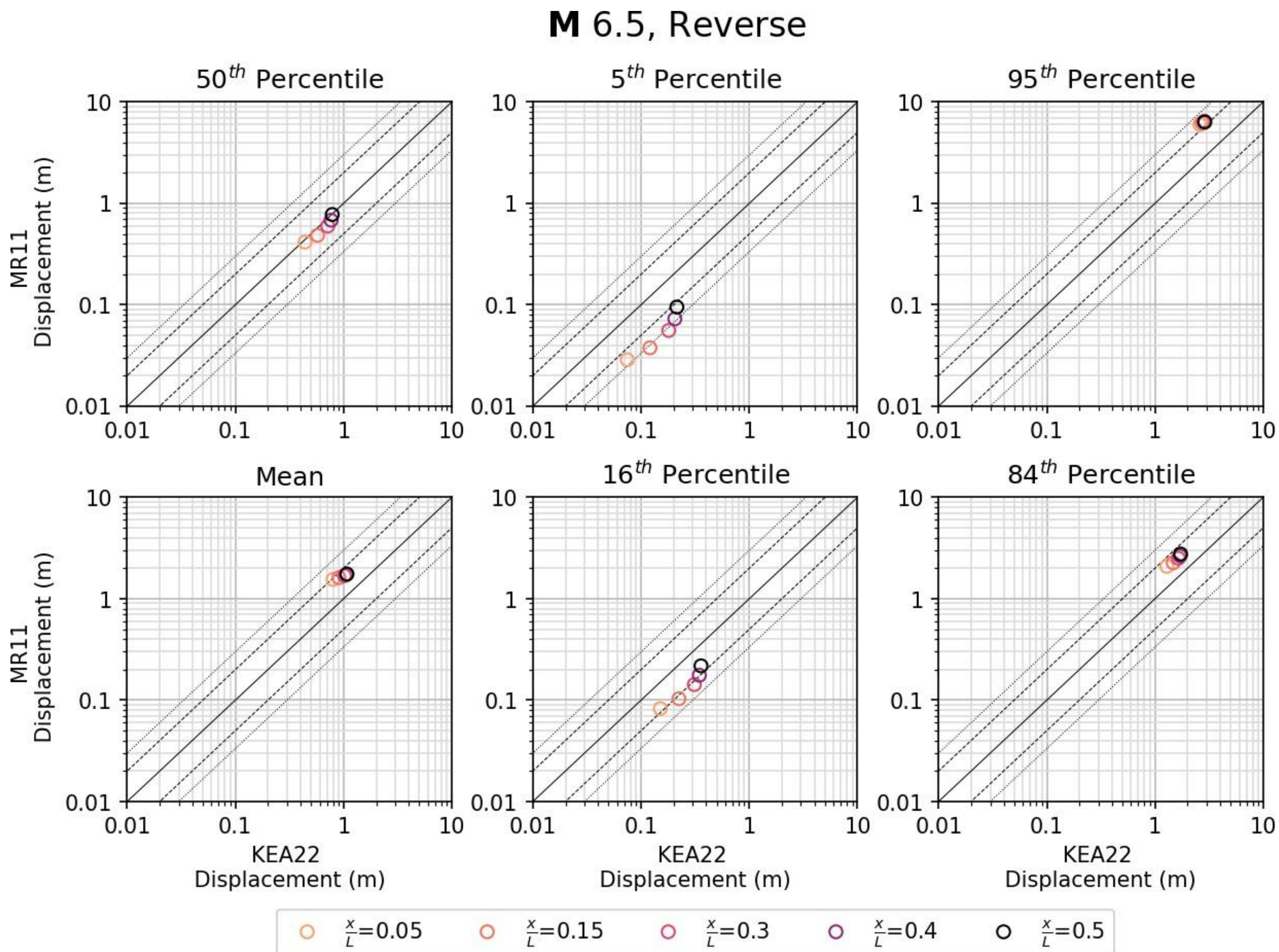

Figure 7.9. Comparison of predicted displacements fractles for various normalized positons along rupture, x/L, for **M** 7.2 reverse earthquakes. Solid line is identty (1:1) line; dashed lines are factor of two; doted lines are factor of three. "MR11" is Moss and Ross (2011). We thank Dr. Robb Moss for calculatng the "MR11" displacements shown here.

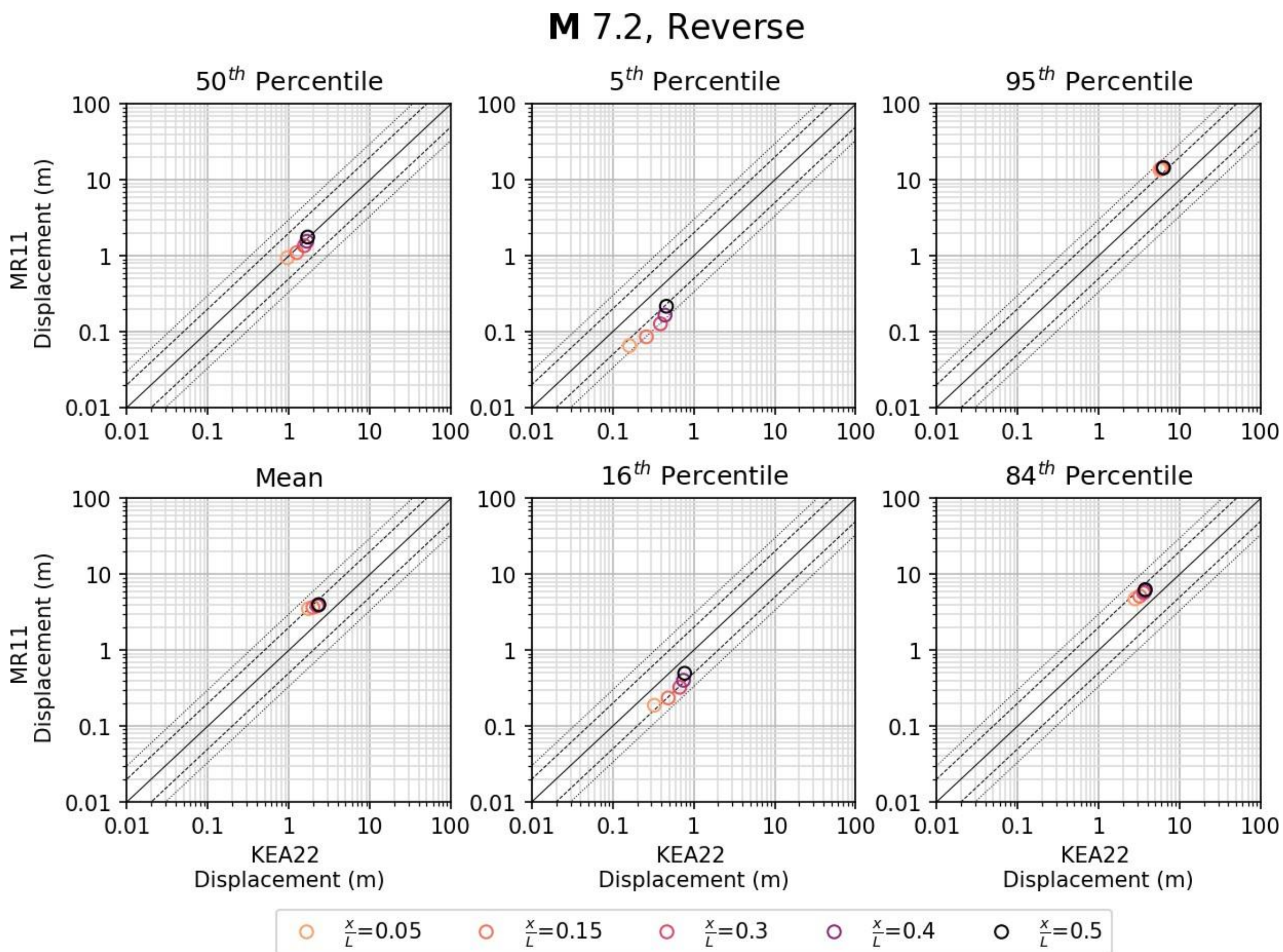

Figure 7.10. Comparison of predicted displacements fractles for various normalized positons along rupture, x/L, for **M** 7.2 reverse earthquakes. Solid line is identty (1:1) line; dashed lines are factor of two; doted lines are factor of three. “MR11” is Moss and Ross (2011). We thank Dr. Robb Moss for calculatng the “MR11” displacements shown here.

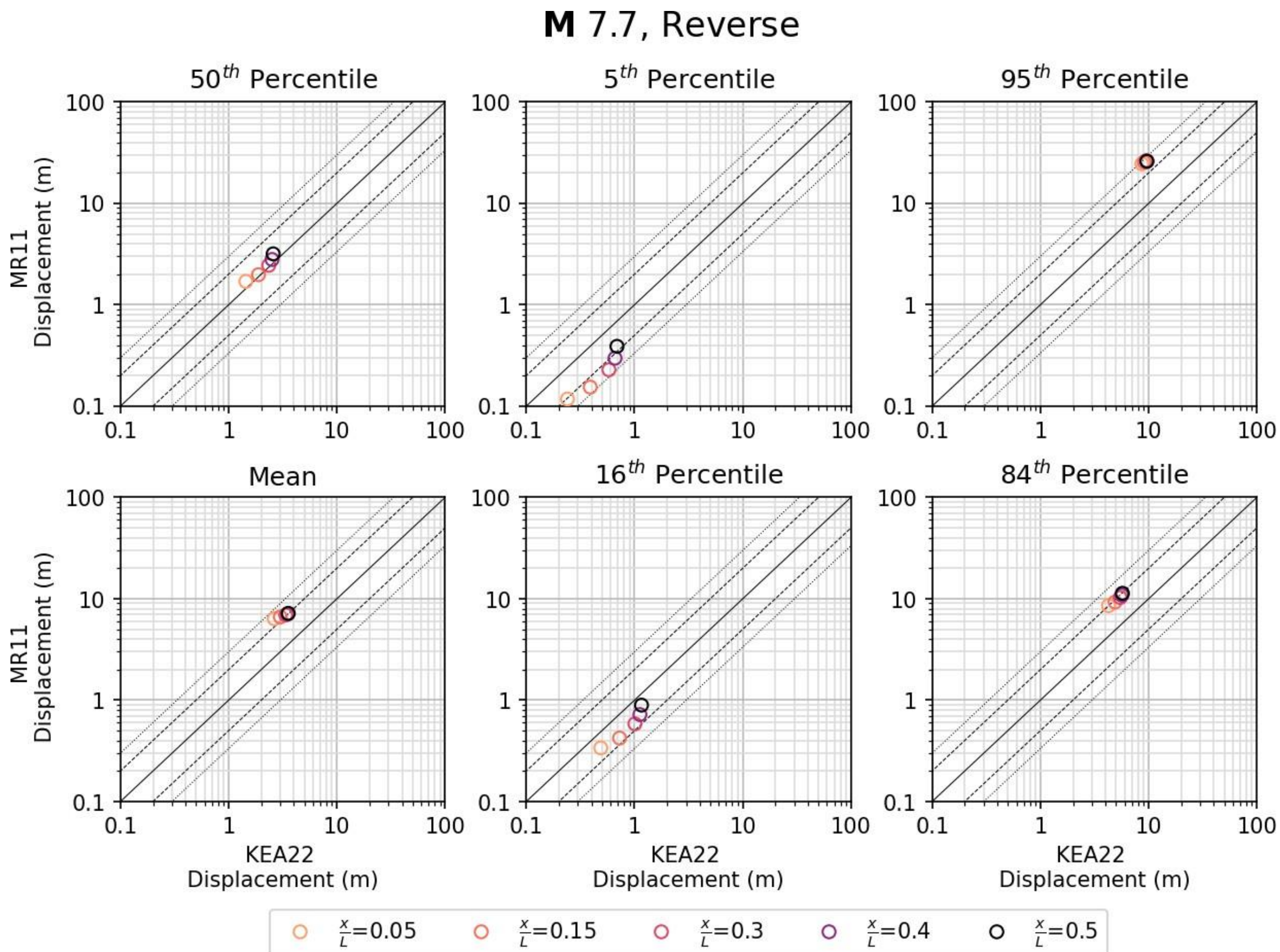

Figure 7.11. Comparison of predicted displacements fractles for various normalized positons along rupture, x/L, for **M** 7.2 reverse earthquakes. Solid line is identty (1:1) line; dashed lines are factor of two; doted lines are factor of three. “MR11” is Moss and Ross (2011). We thank Dr. Robb Moss for calculatng the “MR11” displacements shown here.

7.3 NORMAL MODELS

Youngs et al. (2003), denoted as YEA03 herein, provided the first complete methodology to calculate probabilistc fault displacement for principal and distributed displacements and is applicable to normal fault systems. Our comparison here focuses on their predictons for principal vertcal fault displacement, D.

YEA03 provide two alternatve locaton scaling models to provide within-model epistemic uncertainty on the along-strike displacement variability: (i) conditoned on the maximum displacement, MD using a Beta distributon, and (ii) conditoned on the average displacement, AD, using a Gamma distributon. All regressions are conditoned on the normalized rupture length $\mathrm{x/L}$, and the range is folded to the interval $[0,\ 0.5]$ because the rupture directon is not known *a priori*. YEA03 do not provide a magnitude scaling model; however, any appropriate average or maximum displacement model can be used. The YEA03 results shown herein used the second formulaton with direct dependence on average displacement. The average displacement was calculated using the log-linear magnitude – average displacement regression for all styles of faultng in Wells and Coppersmith (1994).

The YEA03 model does not directly capture epistemic uncertainty in magnitude nor locaton scaling, but different implementatons can capture such uncertaintes. Here, our comparisons do not include epistemic uncertainty. The range implied by the Gamma distributon is the aleatory variability in the locaton.

Figure 7.12 compares the magnitude scaling functons used in our model and the YEA03 model. The results are shown for the rupture ends and midpoint for various fractles. Our new model generally produces lower displacements at all magnitudes for the mean and 5th through 95th fractles, with the excepton of higher fractles where our model produces slightly higher displacements near the magnitude break-point.

Figures 7.13 through 7.17 compare the predictons from our model with the YEA03 model for a range of magnitudes, various normalized positons along the rupture length (x/L), and various fractles. Differences in our median model predictons, relatve to the YEA03 model, are mainly due to our inclusion of a magnitude break-point (e.g., Figure 7.12) and are most apparent at smaller and larger magnitudes. At smaller magnitudes (**M** $\lesssim 6$), our median predictons are lower by roughly a factor of 5. Our median predictons for **M**± 6.5 magnitude earthquakes are in good agreement with the PEA11 model, producing values with a factor of 1.5 or beter. For larger earthquake magnitudes (**M** $\sim$ 7 to $\sim$ 8), our median predictons are higher by a factor of roughly 1.5 to 3. Finally, for **M** 8.5, our median predictons are with a factor of 1.5 of the PEA11 values.

In general, our new model predicts smaller displacements for most of the cases evaluated on Table 7.1. We use a different magnitude scaling functon (Figure 7.12), which causes most of key the differences in the predicted displacements. Our magnitude scaling model is bilinear with a smooth hinge at (**M** 7) and based only on normal events, whereas the YEA03 model evaluated herein uses the log-linear magnitude scaling functon for all styles of faultng from Wells and Coppersmith (1994). Our predictons are generally within a factor of 3 of the YEA03 model for the mean and 5th through 95th fractles, and most magnitudes and rupture positons are within a factor 2 or beter. Significant differences are observed for small magnitudes (**M** $\lesssim 6$) and large magnitudes (**M** $\gtrsim$ 8), where our predictons are lower by roughly a factor of 10 and 3.5, respectvely, due to our bilinear magnitude scaling model.

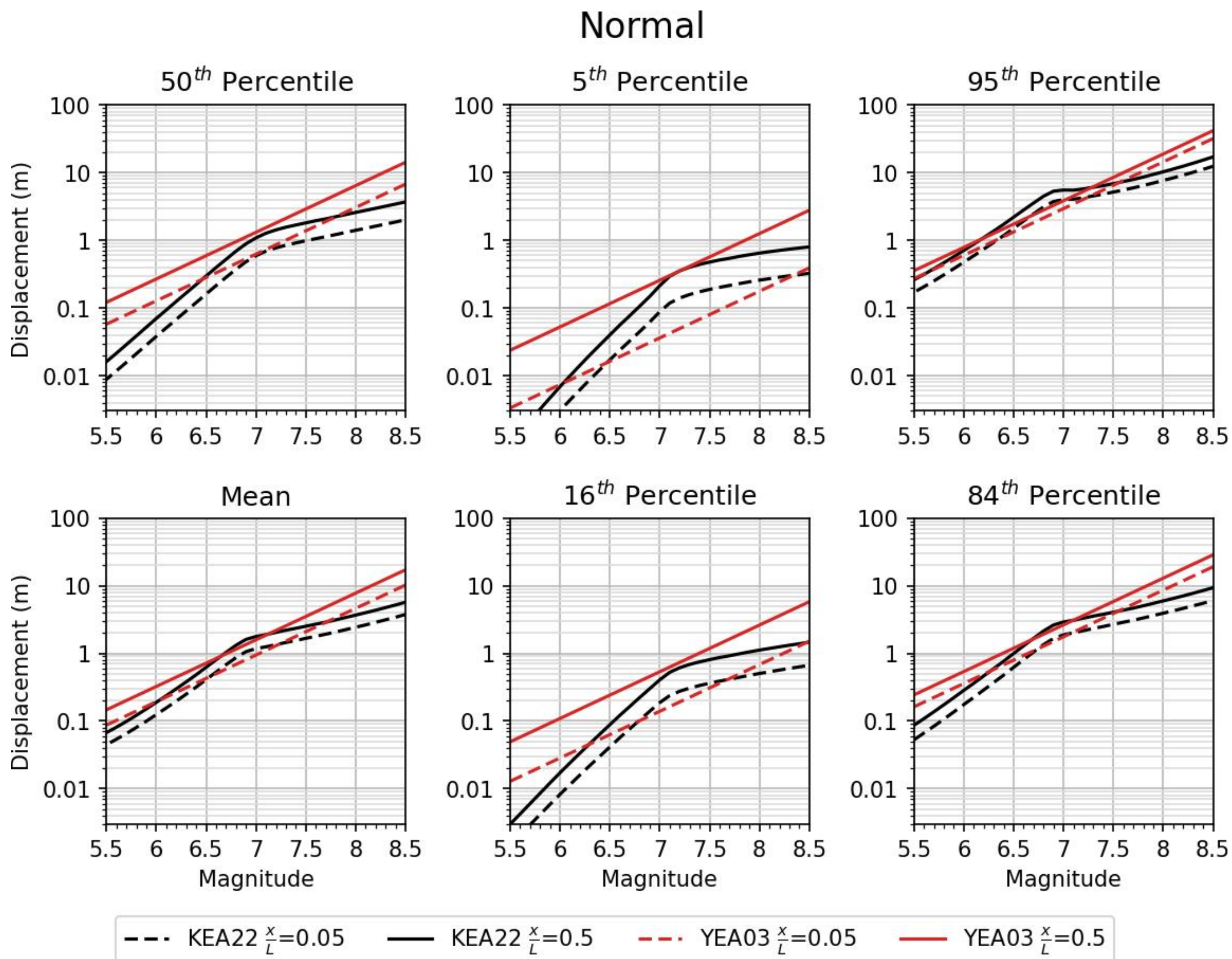

Figure 7.12. Comparison of magnitude scaling models for normal events near end of rupture ($x/L = 0.05$) and midpoint ($x/L = 0.5$) at various fractles. "YEA03" in legend is Youngs et al. (2003). We thank Dr. Grigorios Lavrentadis for calculatng the "YEA03" displacements shown here.

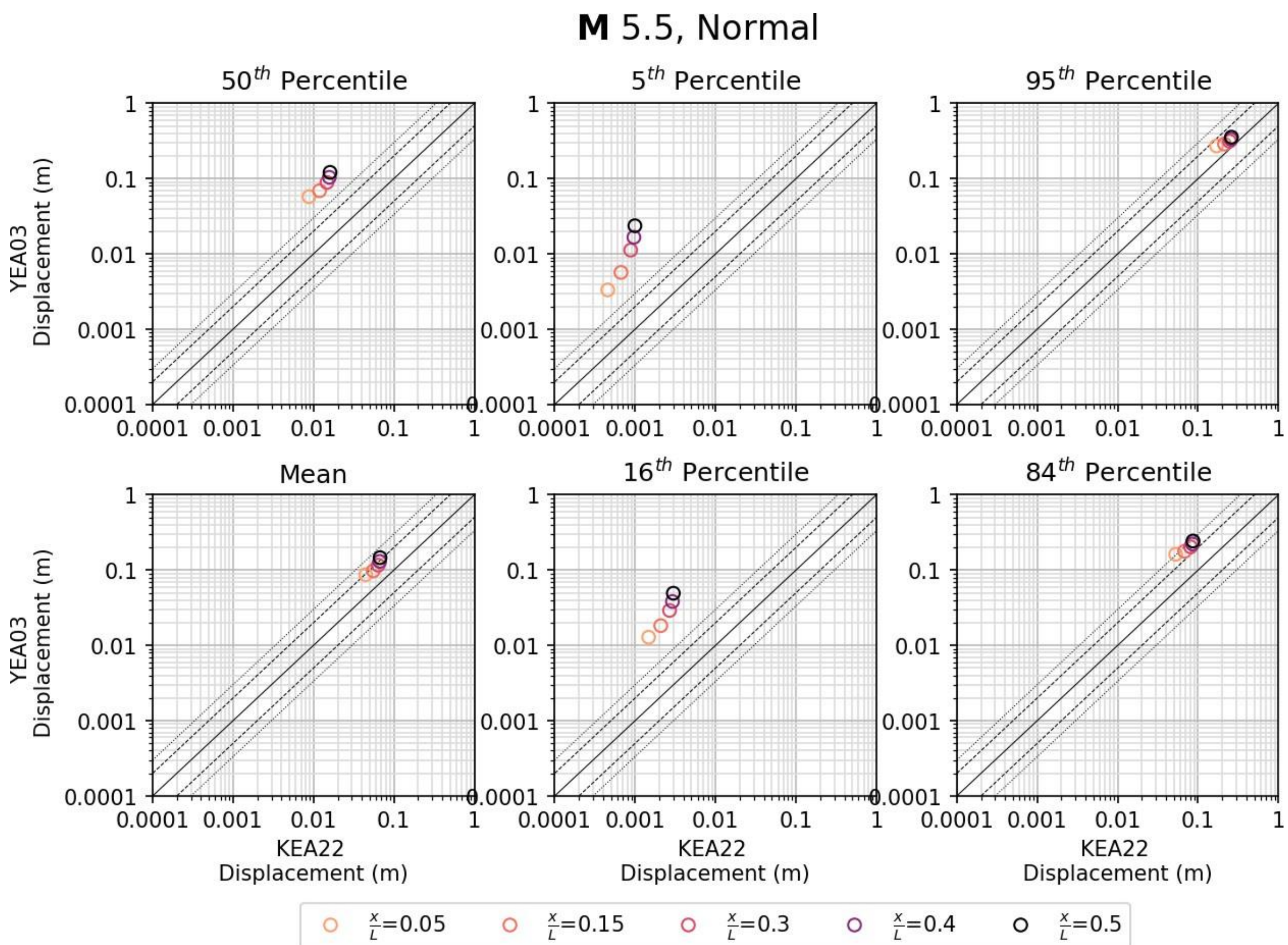

Figure 7.13. Comparison of predicted displacements fractles for various normalized positons along rupture, x/L, for **M** 5.5 normal earthquakes. Solid line is identty (1:1) line; dashed lines are factor of two; doted lines are factor of three. “YEA03” is Youngs et al. (2003). We thank Dr. Grigorios Lavrentadis for calculatng the “YEA03” displacements shown here.

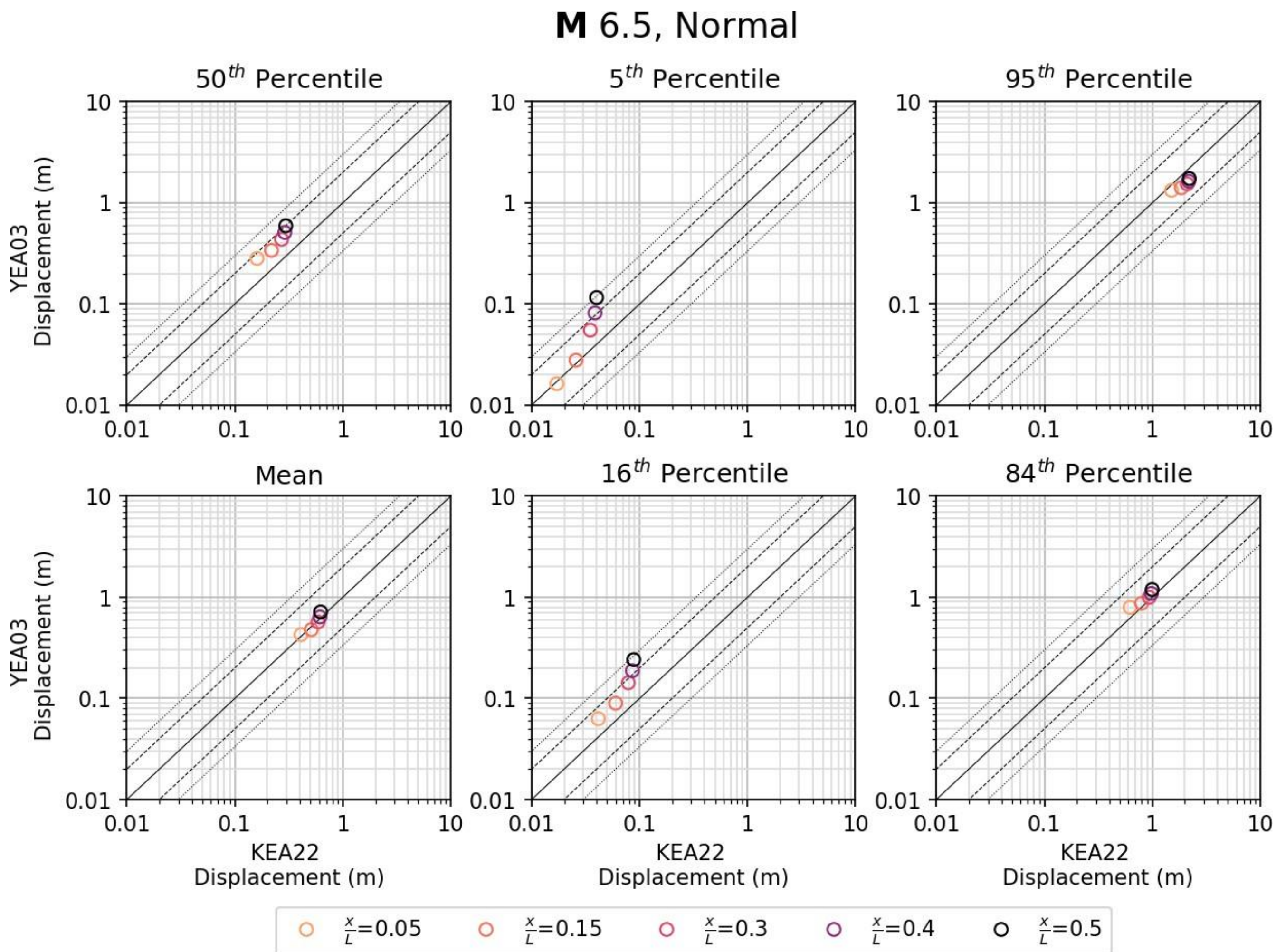

Figure 7.14. Comparison of predicted displacements fractles for various normalized positons along rupture, x/L, for **M** 6.5 normal earthquakes. Solid line is identty (1:1) line; dashed lines are factor of two; doted lines are factor of three. “YEA03” is Youngs et al. (2003). We thank Dr. Grigorios Lavrentadis for calculatng the “YEA03” displacements shown here.

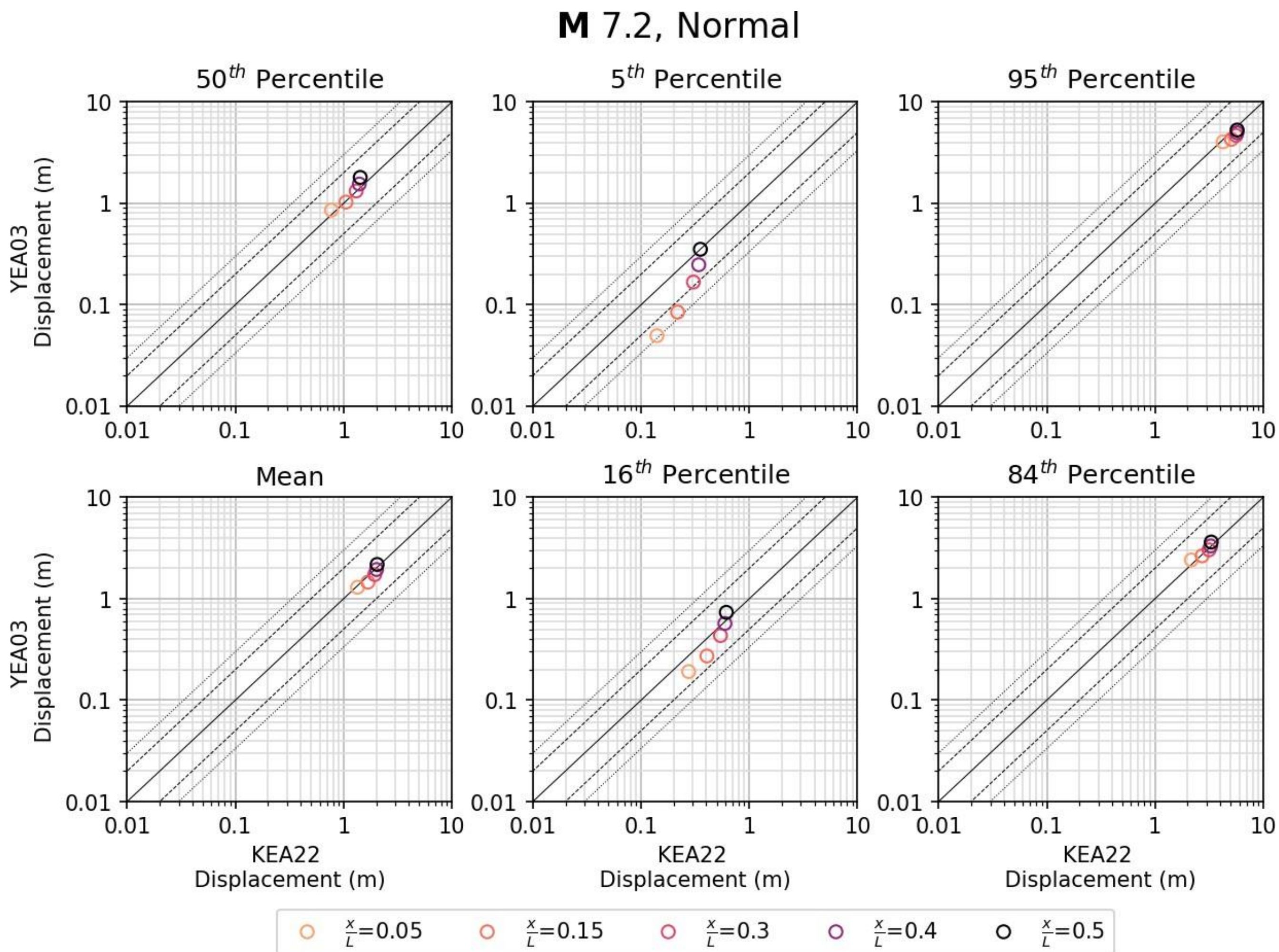

Figure 7.15. Comparison of predicted displacements fractles for various normalized positons along rupture, x/L, for **M** 6.5 normal earthquakes. Solid line is identty (1:1) line; dashed lines are factor of two; doted lines are factor of three. "YEA03" is Youngs et al. (2003). We thank Dr. Grigorios Lavrentadis for calculatng the "YEA03" displacements shown here.

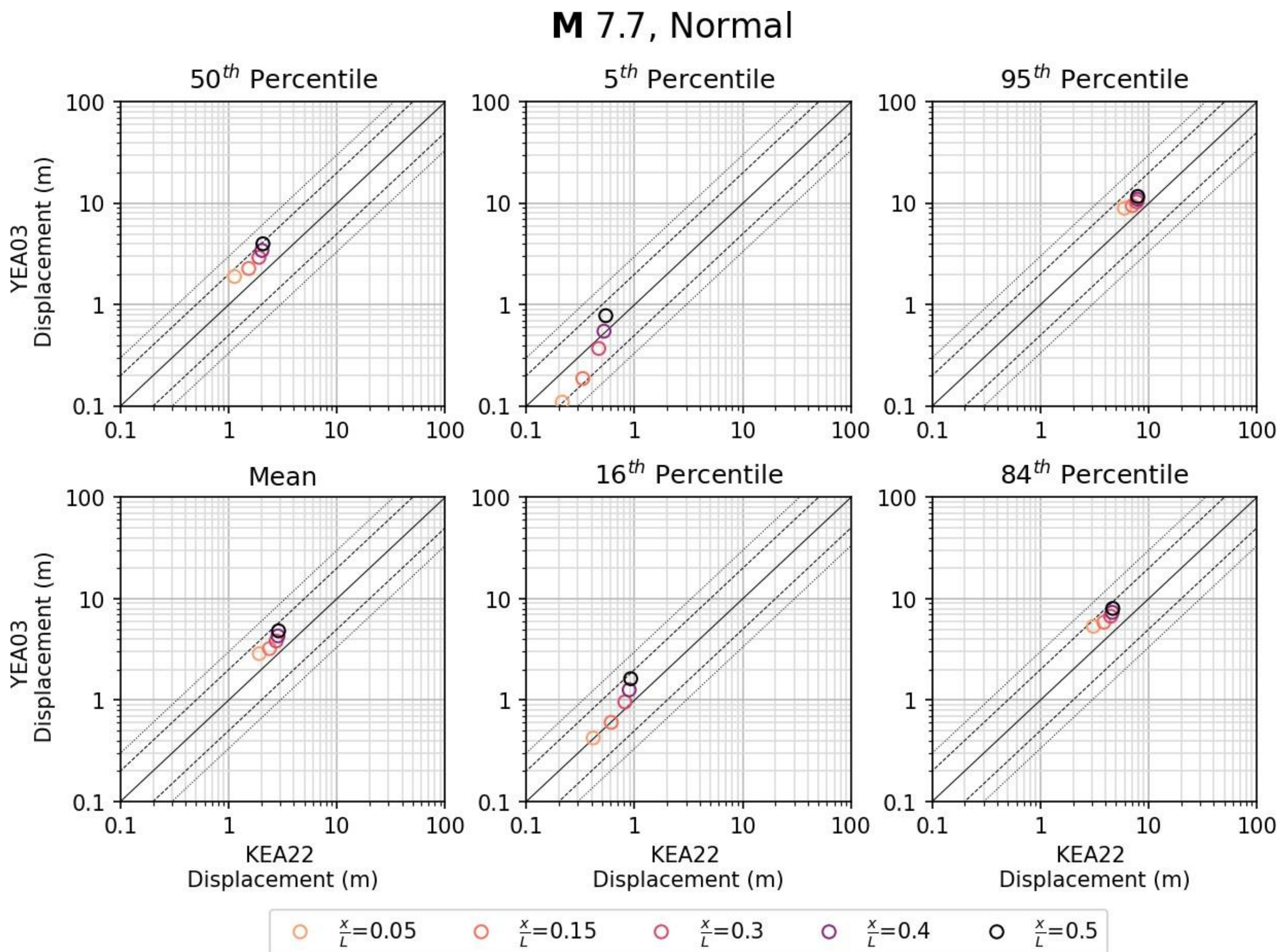

Figure 7.16. Comparison of predicted displacements fractles for various normalized positons along rupture, x/L, for **M** 6.5 normal earthquakes. Solid line is identty (1:1) line; dashed lines are factor of two; doted lines are factor of three. “YEA03” is Youngs et al. (2003). We thank Dr. Grigorios Lavrentadis for calculatng the “YEA03” displacements shown here.

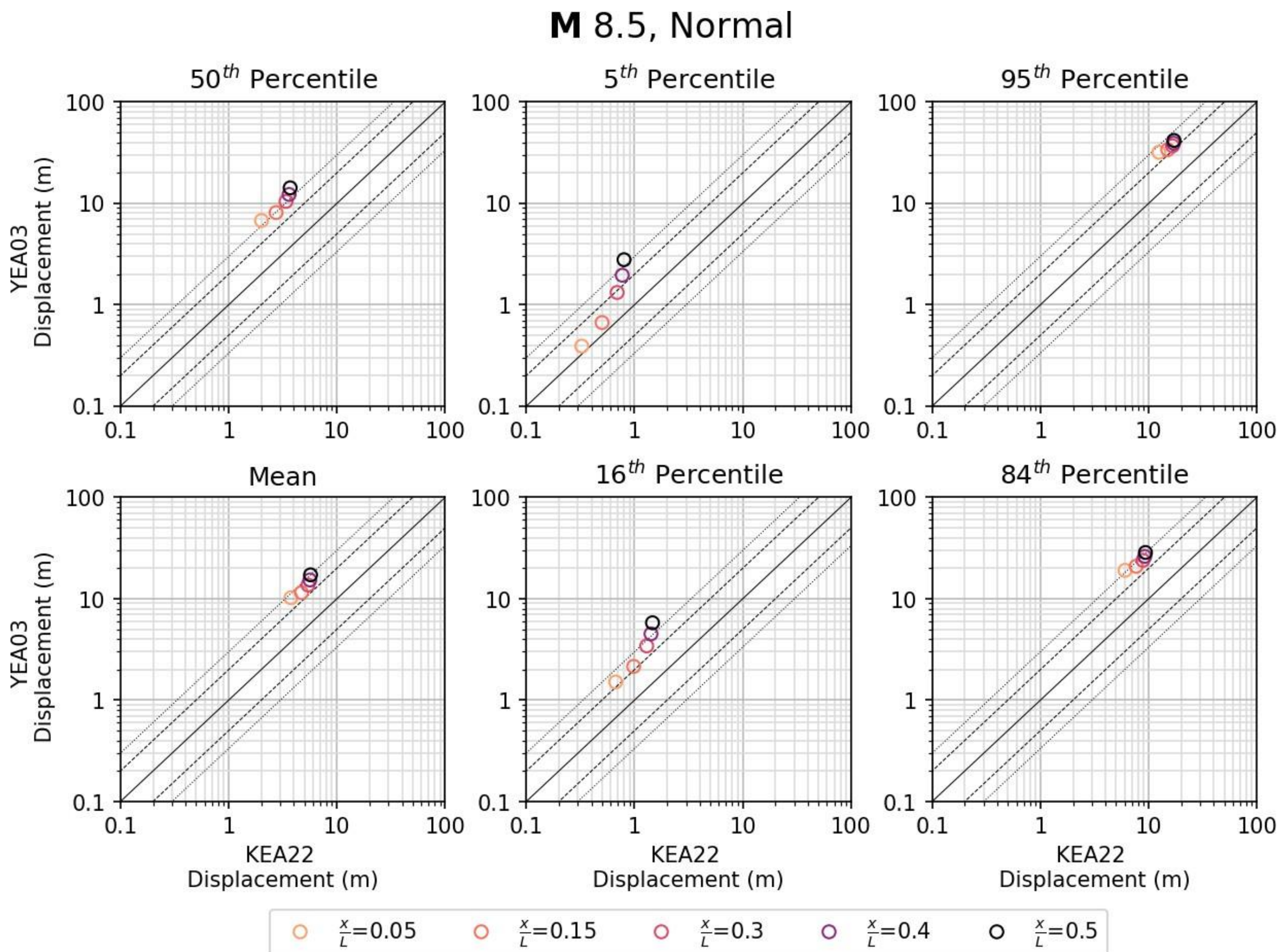

Figure 7.17. Comparison of predicted displacements fractles for various normalized positons along rupture, x/L, for **M** 6.5 normal earthquakes. Solid line is identty (1:1) line; dashed lines are factor of two; doted lines are factor of three. “YEA03” is Youngs et al. (2003). We thank Dr. Grigorios Lavrentadis for calculatng the “YEA03” displacements shown here.

7.4 SUMMARY

Comparisons between our new model and published models commonly used in engineering practce were presented in this chapter for a suite of deterministc scenarios. For **M** 6.5 – 7.7 events of all styles of faultng, our model produces median and mean results within a factor of 2 of the existng models, and within a factor of 1.5 in most cases. This corresponds to a magnitude range that is generally well-represented in historical surface rupture databases. Differences for smaller and larger magnitudes can be significant and are primarily due to different model formulatons.

Our new model includes two key features that are responsible for differences, relatve to published models, at smaller (e.g., < 6.5) and larger (e.g., > 7.7) magnitudes. First, we include a style of faultng-dependent magnitude break-point for the maximum displacement. Second, we include magnitude and style of faultng-dependent uncertainty (Figure 6.5). The former generally produces lower displacements for both smaller and larger magnitudes relatve to the existng models. The later generally leads to narrower fractles for larger magnitudes and wider fractles for smaller magnitudes (except for reverse faultng, for which the data do not show a meaningful dependence on magnitude for standard deviaton). For normal style of faultng, the large uncertainty at small magnitudes controls the hazard and effectvely cancels the impact of the reduced displacement caused by the magnitude break point. Due to the limited data and therefore large uncertainty at small magnitudes, the mean hazard for both strike-slip and normal earthquakes is closer to the 84th percentile for small magnitudes.

8 PARTITIONING AGGREGATED SLIP ONTO PRINCIPAL AND DISTRIBUTED SOURCES

Our new model predicts aggregated net displacement over an unspecified number of faults or splays. Future work will evaluate parttoning or disaggregatng the predicted displacement onto individual sources in site-specific analysis. In the interim, we present disaggregated results of the displacement aggregaton analysis based on style of faultng and source type. The general trends may serve as a guide to develop a rough estmate of the percentage of the predicted aggregated displacement that might occur on (sub)parallel principal or distributed faults.

The aggregated displacements algorithm (see Displacement Aggregaton Methodology) tracks the contributon of other principal- and distributed-*rank* measurements for each origin measurement (Figure 3.3). Disaggregatng the contributons to each origin measurement based on *rank* is therefore simple. For example, Figure 8.1 shows the distributon of principal- and distributed-*rank* measurements for all aggregated net displacement calculatons for strike-slip events. Most of the aggregated net displacement values are equal to the origin measurements (i.e., $\mathrm{D}_{agg} = \mathrm{D}_0$) because no additonal measurements were captured in the hourglass search window, as shown in the lef histograms on Figure 8.1. When there are contributons from other faults or splays (right histograms on Figure8.1, the *principal*-rank contributon has a relatvely flat distributon, whereas *distributed*-rank contributon is skewed to lower fractonal contributons.

Two examples are used to illustrate the aggregaton contributons. Figure 8.2 shows an example hourglass algorithm search window from the 1992 **M** 7.28 Landers, California earthquake in which no additonal measurements contribute to the aggregated net displacement. However, the distributon of the non-zero fractonal contributons to the aggregated net displacement values (i.e., $\mathrm{D}_{agg} > \mathrm{D}_0$; right histograms on Figure 8.1) provides useful informaton on the percentage of distributed and principal displacement observed on (sub)parallel faults or splays. Figure 8.3 is an example from the Landers earthquake in which the hourglass search window captures additonal principal and distributed measurements. In this example, the origin measurement contributes $\sim$34% of the aggregated net displacement, whereas other principal and distributed measurements contribute $\sim$13% and $\sim$53%, respectvely.

The data distributon in Figure 8.1 is based on all strike-slip earthquakes in our selected subset of the FDHI database (see Data Selecton). The example in Figure 8.2 represents the most common case in which there is only one fault. Alternatvely, the example in Figure 8.3 represents an outlier case in three ways. First, the surface faultng patern is complex and both principal-and distributed-*rank* measurements contribute to the aggregated net displacement value (Figure 8.3a). Second, the parttoning of the contributng principal-*rank* measurements is at the lower tail of the distributon from all strike-slip data, as observed in the upper right histogram in Figure 8.3b. Third, the parttoning of the distributed-*rank* measurements is also an outlier relatve to the distributon of all strike-slip data, as observed in the lower right histogram in Figure 8.3b.

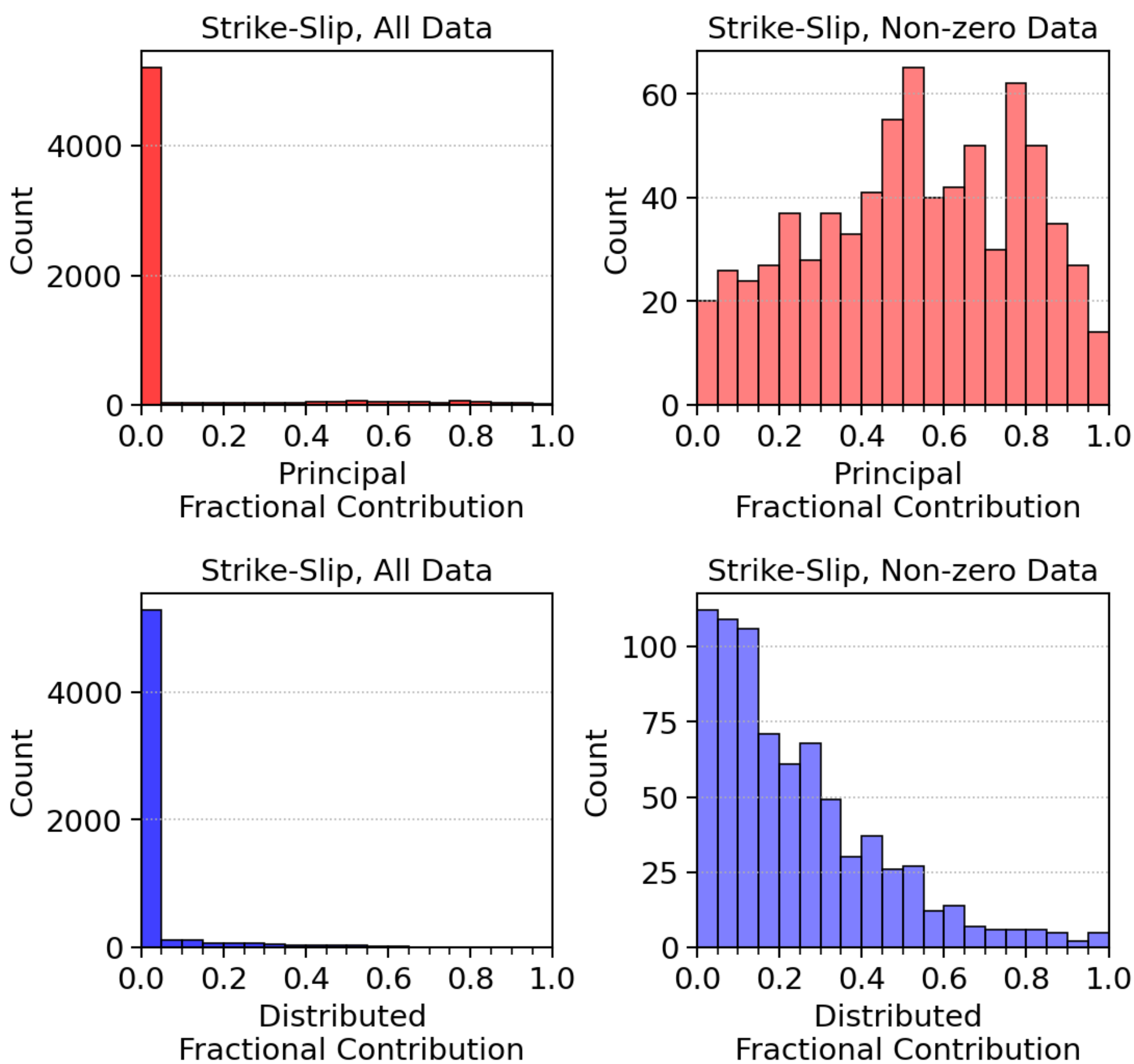

Figure 8.1. *Rank*-based contributons to aggregated net displacement values for strike-slip events. Top panels (red histograms) show principal-*rank* contributons; botom panels (blue histograms) show distributed-*rank* contributons. Lef panels show all data; right panels show distributon of non-zero porton of lef panels.

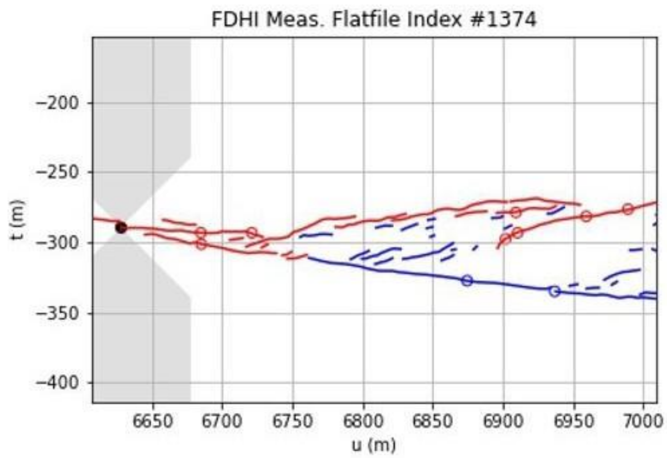

index	1374
u	6627.62
t	-289.284
location_id	38
reco_net	1.15974
agg_total	1.15974
fraction_dist	0.00%
fraction_prin	0.00%

(a) (Lef) Map of surface ruptures (lines) and displacement measurements (circles) in *u,t* event-specific coordinate system. Origin measurement (D_0) is black filled circle. Red, blue correspond to principal- and distributed-*rank*, respectvely. (Right) Table showing aggregaton results for origin measurement. Arrows emphasize fractonal contributons based on *rank*.

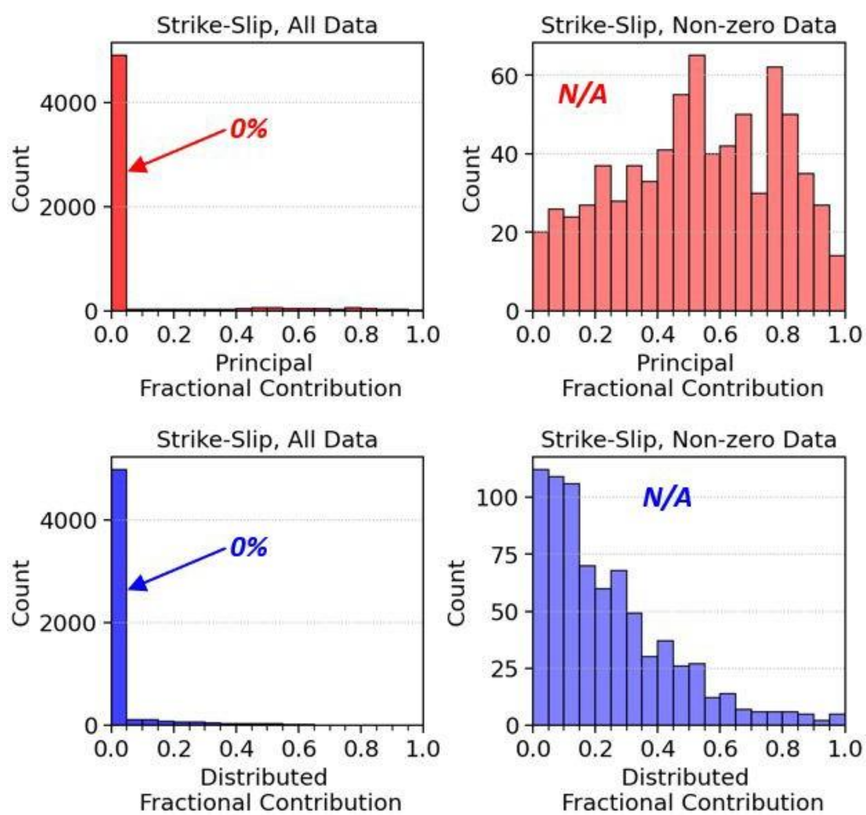

(b) Histogram bins corresponding to aggregaton results (fractonal contributons) from (a). N/A is not applicable.

Figure 8.2. Example hourglass search window from 1992 **M** 7.28 Landers, California earthquake. D_{agg} = D_0 because no additonal measurements are captured in hourglass search window.

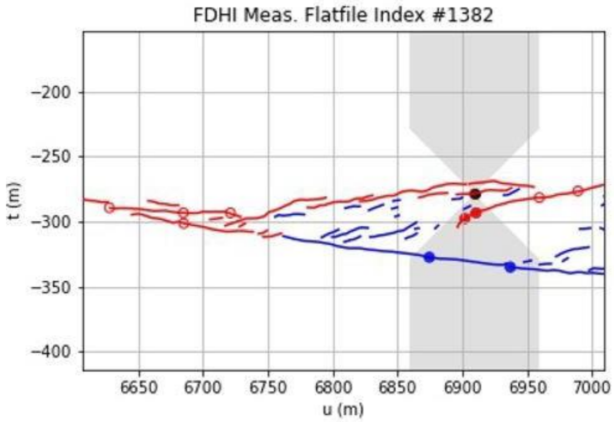

index	1382
u	6909.27
t	-278.671
location_id	46
reco_net	0.570088
agg_subtotal_distributed	0.916624
agg_subtotal_principal	0.23071
agg_total	1.71742
fraction_dist	53.37%
fraction_prin	13.43%

(a) (Lef) Map of surface ruptures (lines) and displacement measurements (circles) in *u,t* event-specific coordinate system. Origin measurement (D_0) is black filled circle. Red, blue correspond to principal- and distributed-*rank*, respectvely. (Right) Table showing aggregaton results for origin measurement. Arrows emphasize fractonal contributons based on *rank*.

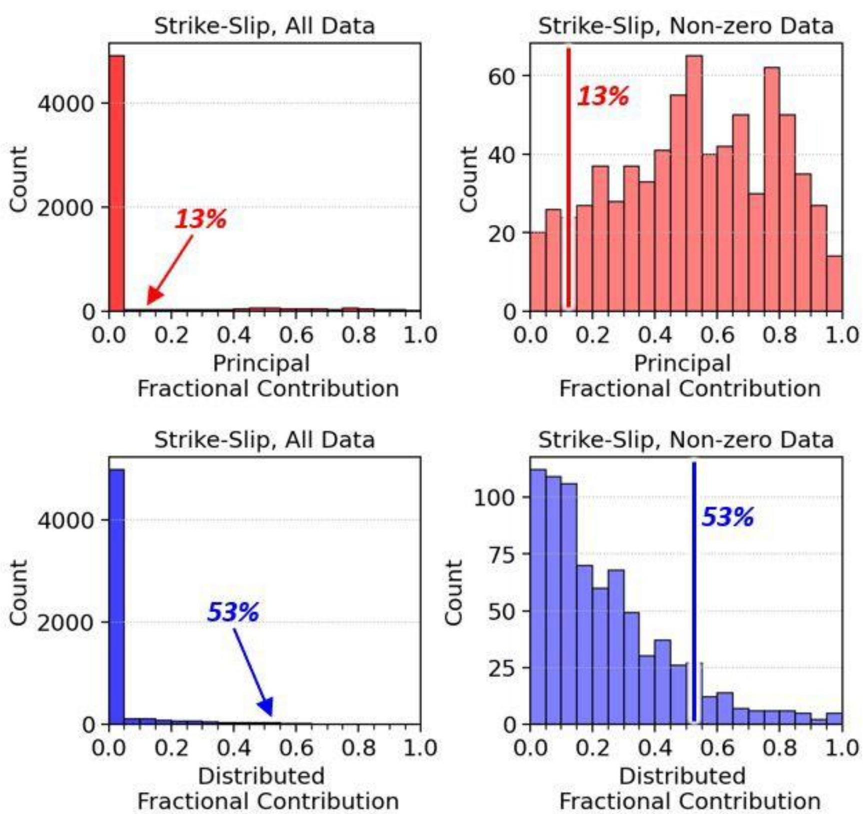

(b) Histogram bins corresponding to aggregaton results (fractonal contributons) from (a).

Figure 8.3. Example hourglass search window from 1992 **M** 7.28 Landers, California earthquake. D_{agg} > D_0 because additonal measurements are captured in hourglass search window.

The distributon of the non-zero fractonal contributons varies based on style of faultng. Histograms similar to those on Figure 8.1, which reflect strike-slip faultng, are shown on Figures 8.4 and 8.5 for reverse and normal events, respectvely. In general, the strike-slip distributon for principal-*rank* contributons is bimodal with peaks near 50% and 80%, suggestng that when (sub)parallel principal faultng occurs in strike-slip earthquakes, the displacement is commonly parttoned such that 50% or more occurs on other (sub)parallel principal faults (Figure 8.1). The distributon for principal-*rank* contributons to reverse faults is symmetrical and unimodal with a peak near 50%, suggestng that when (sub)parallel principal faultng occurs, ∼50% is commonly parttoned onto other principal sources (Figure 8.4). For normal fault systems, the distributon of principal-*rank* contributons is right-skewed with a peak near 25%, indicatng only ∼25% is commonly parttoned onto other principal sources (Figure 8.5). The distributons for distributed faultng are right-skewed for strike-slip and reverse faults (Figures 8.1 and 8.4), with respectve peaks near 10% and 20%. This suggests that when distributed faults are present, ∼10% of the aggregated net displacement predicted from our model is most likely to occur on one or more distributed faults or splays in strike-slip systems (or ∼20% in reverse systems). For normal fault systems, the distributon for distributed faultng is symmetrical and unimodal with a peak near 50%.

The histograms in Figures 8.1, 8.4, and 8.5 can be used in combinaton with our new model and site-specific geologic mapping to estmate the percentage of the predicted aggregated displacement that might occur on (sub)parallel principal or distributed faults. For example, if site-specific geologic mapping identfies a mix of principal and distributed faults or splays in a strike-slip system, Figure 8.1 suggests ∼10% of the aggregated net displacement predicted from our model is most likely to occur on distributed faults, and ∼50% to ∼80% of the predicted aggregated net displacement is most likely to occur on any of the principal faults. However, the histograms indicate that a wide range of percentages is observed in the global dataset and simply using the most likely value might not be adequate. Accordingly, the range of fractonal contributons can be captured in a logic tree and treated as epistemic uncertainty with weights based on expert geologic opinion for the site-specific conditons. Figures 8.6 and 8.7 show the same non-zero fractonal contributon histograms paired with the cumulatve distributons of the contributons, which can help inform logic tree values.

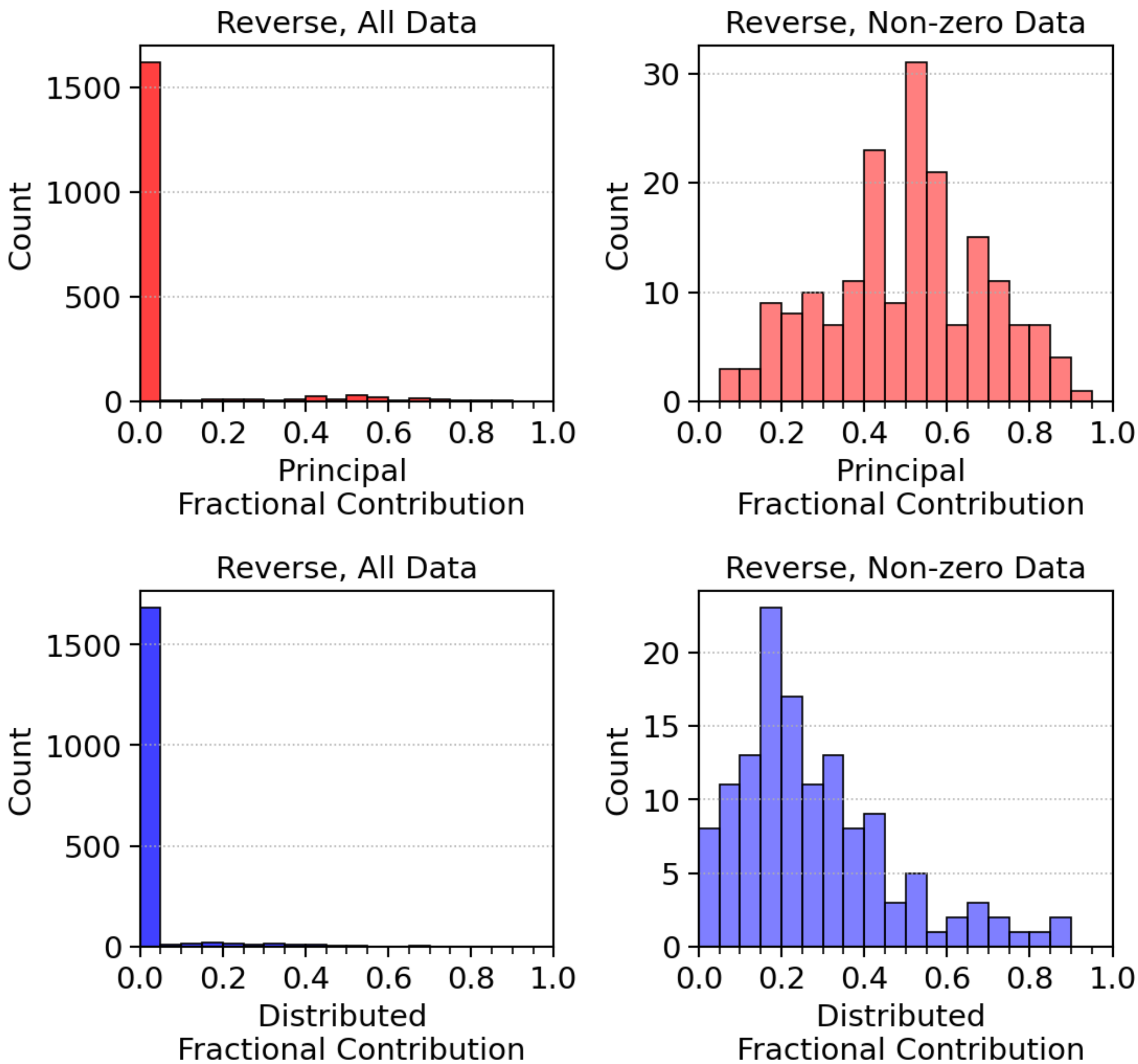

Figure 8.4. *Rank*-based contributons to aggregated net displacement values for reverse events. Top panels (red histograms) show principal-*rank* contributons; botom panels (blue histograms) show distributed-*rank* contributons. Lef panels show all data; right panels show distributon of non-zero porton of lef panels.

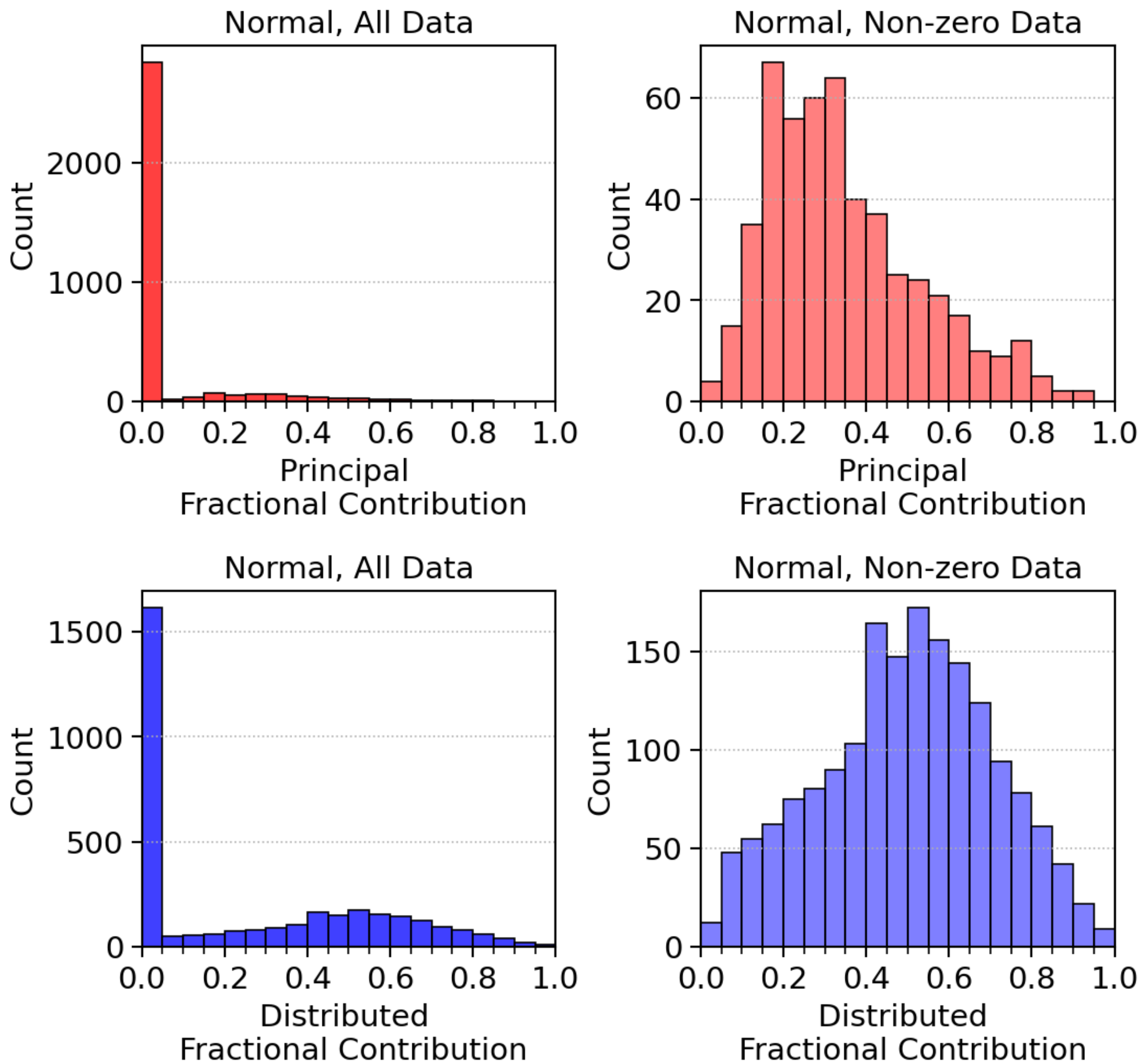

Figure 8.5. *Rank*-based contributons to aggregated net displacement values for normal events. Top panels (red histograms) show principal-*rank* contributons; botom panels (blue histograms) show distributed-*rank* contributons. Lef panels show all data; right panels show distributon of non-zero porton of lef panels.

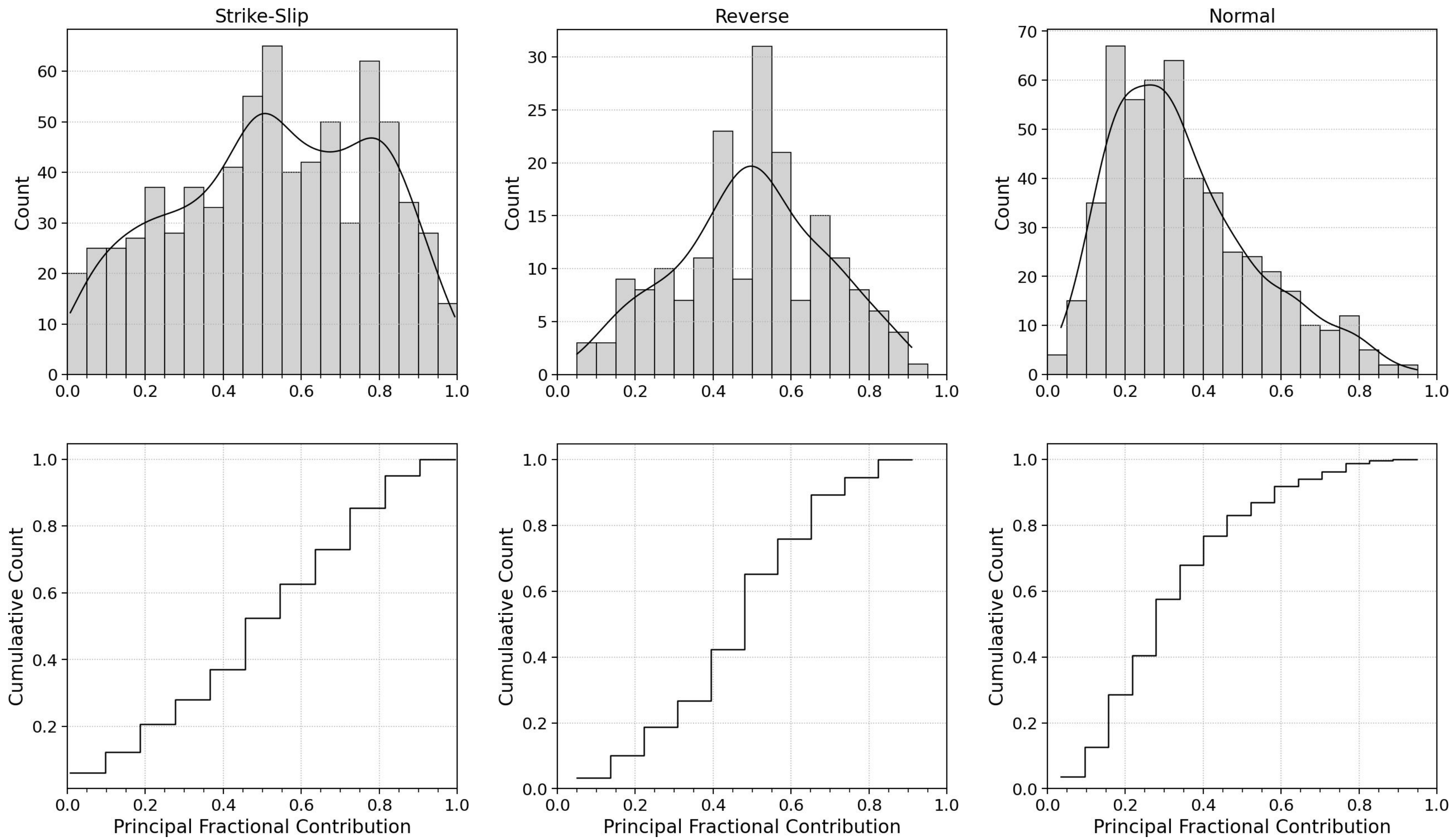

(a) Strike-slip events.

(b) Reverse events.

(c) Normal events.

Figure 8.6. (Top) Histogram of principal-*rank* fractonal contributon to aggregated net displacement based on style of faultng. Solid line is probability density functon. (Botom) Cumulatve distributon of histogram in upper plot.

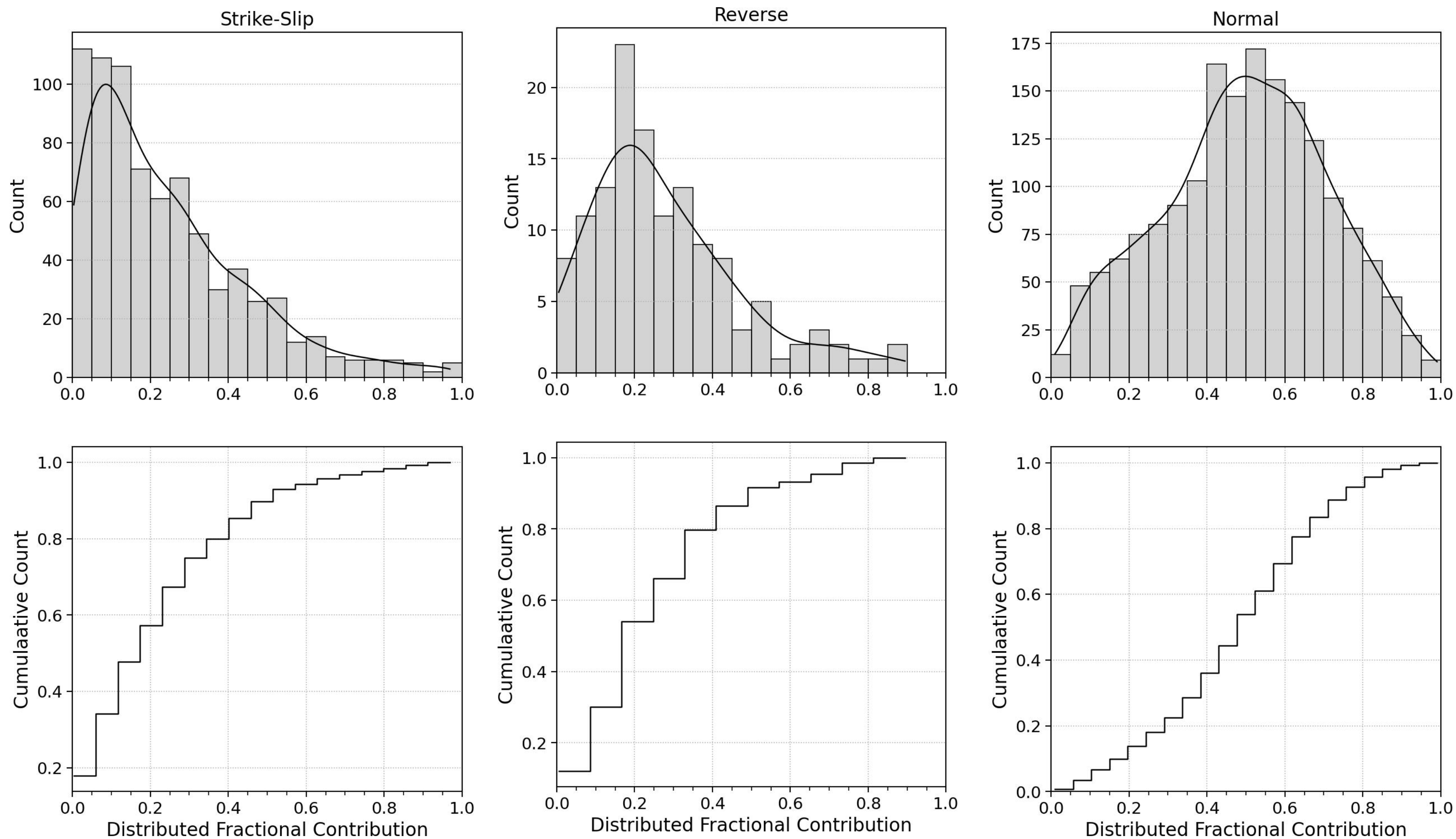

(a) Strike-slip events.

(b) Reverse events.

(c) Normal events.

Figure 8.7. (Top) Histogram of distributed-*rank* fractonal contributon to aggregated net displacement based on style of faultng. Solid line is probability density functon. (Botom) Cumulatve distributon of histogram in upper plot.

9 SUMMARY AND FUTURE WORK

9.1 SUMMARY

This report documents the development of a new fault displacement model that predicts the total discrete net displacement amplitude across one or more surface ruptures, which is referred to as ”aggregated net displacement.” We use moment magnitude and normalized locaton along rupture as predictor variables, and different functonal forms are developed for different styles of faultng. Aleatory variability is included in both the magnitude and locaton scaling models. Within-model epistemic uncertainty is estmated from 2000 samples of the posterior distributons of the model coefficients.

The aggregated displacement is modeled as a lognormal distributon. Chapter Model Implementaton describes how the model can be implemented by practtoners, and model predictons for a range of earthquake magnitudes are provided in Model Predictons. Model coefficients and example code can be found at https://github.com/NHR3-UCLA/KKMSB22_Displacement_Model. In general, smaller and larger magnitude events (e.g., **M** $\lesssim 6$ and **M** $\gtrsim 8$) are poorly constrained by the available data, and we recommend including within-model epistemic uncertainty. It is also important to note that our new model is not symmetric about the rupture midpoint, but is skewed such that the peak displacement occurs at $\mathrm{U}_* \leq 0.5$. The skewness is more severe for dip-slip events than strike-slip. In most cases, practtoners should evaluate both the median and aleatory variability for both U_* and $1 - \mathrm{U}_*$ and equally weight the predictons.

While our final model formulaton only uses moment magnitude and normalized rupture positon as predictor variables, we evaluated several other approaches and metrics. In partcular, we sought to develop site factors that could beter predict along-strike fault segmentaton or fault-normal displacement parttoning onto (sub)parallel ruptures. We tested several automated and manual methods to capture along-strike fault segmentaton; however, we did not find methods or metrics that were both consistent predictors of segment boundaries in the FDHI Database and usable in a forward-modeling sense. To provide preliminary guidance on parttoning the predicted aggregated displacement onto (sub)parallel ruptures at a site, we include deaggregated results of our displacement aggregaton analysis in Chapter Parttoning Aggregated Slip onto Principal and Distributed Sources.

9.2 FUTURE WORK

While our fault displacement model is an improvement over existng models, we recognize areas of future work. For example, our model can be improved with more data. Extensions of the model, such as parttoning predicted aggregated displacements across multple faults or developing correlaton models for scenario-based hazard, will be useful for practtoners and planners. Finally, other components of the hazard integral, such as rupture probability as a functon of magnitude or probability of rupture where no fault has been mapped, are not a part of the current scope but are important for a fault displacement hazard evaluaton.

9.2.1 Reduce Uncertainty for Small Magnitude Earthquakes

Our FDHI database contains only seven events smaller than **M** 6 (Figure 2.3). Five of those events are reverse faultng, providing reasonable constraints on the uncertainty associated with small magnitude reverse events. The other two events are both M_L 5.2 strike-slip earthquakes from the same region in California, and the maximum displacements vary by a factor of $\sim$15; therefore, our model reflects significant uncertainty for small magnitude strike slip earthquakes (Figure 6.5). There are no normal faultng events smaller than **M** 6, which also causes large uncertainty in this range.

The performance of our model for small magnitude earthquakes can be improved with more data from small events for strike-slip and normal style events. Empirical data is preferred, but data from dynamic rupture simulatons (e.g. Wang and Goulet, 2021) could also provide guidance. Although fault displacement hazard for small magnitude events is not significant in actve tectonic setngs like California, the hazard in many global setngs is controlled by small magnitude events (e.g., Europe, Australia).

9.2.2 Parttoning Aggregated Displacement Across Multple Faults

The fault displacement model presented in Model predicts the total discrete net displacement (D_{agg}) across an unspecified number of faults or splays. When there is only one principal fault present, then the D_{agg} represents the displacement on that source. In the case of complex or mult-stranded faultng, the D_{agg} represents the aggregated net displacement across all principal and distributed faults at the site positon along the rupture length ($\mathrm{x/L}$). We recognize that in the case of complex faultng, the aggregated net displacement needs to be parttoned or disaggregated onto individual sources for site-specific analysis. Deaggregated results of the displacement aggregaton analysis are provided in Parttoning Aggregated Slip onto Principal and Distributed Sources and can help practtoners develop estmates of principal and distributed parttoning. Related future work includes (i) providing a disaggregaton model that is a companion to our aggregated displacement model, or (ii) developing a companion distributed displacement model.

9.2.3 Rupture Probability Models

There are three main models used in PFDHA: (i) an earthquake rate or magnitude-frequency model, (ii) a surface rupture likelihood model, and (iii) a fault displacement amplitude model, which is the subject of this report. The magnitude-frequency distributon is a source-specific issue that is handled in the seismic source characterizaton. Future work in the FDHI Project is antcipated to address surface rupture probability models.

REFERENCES

Al-Atk, L. and Youngs, R. R. (2014). "Epistemic Uncertainty for NGA-West2 Models." *Earthquake Spectra*, 30(3), 1301–1318.

Aydin, A. and Du, Y. (1995). "Surface rupture at a fault bend: The 28 June 1992 Landers, California, earthquake." *Bulletn of the Seismological Society of America*, 85(1), 111–128.

Biasi, G. P. and Wesnousky, S. G. (2016). "Steps and gaps in ground ruptures: Empirical bounds on rupture propagaton." *Bulletn of the Seismological Society of America*, 106(3), 1110–1124.

Biasi, G. P. and Wesnousky, S. G. (2017). "Bends and ends of surface ruptures." *Bulletn of the Seismological Society of America*, 107(6), 2543–2560.

Bommer, J. J. (2003). "Uncertainty about the uncertainty in seismic hazard analysis." *Engineering Geology*, 70(1-2), 165–168.

Bozorgnia, Y., Abrahamson, N. A., Atk, L. A., Ancheta, T. D., Atkinson, G. M., Baker, J. W., Baltay, A., Boore, D. M., Campbell, K. W., Chiou, B. S.-J., Darragh, R., Day, S., Donahue, J., Graves, R. W., Gregor, N., Hanks, T., Idriss, I. M., Kamai, R., Kishida, T., Kotke, A., Mahin, S. A., Rezaeian, S., Rowshandel, B., Seyhan, E., Shahi, S., Shantz, T., Silva, W., Spudich, P., Stewart, J. P., Watson-Lamprey, J., Wooddell, K., and Youngs, R. (2014). "NGA-West2 Research Project." *Earthquake Spectra*, 30(3), 973–987.

Brooks, B. A., Minson, S. E., Glennie, C. L., Nevit, J. M., Dawson, T., Rubin, R., Ericksen, T. L., Lockner, D., Hudnut, K., Langenheim, V., et al. (2017). "Buried shallow fault slip from the South Napa earthquake revealed by near-field geodesy." *Science advances*, 3(7), e1700525.

Carpenter, B., Gelman, A., Hoffman, M. D., Lee, D., Goodrich, B., Betancourt, M., Brubaker, M., Guo, J., Li, P., and Riddell, A. (2017). "Stan : A Probabilistc Programming Language." *Journal of Statstcal Sofware*, 76(1), 1–32.

Champenois, J., Baize, S., Vallee, M., Jomard, H., Alvarado, A., Espin, P., Ekströ m, G., and Audin, L. (2017). "Evidences of surface rupture associated with a low-magnitude (Mw 5.0) shallow earthquake in the Ecuadorian Andes." *Journal of Geophysical Research: Solid Earth*, 122(10), 8446–8458.

Clark, M. M. (1972). "Surface rupture along the coyote creek fault." *US Geol. Surv. Profess. Paper*, 787, 55–86.

Cluff, L. S., Page, R. A., Slemmons, D. B., and Crouse, C. (2003). "Seismic hazard exposure for the trans-alaska pipeline." *Advancing Mitgaton Technologies and Disaster Response for Lifeline Systems*, 535–546.

Coppersmith, K. and Youngs, R. (2000). "Data needs for probabilistc fault displacement hazard analysis." *Journal of Geodynamics*, 29(3-5), 329–343.

Dolan, J. F. and Haravitch, B. D. (2014). "How well do surface slip measurements track slip at depth in large strike-slip earthquakes? The importance of fault structural maturity in controlling on-fault slip versus off-fault surface deformaton." *Earth and Planetary Science Leters*, 388, 38–47.

Douglas, J., Akkar, S., Ameri, G., Bard, P.-Y., Bindi, D., Bommer, J. J., Bora, S. S., Coton, F., Derras, B., Hermkes, M., Kuehn, N. M., Luzi, L., Massa, M., Pacor, F., Riggelsen, C., Sandıkkaya, M. A., Scherbaum, F., Stafford, P. J., and Traversa, P. (2014). "Comparisons among the five ground-moton models developed using RESORCE for the predicton of response spectral acceleratons due to earthquakes in Europe and the Middle East." *Bulletn of Earthquake Engineering*, 12(1), 341–358.

Elliot, A. J., Oskin, M. E., Liu-Zeng, J., and Shao, Y. (2015). "Rupture terminaton at restraining bends: The last great earthquake on the altyn tagh fault." *Geophysical Research Leters*, 42(7), 2164–2170.

ESRI (2019). "ArcGIS Desktop, v. 10.7." *Redlands, CA: Environmental Systems Research Insttute.*

Fialko, Y., Sandwell, D., Simons, M., and Rosen, P. (2005). “Three-dimensional deformaton caused by the Bam, Iran, earthquake and the origin of shallow slip deficit.” *Nature*, 435(7040), 295–299.

Gabry, J. and Češnovar, R. (2021). *cmdstanr: R Interface to ’CmdStan’*. htps://mc-stan.org/cmdstanr, htps://discourse.mc-stan.org.

Gelman, A., Carlin, J. B., Stern, H. S., Dunson, D. B., Vehtari, A., and Rubin, D. B. (2013). *Bayesian Data Analysis*. Number February. Chapman and Hall/CRC, <htps://www.taylorfrancis.com/books/9781439898208> (11).

Goulet, C., Abrahamson, N., Kuehn, N., Atk, L. A., Youngs, R., Graves, R., and Atkinson, G. (2018). “Central and Eastern North America Ground-Moton Characterizaton - NGA-East Final Report.” *Report no.*, Pacific Earthquake Engineering Research Center.

Goulet, C. A., Bozorgnia, Y., Kuehn, N., Al Atk, L., Youngs, R. R., Graves, R. W., and Atkinson, G. M. (2021). “NGA-East Ground-Moton Characterizaton model part I: Summary of products and model development.” *Earthquake Spectra*, 37(1 suppl), 1231–1282.

Gregor, N., Abrahamson, N. A., Atkinson, G. M., Boore, D. M., Bozorgnia, Y., Campbell, K. W., Chiou, B. S.-J., Idriss, I. M., Kamai, R., Seyhan, E., Silva, W., Stewart, J. P., and Youngs, R. (2014). “Comparison of NGA-West2 GMPEs.” *Earthquake Spectra*, 30(3), 1179–1197.

Hemphill-Haley, M. A. and Weldon, R. J. (1999). “Estmatng prehistoric earthquake magnitude from point measurements of surface rupture.” *Bulletn of the Seismological Society of America*, 89(5), 1264–1279.

Iwahashi, J., Kamiya, I., Matsuoka, M., and Yamazaki, D. (2018). “Global terrain classificaton using 280 m dems: segmentaton, clustering, and reclassificaton.” *Progress in Earth and Planetary Science*, 5(1), 1–31.

Jekel, C. F. and Venter, G. (2019). “pwlf: a python library for fitng 1d contnuous piecewise linear functons.” *URL: htps://github. com/cjekel/piecewise linear fit py*.

Jua´rez, M. A. and Steel, M. F. J. (2010). “Model-Based Clust ering of Non-Gaussian Panel Data Based on Skew- t Distributons.” *Journal of Business & Economic Statstcs*, 28(1), 52–66.

Kim, S.-J., Koh, K., Boyd, S., and Gorinevsky, D. (2009). “L1 trend filtering.” *SIAM review*, 51(2), 339–360.

Klinger, Y. (2010). “Relaton between contnental strike-slip earthquake segmentaton and thickness of the crust.” *Journal of Geophysical Research*, 115(B7), B07306.

Knuepfer, P. (1989). “Implicatons of the characteristcs of end-points of historical surface fault ruptures for the nature of fault segmentaton.” *Fault Segmentaton and Controls of Rupture Initaton and Terminaton*, 89, 193–228.

Lavrentadis, G. and Abrahamson, N. (2019). “Generaton of Surface-Slip Profiles in the Wavenumber Domain.” *Bulletn of the Seismological Society of America*, 109(3), 888–907.

Milliner, C., Avouac, J.-P., Chen, R., Aat, S., Chiou, B., Donnellan, A., Dawson, T., Madugo, C., and Dolan, J. F. (2020). “Development of a geodetc-based probabilistc fault displacement hazard analysis using near-field geodetc imaging data.” *AGU Fall Meetng Abstracts*, Vol. 2020, T042–07.

Milliner, C. and Donnellan, A. (2020). “Using daily observatons from Planet Labs satellite imagery to separate the surface deformaton between the 4 July Mw 6.4 foreshock and 5 July Mw 7.1 mainshock during the 2019 Ridgecrest earthquake sequence.” *Seismological Research Leters*, 91(4), 1986–1997.

Milliner, C. W., Dolan, J. F., Hollingsworth, J., Leprince, S., Ayoub, F., and Sammis, C. G. (2015). “Quantfying near-field and off-fault deformaton paterns of the 1992 Mw 7.3 Landers earthquake.” *Geochemistry, Geophysics, Geosystems*, 16(5), 1577–1598.

Moss, R. E. S. and Ross, Z. E. (2011). “Probabilistc Fault Displacement Hazard Analysis for Reverse Faults.” *Bulletn of the Seismological Society of America*, 101(4), 1542–1553.

Nurminen, F., Boncio, P., Visini, F., Pace, B., Valentni, A., Baize, S., and Scot, O. (2020). “Probability of occurrence and displacement regression of distributed surface rupturing for reverse earthquakes.” *Fronters in Earth Science*, 8, 456.

Oglesby, D. D. (2020). “What can surface-slip distributons tell us about fault connectvity at depth?.” *Bulletn of the Seismological Society of America*, 110(3), 1025–1036.

Pedregosa, F., Varoquaux, G., Gramfort, A., Michel, V., Thirion, B., Grisel, O., Blondel, M., Pretenhofer, P., Weiss, R., Dubourg, V., Vanderplas, J., Passos, A., Cournapeau, D., Brucher, M., Perrot, M., and Duchesnay, E. (2011). “Scikit-learn: Machine learning in Python.” *Journal of Machine Learning Research*, 12, 2825–2830.

Petersen, M. D., Dawson, T. E., Chen, R., Cao, T., Wills, C. J., Schwartz, D. P., and Frankel, A. D. (2011). “Fault displacement hazard for strike-slip faults.” *Bulletn of the Seismological Society of America*, 101(2), 805–825.

R Core Team (2021). *R: A Language and Environment for Statstcal Computng.* R Foundaton for Statstcal Computng, Vienna, Austria, <htps://www.R-project.org>.

Rai, M., Rodriguez-Marek, A., and Chiou, B. S. (2017). “Empirical terrain-based topographic modificaton factors for use in ground moton predicton.” *Earthquake Spectra*, 33(1), 157–177.

Riley, S., DeGloria, S., and Elliot, R. (1999). “A terrain ruggedness index that quantfies topographic heterogeneity. int.” *J. Soil Sci*, 5.

Sarmiento, A., Madugo, D., Bozorgnia, Y., Shen, A., Mazzoni, S., Lavrentadis, G., Dawson, T., Madugo, C., Kotke, A., Thompson, S., Baize, S., Milliner, C., Nurminen, F., Boncio, P., and Visini, F. (2021). “Fault Displacement Hazard Initatve Database.” *Report no.*, GIRS-2021-08, <htps://www.risksciences.ucla.edu/girs-reports/2021/08>.

Schwartz, D. and Sibson, R. (1989). “Proceedings of conference xlv; a workshop on fault segmentaton and controls of rupture initaton and terminaton.” *Report no.*, US Geological Survey,.

Scot, C. P., Arrowsmith, J. R., Nissen, E., Lajoie, L., Maruyama, T., and Chiba, T. (2018). “The M7 2016 Kumamoto, Japan, earthquake: 3-D deformaton along the fault and within the damage zone constrained from differental lidar topography.” *Journal of Geophysical Research: Solid Earth*, 123(7), 6138–6155.

Sieh, K., Jones, L., Hauksson, E., Hudnut, K., Eberhart-Phillips, D., Heaton, T., Hough, S., Huton, K., Kanamori, H., Lilje, A., et al. (1993). “Near-field investgatons of the landers earthquake sequence, april to july 1992.” *Science*, 260(5105), 171–176.

Spiegelhalter, D. and Rice, K. (2009). “Bayesian statstcs.” *Scholarpedia*, 4(8), 5230.

Stan Development Team (2022). “Stan modeling language users guide and reference manual, version 2.29, <htp://mc-stan.org/>.

Teran, O. J., Fletcher, J. M., Oskin, M. E., Rockwell, T. K., Hudnut, K. W., Spelz, R. M., Akciz, S. O., Hernandez-Flores, A. P., and Morelan, A. E. (2015). “Geologic and structural controls on rupture zone fabric: A field-based study of the 2010 Mw 7.2 El Mayor-Cucapah earthquake surface rupture.” *Geosphere*, 11(3), 899–920.

U.S. Geological Survey (2021). “*Earthquake Photo Collectons*”, <htps://www.usgs.gov/natural-hazards/earthquake-hazards/science/earthquake-photo-collectons?qt-science_center_objects=0#qt-science_center_objects>. Accessed 10 February 2021.

Veht ari, A., Gelman, A., Simpson, D., Carpenter, B., and Bürkner, P.-C. (2020). “Rank-Normalizaton, Folding, and Localizaton: An Improved $\widehat{R}$ for Assessing Convergence of MCMC.” *Bayesian Analysis*, 1–23.

Wang, Y. and Goulet, C. (2021). “Validaton of fault displacements from dynamic rupture simulatons against the observatons from the 1992 landers earthquake.” *Bulletn of the Seismological Society of America*, 111(5), 2574–2594.

Wells, D. L. and Coppersmith, K. J. (1994). “New empirical relatonships among magnitude, rupture length, rupture width, rupture area, and surface displacements.” *Bulletn of the Seismological Society of America*, 84(4), 974–1002.

Wesnousky, S. G. (2008). “Displacement and geometrical characteristcs of earthquake surface ruptures: Issues and implicatons for seismic-hazard analysis and the process of earthquake rupture.” *Bulletn of the Seismological Society of America*, 98(4), 1609–1632.

Xu, X., Tong, X., Sandwell, D. T., Milliner, C. W., Dolan, J. F., Hollingsworth, J., Leprince, S., and Ayoub, F. (2016). “Refining the shallow slip deficit.” *Geophysical Journal Internatonal*, 204(3), 1867–1886.

Youngs, R. R., Arabasz, W. J., Anderson, R. E., Ramelli, A. R., Ake, J. P., Slemmons, D. B., McCalpin, J. P., Doser, D. I., Fridrich, C. J., Swan, F. H., Rogers, A. M., Yount, J. C., Anderson, L. W., Smith, K. D., Bruhn, R. L., Knuepfer, P. L. K., Smith, R. B., DePolo, C. M., O’Leary, D. W., Coppersmith, K. J., Pezzopane, S. K., Schwartz, D. P., Whitney, J. W., Olig, S. S., and Toro, G. R. (2003). “A Methodology for Probabilistc Fault Displacement Hazard Analysis (PFDHA).” *Earthquake Spectra*, 19(1), 191–219.

APPENDIX A

GEOLOGIC COMPLEXITY EVALUATIONS

A GEOLOGIC COMPLEXITY EVALUATIONS

A1 INTRODUCTION

One potental improvement to the estmatng fault displacement at a site is the incorporaton of site-specific informaton. This Appendix documents efforts to identfy geologic controls on the along-strike variability ubiquitous in displacement profiles. In partcular, we tested various automated and manual fault segment identficaton approaches, as described below in Automated Fault Segment Detecton and Geologic Evaluatons. The predictve capability of various terrain metrics to improve fault displacement and surface rupture complexity were also investgated in Terrain-Based Indicators. A brief summary of our evaluatons are provided at the end of this Appendix.

A2 AUTOMATED FAULT SEGMENT DETECTION

Fault segmentaton is generally defined as a discontnuity or break in the surface trace of a fault. Geometric features associated with segment boundaries include gaps, step-overs, bends and changes in rupture contnuity or complexity (Biasi and Wesnousky, 2016, 2017; Knuepfer, 1989). Geologic features can also control segmentaton, such as shallow or deep lithologic changes, as well as changes in the rate or style of deformaton (e.g. Knuepfer, 1989). Fault segmentaton is well-documented in historical surface-rupturing earthquakes and the geomorphic expression of actve faults (e.g. Schwartz and Sibson, 1989).

Rupture segmentaton can also be a first-order control on fault displacement amplitudes. While displacements are expected and observed to taper to zero at the ends of surface ruptures (e.g. Hemphill-Haley and Weldon, 1999; Wesnousky, 2008), displacement tapering is also found at segment boundaries (e.g. Oglesby, 2020). Well-known examples include the 1968 Borrego Mountain, California earthquake (Clark, 1972) and 1992 Landers, California earthquake (Sieh et al., 1993).

We performed a qualitatve (visual) analysis of the rupture and displacement paterns in the FDHI Database to beter understand the role of segmentaton in along-strike displacement variability. In general, we found geologically-distnct segment boundaries were relatvely common in the surface ruptures, and these boundaries were ofen associated with lower displacement amplitudes that produced parabolic displacement profiles along the segment (e.g., the 1999 **M** 7.51 Izmit-Kocaeli, Turkey earthquake, Figure A.1; the **M** 6.54 Superstton Hills, California earthquake, Figure A.2). Accordingly, we sought to develop an algorithm to identfy segment boundaries based on surface rupture data and match displacement measurements to the identfied segments to test our speculaton that fault displacement profiles are parabolic in shape at the segment-level. Two approaches were considered:

1 Piece-wise linear fitng of mapped ruptures, constrained by displacement profile shapes.

2 Hierarchical cluster analysis of re-sampled rupture data, constrained by displacement profile shapes.

While the second approach was found to perform well for several events in the FDHI Database, complex ruptures were difficult to resolve without manually adjustng the algorithm for individual errors.

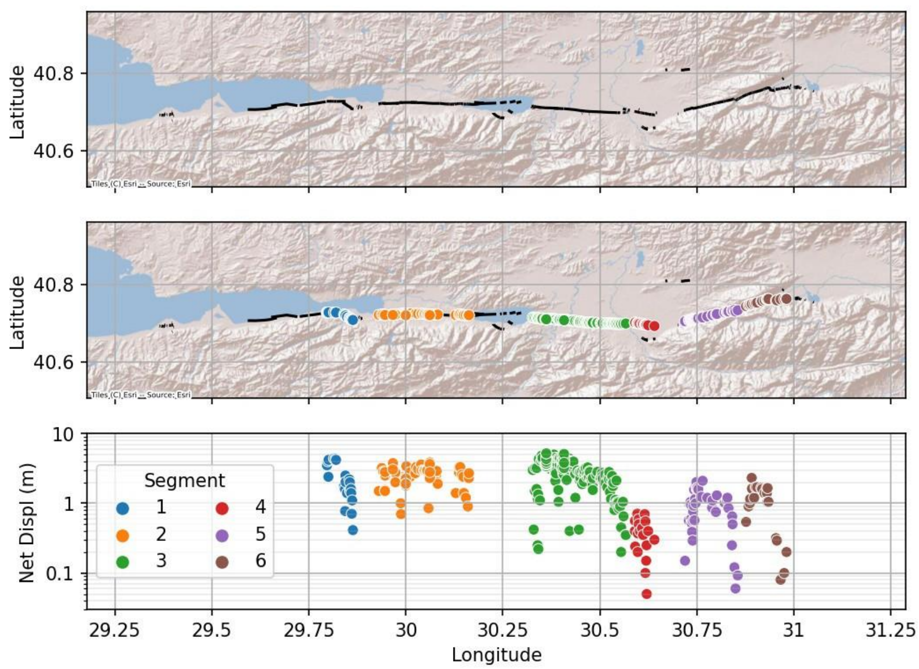

Figure A.1. Displacement amplitude tapering at segment boundaries in 1999 **M** 7.51 Izmit-Kocaeli, Turkey earthquake. (Top) Mapped surface ruptures. (Middle) Displacement measurements color-coded by rupture segment. (Botom) Net displacement amplitudes color-coded by rupture segment.

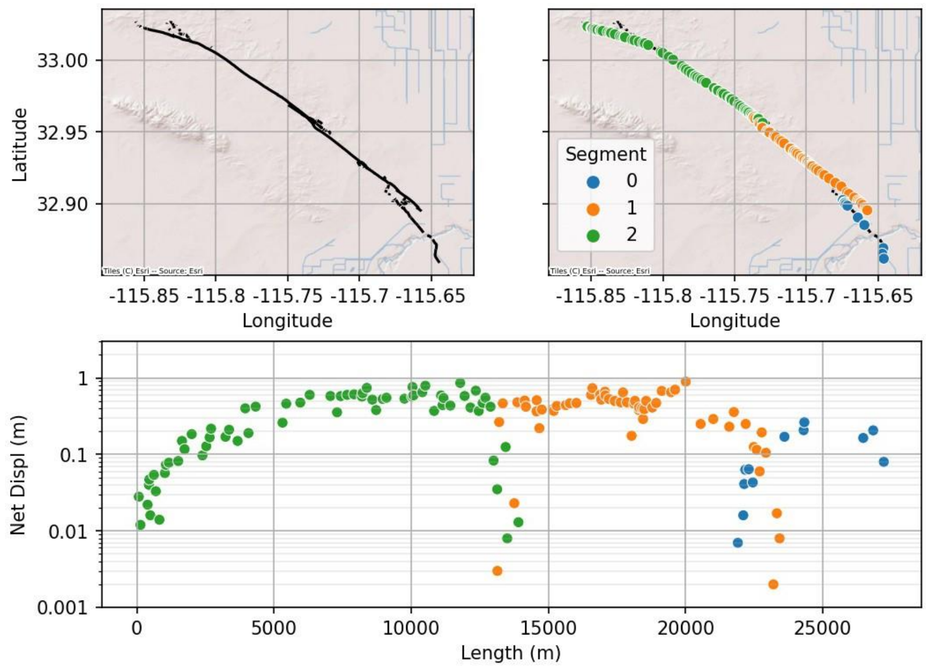

Figure A.2. Displacement amplitude tapering at segment boundaries in 1989 **M** 6.54 Superstton Hills, California earthquake. (Top Lef) Mapped surface ruptures. (Top Right) Displacement measurements color-coded by rupture segment. (Botom) Net displacement amplitudes color-coded by rupture segment.

A21 Piece-wise Linear Fitng

We followed an approach similar to Klinger (2010), which used piece-wise linear fits to determine segmentaton based on the mapped ruptures. We optmized the smoothing parameter and number of segments based on fitng the segment displacement profiles to an idealized parabolic model. Two piece-wise linear fit models were evaluated (Jekel and Venter, 2019; Kim et al., 2009), and the displacements on each segment were fit to a Beta distributon to allow for symmetric or skewed profile shapes.

The algorithm performed well for first-order approximatons of segment boundaries when the surface rupture paterns were relatvely simple. For example, the algorithm identfied five segments in the 1999 **M** 7.51 Izmit-Kocaeli, Turkey earthquake (Figure A.3). The segment boundaries are generally geologically appropriate, and the displacement profiles reflect the expected tapering at segment boundaries. However, we would expect the division between Segments 1 and 2 (blue and orange) near the *-40000 m* tck mark (top panel, Figure A.3) to be closer to *-35000* m. While the algorithm could be adjusted to achieve the desired segment boundary, the cumulatve effect of adjustng the algorithm for individual errors for every earthquake in the database was judged to be inefficient and against the spirit and intent of an automated procedure.

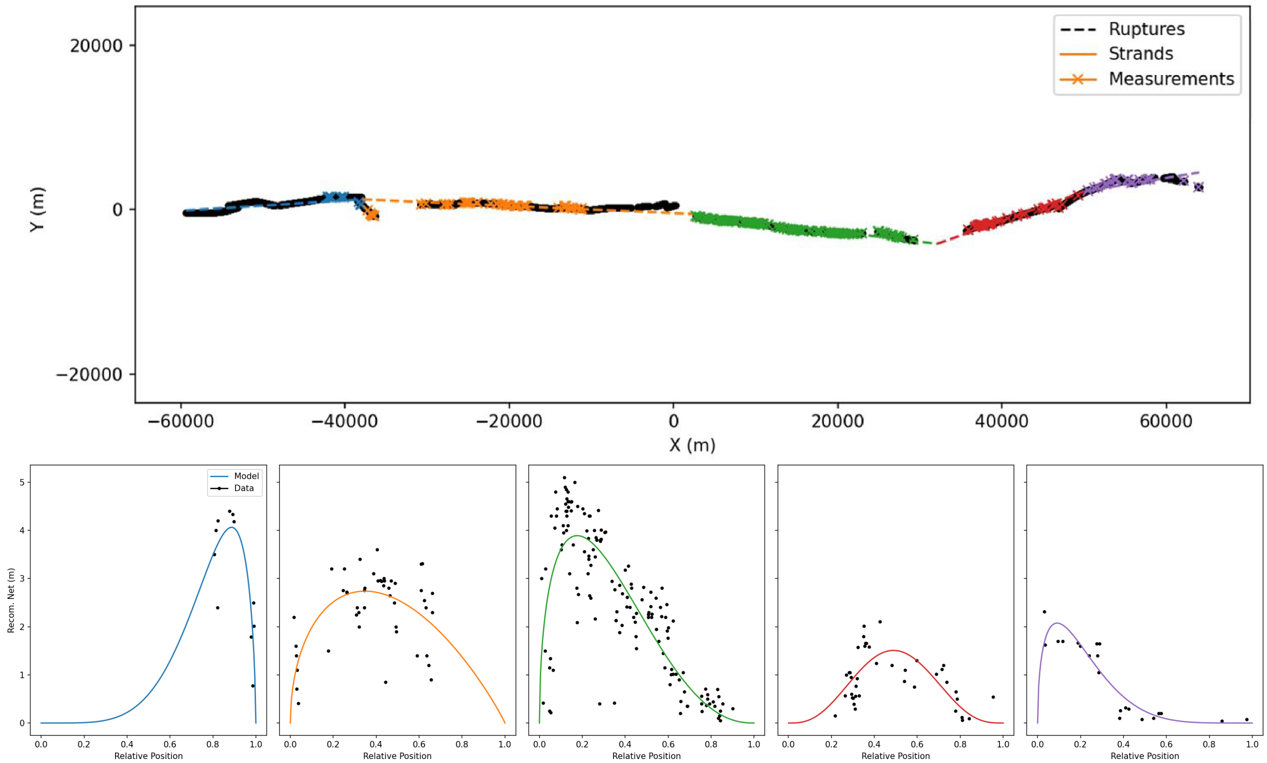

Figure A.3. Piece-wise linear fault segmentaton algorithm results for 1999 **M** 7.51 Izmit-Kocaeli, Turkey earthquake. (Top) Surface rupture map (thick black lines) with segments (dashed lines) and measurement sites (cross marks) color-coded by segment. (Botom) Displacement measurements for each segment (dots) with Beta distributon fits (lines).

The algorithm did not perform as well for events with overlapping segments. For example, the 2010 **M** 7.0 Darfield, New Zealand (Figure A.4) and 1992 **M** 7.28 Landers, California (Figure A.5) earthquakes exhibit geologically distnct segments that were not captured by the algorithm. Accordingly, the piece-wise linear approach was not pursued further.

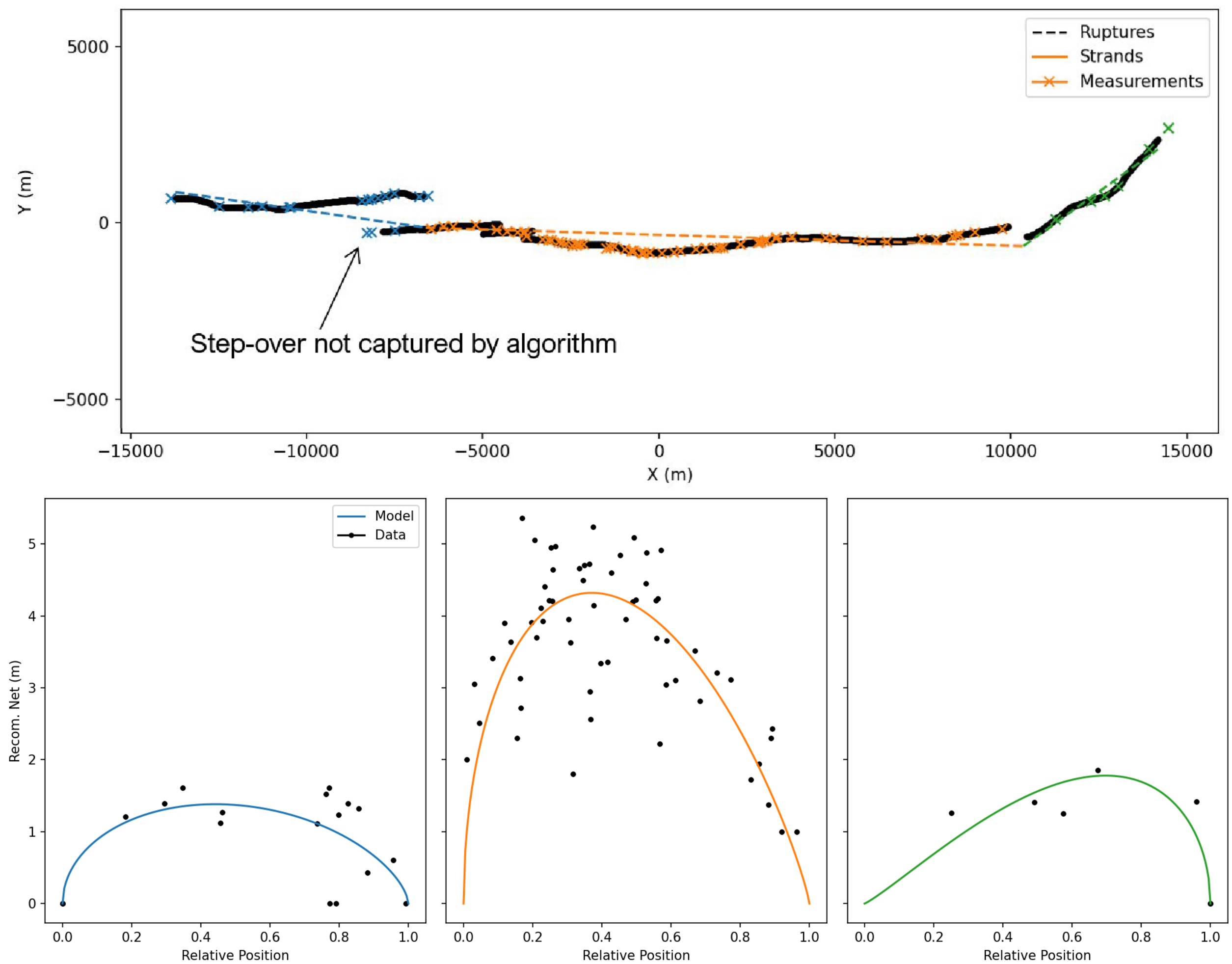

Figure A.4. Piece-wise linear fault segmentaton algorithm results for 2010 **M** 7.0 Darfield, New Zealand earthquake. (Top) Surface rupture map (thick black lines) with segments (dashed lines) and measurement sites (cross marks) color-coded by segment. (Botom) Displacement measurements for each segment (dots) with Beta distributon fits (lines).

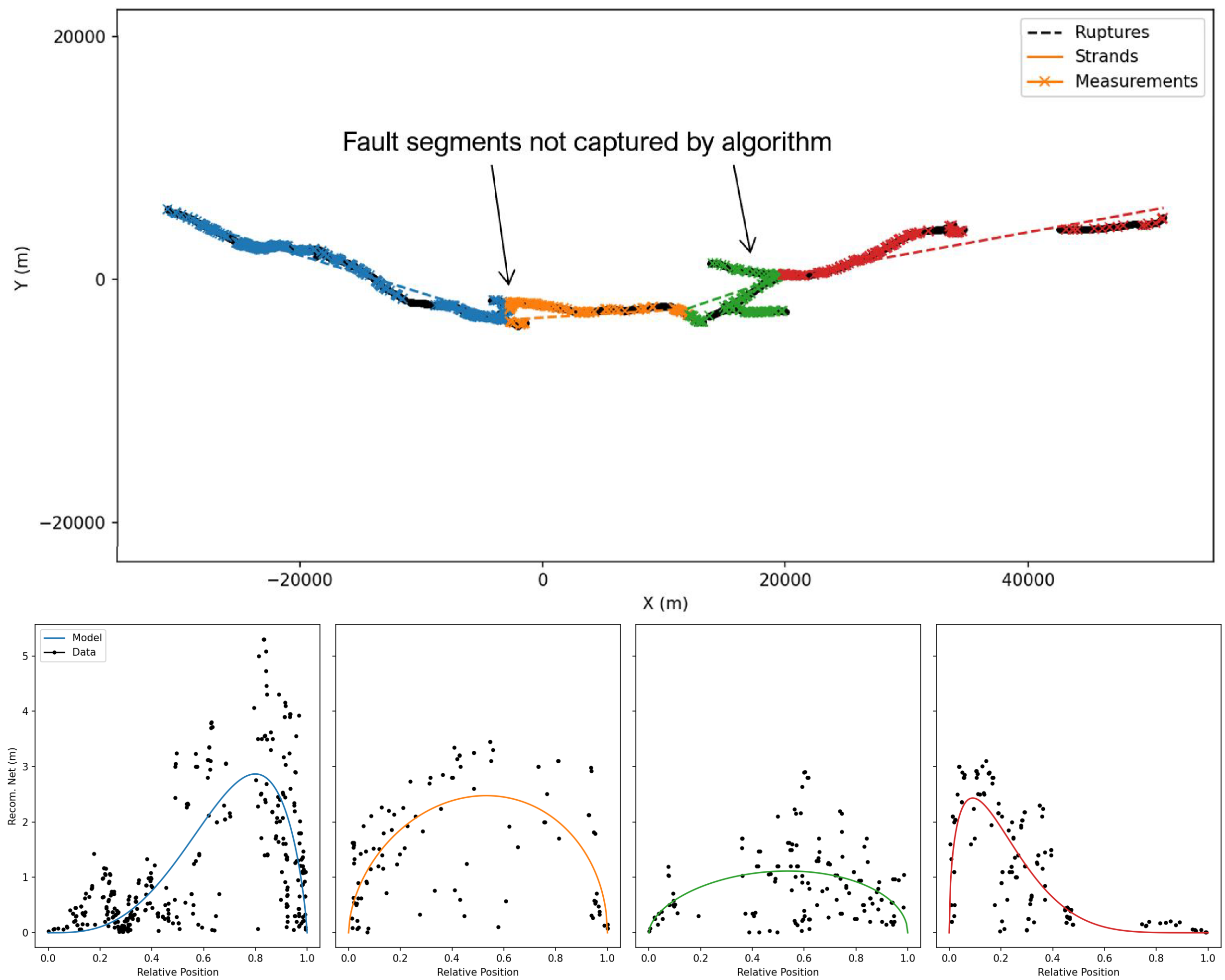

Figure A.5. Piece-wise linear fault segmentaton algorithm results for 1992 **M** 7.28 Landers, California earthquake. (Top) Surface rupture map (thick black lines) with segments (dashed lines) and measurement sites (cross marks) color-coded by segment. (Botom) Displacement measurements for each segment (dots) with Beta distributon fits (lines).

A22 Hierarchical Cluster Analysis

We also used botom-up (agglomeratve) hierarchical cluster analysis (Pedregosa et al., 2011) to determine segmentaton based on the mapped ruptures. As with the piece-wise linear approach, we optmized the groupings and number of segments by fitng the segment displacement profiles to a Beta distributon. The algorithm performed well for simple surface rupture paterns, including simple step-overs, and in general was a significant improvement over the piece-wise linear fits (Figures A.6 and A.7). However, complex ruptures such as the Landers earthquake (Figure A.8) were stll difficult to resolve without manually adjustng the algorithm for individual errors. While this approach seemed promising, we struggled to develop a methodology that could be readily used for forward predictons. This is an area that needs future research.

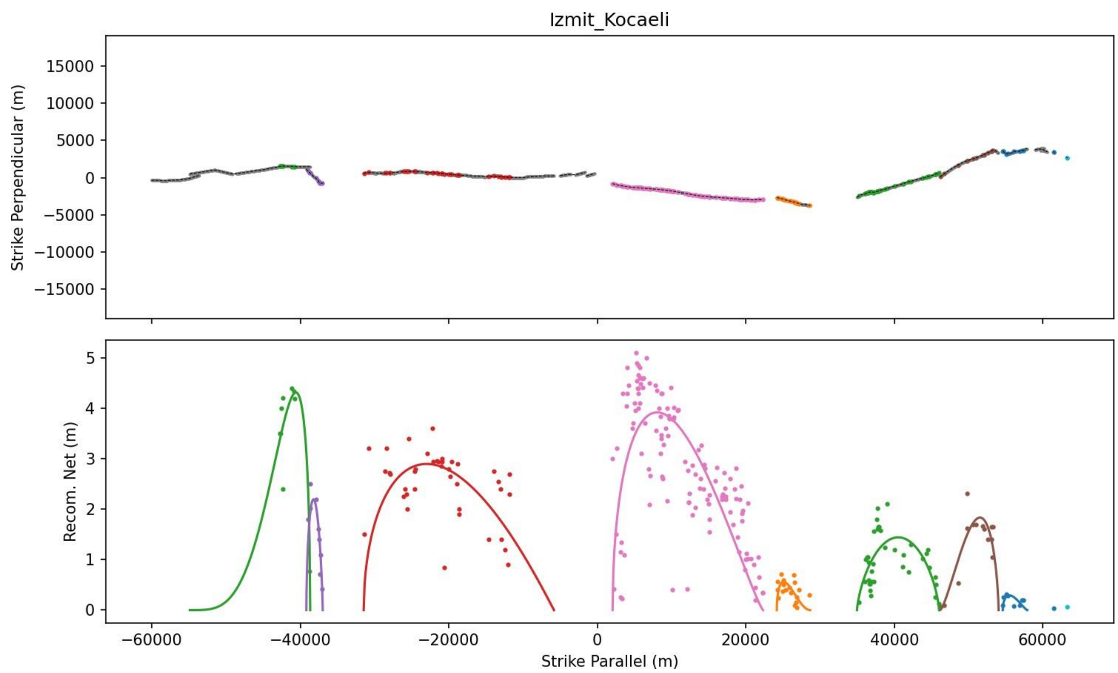

Figure A.6. Clustering algorithm results for 1999 **M** 7.51 Izmit-Kocaeli, Turkey earthquake. (Top) Surface rupture map (thick gray lines) with segments (dashed black lines) and measurement sites (filled circles) color-coded by segment. (Botom) Displacement measurements for each segment (dots) with Beta distributon fits (lines).

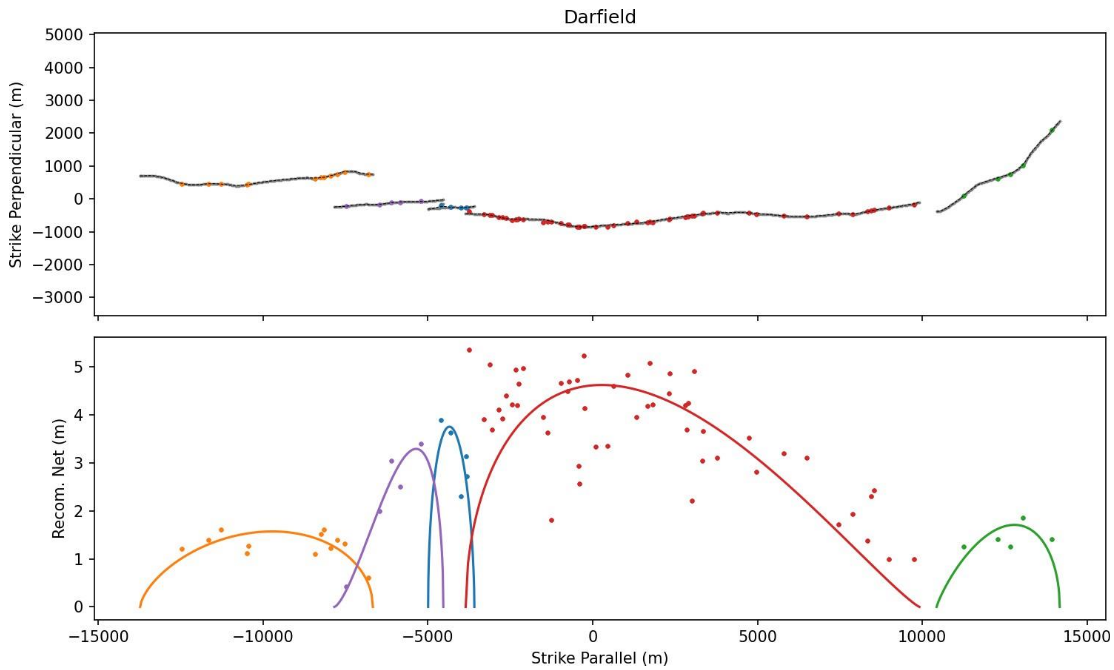

Figure A.7. Clustering algorithm results for 2010 **M** 7.0 Darfield, New Zealand earthquake. (Top) Surface rupture map (thick gray lines) with segments (dashed black lines) and measurement sites (filled circles) color-coded by segment. (Botom) Displacement measurements for each segment (dots) with Beta distributon fits (lines).

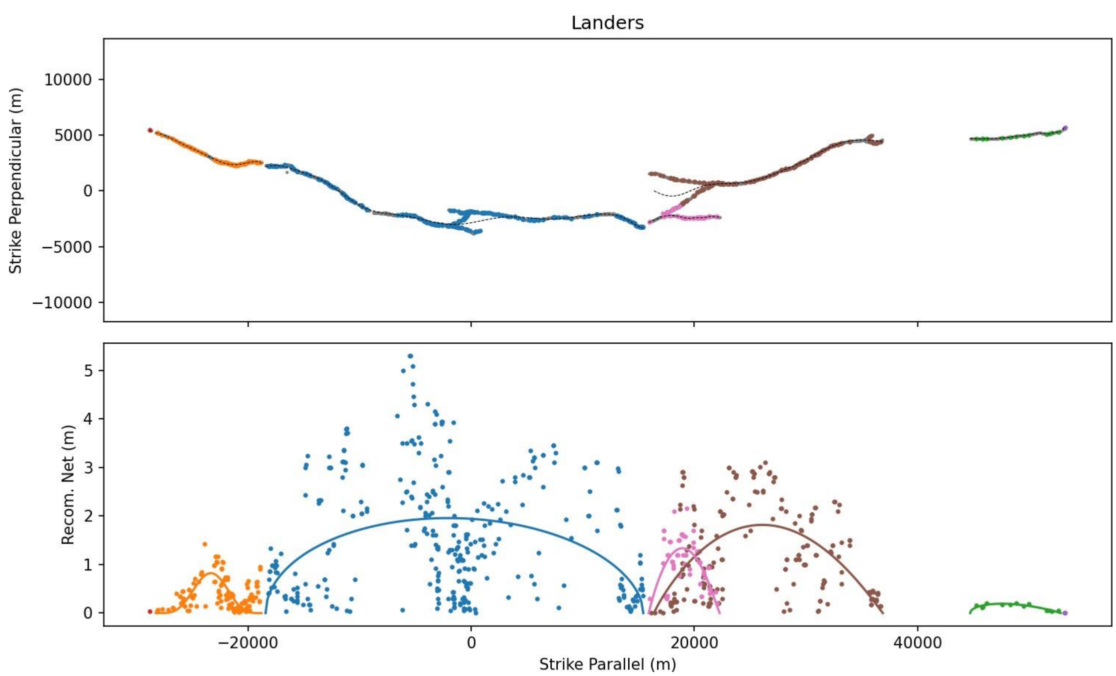

Figure A.8. Clustering algorithm results for 1992 **M** 7.28 Landers, California earthquake. (Top) Surface rupture map (thick gray lines) with segments (dashed black lines) and measurement sites (filled circles) color-coded by segment. (Botom) Displacement measurements for each segment (dots) with Beta distributon fits (lines).

A3 GEOLOGIC EVALUATIONS

We conducted geologic evaluatons of the events in the FDHI Database with the aim of beter understanding structural controls on the along-strike variability in displacement amplitude. As discussed in Automated Fault Segment Detecton, distnct fault segments can ofen be identfied *ex post facto* based on the rupture and displacement paterns; therefore, the algorithms tested in Automated Fault Segment Detecton were based solely on mapped rupture linework and displacement measurements. To test the feasibility of extending the algorithms to include structural controls, we performed manual geologic evaluatons of a subset of the earthquakes in FDHI Database to assess potental predictor variables for fault segmentaton. Two approaches were considered:

1 Defining segments by applying quanttatve rules to mapped ruptures.

2 Correlatng geologic complexites with low displacements using a robust complexity classificaton system.

The evaluatons were performed in ArcGIS sofware (ESRI, 2019). In each approach, we digitzed polygons around the rupture linework and used atribute fields to track details for the polygons. In all cases, only the rupture linework was used to define the polygons to ensure the methodology is applicable to forward-modeling. However, we viewed the locatons (but not amplitudes) of the measurement sites to ensure the polygons captured all measurement locatons. This was done because several events in the FDHI Database have distributed displacement measurements that are not along mapped ruptures. The displacement measurements were combined with the polygons to inherit the polygon atributes using the *Identty Analysis* tool in ArcGIS to evaluate the results. The results were visually evaluated with maps of the ruptures, displacements, and polygons alongside displacement profiles.

A3.1 Rules-Based Approach

The goal of this approach is to identfy fault segments based on geologic interpretaton of mapped surface rupture paterns to test our speculaton that fault displacement profiles at the segment-level are parabolic in shape. Toward this end, we digitzed polygons around geologically distnct segments for a subset of the events in the FDHI Database. The polygons were intended to capture kilometer-scale structural features that are typically biased in one directon (e.g., along-strike). Spatally contnuous features were grouped together, and contnuity was defined by bends or gaps in the rupture trace. Different criteria were used for principal ruptures and distributed ruptures. Sub-kilometer scale variatons in rupture contnuity were not considered.

The rules presented below were developed first through a literature review of geometric features associated with segment boundaries. We then refined the rules based on iterated evaluatons of a representatve strike-slip event (the 1999 **M** 7.51 Izmit–Kocaeli, Turkey) and normal event (the 1954 **M** 6.9 Dixie Valley, Nevada). In each iteraton, we digitzed the polygons based on the rules as faithfully as possible, notng where rules needed to be disregarded based on expert geologic judgment, and then refined the broken rules. We applied the final set of rules described below to 23 events and visually assessed the results.

Polygon Rules

The development of individual polygons is based chiefly on the contnuity of principal rupture traces. Three guidelines were used to quantfy contnuity:

P1 The mapped principal rupture trace does not exhibit significant changes in strike. A "significant change" is defined as a bend greater than or equal to 20°, and the change in strike must extend for 2 km in both directons.

P2 The mapped principal rupture trace also does not exhibit significant gaps. A "significant gap" is defined as greater than 1 km for principal ruptures.

P3 Parallel principal rupture traces should be grouped together in the same polygon unless the maximum distance between parallel traces is greater than 1 km or the parallel segments are each 2km or longer.

Guideline P1 is based on work by Elliot et al. (2015) that suggests restraining bends smaller than roughly 20° are not barriers to rupture propagaton, so we treat these as the same segment. The requirement that the bend affects the strike for 2 km in both directons avoids unnecessary excessive division of an otherwise contnuous segment and in partcular is an important requirement for normal faultng events, where the principal trace typically follows a sinuous range front.

Guideline P2 is based on our observaton that gaps in surface rupture appear to be spatally correlated with slip profile tapering. It is noted that forward-predicton of short gaps could be difficult, unless the gap is associated with a step-over.

Guideline P3 is based on our observaton that parallel or sub-parallel principal ruptures are relatvely common in the FDHI database, requiring a specific rule. We use the 1 km metric to be consistent with P2.

The development of the polygons should also consider distributed distributed rupture traces and measurement site locatons. Accordingly, we use the following two guidelines to assess if distributed ruptures and measurements should be assigned to separate polygons or grouped with an adjacent polygon developed using the principal rupture trace guidelines.

D1 When the distributed rupture linework and/or measurements are diffuse, the data should be included in the adjacent polygon containing a principal rupture, regardless of distance.

D2 When the distributed rupture linework and/or measurements are structurally distnct, the data should be included in a separate polygon if both of the following conditons are met; otherwise, the data should be included in the adjacent polygon.

(a) General strike is greater than 20° of the principal rupture strike, and

(b) Feature length is 3 km or greater.

Guideline D1 is based on our observaton that distributed displacement measurements that are not along mapped ruptures are relatvely common in the FDHI database. To avoid excessive polygons of spatally diffuse distributed slip measurements without any linear trend (e.g., a distributed fault segment), we include these diffuse measurements in the adjacent principal rupture polygon, regardless of distance. A cut-off distance may be necessary, depending on the results.

Guideline D2 is based the need to consider secondary structures or fault segments in a systematc way. The geometric relatons allow for proximal features sub-parallel to the principal rupture to be grouped together with the principal rupture, and other secondary structures that are spatally distnct from the principal rupture, such as a bifurcated trace, are assigned a separate polygon. The later case is the only instance in which a polygon may not contain principal ruptures or measurements.

Results

We completed the rules-based approach for 23 events in the FDHI Database (Table A.1). The results were assessed visually using maps and plots, and representatve results are shown in Figures A.9 through A.13. We considered the approach successful when the polygons captured parabolically-shaped displacement profiles. In general, we found the rules in Polygon Rules performed adequately for several events and/or parts of events. The most reliable segment indicators were overlapped or bifurcated principal traces and gaps or step-overs greater than about 3 km. We found that bends or changes in strike alone were not consistent indicators; however, bends that occurred with step-overs or other complexites were generally good indicators.

We identfied several situatons where the rules did not perform well, as summarized below:

1. The rules required adding segment boundaries at locatons that were near parabola peaks. For example, in segments [3,4] in Superstton Hills (Figure A.9); in segments [1,2] and [3,4] in Darfield (Figure A.11); in segments [3,4] in Dixie Valley (Figure A.12) in segments [7,8] and [9,10] in Luzon (Figure A.13).

2. The rules did not capture all segment boundaries, assuming that distnct displacement tapering represents a segment boundary. For example, segment 6 in Izmit-Kocaeli (Figure A.10); segment 6 in Luzon (Figure A.13).

3. Not all low displacement amplitudes are associated with segment boundaries. For example, segments 4 and 5 in Darfield (Figure A.11); segment 3 in Luzon (Figure A.13).

4. Displacement measurement sites are unevenly sampled; as a result, parabolic shapes cannot be discerned for some segments and the performance of the rules cannot be

evaluated. For example, segment 2 in Izmit-Kocaeli (Figure A.10); segment 11 Luzon (Figure A.13).

Based on our evaluaton of the 23 events tested, we concluded that copious event-specific rules adjustments would be required to make the rules-based approach robust. This in turn would limit the applicability of this approach in terms of model development and model applicaton.

Table A.1. Events evaluated in rules-based segment approach.

EQ_ID	Name	Magnitude	Style
56	BorahPeak	6.88	Normal
31	DixieValley	6.9	Normal
34	PleasantValley	7.2	Normal
24	Hebgen	7.3	Normal
30	FairviewPeak	7.3	Normal-Oblique
40	LagunaSalada	7.76	Normal-Oblique
18	Nagano	6.2	Reverse
19	Kashmir	7.6	Reverse
32	GalwayLake	5.2	Strike-Slip
36	ChalfantValley	6.19	Strike-Slip
57	ElmoreRanch	6.22	Strike-Slip
15	Hualien	6.4	Strike-Slip
42	Ridgecrest1	6.4	Strike-Slip
8	SupersttonHills	6.54	Strike-Slip
6	Borrego	6.63	Strike-Slip
9	Kobe	6.9	Strike-Slip
17	Kumamoto	7.0	Strike-Slip
21	Darfield	7.0	Strike-Slip
43	Ridgecrest2	7.1	Strike-Slip
2	HectorMine	7.13	Strike-Slip
5	Izmit_Kocaeli	7.51	Strike-Slip
4	Balochistan	7.7	Strike-Slip
55	Luzon	7.7	Strike-Slip

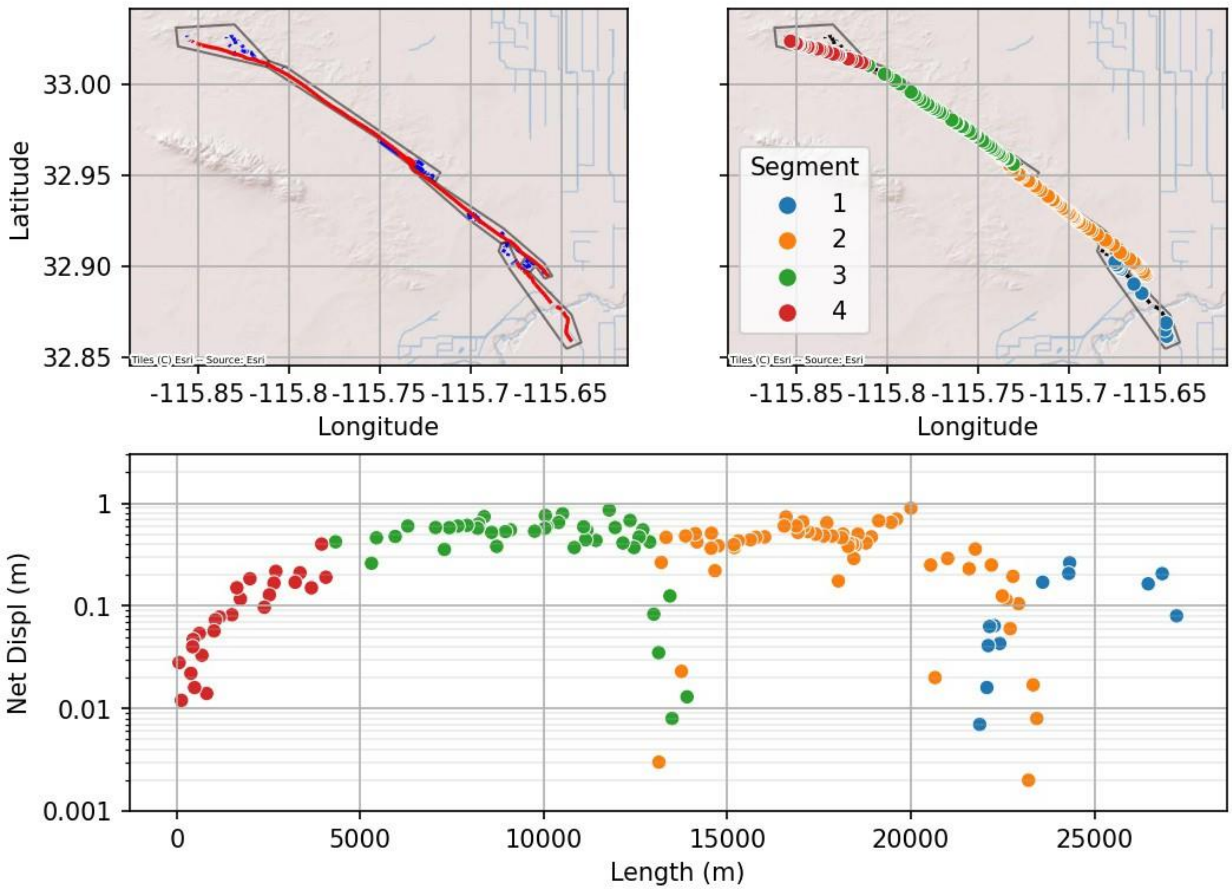

Figure A.9. Rules-based fault segment analysis for 1989 **M** 6.54 Superstton Hills, California earthquake. (Top Lef) Mapped surface ruptures (red = principal, blue = distributed and digitzed polygons (gray). (Top Right) Displacement measurements color-coded by rupture segment. (Botom) Net displacement amplitudes color-coded by rupture segment.

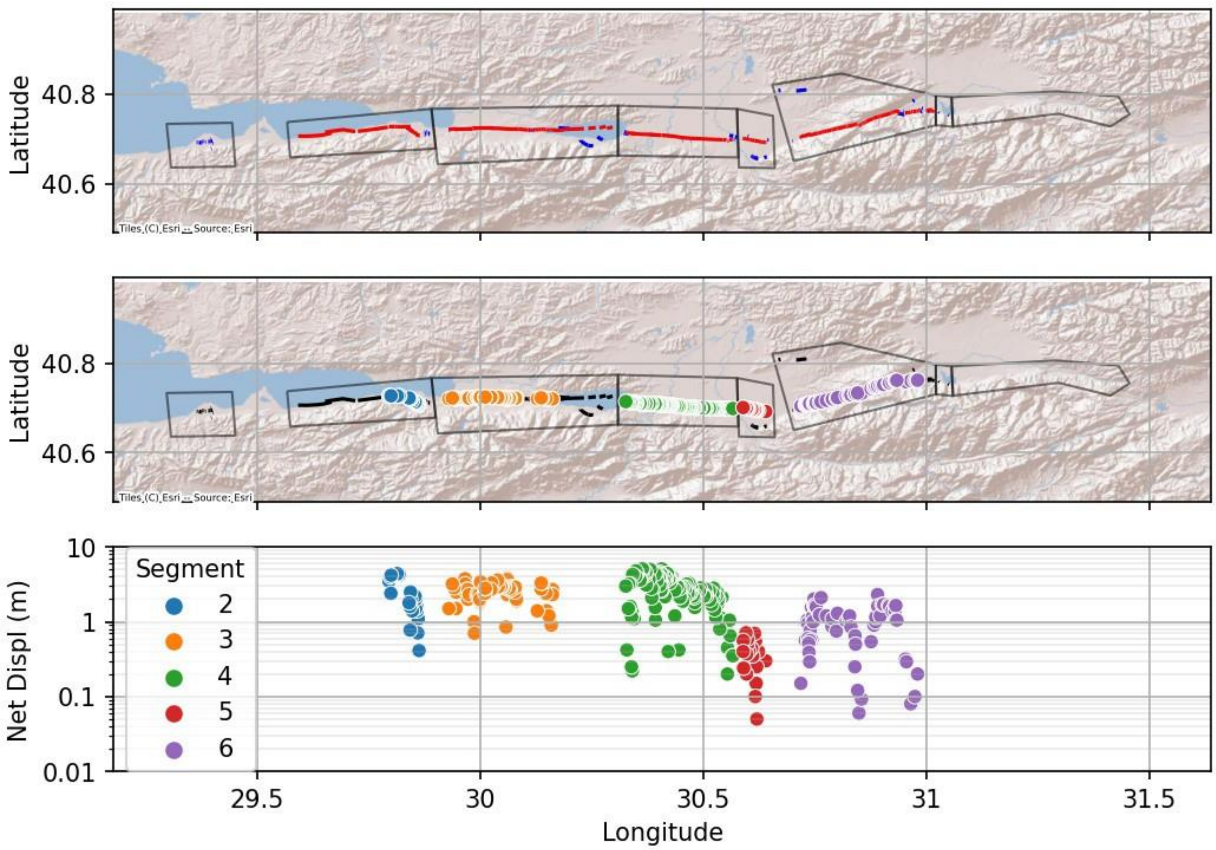

Figure A.10. Rules-based fault segment analysis for 1999 **M** 7.51 Izmit-Kocaeli, Turkey earthquake. (Top) Mapped surface ruptures (red = principal, blue = distributed and digitzed polygons (gray). (Middle) Displacement measurements color-coded by rupture segment. (Botom) Net displacement amplitudes color-coded by rupture segment.

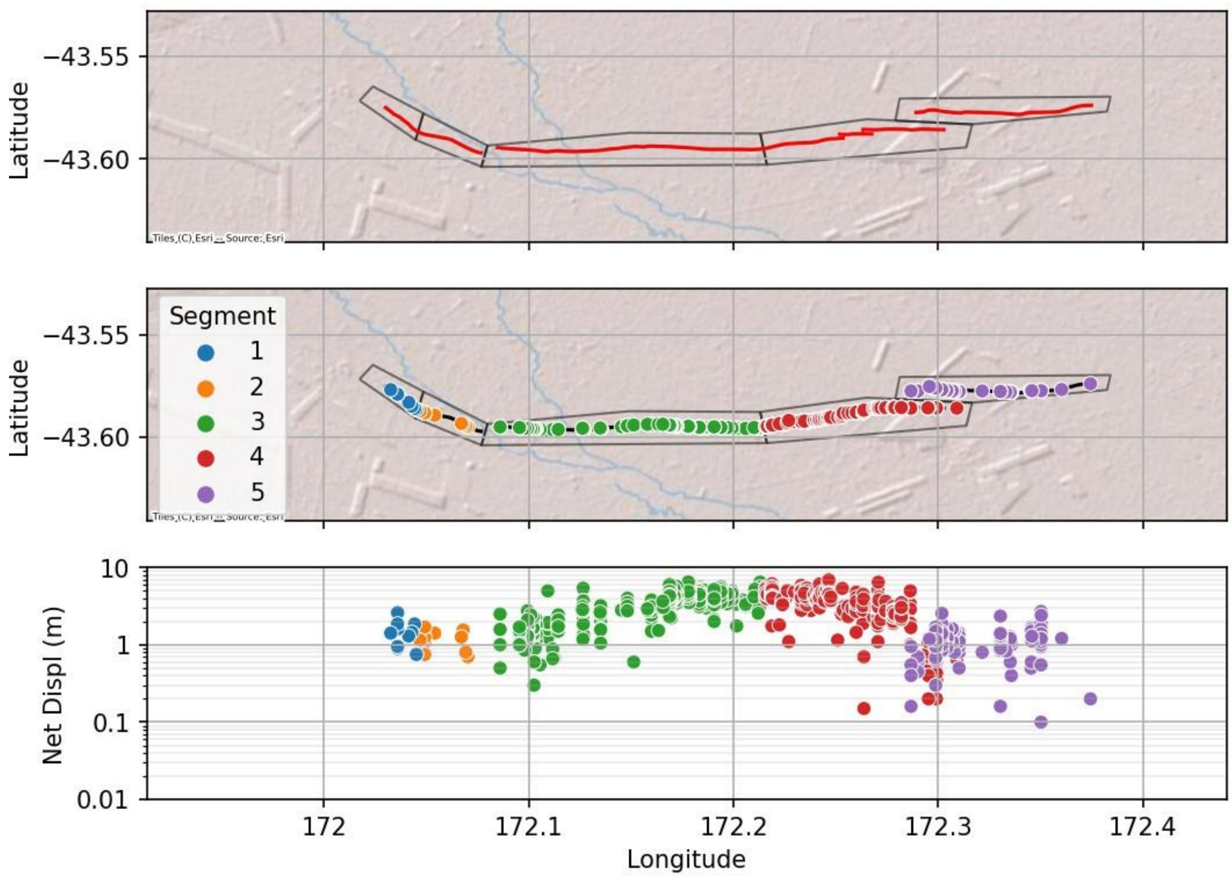

Figure A.11. Rules-based fault segment analysis for 2010 **M** 7.0 Darfield, New Zealand earthquake. (Top) Mapped surface ruptures (red = principal, blue = distributed and digitzed polygons (gray). (Middle) Displacement measurements color-coded by rupture segment. (Botom) Net displacement amplitudes color-coded by rupture segment.

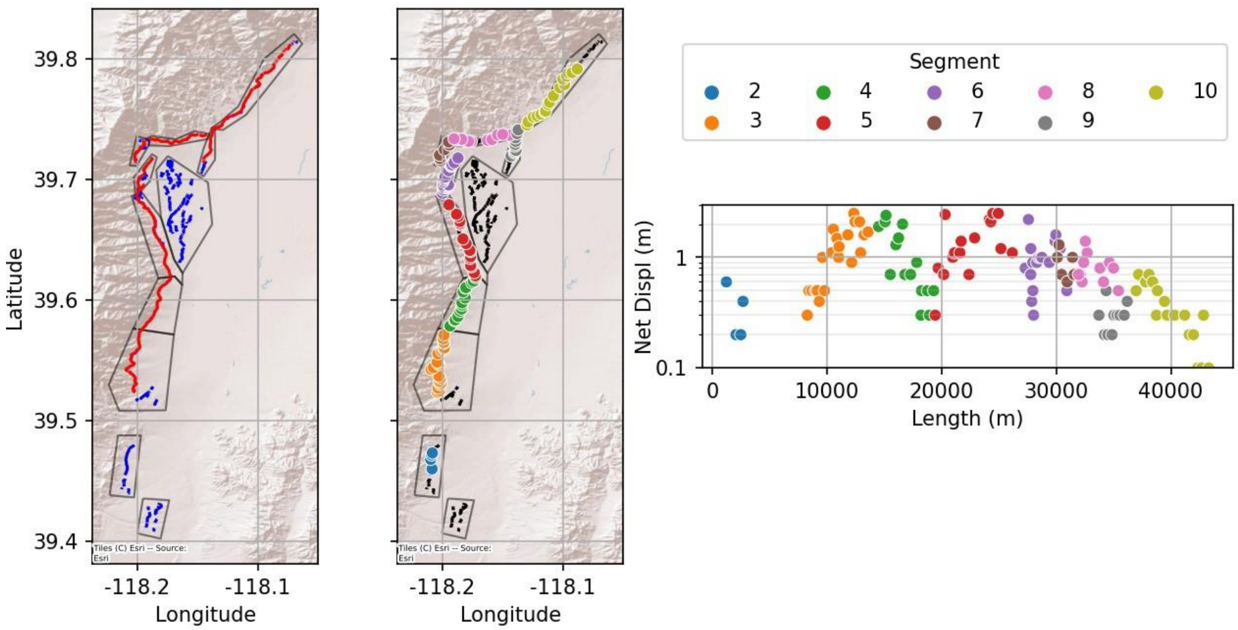

Figure A.12. Rules-based fault segment analysis for 1954 **M** 6.9 Dixie Valley, Nevada earthquake. (Lef) Mapped surface ruptures (red = principal, blue = distributed and digitzed polygons (gray). (Middle) Displacement measurements color-coded by rupture segment. (Right) Net displacement amplitudes color-coded by rupture segment.

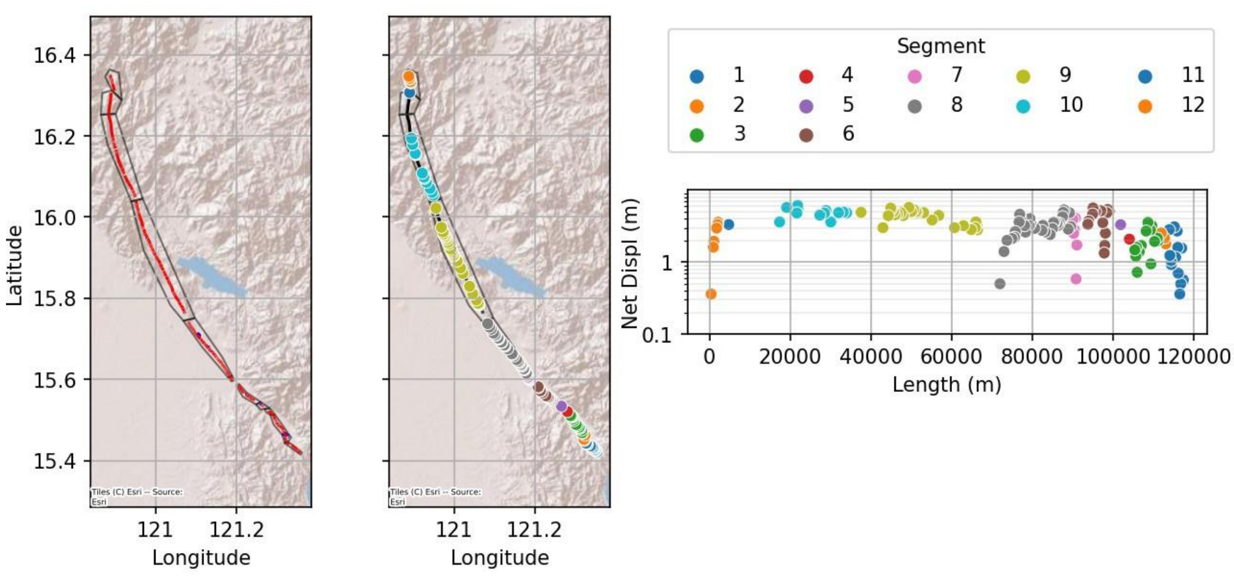

Figure A.13. Rules-based fault segment analysis for 1990 **M** 7.7 Luzon, Philippines earthquake. (Lef) Mapped surface ruptures (red = principal, blue = distributed and digitzed polygons (gray). (Middle) Displacement measurements color-coded by rupture segment. (Right) Net displacement amplitudes color-coded by rupture segment.

A3.2 Complexity Classificaton Approach

Segment boundaries are ofen, but not always, reliable indicators of low displacement amplitudes. However, identfying fault segments in historical surface ruptures is not unequivocal and is also challenging in forward-modeling applicatons. Recognizing these limitatons of a segment-based approach, we pursued a complexity classificaton approach. The goal of this approach is to classify surface rupture complexites to test our speculaton that low displacement amplitudes are associated with certain types of complexites. Toward this end, we devised a complexity code system based on Milliner et al. (2015) and applied it to a subset of the events in the FDHI Database. We also assessed the ability of a geologist to antcipate the manifested complexity *a priori* for use in forward-modeling.

Complexity Code System

Our complexity code system was motvated by the "Qualitatve Complexity Ratng" in Milliner et al. (2015):

1. Straight, contnuous single-stranded
2. Segmented, semi-contnuous trace with smaller secondary faultng
3. Dual-stranded or greater number of secondary faultng
4. Abundant secondary faultng, subtle-moderate bends in fault trace
5. Step-overs, highly diffuse areas of faultng, macroscopic fault bends.

The five-step ratng bookends simple and complex surface rupture paterns. To beter investgate the influence of specific complexites, we expanded on the Milliner et al. (2015) ratng system to explicitly describe principal and distributed ruptures and the interacton between the two types of ruptures. We used a *P-D* paired code system, where *P* and *D* correspond to integer codes describing the principal and distributed rupture characteristcs, respectvely (Tables A.2 and A.3).

Table A.2. Complexity code system for principal ruptures.

Principal Rupture Descripton	Code
No principal strands	0-D
Single principal strand, bends nil to moderate	1-D
Single principal strand, significant bends	2-D
Segmented principal strand, bends nil to moderate	3-D
Segmented principal strand, significant bends	4-D
Anastomizing/en-echelon/parallel principal strands	5-D
Diffuse/segmented principal strands	6-D
Bifurcatng principal strands	7-D

Table A.3. Complexity code system for distributed ruptures.

Distributed Rupture Descripton	Code
No/nil distributed strands	P-0
Contnuous secondary structure, single strand	P-1
Contnuous secondary structure, multple strands	P-2
Segmented/anastomizing/en-echelon distributed strands	P-3
Diffuse distributed strands	P-4

Results

We applied the complexity code system to four events in the FDHI Database (Table A.4). Through this limited subset, we found the approach to be highly sensitve to mapping scale and quality. Importantly, we also noted that many complexites found in the historical data were not mappable prior to the event, such as gaps in the Borah Peak range front rupture or distributed ruptures in Warm Springs Valley (Figure A.14). Accordingly, this approach was not pursued further.

Table A.4. Events evaluated in complexity code system approach.

EQ_ID	Name	Magnitude	Style
56	BorahPeak	6.88	Normal
8	SupersttonHills	6.54	Strike-Slip
2	HectorMine	7.13	Strike-Slip
55	Luzon	7.7	Strike-Slip

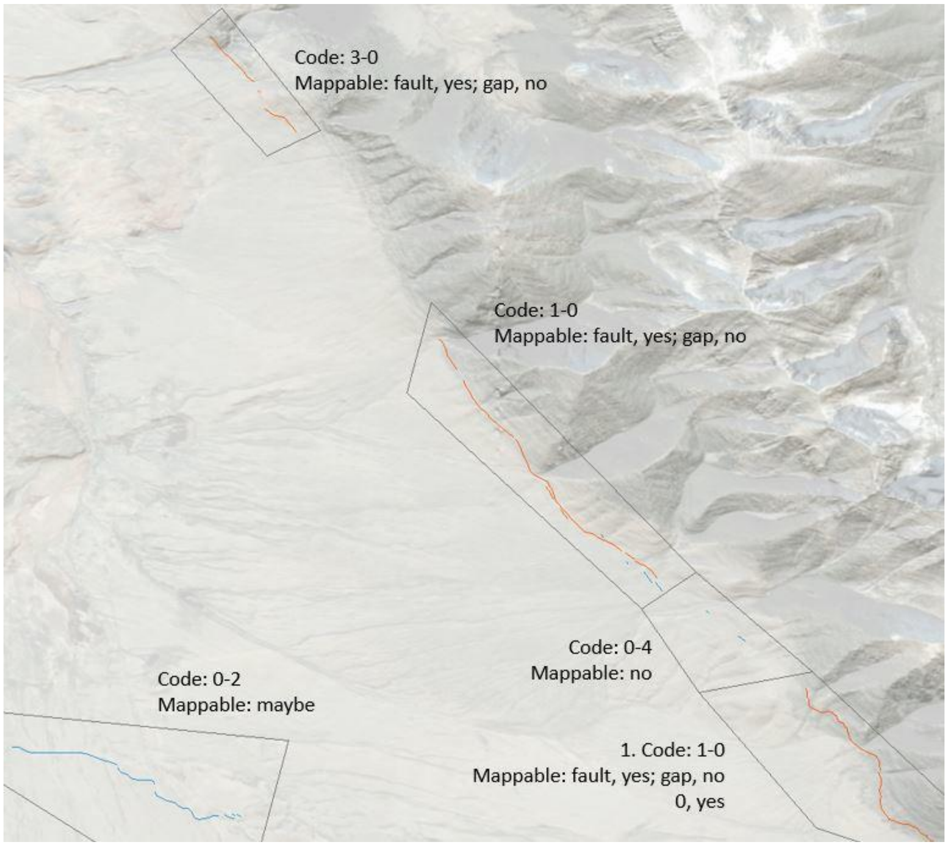

Figure A.14. Complexity code analysis for porton of 1983 **M** 6.88 Borah Peak, Idaho earthquake.

A4 TERRAIN-BASED INDICATORS

In ground-moton modeling, the tme-averaged velocity over the upper 30 m (V_{S30}) has been found to be a robust parameter for estmatng the influence of local conditons on ground motons. Researchers have then examined opportunites to use proxy methods (e.g., geology, terrain, slope) to estmate V_{S30}. Using this process as motvaton, a number of terrain metrics were examine in hopes to beter predict fault displacement. Three questons were asked:

1. Does the terrain influence the tendency for more or less displacement at a locaton?
2. Does the terrain influence the expression of the faultng at the surface?
3. How does the rupture patern or level of complexity influence the parttoning of displacement?

To answer these questons, the model residuals from Model Performance are compared with the elevaton data and metrics in the FDHI Database (Sarmiento et al., 2021) quantfy ground slope and surface irregularites or terrain texture (i.e., density of topographic peaks and troughs) in the vicinity of the measurement site. The following elevaton data and metrics are included in the database:

- Elevaton (meters)
- Ground slope (percent)
- Prominence or relatve elevaton per Rai et al. (2017): difference between pixel elevaton at site and mean elevaton of all pixels in N-meter radius (where N = 125, 250, 500, and 1000)
- Terrain roughness: largest difference between pixel elevaton at site and elevaton of all adjacent pixels
- Topographic Positon Index (TPI): difference between pixel elevaton at site and mean elevaton of all adjacent pixels
- Terrain Ruggedness Index (TRI) per Riley et al. (1999): total elevaton change between pixel elevaton at site and all adjacent pixel elevatons
- Terrain class based on ground slope and texture per Iwahashi et al. (2018) (Table A.5)
- Geology

Table A.5. Terrain classificaton code afer Iwahashi et al. (2018).

Code	Geomorphic Terrain Descripton
1	steep mountain, rough
2	steep mountain, smooth
3	moderate mountain, rough
4	moderate mountain, smooth
5	hills, rough in small and large scales
6	hills, smooth in small scale, rough in large scale
7	upper large slope
8	middle large slope
9	dissected terrace, moderate plateau
10	slope in and around terrace or plateau
11	terrace, smooth plateau
12	alluvial fan, pediment, bajada, pediplain
13	alluvial plain, pediplain
14	alluvial or coastal plain, pediplain
15	alluvial or coastal plain (gentlest), lake plain, playa

A41 Influence of Terrain on Aggregated Displacement

The residuals are shown on Figures A.15 to A.25. The trends within the cloud of residuals are visualized by a LOESS fit through the data, which is a non-parametric trend line. No trends are observed in the residuals, suggestng that the terrain metrics do not impact the predicted aggregated displacement. It is important to note that this comparison is on the aggregated displacements. Thus, the aggregaton process that is being used to sum the discrete fault displacement perpendicular to fault strike results in displacement values that are not sensitve to the terrain.

A42 Surface Rupture Paterns

The surface rupture expression or patern is divided into four categories: simple, distributed only, other only, and complex based on the calculated aggregated net displacement. These are defined as follows:

Simple no other fault rupture included in the aggregaton; offset from only one primary trace

Distributed only aggregaton includes the parent primary trace observaton and other distributed traces

Other only aggregaton includes the parent primary trace observaton and other primary traces

Complex aggregaton includes the parent primary trace observaton, other primary traces, and distributed traces

The residuals are shown on Figures A.26 to A.34. The trends within the cloud of residuals are visualized by a LOESS fit through the data, which is a non-parametric trend line. There appear to be trends in the data—partcularly with respect to the slope or the topographic prominence. For normal faultng events, flat slopes are associated with a higher tendency for simple fault expression. As the slope (or topographic prominence) increases, the normal faultng becomes more distributed. Interestngly, these trends are the opposite for Reverse and Strike-Slip styles of faultng with steep slopes (or high topographic prominence) tending to be simpler in expression. The conclusions here are based on lumping all earthquakes together and the conclusions for the normal style of faultng might be strongly influenced by the large number of observatons from the Norcia3 event.

While not part of this study, a similar inspecton could be performed on the optcal data produced by Milliner et al. (2020) to examine if the fault zone width is influenced by the terrain.

The previous plots (Figures A.26 to A.34) demonstrated a potental connecton between terrain and surface rupture paterns, but for this to be useful for predicton of fault displacement there needs to be a model to relate the aggregated displacement to the other mechanisms. The distributed fracton represents the fracton of the aggregated net displacement that occurs off of the primary observaton. If this value is 0, then the all of the observed displacement occurs on the primary observaton. If this value is 0.50, then half of the aggregated displacement is from other sources. This influence was examined in two ways. First, a functon of the terrain metrics, shown in Figures A.35 to A.43. There is separaton in in the distributed fracton from the different styles of expression, but there don't appear to be a meaningful trends. In other words, the terrain doesn't appear to influence how much offset is parttoned between the primary offset and other aggregated offsets. Another way to look at the data is the distributed fracton by style of faultng and type of expression, shown in Figure A.44. This was done in Secton 8, but did not include all of the surface rupture expressions considered here. Here we can make a few conclusions. For only distributed deformaton, about 50% of the offset is accommodated for Normal faults, and around 10-20% for Reverse and Strike-Slip. For only principal traces, about 50% of the offset is accommodated for all styles of faultng. For complex expression, the distributed fracton is about 70-80%.

While the conclusions of this study are preliminary, there are potental major implicatons for future fault displacement models. The general process would be to compute an aggregated net displacement, and then examine the terrain at the locaton of interest and predict the potental rupture patern (e.g., 80% simple, 15% distributed only, and 5% complex). For each of these cases, the distributed fracton could then be used to estmate the amount of displacement at the site and its uncertainty.

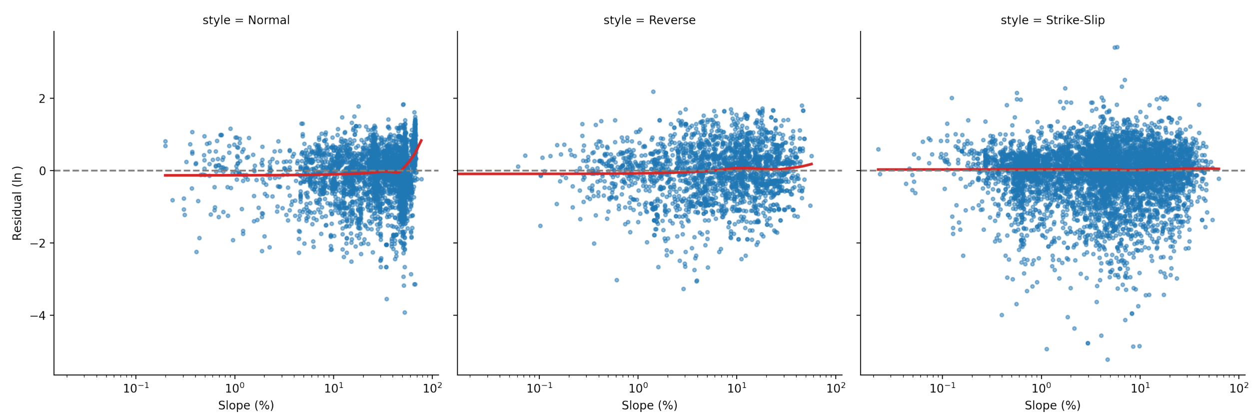

Figure A.15. Model residuals relatve to Slope (m/m), Gaussian gradient model.

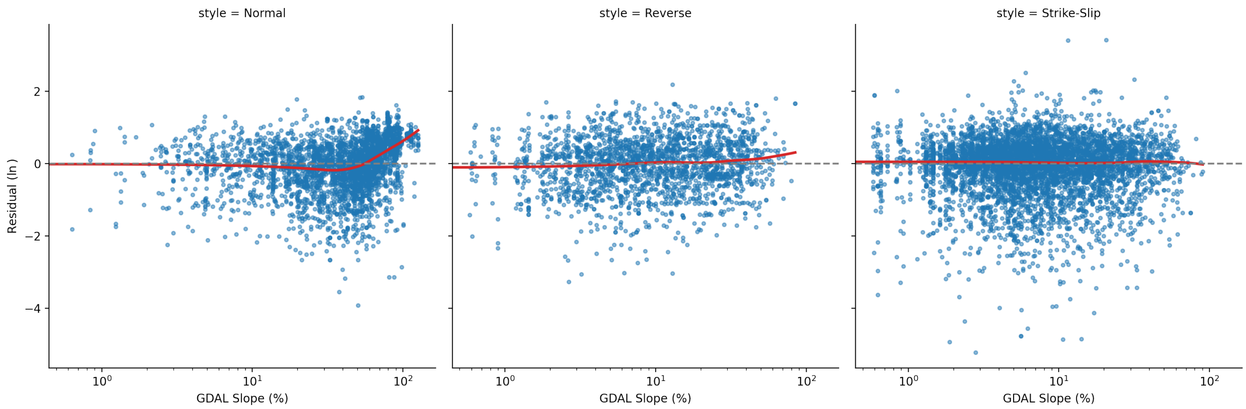

Figure A.16. Model residuals relatve to Slope (m/m), GDAL Horn's formula.

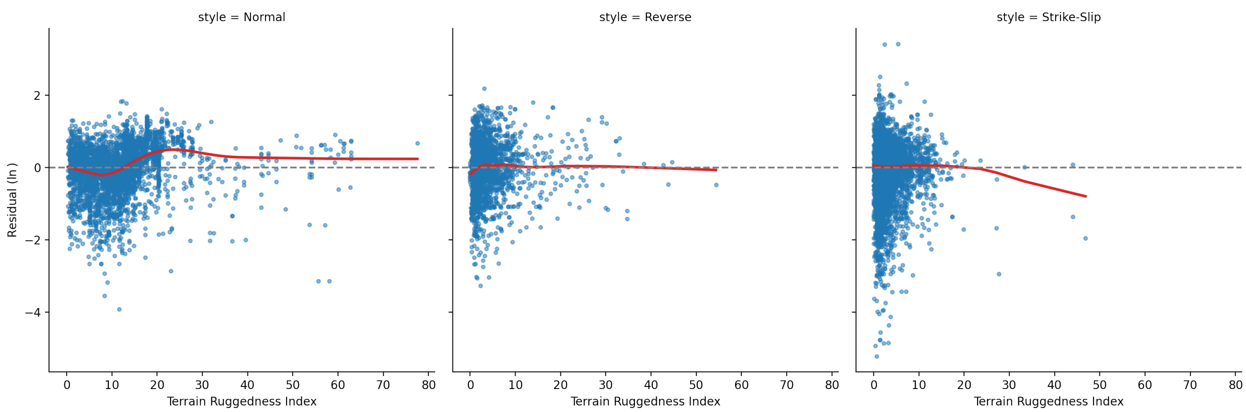

Figure A.17. Model residuals relatve to Terrain Ruggedness Index (TRI).

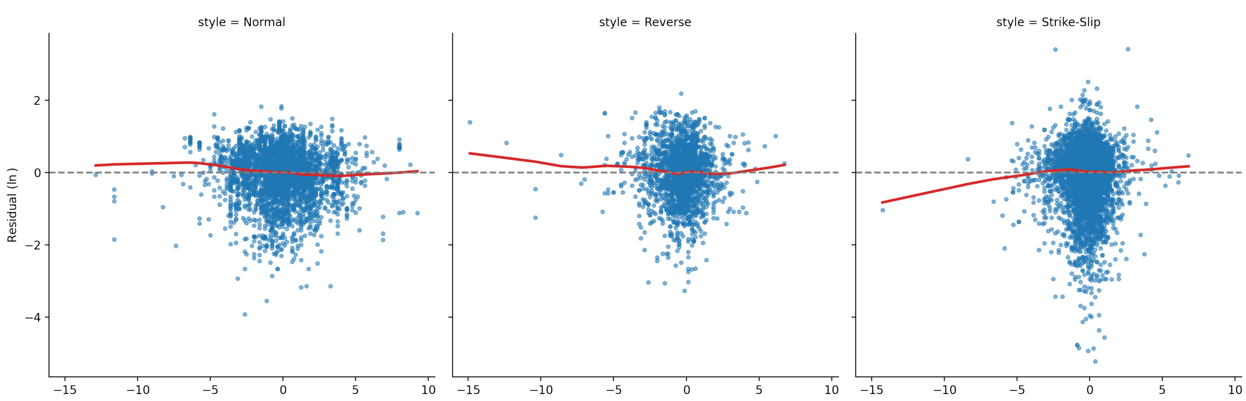

Figure A.18. Model residuals relatve to Slope (m/m), Gaussian gradient model.

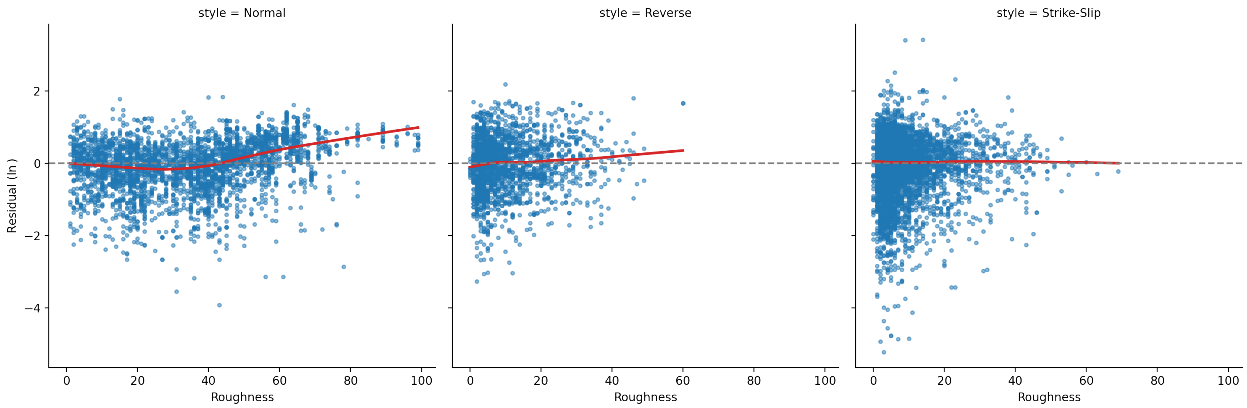

Figure A.19. Model residuals relatve to Topographic Positon Index (TPI).

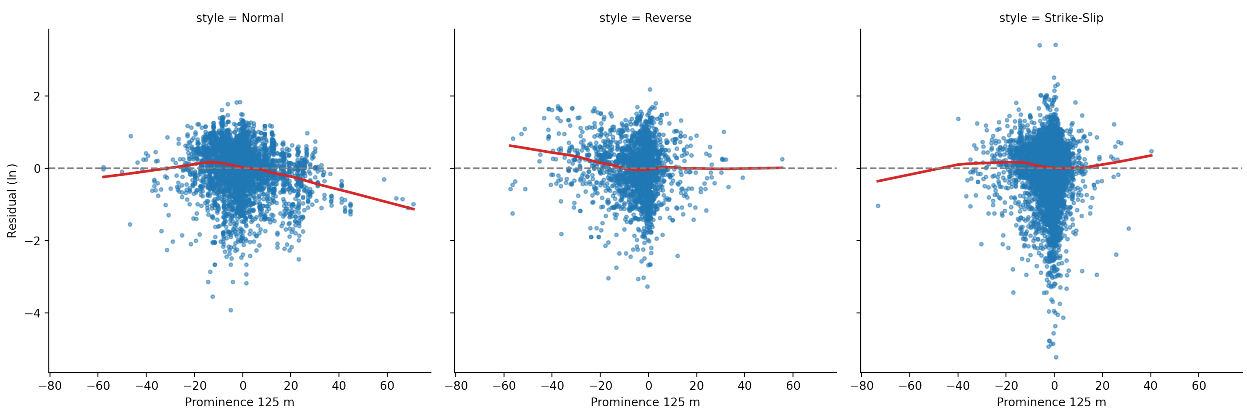

Figure A.20. Model residuals relatve to terrain Roughness.

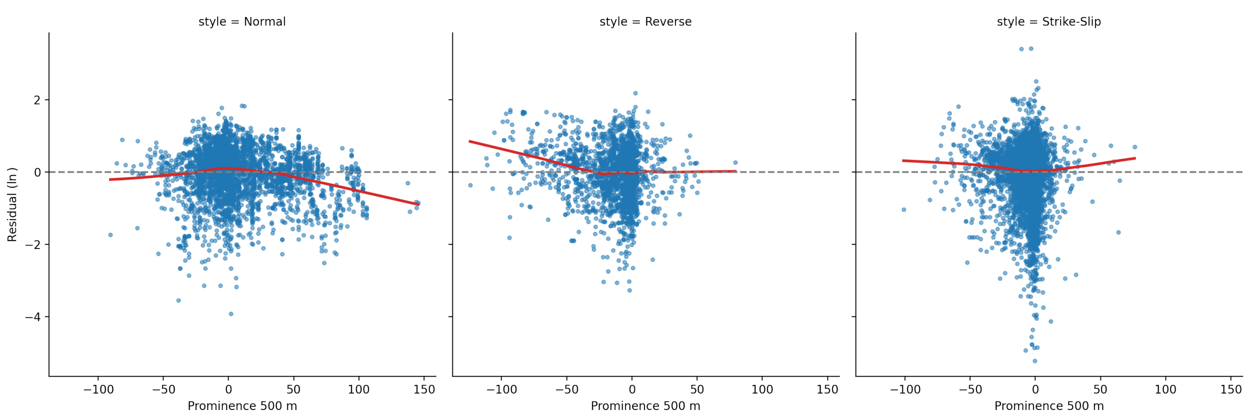

Figure A.21. Model residuals relatve to Prominence, 125-m radius.

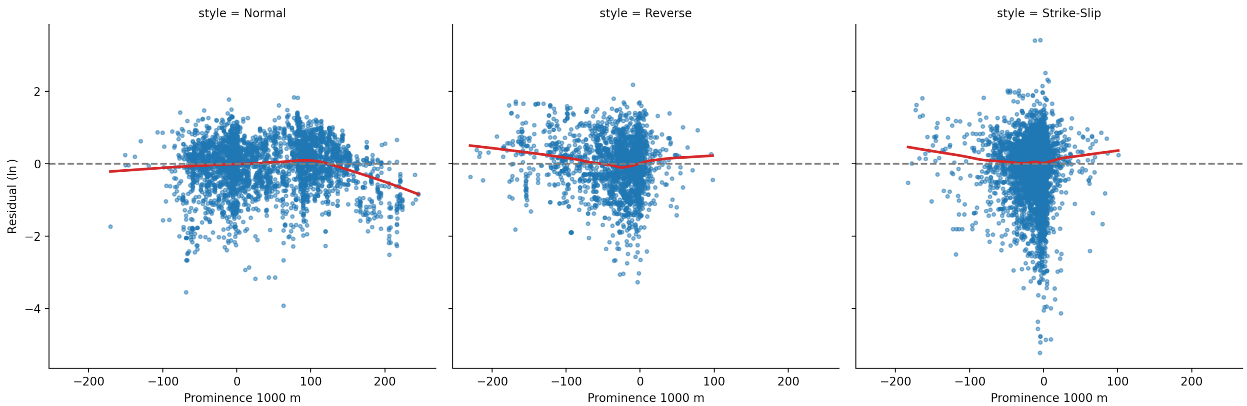

Figure A.22. Model residuals relatve to Prominence, 500-m radius.

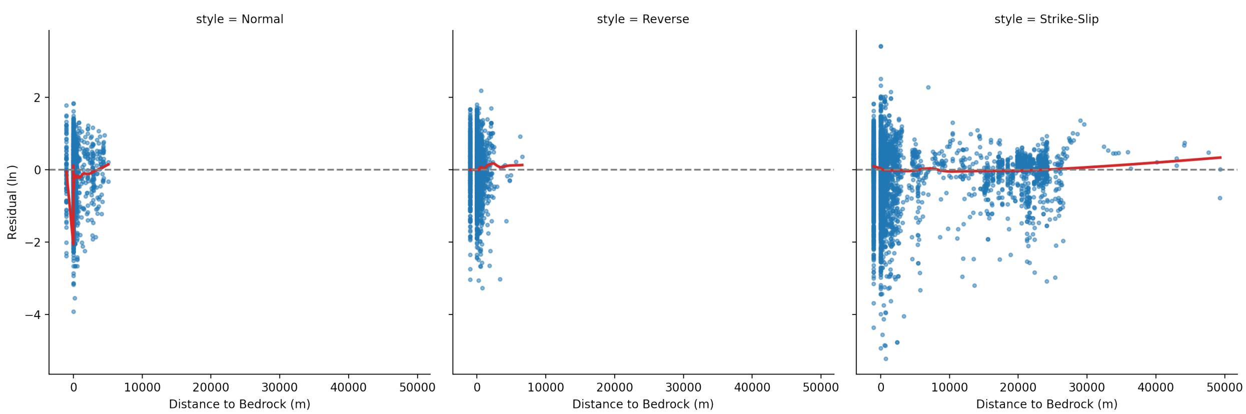

Figure A.23. Model residuals relatve to Prominence, 1000-m radius.

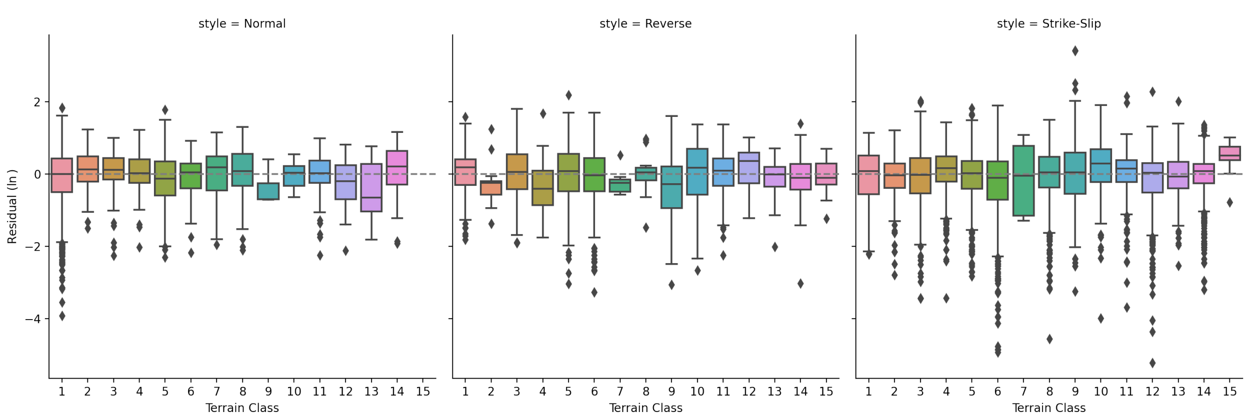

Figure A.24. Model residuals relatve to Terrain Class from Iwahashi et al. (2018).

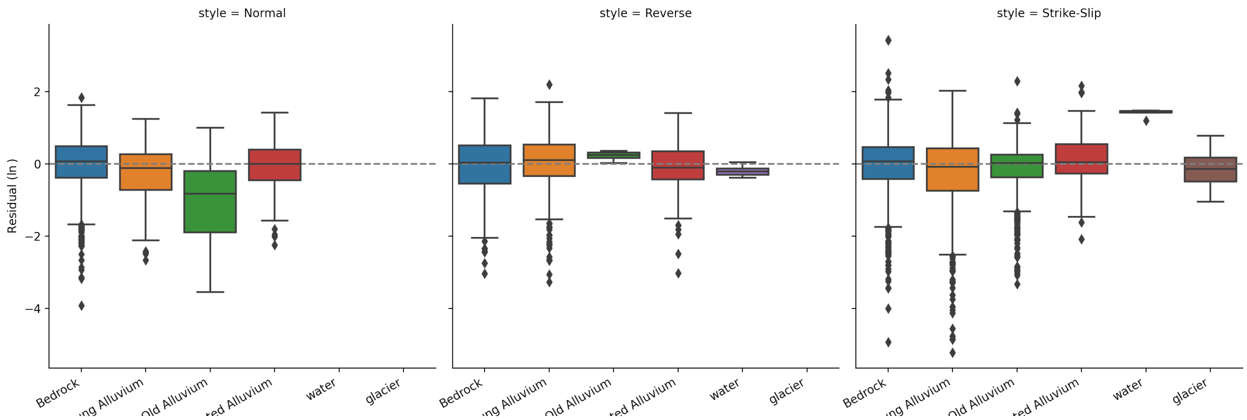

Figure A.25. Model residuals relatve to distance to bedrock (m).

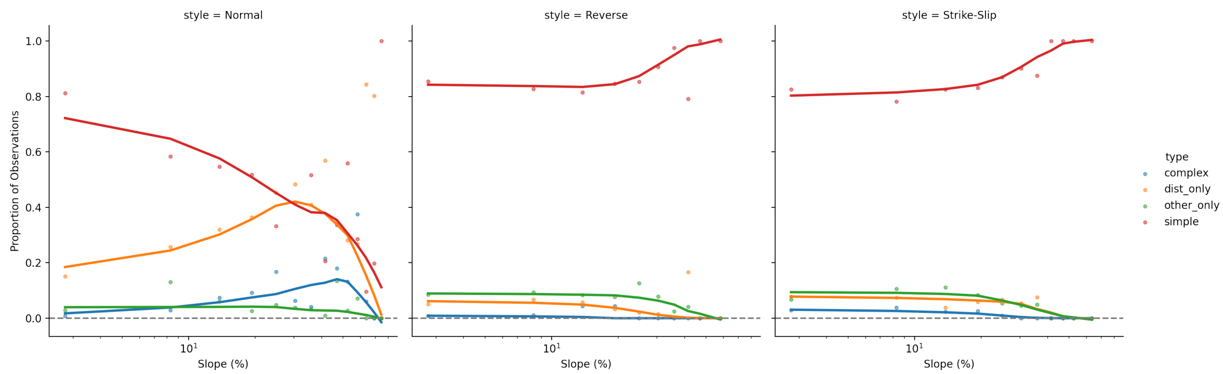

Figure A.26. Proporton of observatons of expression relatve to Slope (m/m), Gaussian gradient model.

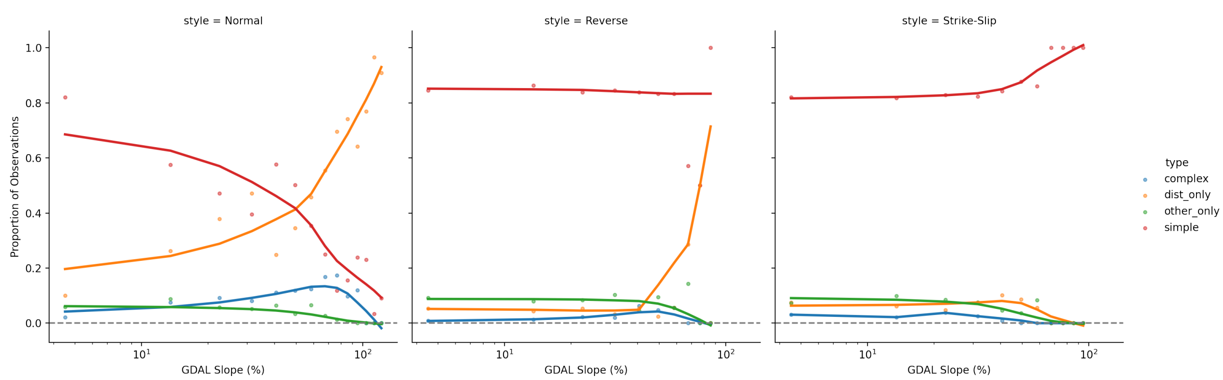

Figure A.27. Proporton of observatons of expression relatve to Slope (m/m), GDAL Horn's formula.

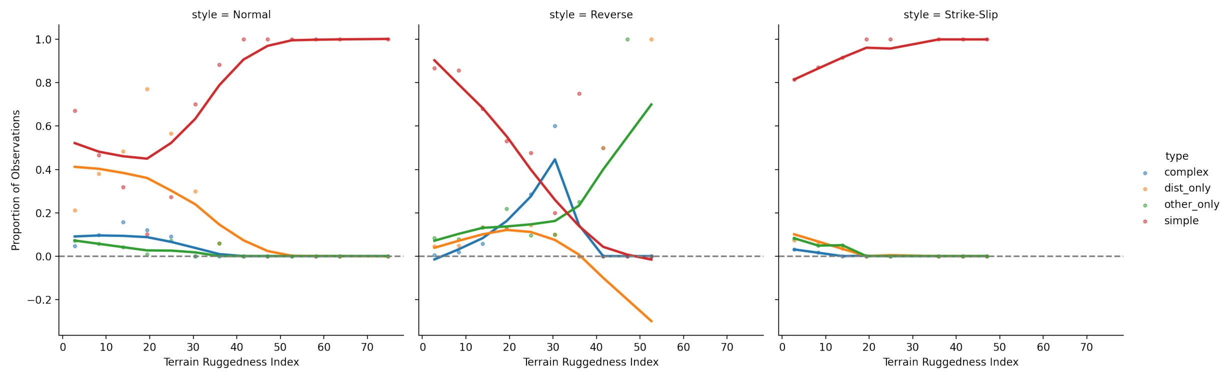

Figure A.28. Proporton of observatons of expression relatve to Terrain Ruggedness Index (TRI).

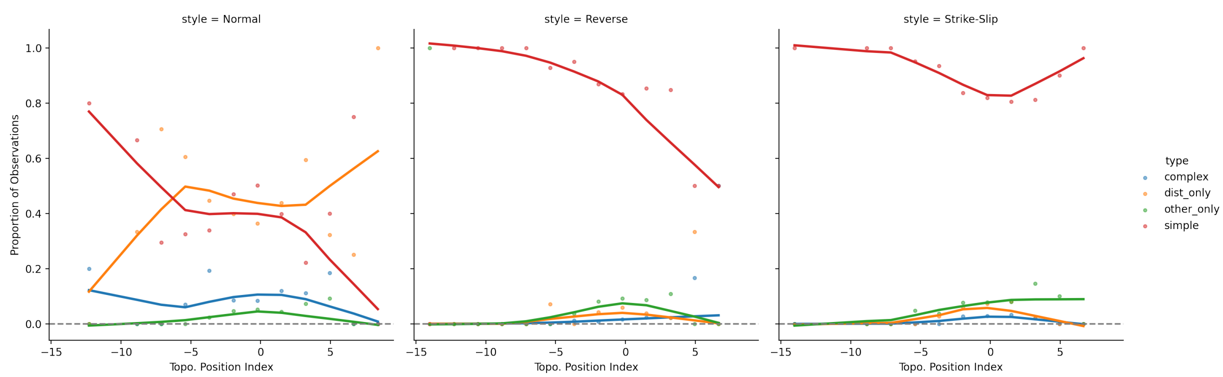

Figure A.29. Proporton of observatons of expression relatve to Slope (m/m), Gaussian gradient model.

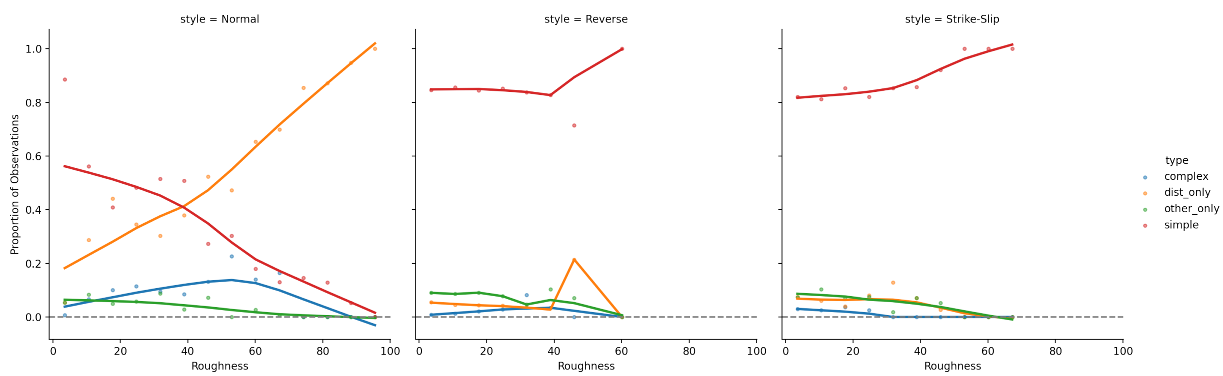

Figure A.30. Proporton of observatons of expression relatve to Topographic Positon Index (TPI).

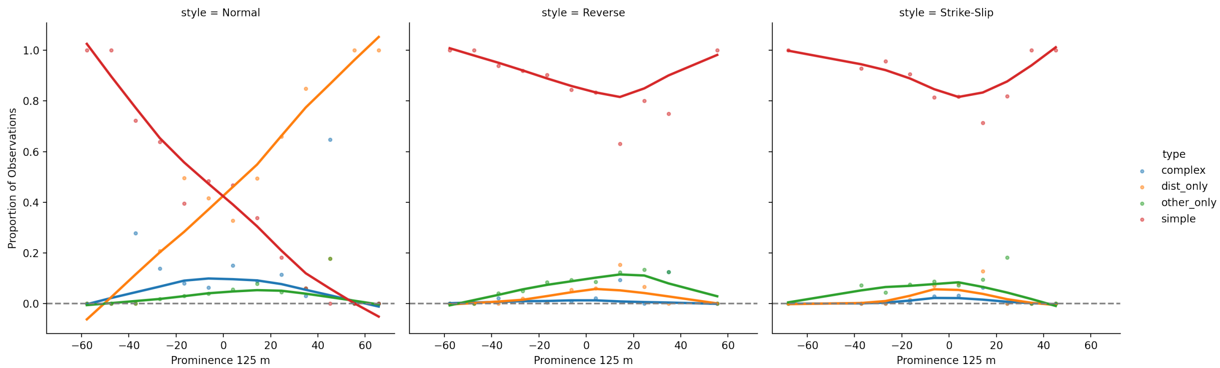

Figure A.31. Proporton of observatons of expression relatve to terrain Roughness.

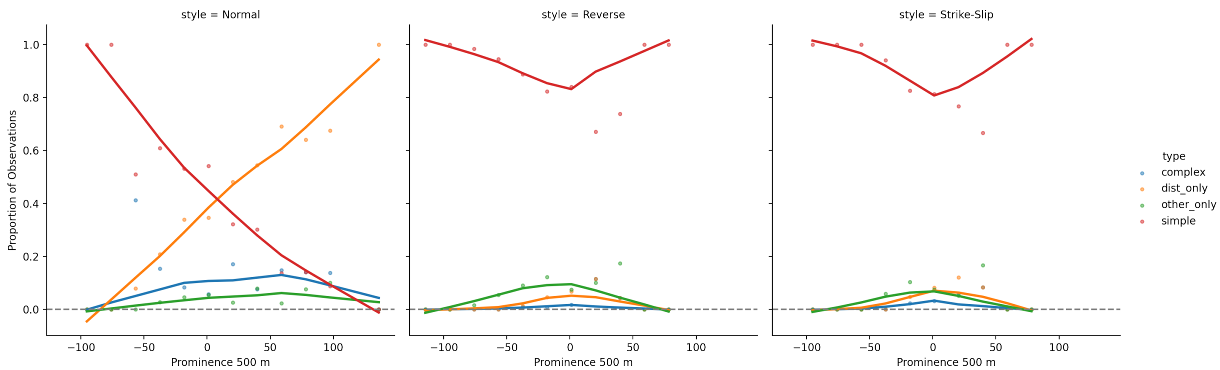

Figure A.32. Proporton of observatons of expression relatve to Prominence, 125-m radius.

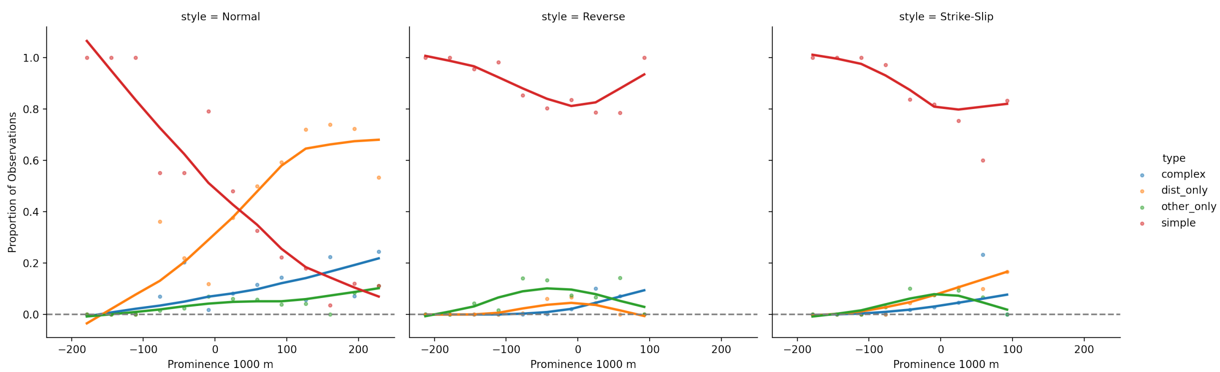

Figure A.33. Proporton of observatons of expression relatve to Prominence, 500-m radius.

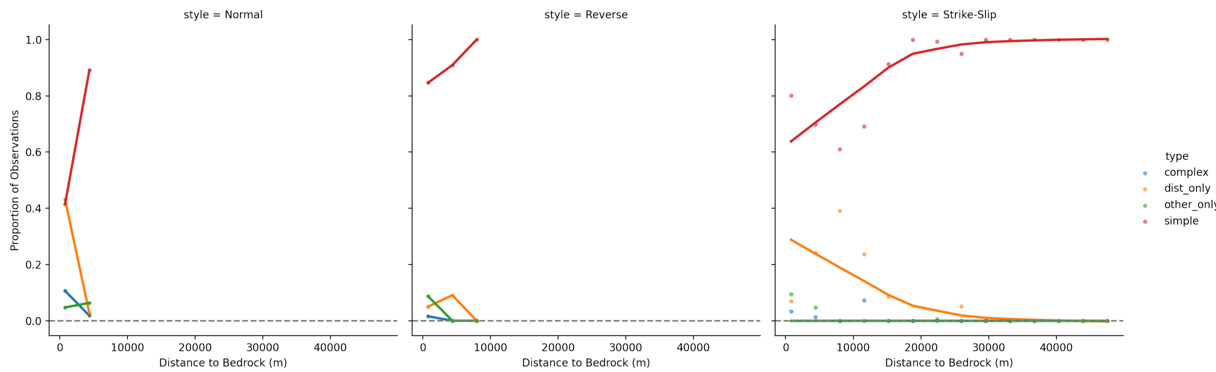

Figure A.34. Proporton of observatons of expression relatve to Prominence, 1000-m radius.

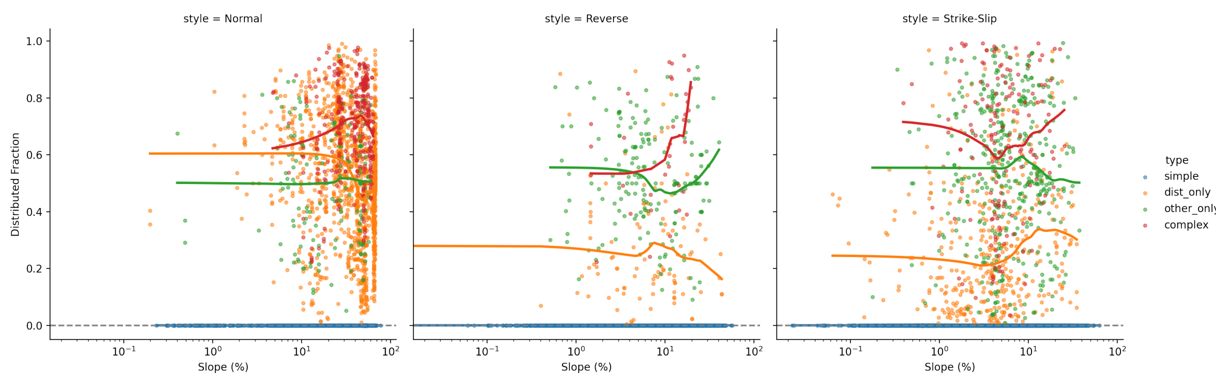

Figure A.35. Distributed fracton relatve to Slope (m/m), Gaussian gradient model.

Figure A.36. Distributed fracton relatve to Slope (m/m), GDAL Horn's formula.

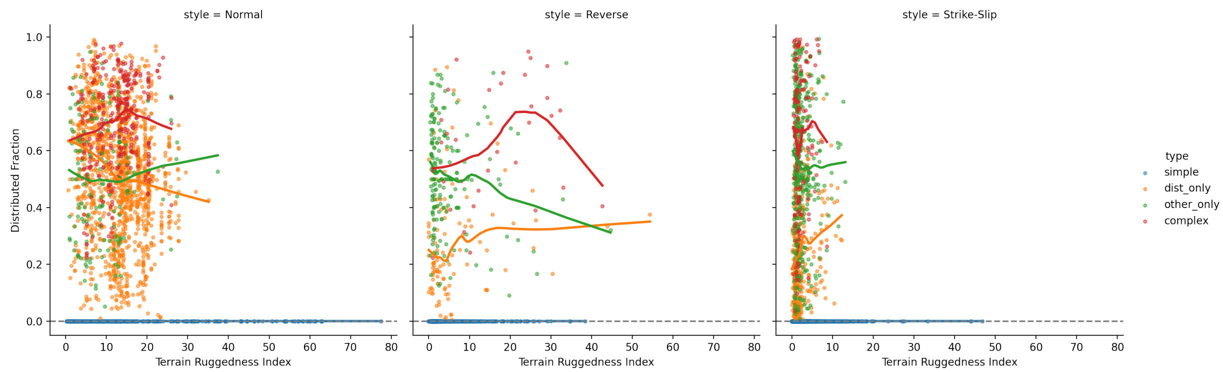

Figure A.37. Distributed fracton relatve to Terrain Ruggedness Index (TRI).

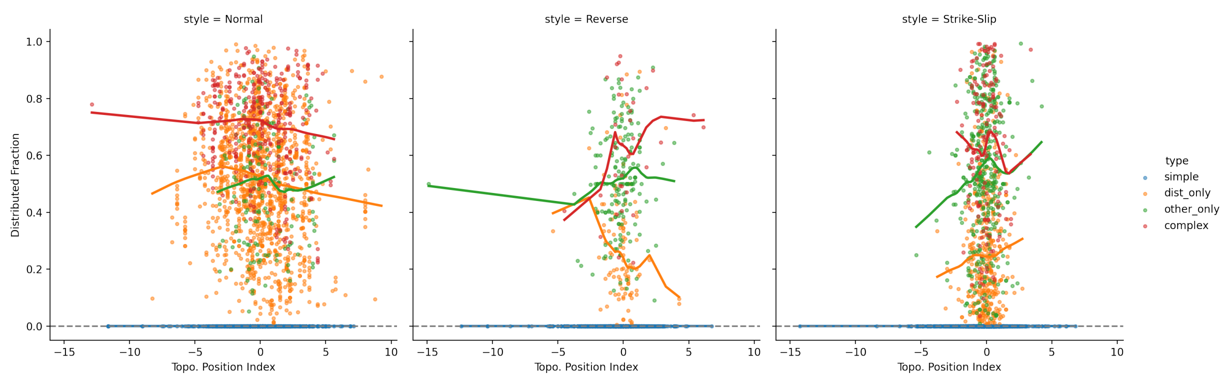

Figure A.38. Distributed fracton relatve to Slope (m/m), Gaussian gradient model.

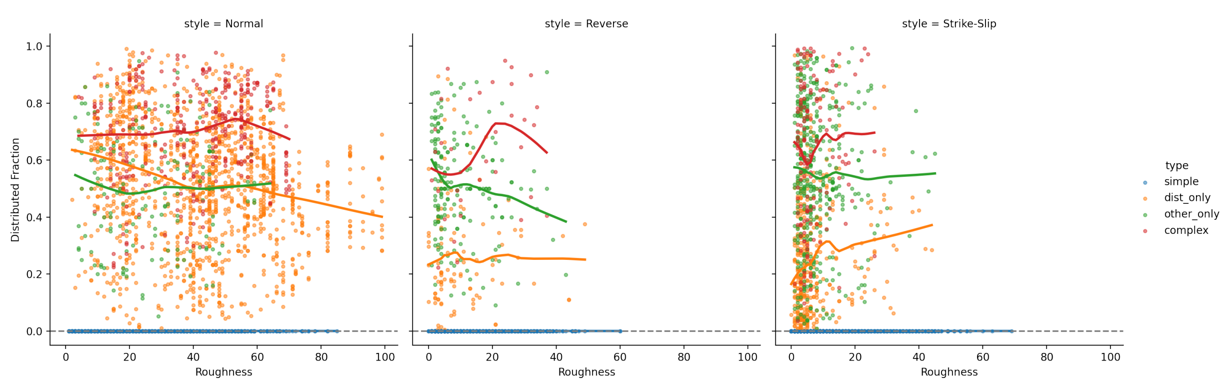

Figure A.39. Distributed fracton relatve to Topographic Positon Index (TPI).

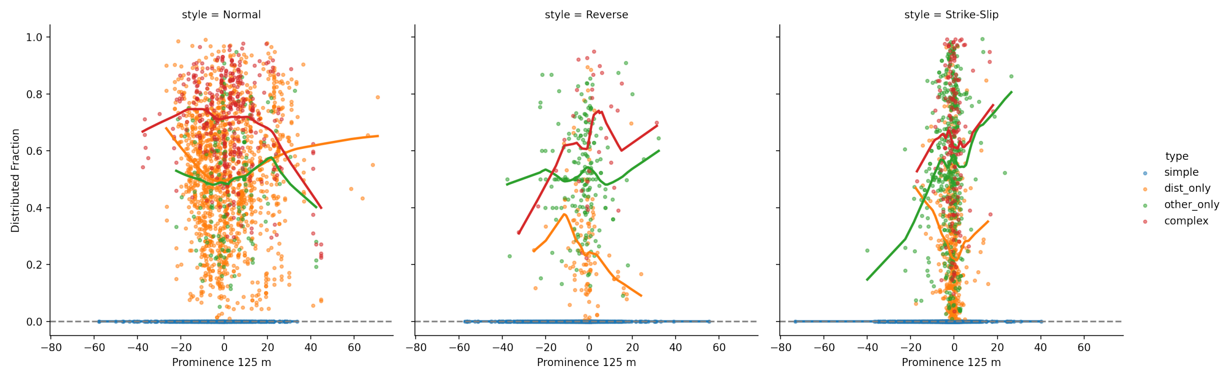

Figure A.40. Distributed fracton relatve to terrain Roughness.

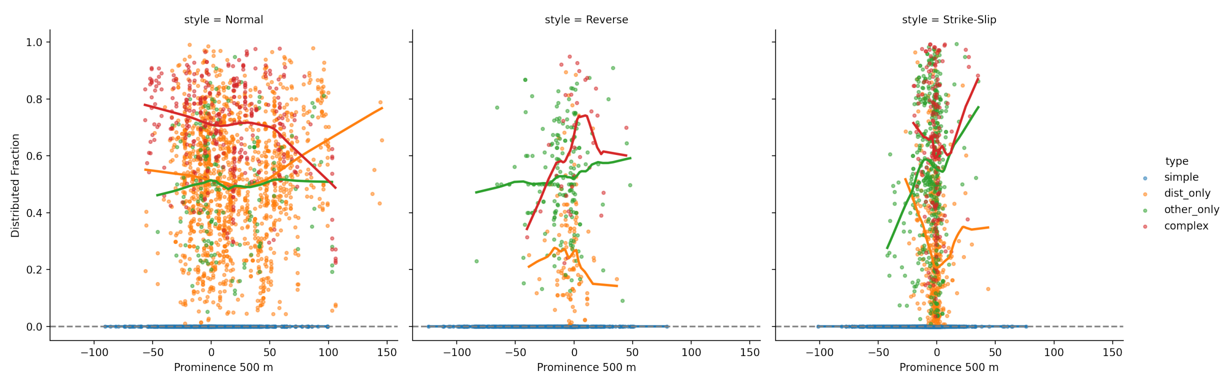

Figure A.41. Distributed fracton relatve to Prominence, 125-m radius.

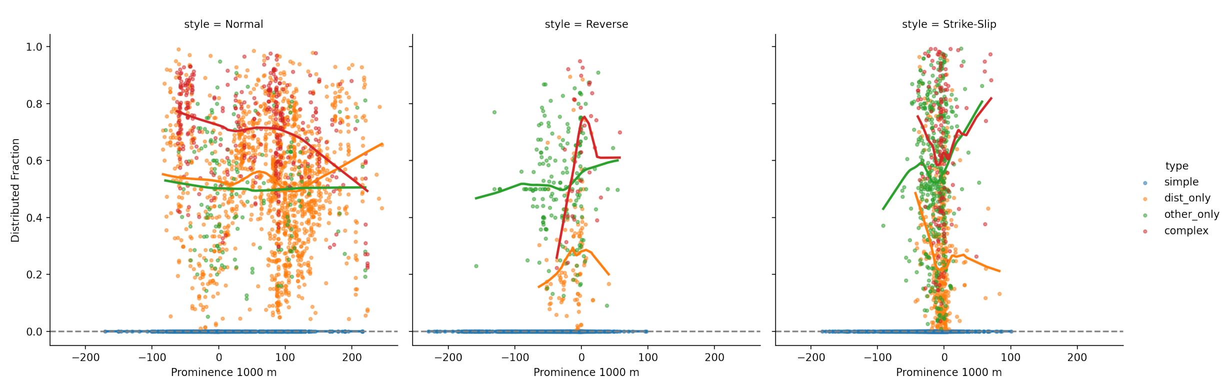

Figure A.42. Distributed fracton relatve to Prominence, 500-m radius.

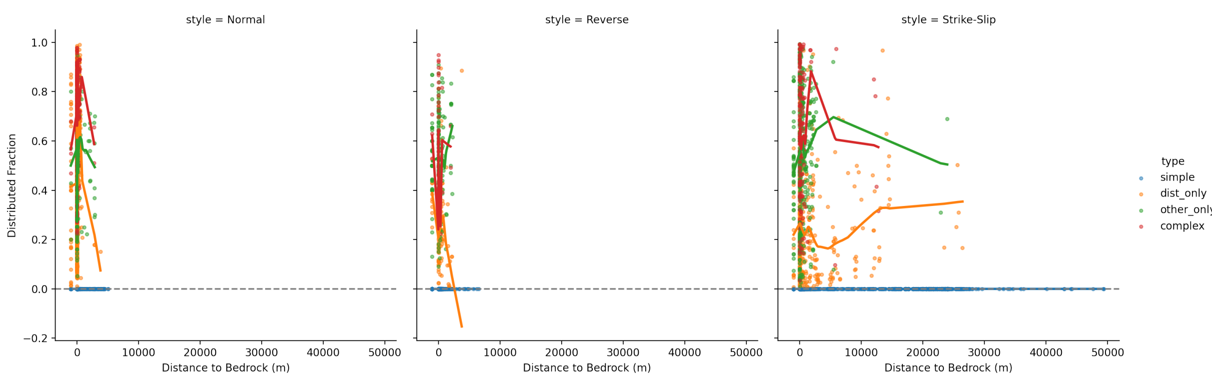

Figure A.43. Distributed fracton relatve to Prominence, 1000-m radius.

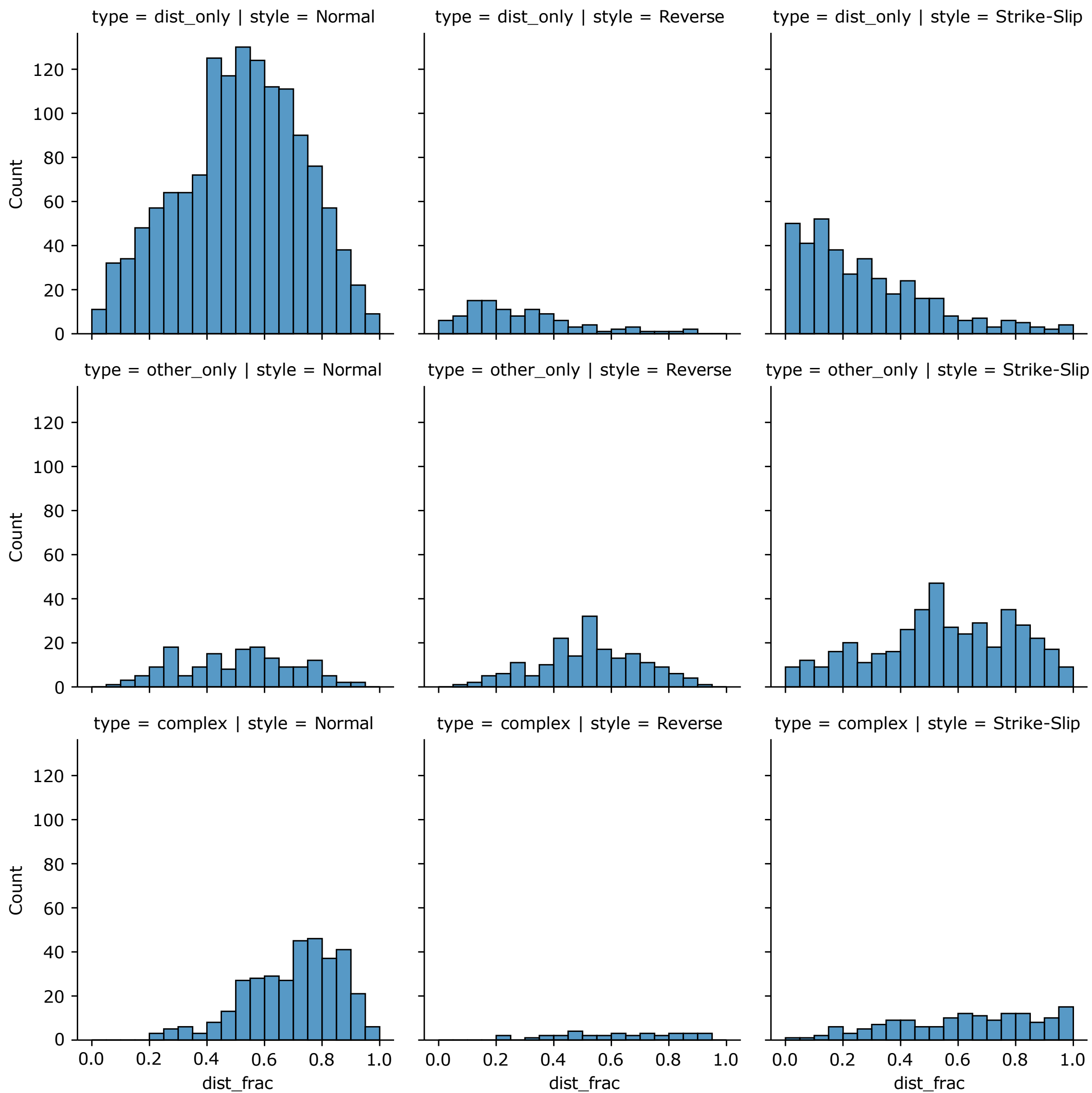

Figure A.44. Distributed fracton based on the surface fault expression and the style of faultng.

A5 CONCLUSIONS

We evaluated several approaches and metrics to include site-specific parameters in our new model. Specifically, approaches to predict along-strike fault segmentaton and the influence of terrain on fault-perpendicular rupture complexity were studied. While the efforts documented in this Appendix were unsuccessful and not incorporated in our final model, the insights gained may help in the development of new models.

The various approaches of considering geologic controls were successful for some events or portons of events. However, we did not find a method that was both a consistent predictor of displacement variability in the FDHI Database *and* usable in a forward-modeling sense. As a result, we addressed modeling challenges related to large along-strike variability by first aggregatng displacements in the strike-normal directon (Motvaton for Aggregatng Displacements and Displacement Aggregaton Methodology), and then statstcally accountng for remaining low amplitude outliers with a Student-T distributon in a Bayesian robust regression (Model). We also note that no trends in the aggregated displacement residuals were observed for the terrain metrics considered; therefore, there is no need to include a terrain parameter in the predicton of aggregated displacement.

Our preliminary evaluatons relatng terrain to rupture complexity at a site (i.e, the influence of terrain on fault-perpendicular rupture and displacement paterns) found potental relatonships that should be examined in future work. Specifically, we classified the aggregated measurements based on rupture paterns—from simple to complex—and found the classificatons could be predicted by some terrain metrics (partcularly slope and topographic prominence) and style of faultng. We also found that the rupture patern classificaton influences the amount of displacement on principal and distributed (sub) parallel faults. With more data and tme, a model could be developed that would describe how aggregated displacements can be parttoned into principal and distributed sources at a site considering terrain. We also note that while terrain metrics are atractve model parameters because they are easily quantfied from digital elevaton models (DEMs), they may be sensitve to the resoluton of the DEM and a standard resoluton may need to be defined. Finally, other parameters that describe the structural characteristcs of the fault (e.g., along-strike gradient) might be useful, but were not considered in this effort.

APPENDIX B

PLOTS OF EVENT DATA AND PREDICTIONS

B PLOTS OF EVENT DATA AND PREDICTIONS

In this chapter, plots of the aggregated displacement, together with event-specific predictons (i.e. including event terms $\delta\mathrm{m}$ and $\delta\gamma$) are shown for each event. Shown are also the values of the degrees-of-freedom parameter ν across the rupture.

B1 STRIKE-SLIP

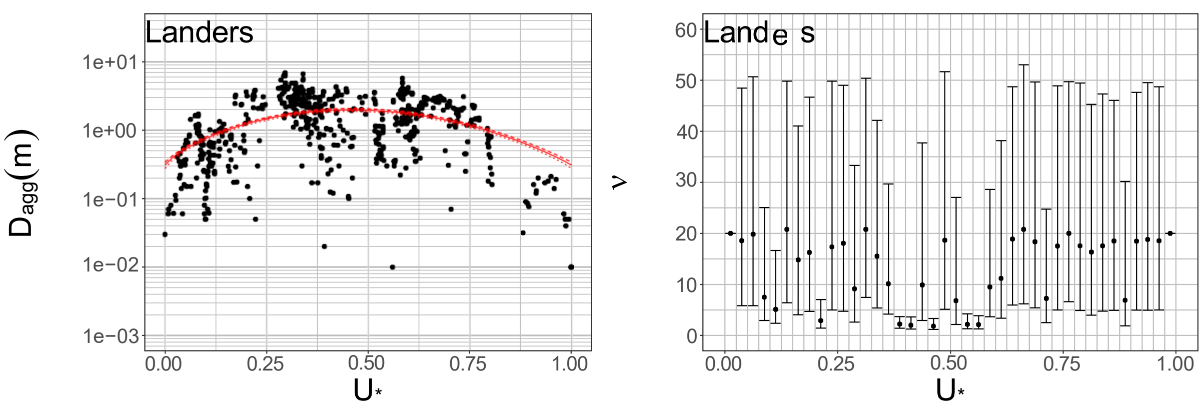

Figure B.1. Slip for Landers, and ν of Student T distributon. Uncertainty bands are the 5% and 95% fractles of the posterior distributon.

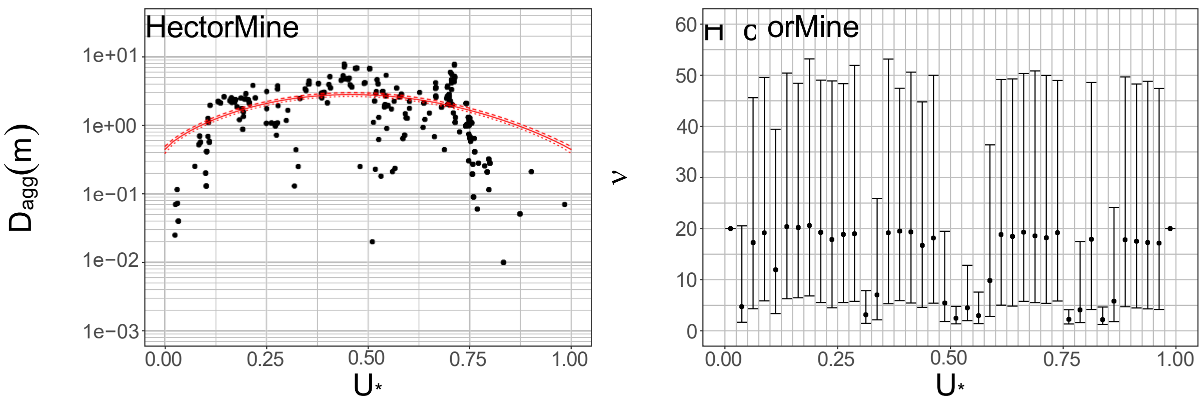

Figure B.2. Slip for HectorMine, and ν of Student T distributon. Uncertainty bands are the 5% and 95% fractles of the posterior distributon.

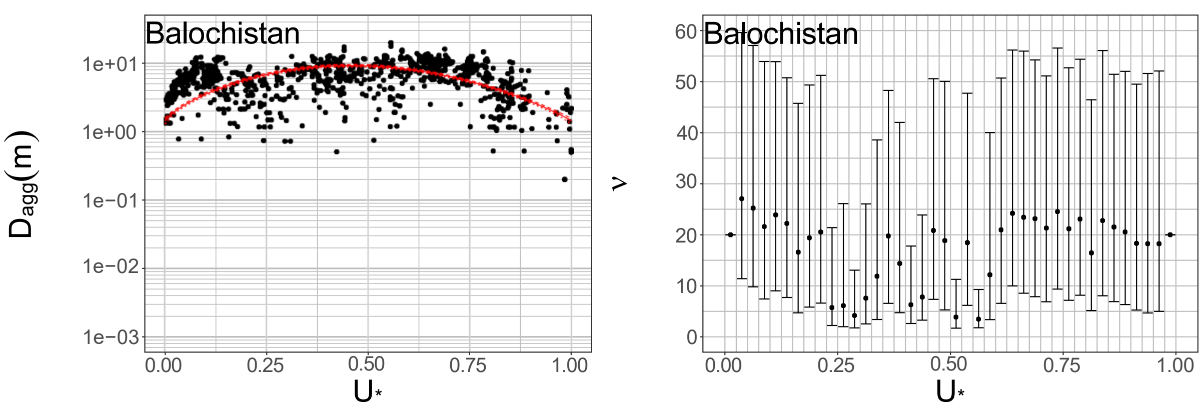

Figure B.3. Slip for Balochistan, and ν of Student T distributon. Uncertainty bands are the 5% and 95% fractles of the posterior distributon.

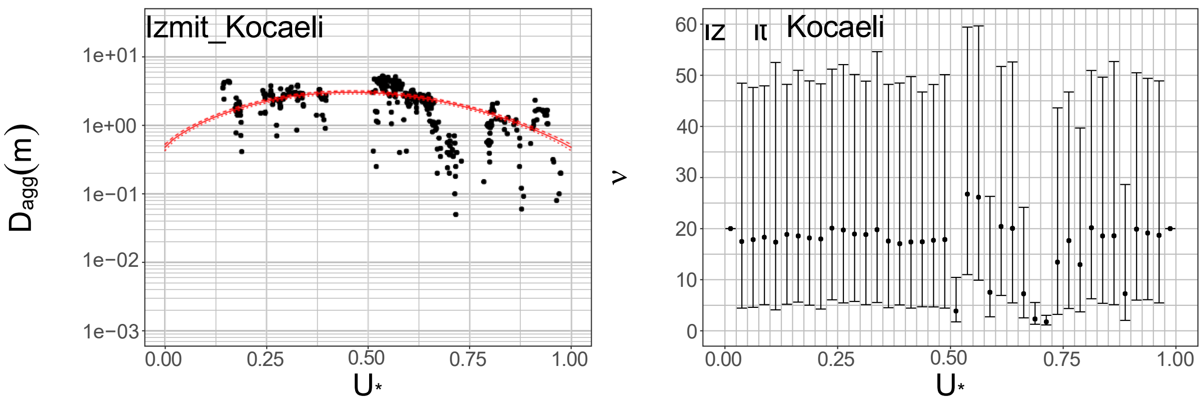

Figure B.4. Slip for Izmit_Kocaeli, and ν of Student T distributon. Uncertainty bands are the 5% and 95% fractles of the posterior distributon.

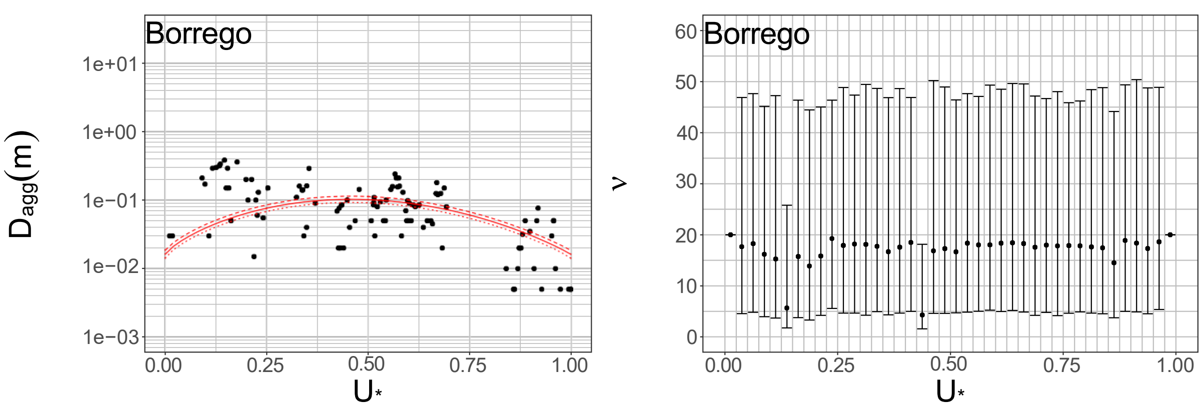

Figure B.5. Slip for Borrego, and ν of Student T distributon. Uncertainty bands are the 5% and 95% fractles of the posterior distributon.

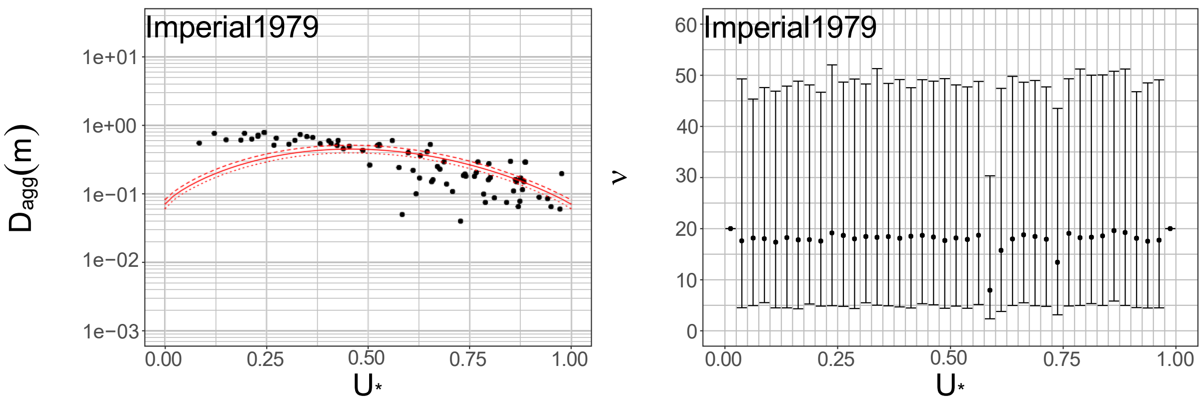

Figure B.6. Slip for Imperial1979, and ν of Student T distributon. Uncertainty bands are the 5% and 95% fractles of the posterior distributon.

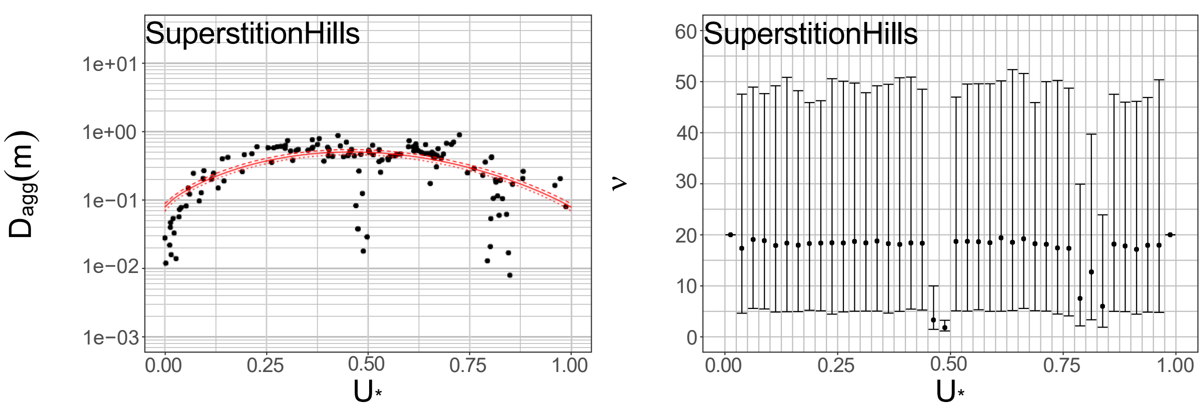

Figure B.7. Slip for SupersttonHills, and ν of Student T distributon. Uncertainty bands are the 5% and 95% fractles of the posterior distributon.

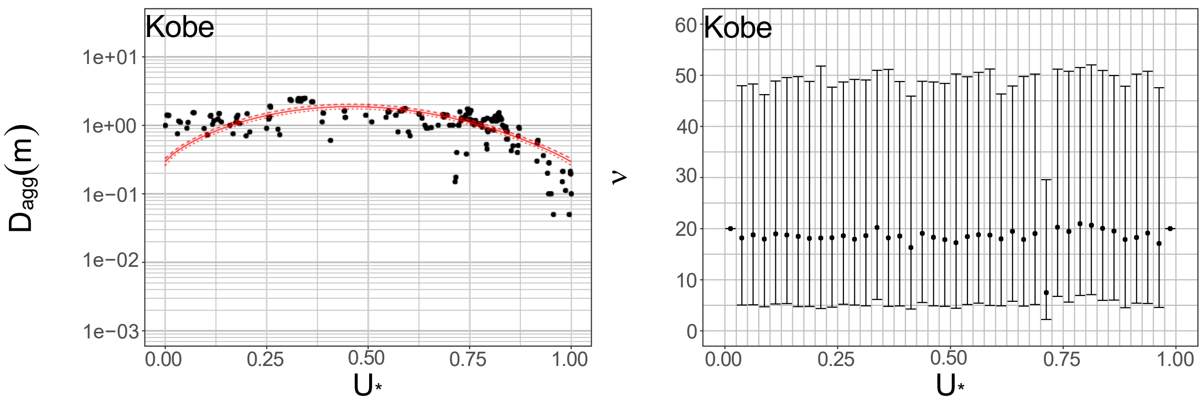

Figure B.8. Slip for Kobe, and ν of Student T distributon. Uncertainty bands are the 5% and 95% fractles of the posterior distributon.

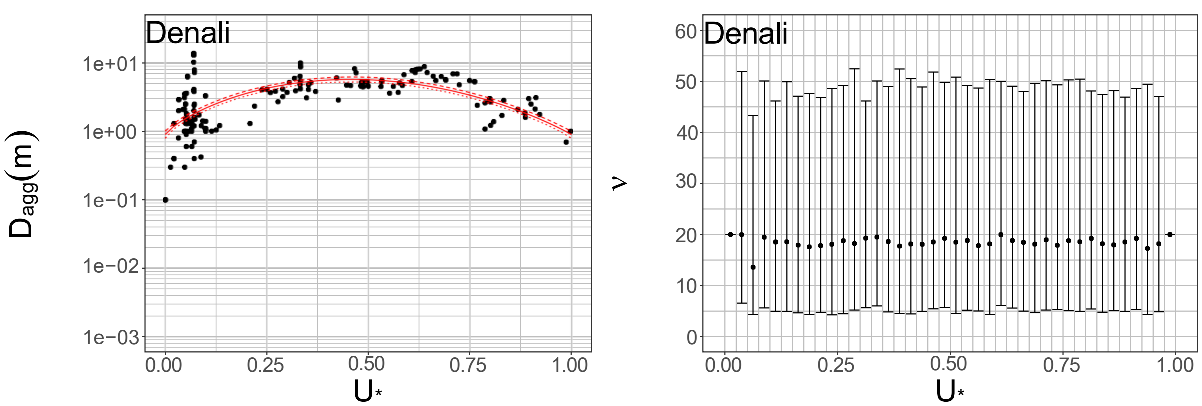

Figure B.9. Slip for Denali, and ν of Student T distributon. Uncertainty bands are the 5% and 95% fractles of the posterior distributon.

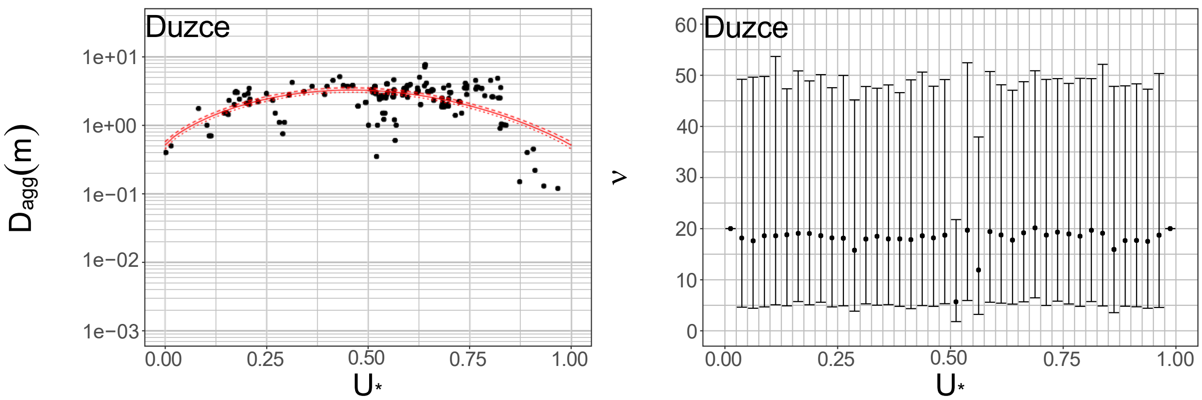

Figure B.10. Slip for Duzce, and ν of Student T distributon. Uncertainty bands are the 5% and 95% fractles of the posterior distributon.

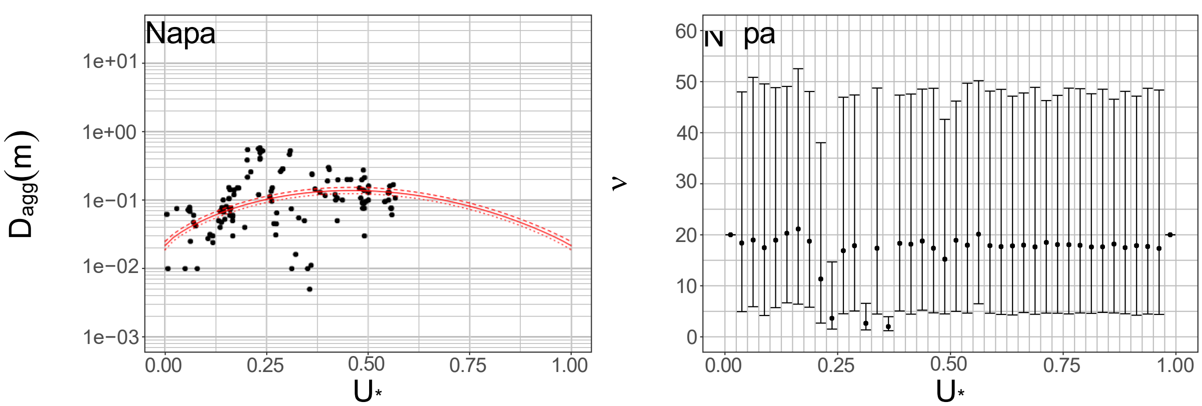

Figure B.11. Slip for Napa, and ν of Student T distributon. Uncertainty bands are the 5% and 95% fractles of the posterior distributon.

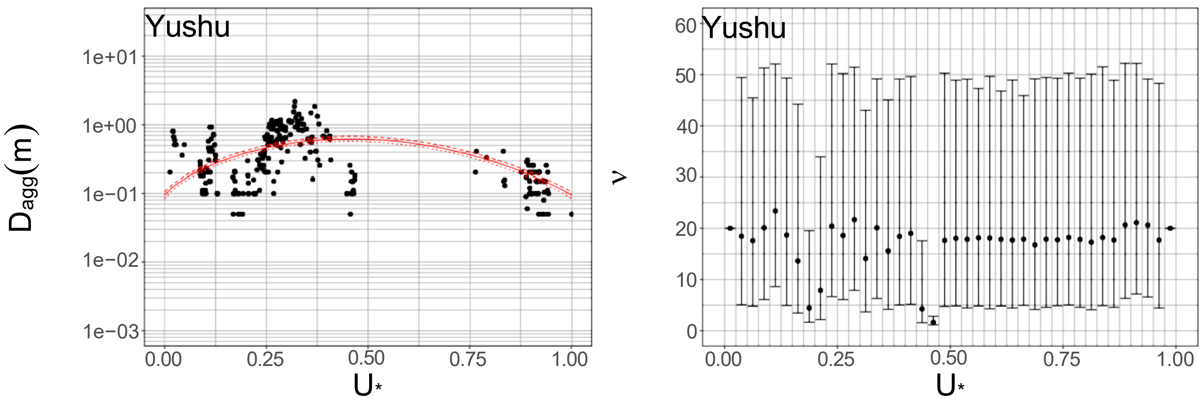

Figure B.12. Slip for Yushu, and ν of Student T distributon. Uncertainty bands are the 5% and 95% fractles of the posterior distributon.

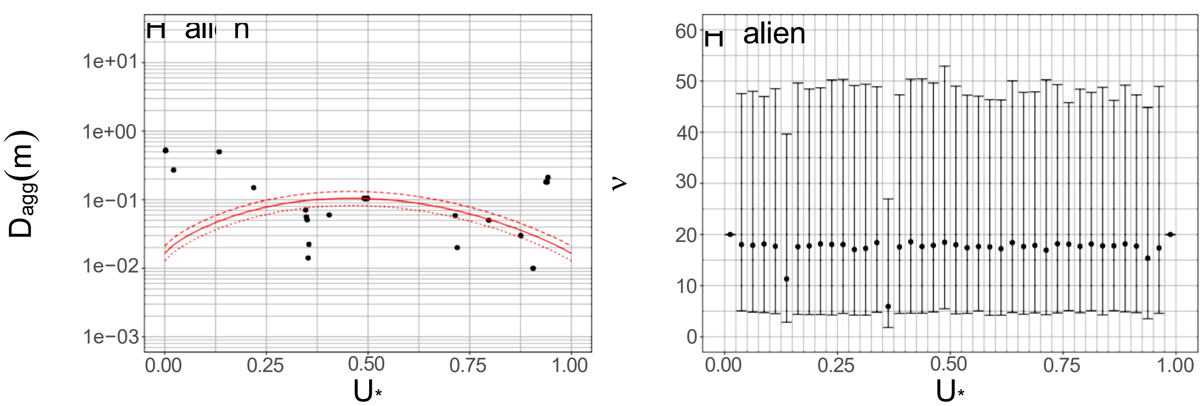

Figure B.13. Slip for Hualien, and ν of Student T distributon. Uncertainty bands are the 5% and 95% fractles of the posterior distributon.

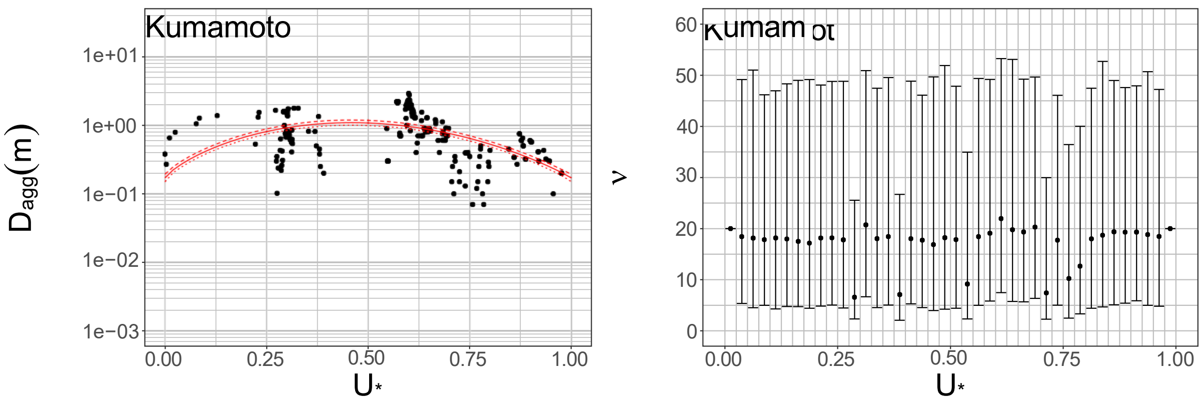

Figure B.14. Slip for Kumamoto, and ν of Student T distributon. Uncertainty bands are the 5% and 95% fractles of the posterior distributon.

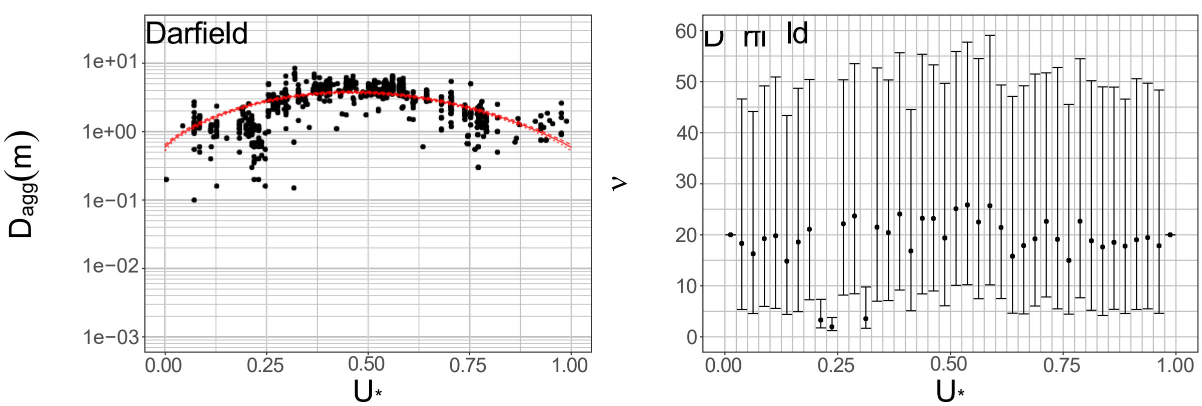

Figure B.15. Slip for Darfield, and ν of Student T distributon. Uncertainty bands are the 5% and 95% fractles of the posterior distributon.

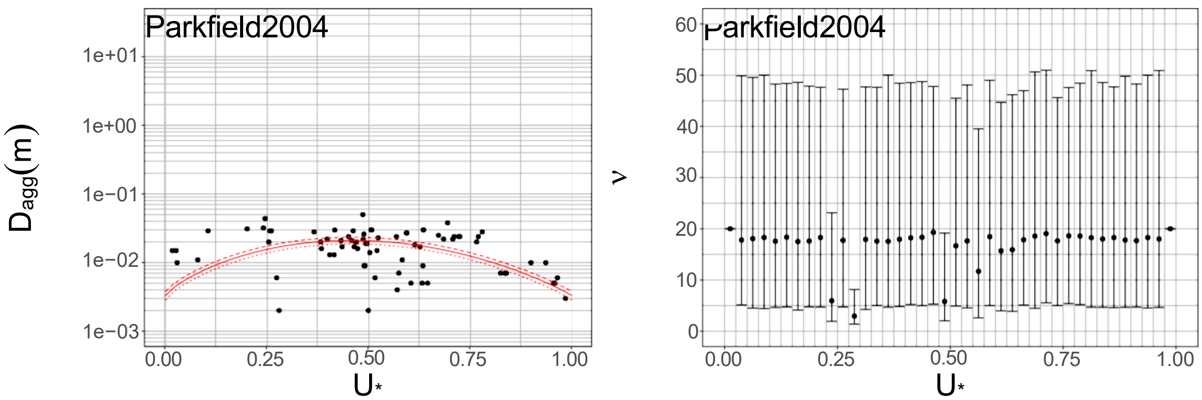

Figure B.16. Slip for Parkfield2004, and ν of Student T distributon. Uncertainty bands are the 5% and 95% fractles of the posterior distributon.

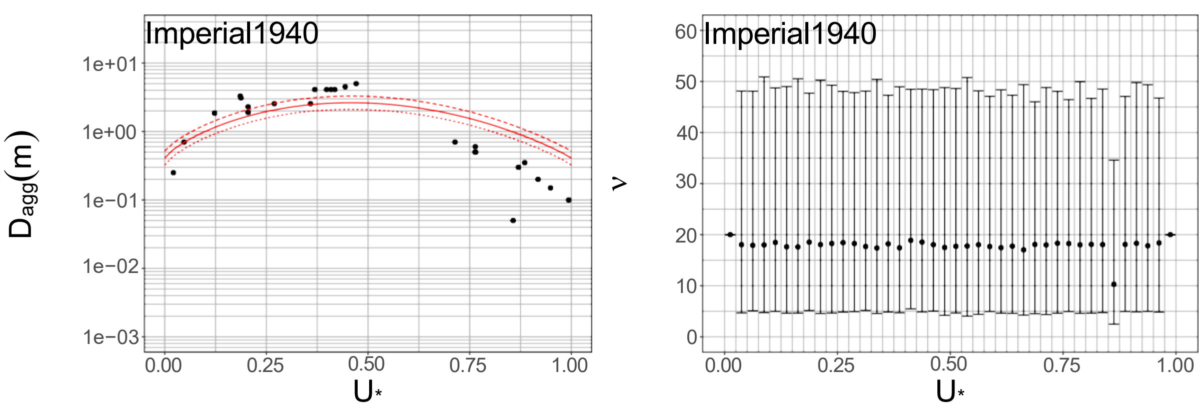

Figure B.17. Slip for Imperial1940, and ν of Student T distributon. Uncertainty bands are the 5% and 95% fractles of the posterior distributon.

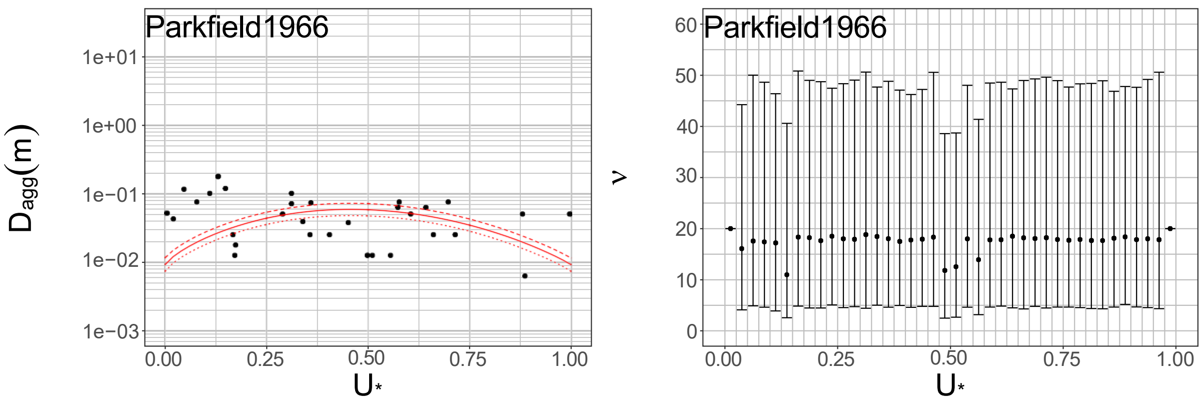

Figure B.18. Slip for Parkfield1966, and ν of Student T distributon. Uncertainty bands are the 5% and 95% fractles of the posterior distributon.

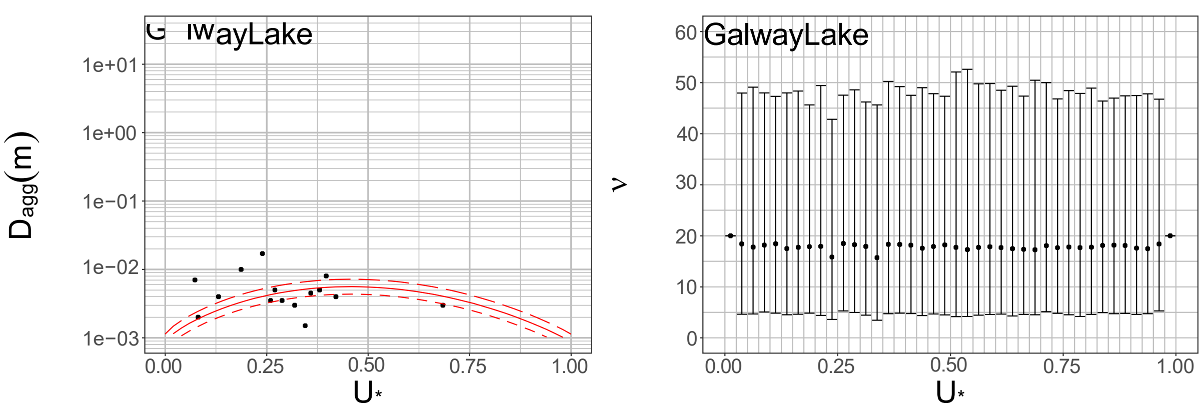

Figure B.19. Slip for GalwayLake, and ν of Student T distributon. Uncertainty bands are the 5% and 95% fractles of the posterior distributon.

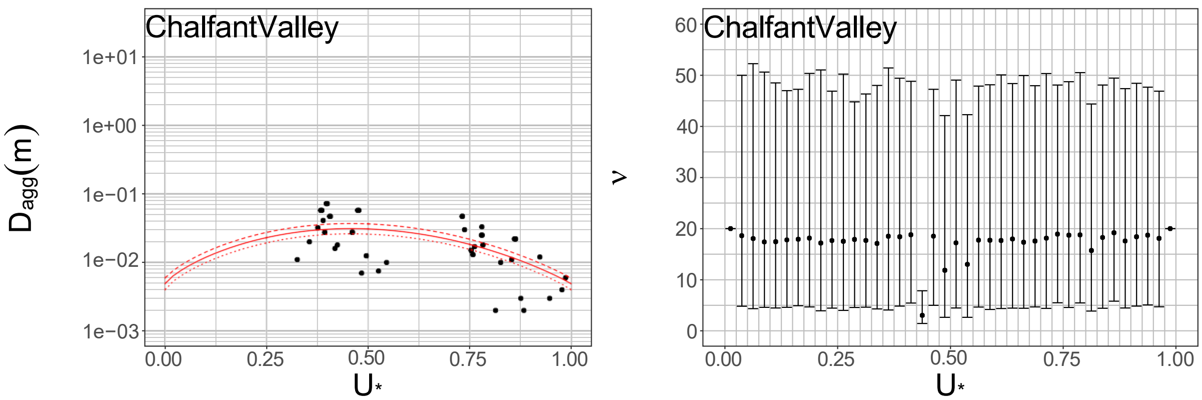

Figure B.20. Slip for ChalfantValley, and ν of Student T distributon. Uncertainty bands are the 5% and 95% fractles of the posterior distributon.

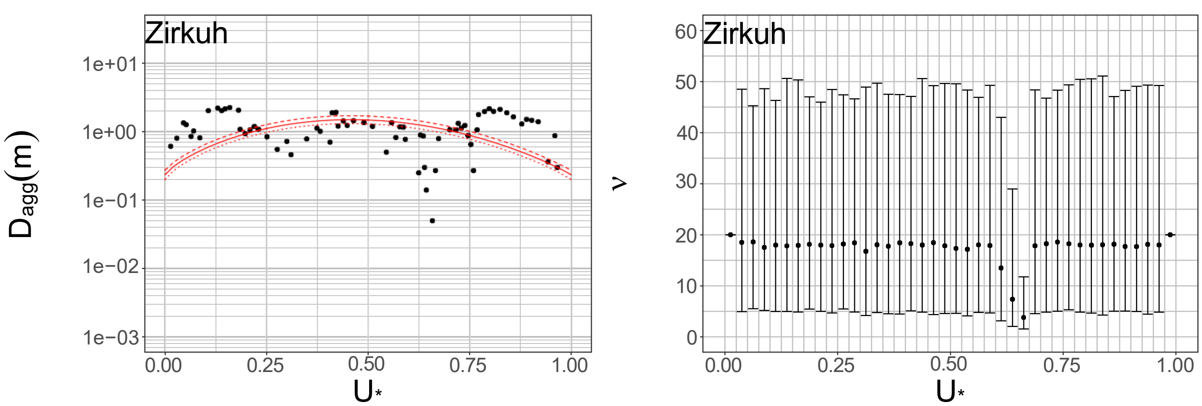

Figure B.21. Slip for Zirkuh, and ν of Student T distributon. Uncertainty bands are the 5% and 95% fractles of the posterior distributon.

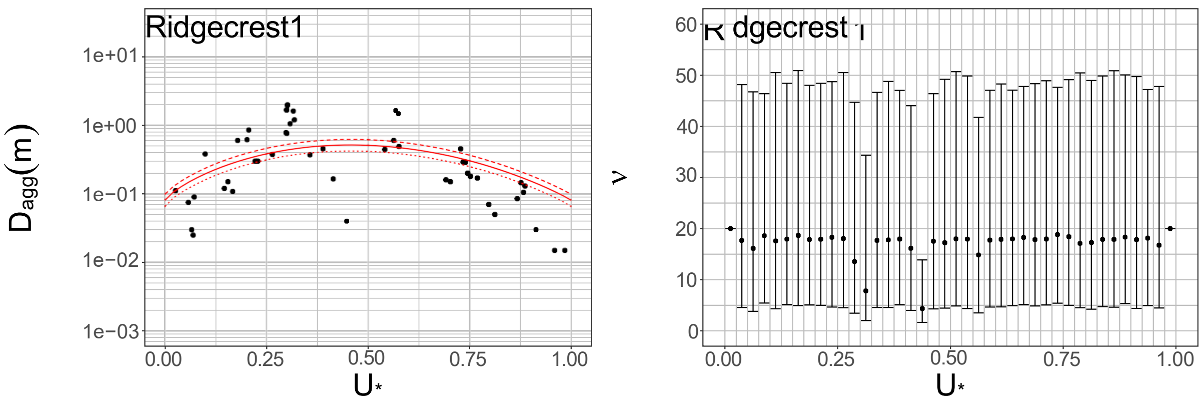

Figure B.22. Slip for Ridgecrest1, and ν of Student T distributon. Uncertainty bands are the 5% and 95% fractles of the posterior distributon.

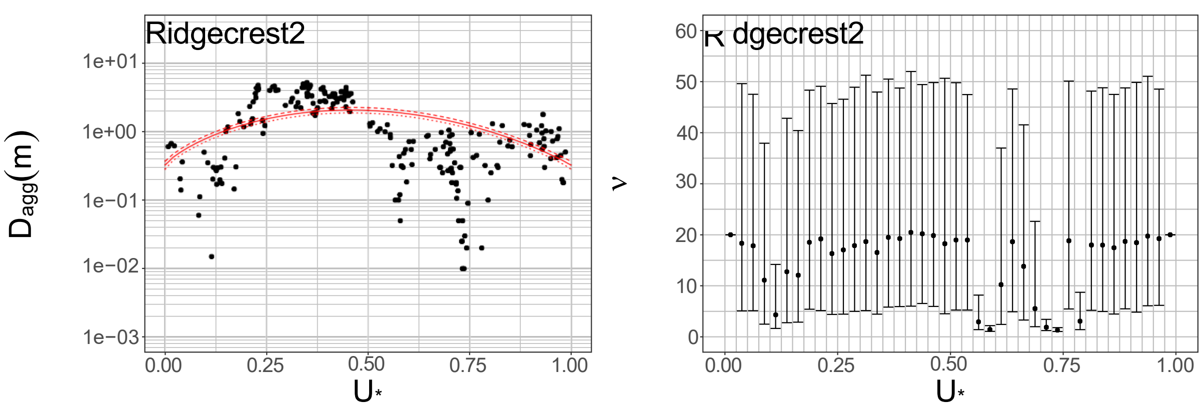

Figure B.23. Slip for Ridgecrest2, and ν of Student T distributon. Uncertainty bands are the 5% and 95% fractles of the posterior distributon.

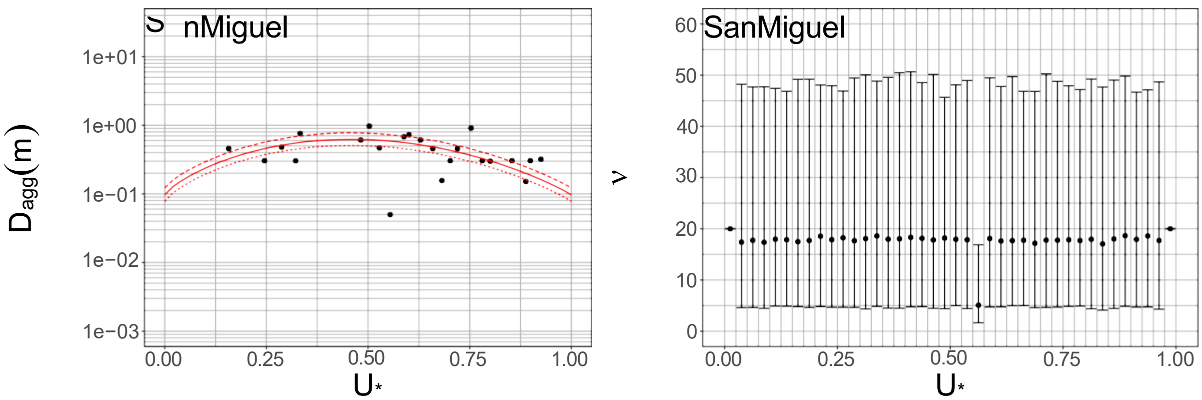

Figure B.24. Slip for SanMiguel, and ν of Student T distributon. Uncertainty bands are the 5% and 95% fractles of the posterior distributon.

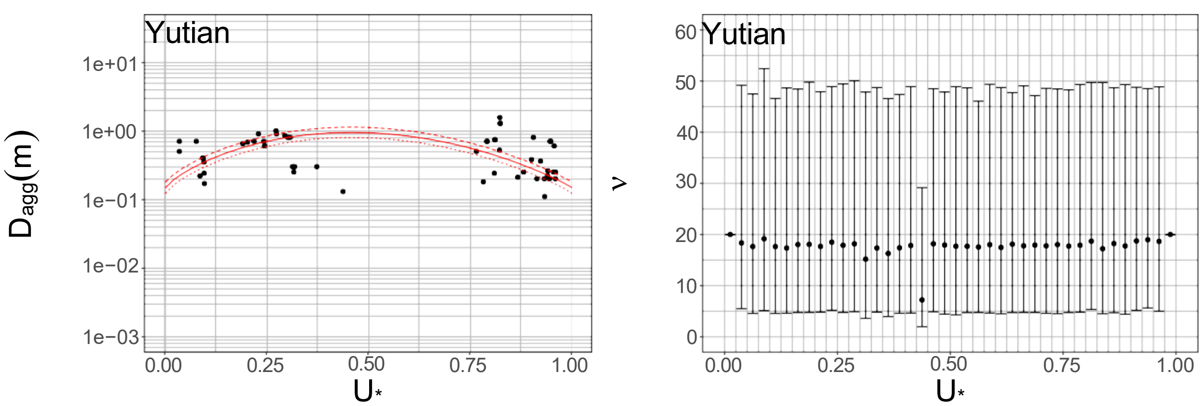

Figure B.25. Slip for Yutan, and ν of Student T distributon. Uncertainty bands are the 5% and 95% fractles of the posterior distributon.

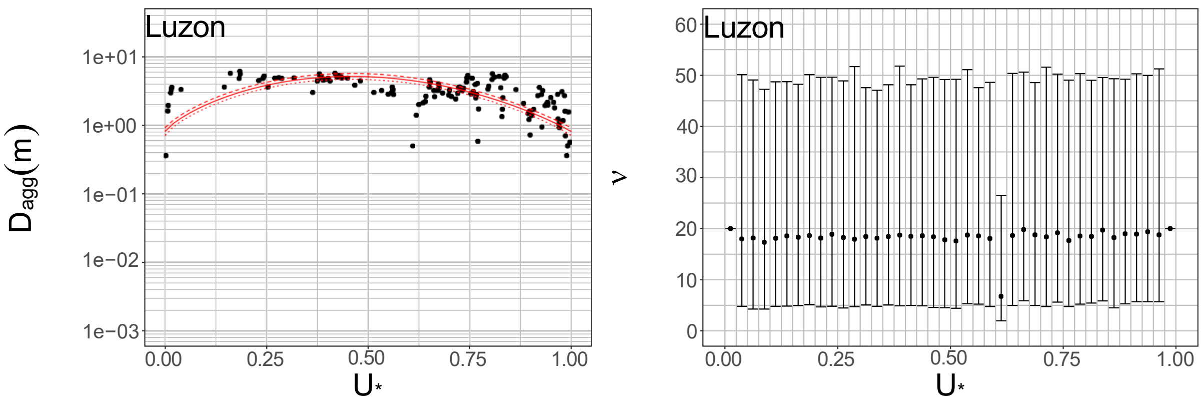

Figure B.26. Slip for Luzon, and ν of Student T distributon. Uncertainty bands are the 5% and 95% fractles of the posterior distributon.

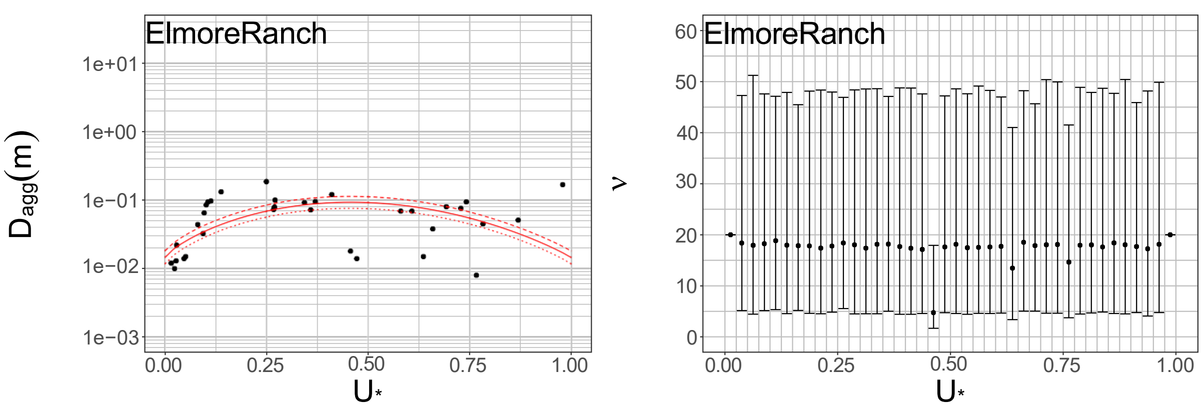

Figure B.27. Slip for ElmoreRanch, and ν of Student T distributon. Uncertainty bands are the 5% and 95% fractles of the posterior distributon.

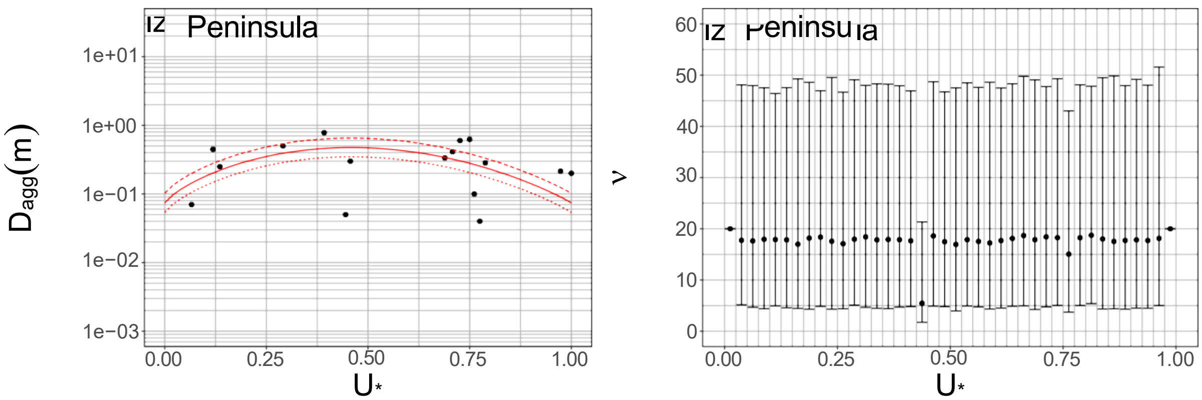

Figure B.28. Slip for IzuPeninsula, and ν of Student T distributon. Uncertainty bands are the 5% and 95% fractles of the posterior distributon.

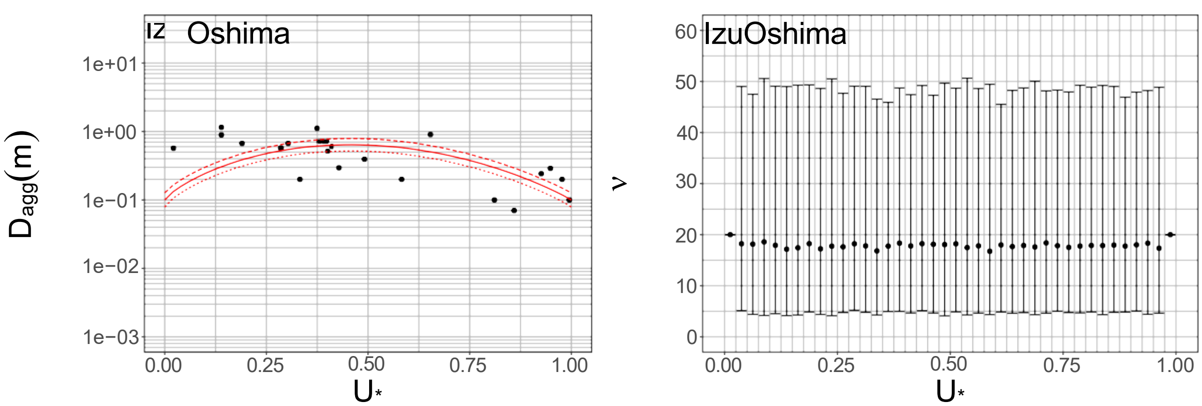

Figure B.29. Slip for IzuOshima, and ν of Student T distributon. Uncertainty bands are the 5% and 95% fractles of the posterior distributon.

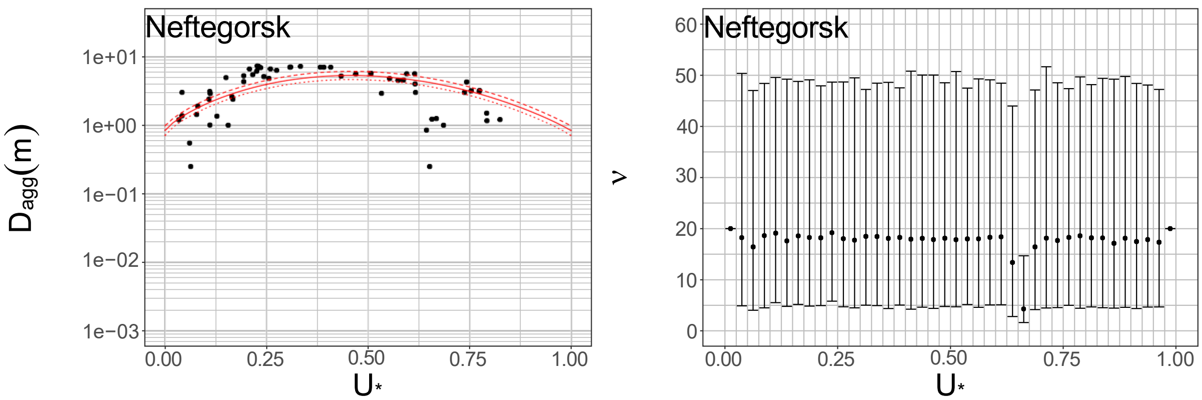

Figure B.30. Slip for Neftegorsk, and ν of Student T distributon. Uncertainty bands are the 5% and 95% fractles of the posterior distributon.

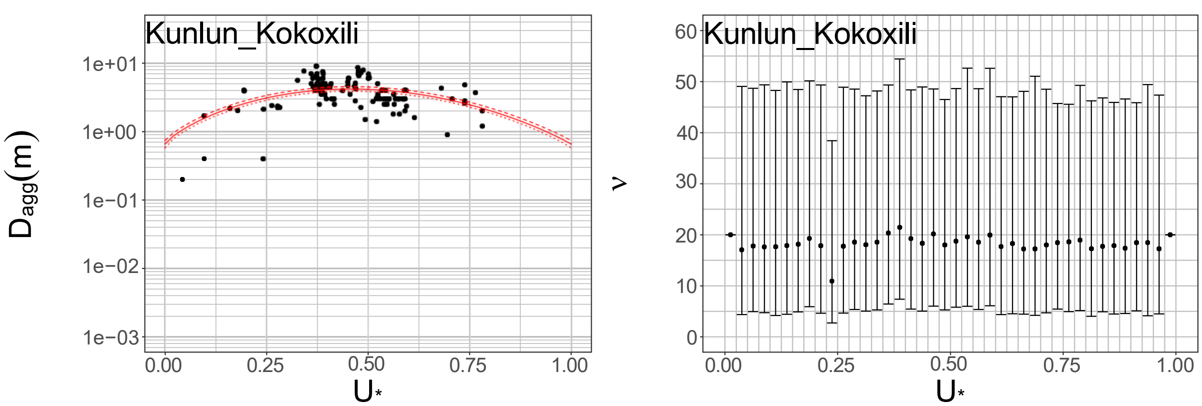

Figure B.31. Slip for Kunlun_Kokoxili, and ν of Student T distributon. Uncertainty bands are the 5% and 95% fractles of the posterior distributon.

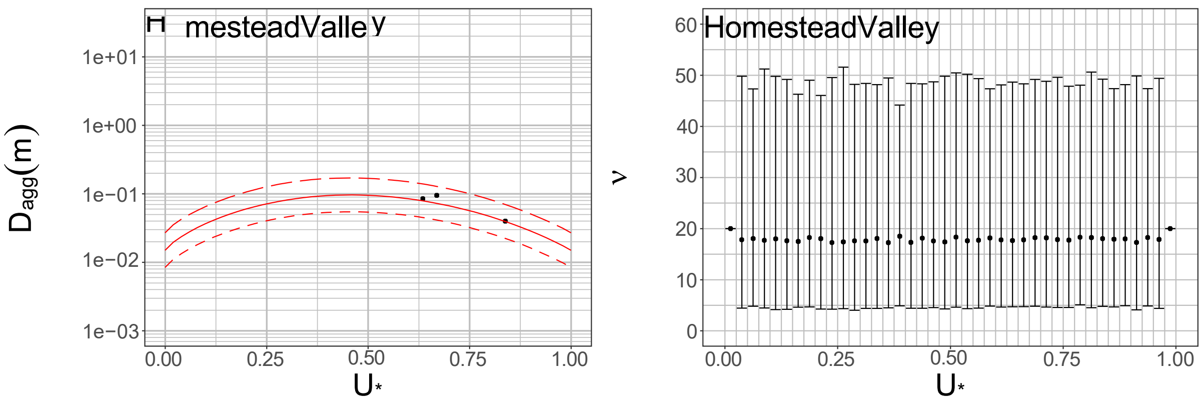

Figure B.32. Slip for HomesteadValley, and ν of Student T distributon. Uncertainty bands are the 5% and 95% fractles of the posterior distributon.

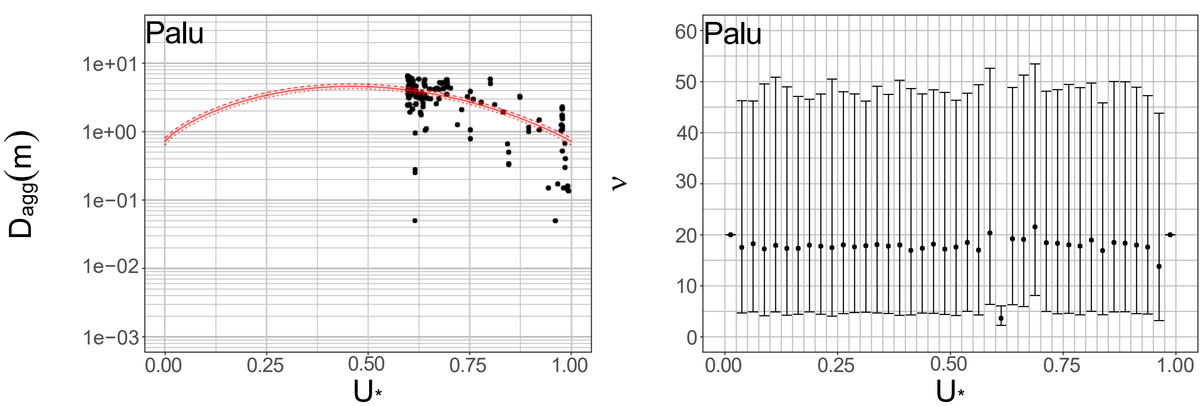

Figure B.33. Slip for Palu, and ν of Student T distributon. Uncertainty bands are the 5% and 95% fractles of the posterior distributon.

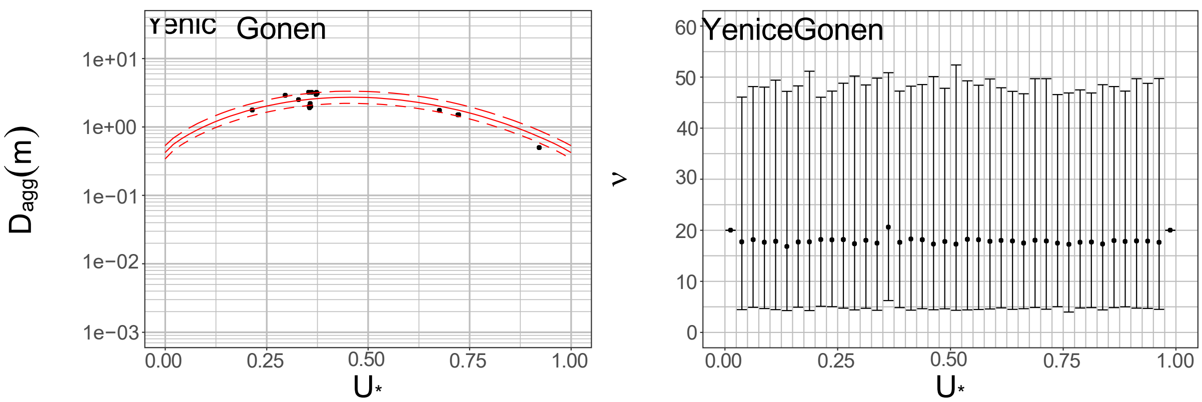

Figure B.34. Slip for YeniceGonen, and ν of Student T distributon. Uncertainty bands are the 5% and 95% fractles of the posterior distributon.

B2 NORMAL

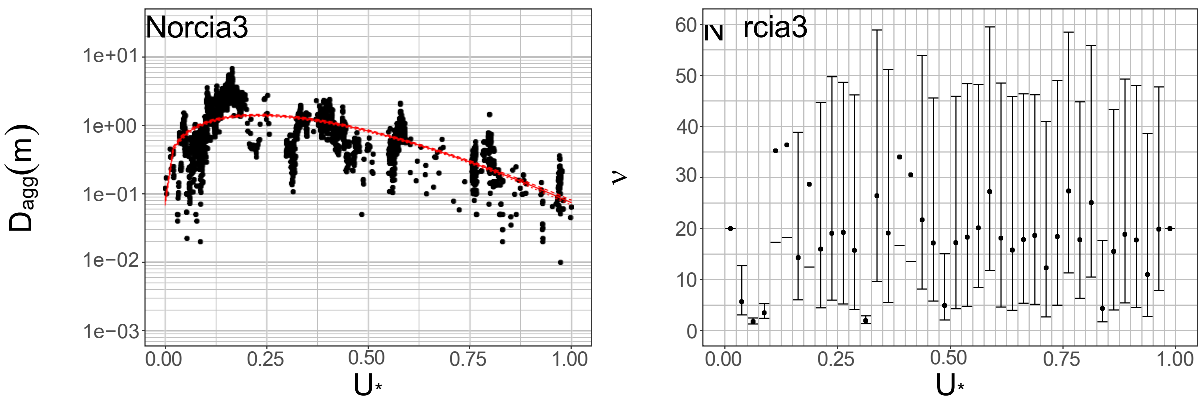

Figure B.35. Slip for Norcia3, and ν of Student T distributon. Uncertainty bands are the 5% and 95% fractles of the posterior distributon.

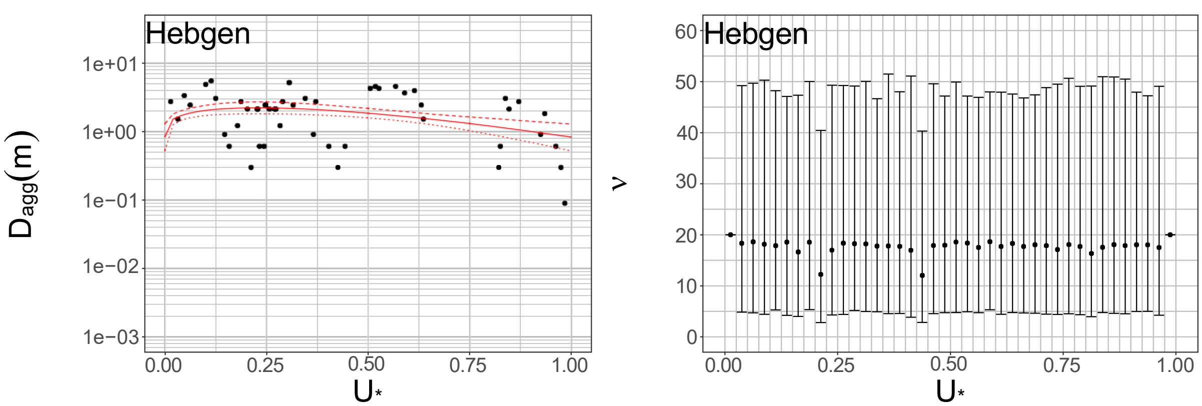

Figure B.36. Slip for Hebgen, and ν of Student T distributon. Uncertainty bands are the 5% and 95% fractles of the posterior distributon.

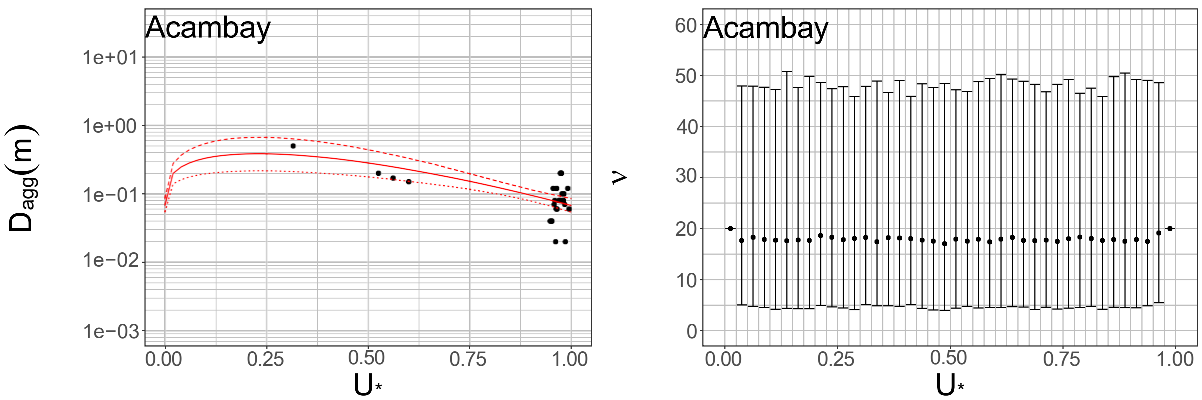

Figure B.37. Slip for Acambay, and ν of Student T distributon. Uncertainty bands are the 5% and 95% fractles of the posterior distributon.

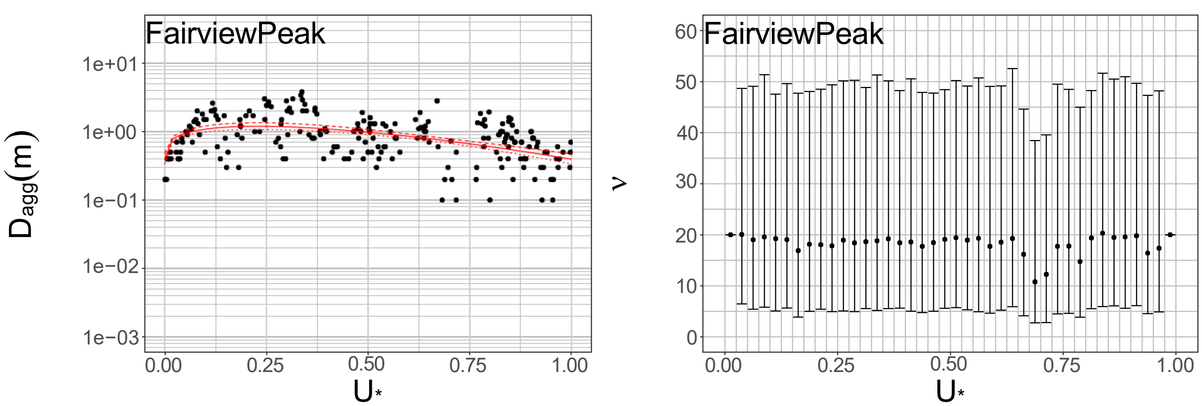

Figure B.38. Slip for FairviewPeak, and ν of Student T distributon. Uncertainty bands are the 5% and 95% fractles of the posterior distributon.

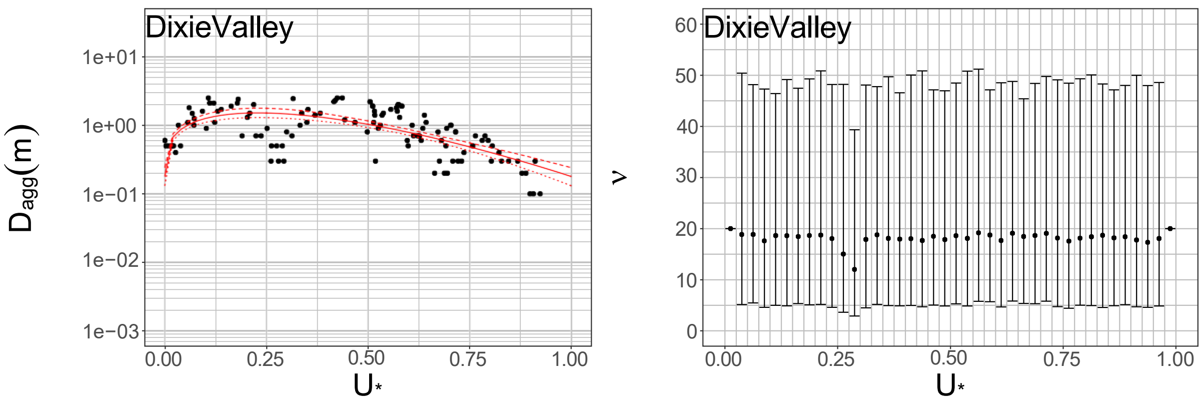

Figure B.39. Slip for DixieValley, and ν of Student T distributon. Uncertainty bands are the 5% and 95% fractles of the posterior distributon.

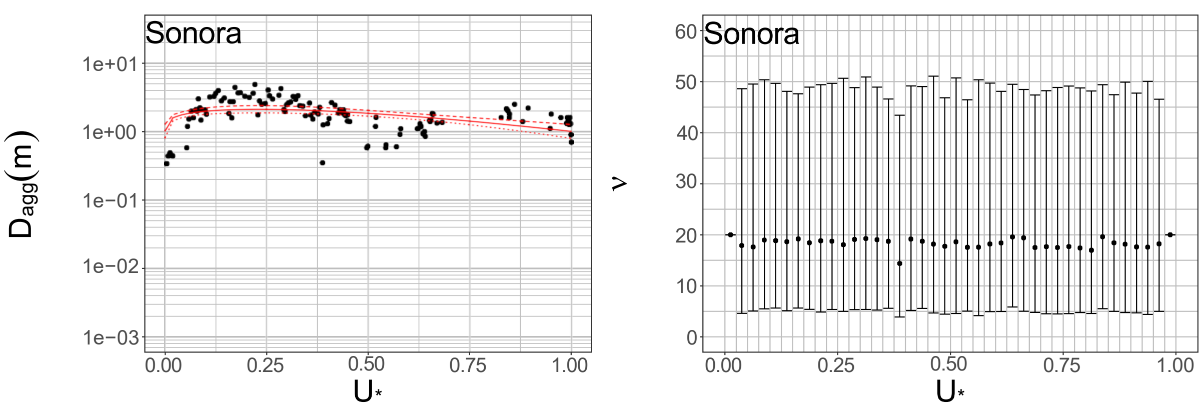

Figure B.40. Slip for Sonora, and ν of Student T distributon. Uncertainty bands are the 5% and 95% fractles of the posterior distributon.

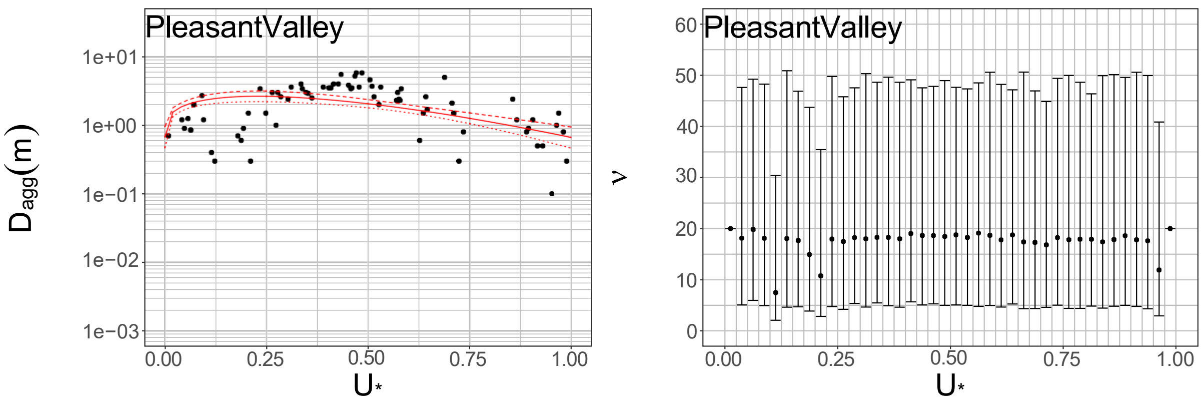

Figure B.41. Slip for PleasantValley, and ν of Student T distributon. Uncertainty bands are the 5% and 95% fractles of the posterior distributon.

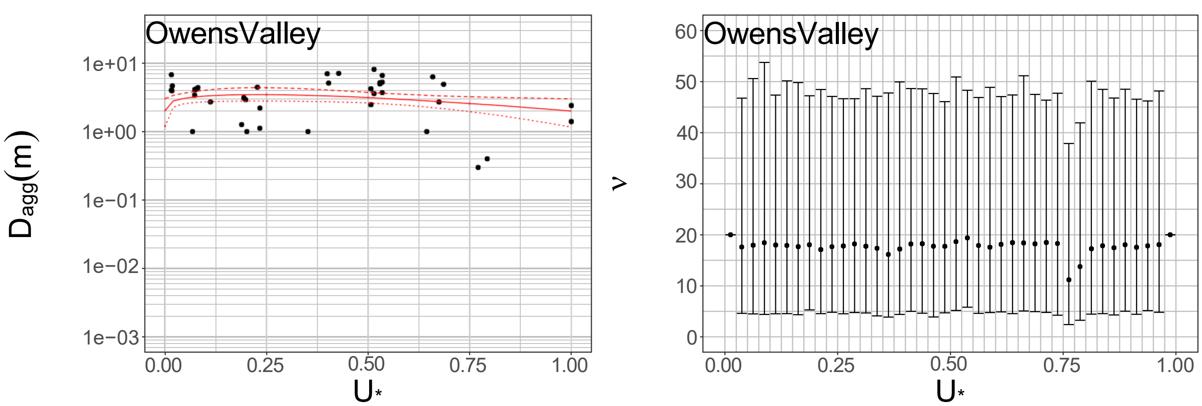

Figure B.42. Slip for OwensValley, and ν of Student T distributon. Uncertainty bands are the 5% and 95% fractles of the posterior distributon.

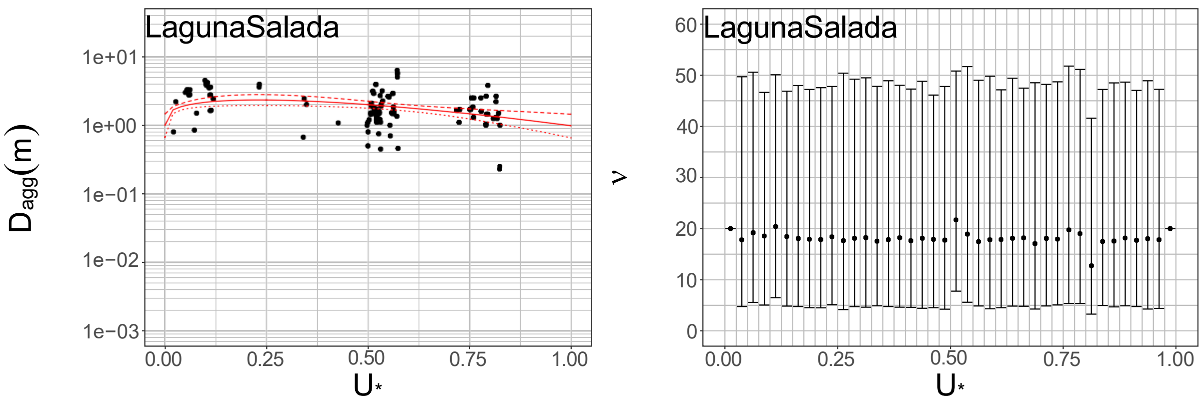

Figure B.43. Slip for LagunaSalada, and ν of Student T distributon. Uncertainty bands are the 5% and 95% fractles of the posterior distributon.

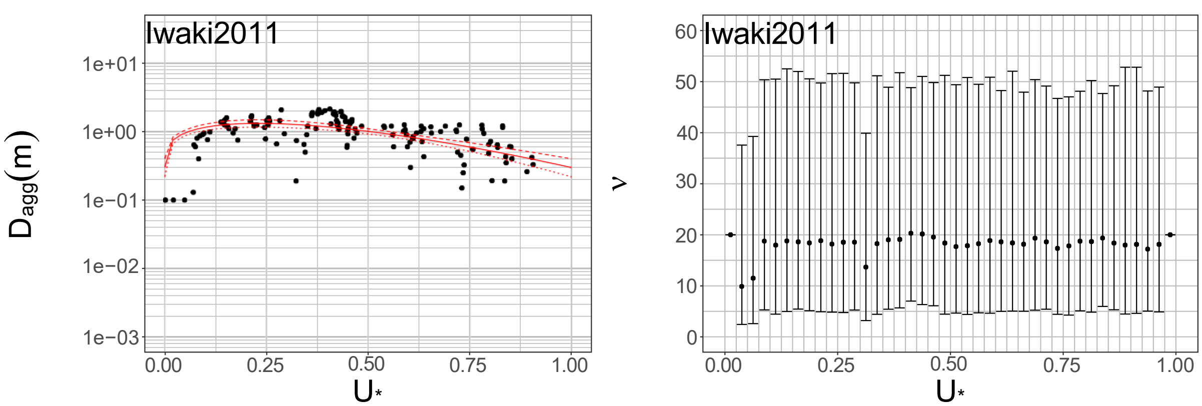

Figure B.44. Slip for Iwaki2011, and ν of Student T distributon. Uncertainty bands are the 5% and 95% fractles of the posterior distributon.

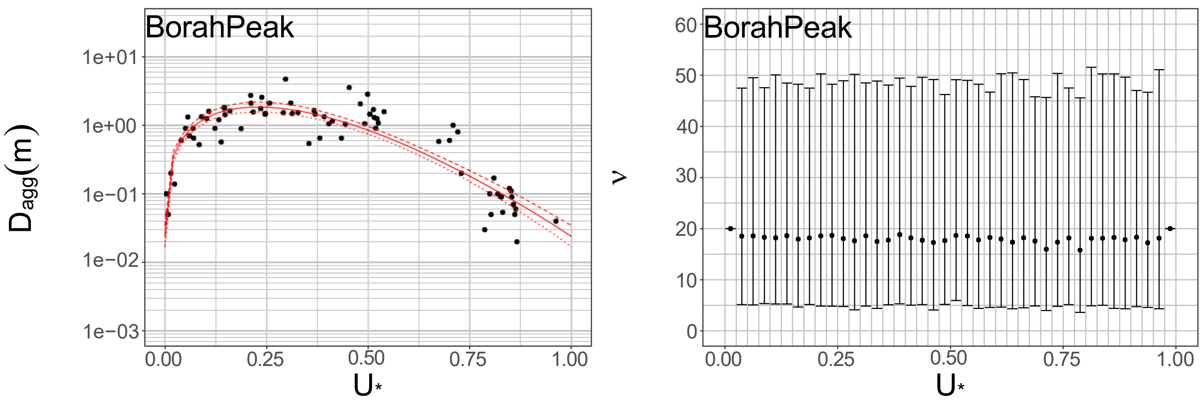

Figure B.45. Slip for BorahPeak, and ν of Student T distributon. Uncertainty bands are the 5% and 95% fractles of the posterior distributon.

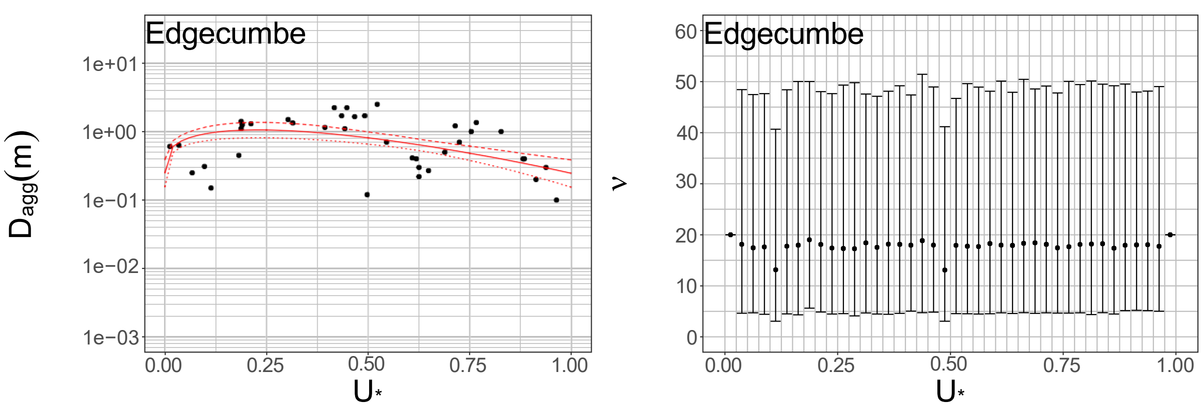

Figure B.46. Slip for Edgecumbe, and ν of Student T distributon. Uncertainty bands are the 5% and 95% fractles of the posterior distributon.

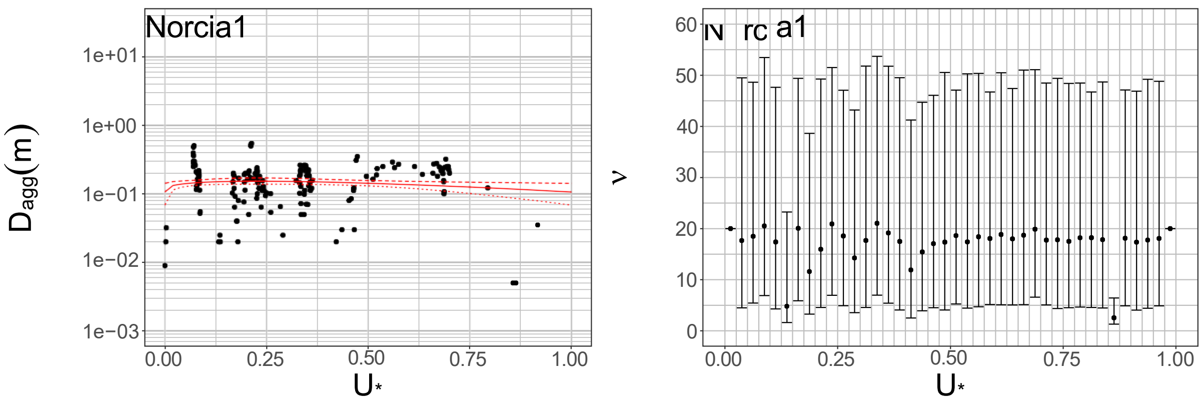

Figure B.47. Slip for Norcia1, and ν of Student T distributon. Uncertainty bands are the 5% and 95% fractles of the posterior distributon.

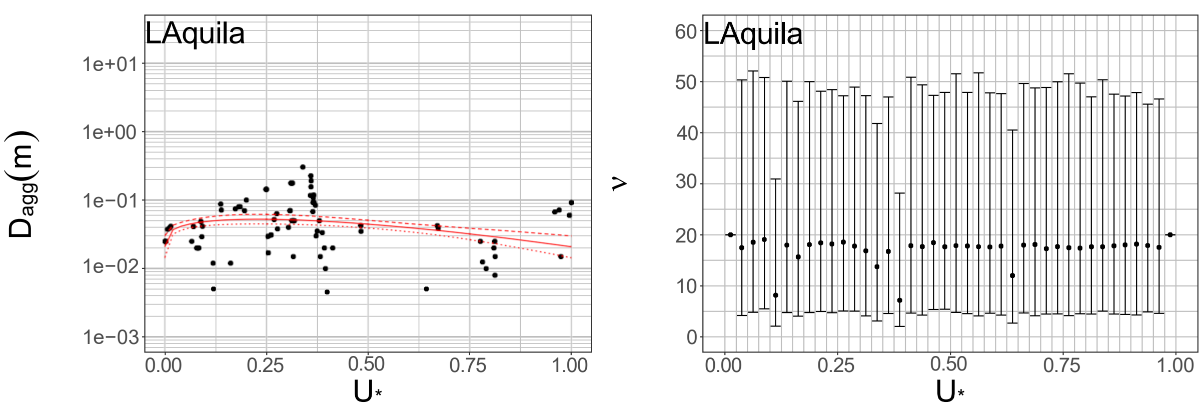

Figure B.48. Slip for LAquila, and ν of Student T distributon. Uncertainty bands are the 5% and 95% fractles of the posterior distributon.

B3 REVERSE

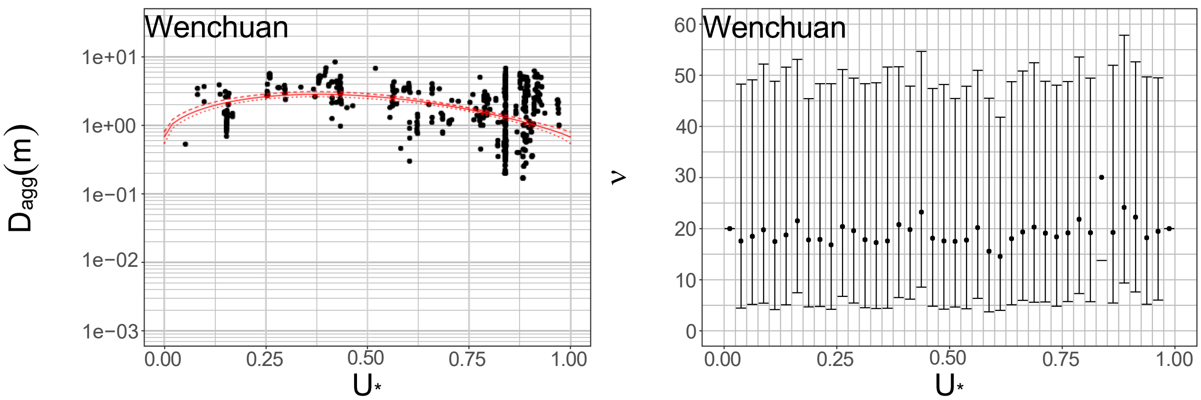

Figure B.49. Slip for Wenchuan, and ν of Student T distributon. Uncertainty bands are the 5% and 95% fractles of the posterior distributon.

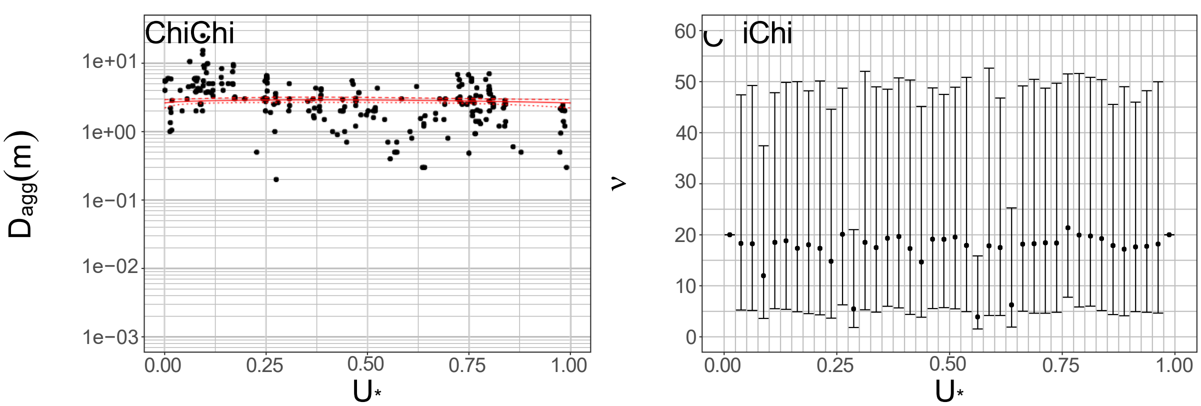

Figure B.50. Slip for ChiChi, and ν of Student T distributon. Uncertainty bands are the 5% and 95% fractles of the posterior distributon.

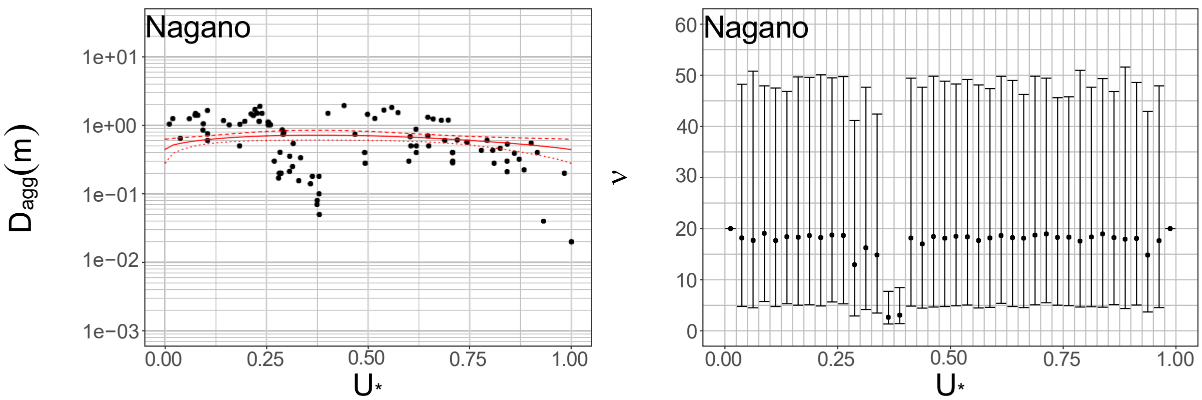

Figure B.51. Slip for Nagano, and ν of Student T distributon. Uncertainty bands are the 5% and 95% fractles of the posterior distributon.

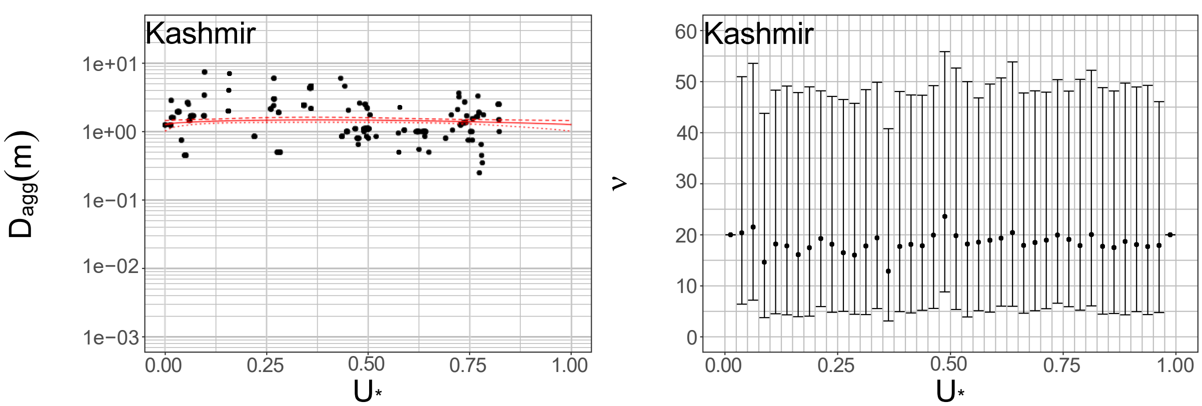

Figure B.52. Slip for Kashmir, and ν of Student T distributon. Uncertainty bands are the 5% and 95% fractles of the posterior distributon.

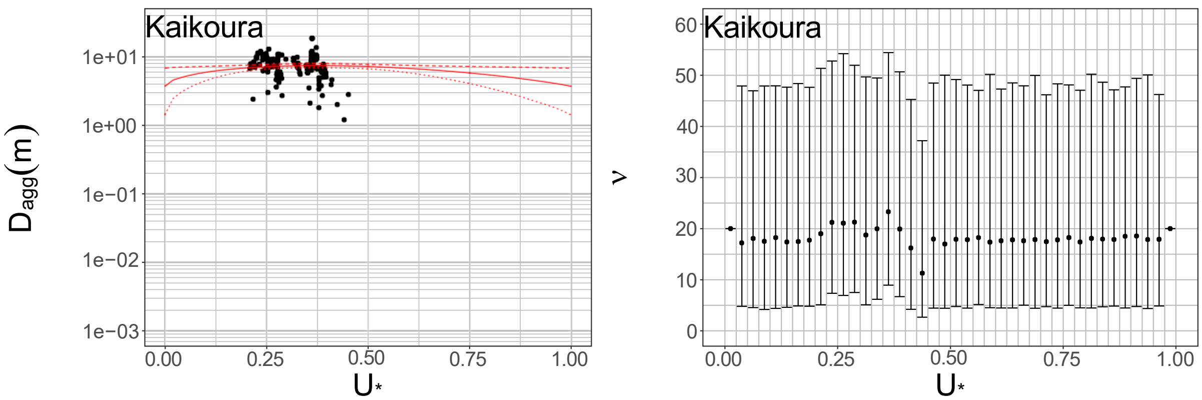

Figure B.53. Slip for Kaikoura, and ν of Student T distributon. Uncertainty bands are the 5% and 95% fractles of the posterior distributon.

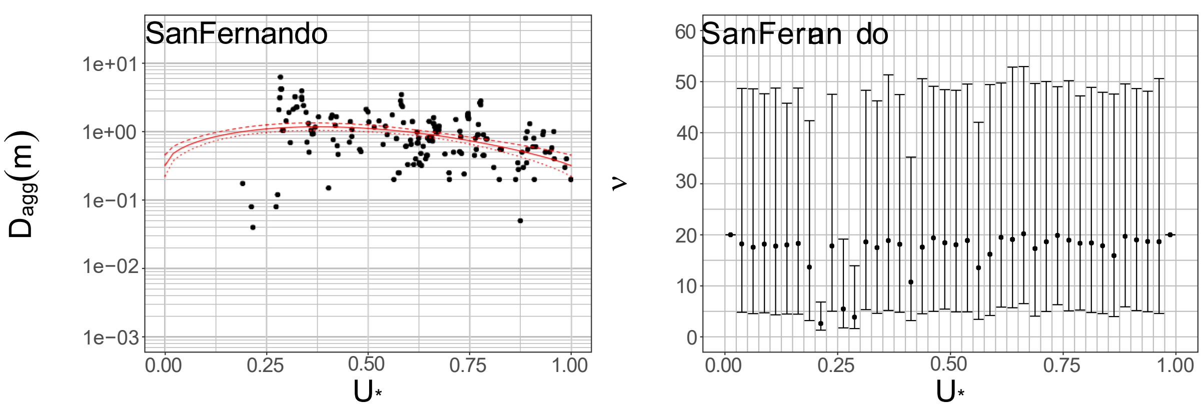

Figure B.54. Slip for SanFernando, and ν of Student T distributon. Uncertainty bands are the 5% and 95% fractles of the posterior distributon.

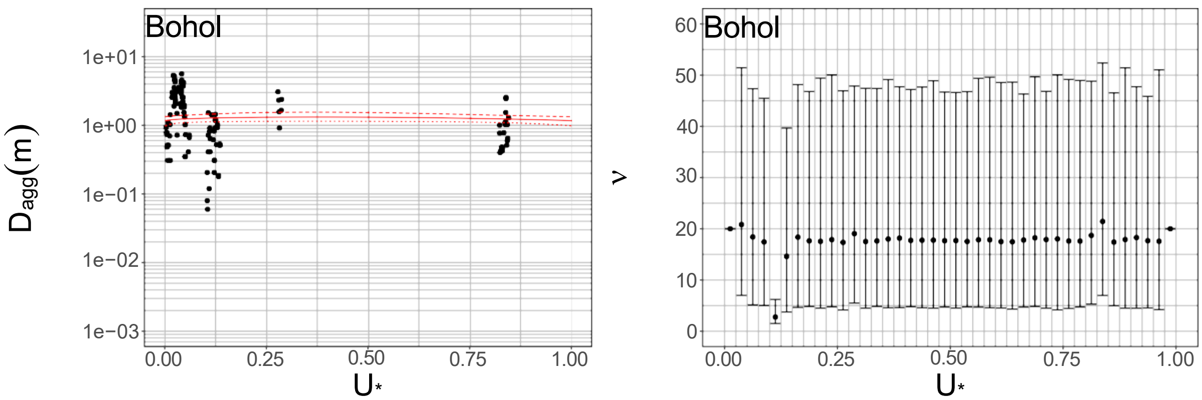

Figure B.55. Slip for Bohol, and ν of Student T distributon. Uncertainty bands are the 5% and 95% fractles of the posterior distributon.

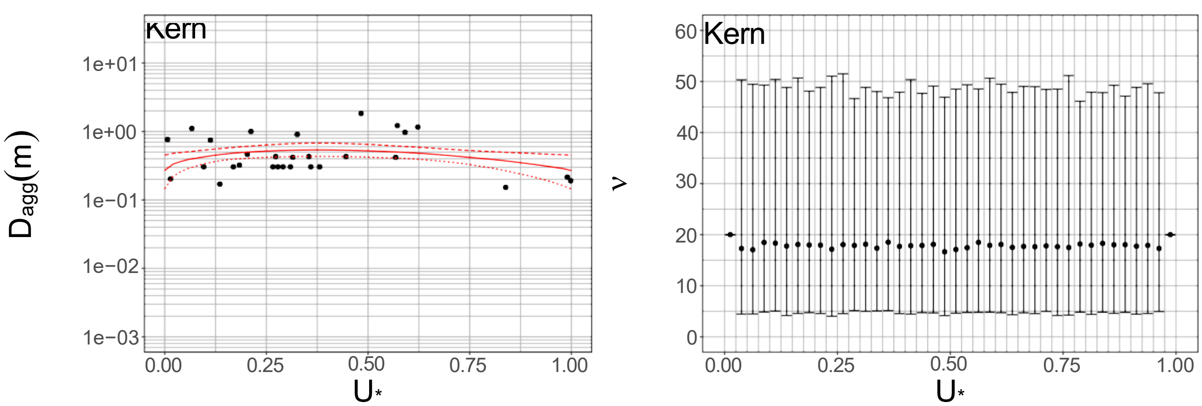

Figure B.56. Slip for Kern, and ν of Student T distributon. Uncertainty bands are the 5% and 95% fractles of the posterior distributon.

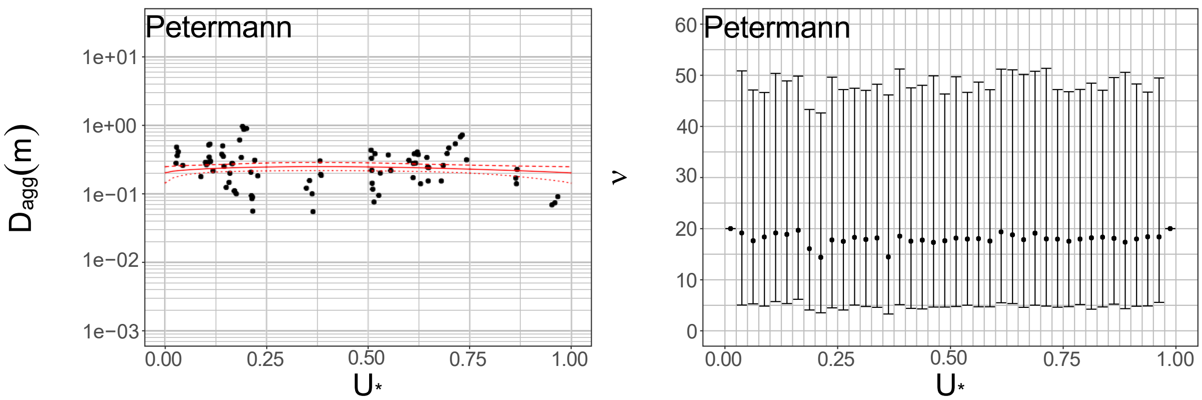

Figure B.57. Slip for Petermann, and ν of Student T distributon. Uncertainty bands are the 5% and 95% fractles of the posterior distributon.

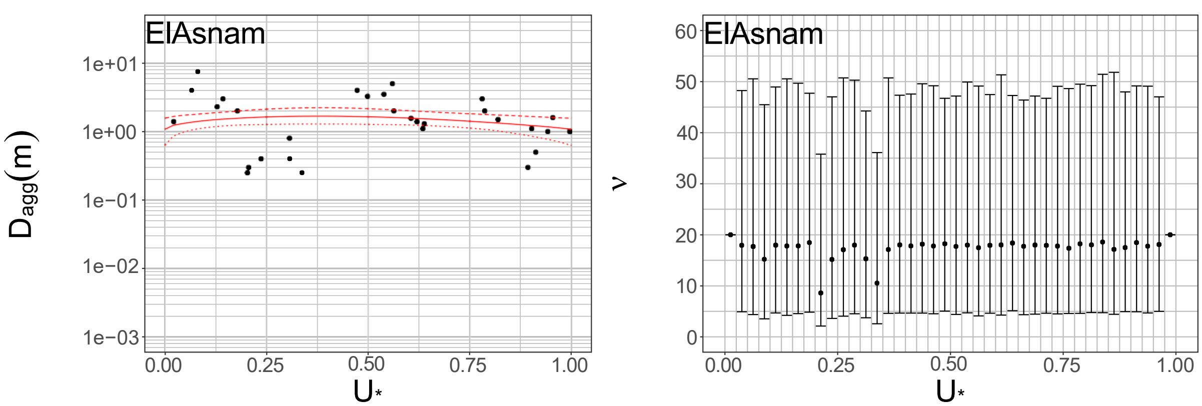

Figure B.58. Slip for ElAsnam, and ν of Student T distributon. Uncertainty bands are the 5% and 95% fractles of the posterior distributon.

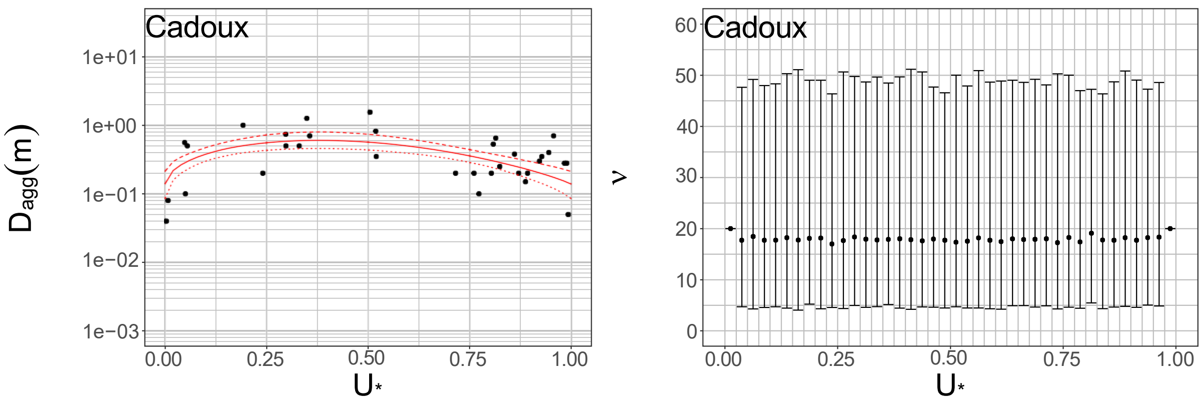

Figure B.59. Slip for Cadoux, and ν of Student T distributon. Uncertainty bands are the 5% and 95% fractles of the posterior distributon.

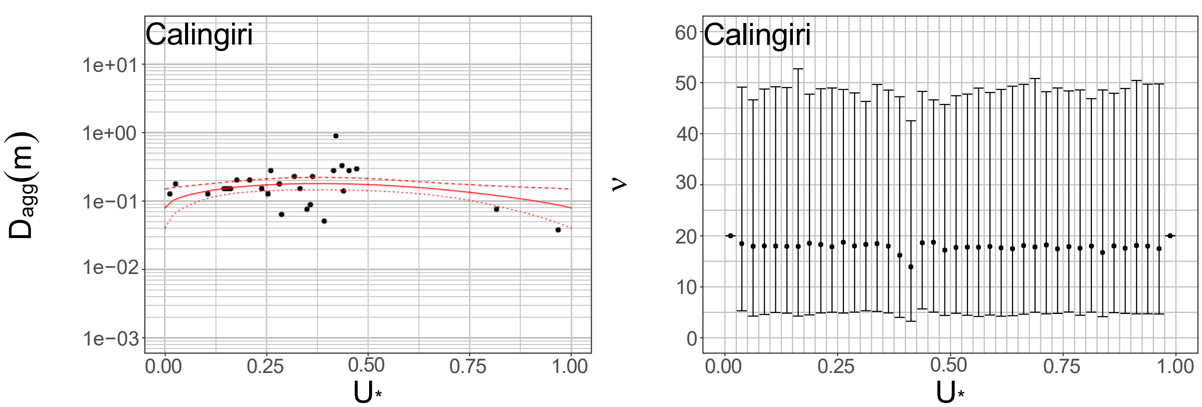

Figure B.60. Slip for Calingiri, and ν of Student T distributon. Uncertainty bands are the 5% and 95% fractles of the posterior distributon.

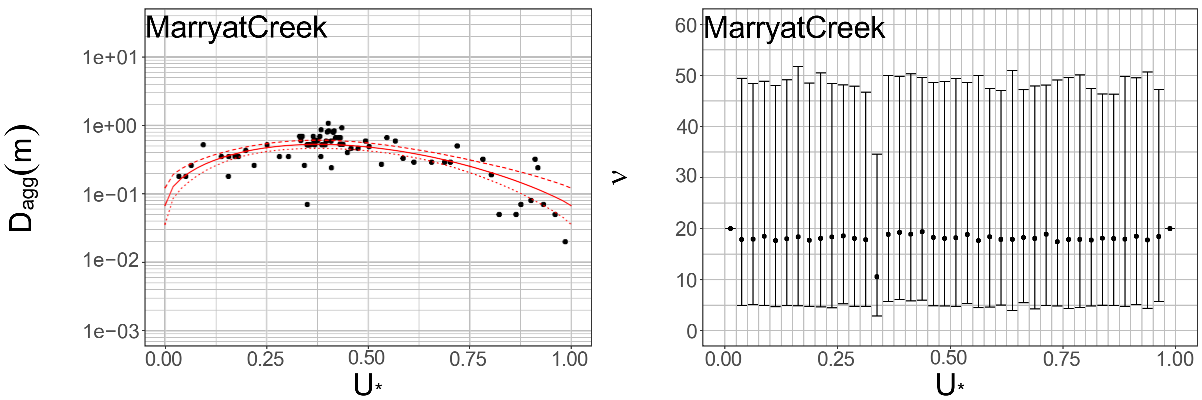

Figure B.61. Slip for MarryatCreek, and ν of Student T distributon. Uncertainty bands are the 5% and 95% fractles of the posterior distributon.

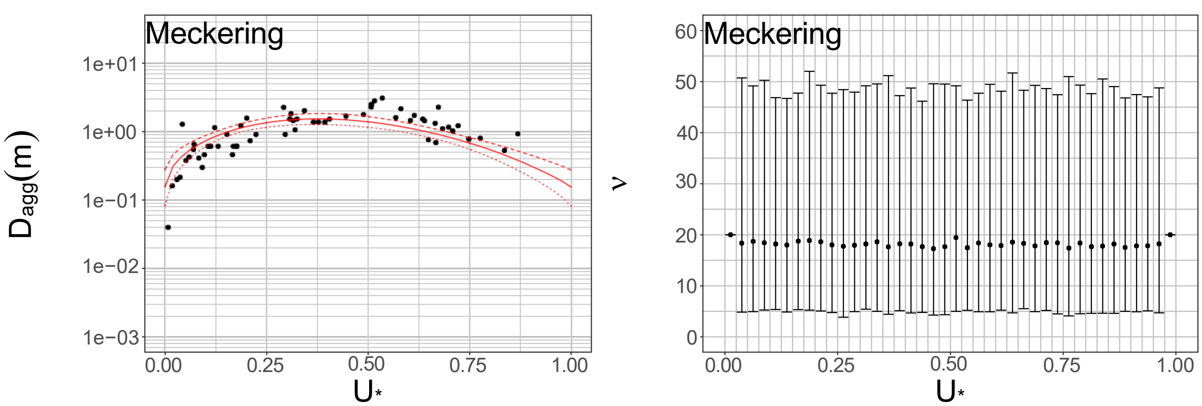

Figure B.62. Slip for Meckering, and ν of Student T distributon. Uncertainty bands are the 5% and 95% fractles of the posterior distributon.

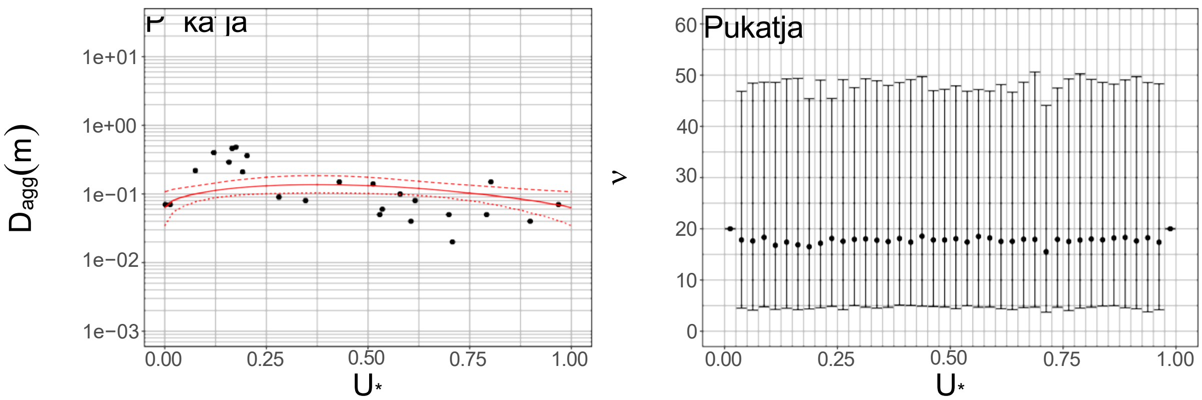

Figure B.63. Slip for Pukatja, and ν of Student T distributon. Uncertainty bands are the 5% and 95% fractles of the posterior distributon.

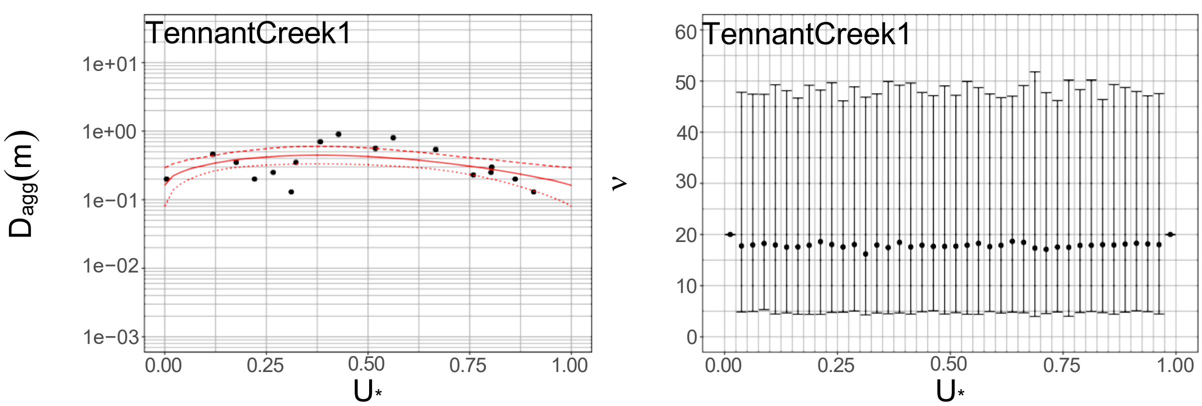

Figure B.64. Slip for TennantCreek1, and ν of Student T distributon. Uncertainty bands are the 5% and 95% fractles of the posterior distributon.

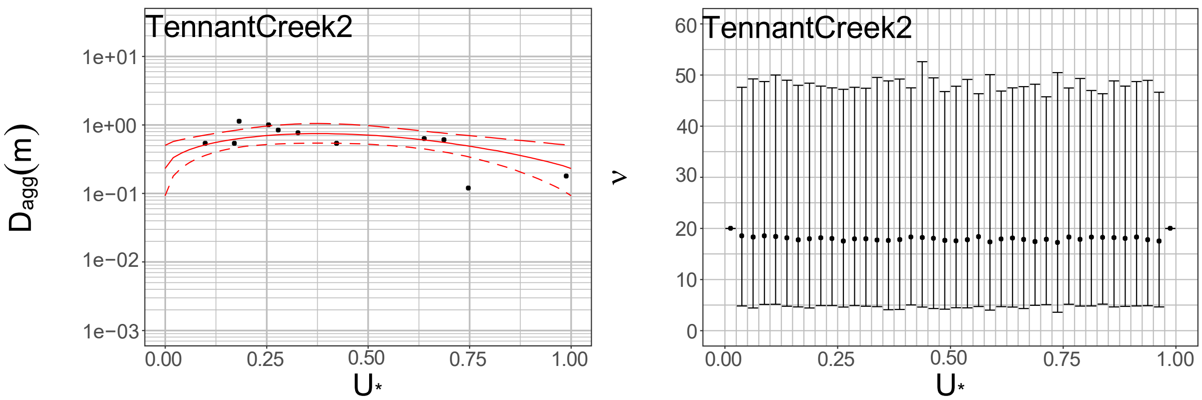

Figure B.65. Slip for TennantCreek2, and ν of Student T distributon. Uncertainty bands are the 5% and 95% fractles of the posterior distributon.

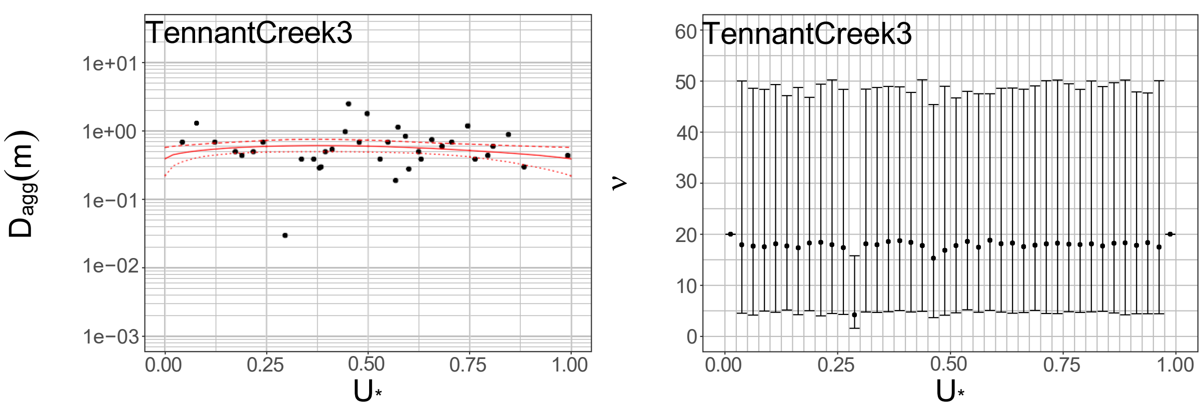

Figure B.66. Slip for TennantCreek3, and ν of Student T distributon. Uncertainty bands are the 5% and 95% fractles of the posterior distributon.

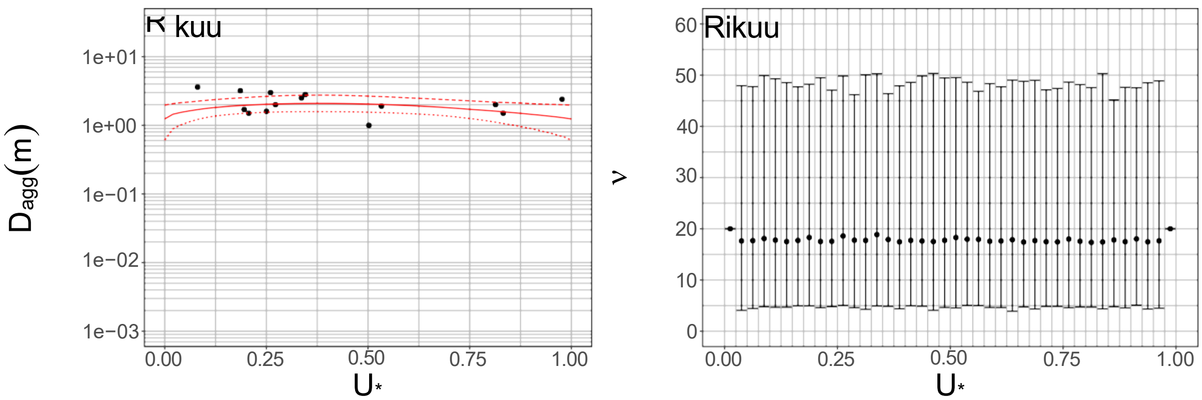

Figure B.67. Slip for Rikuu, and ν of Student T distributon. Uncertainty bands are the 5% and 95% fractles of the posterior distributon.

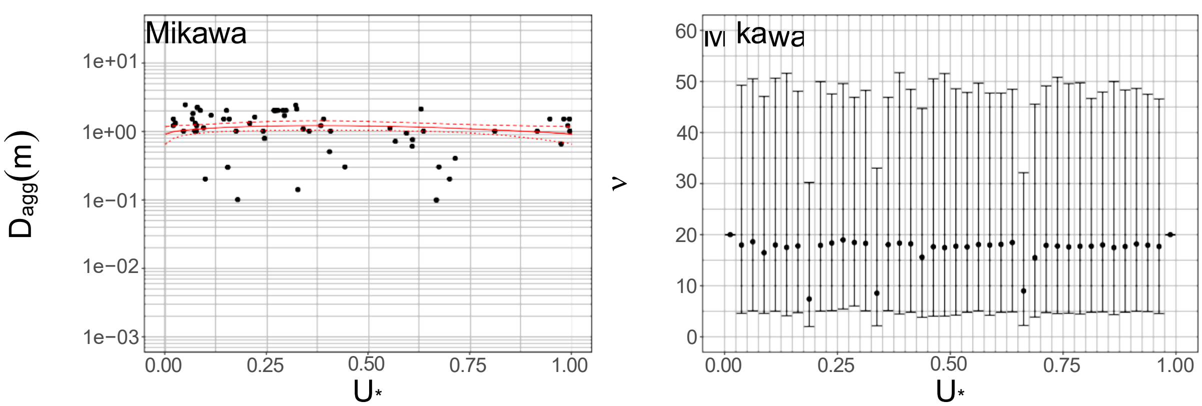

Figure B.68. Slip for Mikawa, and ν of Student T distributon. Uncertainty bands are the 5% and 95% fractles of the posterior distributon.

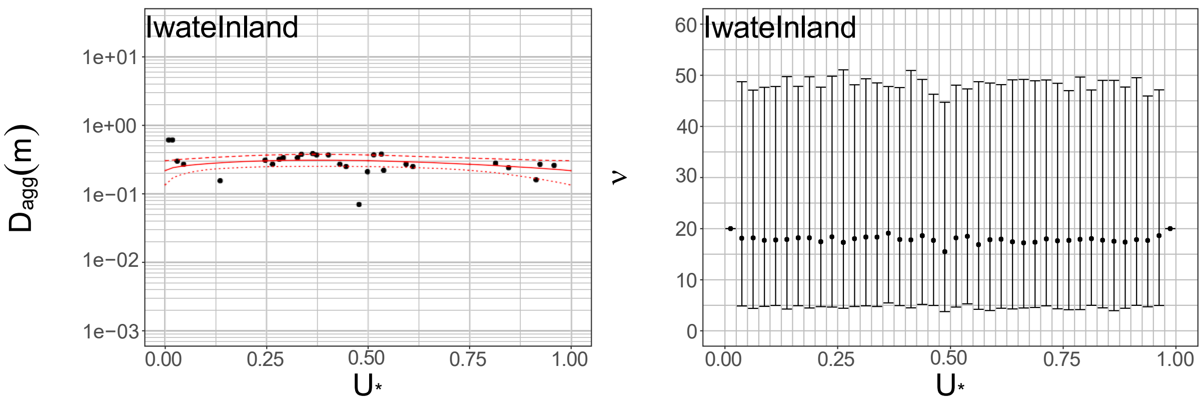

Figure B.69. Slip for IwateInland, and ν of Student T distributon. Uncertainty bands are the 5% and 95% fractles of the posterior distributon.

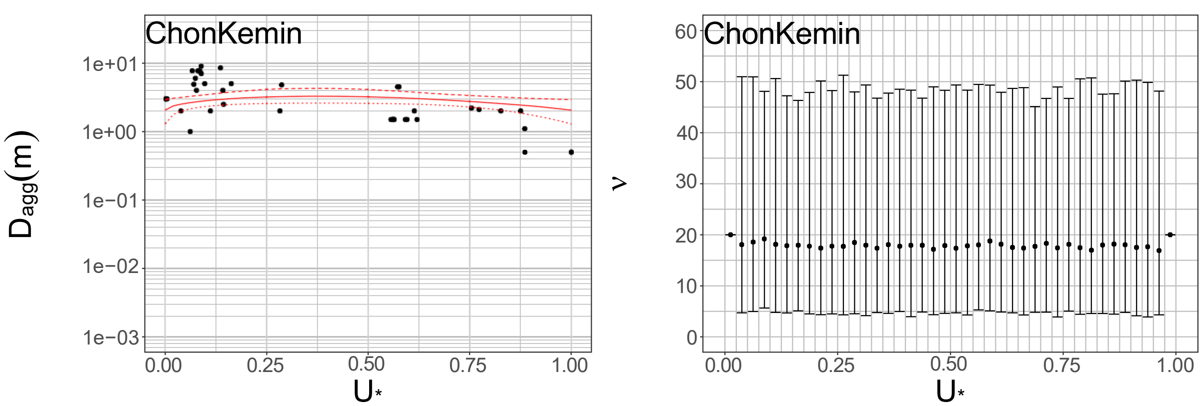

Figure B.70. Slip for ChonKemin, and ν of Student T distributon. Uncertainty bands are the 5% and 95% fractles of the posterior distributon.

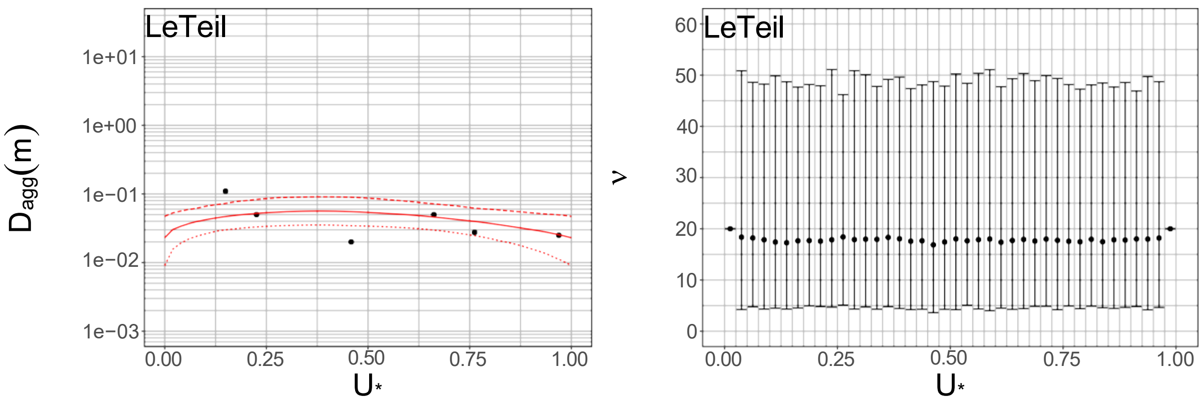

Figure B.71. Slip for LeTeil, and ν of Student T distributon. Uncertainty bands are the 5% and 95% fractles of the posterior distributon.

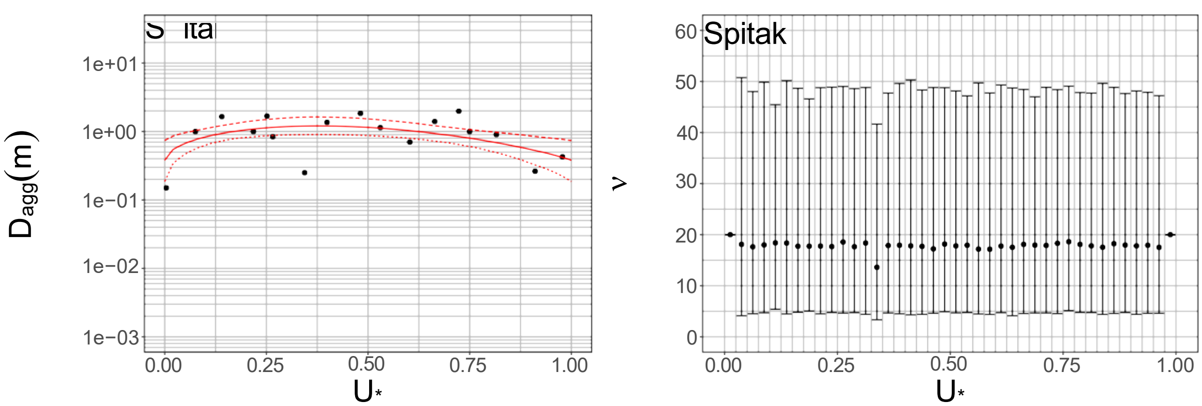

Figure B.72. Slip for Spitak, and ν of Student T distributon. Uncertainty bands are the 5% and 95% fractles of the posterior distributon.

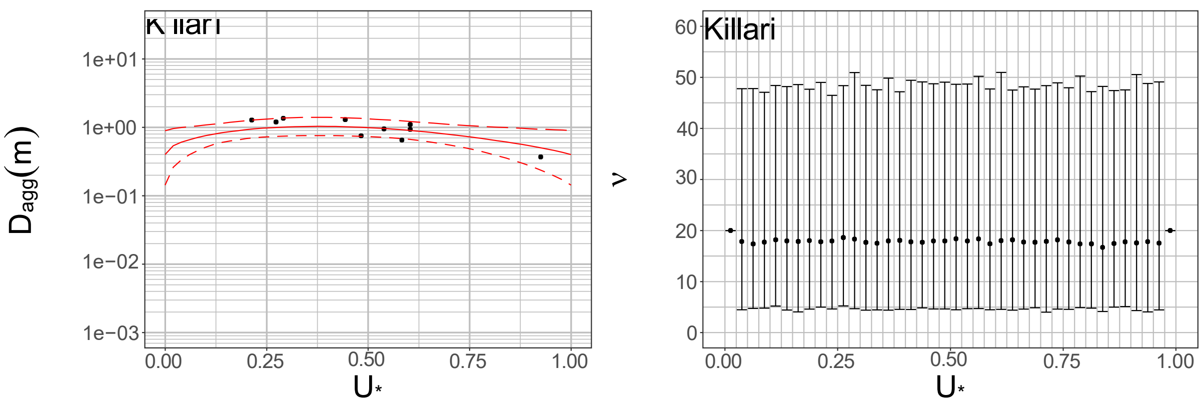

Figure B.73. Slip for Killari, and ν of Student T distributon. Uncertainty bands are the 5% and 95% fractles of the posterior distributon.